INFORMATION TO USERS

This manuscript has been reproduced from the microfilm master. UMI films the text directly from the original or copy submitted. Thus, some thesis and dissertation copies are in typewriter face, while others may be from any type of computer printer.

The quality of this reproduction is dependent upon the quality of the copy submitted. Broken or indistinct print, colored or poor quality illustrations and photographs, print bleedthrough, substandard margins, and improper alignment can adversely affect reproduction.

In the unlikely event that the author did not send UMI a complete manuscript and there are missing pages, these will be noted. Also, if unauthorized copyright material had to be removed, a note will indicate the deletion.

Oversize materials (e.g., maps, drawings, charts) are reproduced by sectioning the original, beginning at the upper left-hand corner and continuing from left to right in equal sections with small overlaps. Each original is also photographed in one exposure and is included in reduced form at the back of the book.

Photographs included in the original manuscript have been reproduced xerographically in this copy. Higher quality 6" x 9" black and white photographic prints are available for any photographs or illustrations appearing in this copy for an additional charge. Contact UMI directly to order.

UMI®

Bell & Howell Information and Learning
300 North Zeeb Road, Ann Arbor, MI 48106-1346 USA
800-521-0600

APPLICATION OF COMPLEX SPECTROSCOPIC TECHNIQUES TO THE CHARACTERIZATION OF PARTICLES IN SUSPENSION

By

STEVEN L. CARSON

A DISSERTATION PRESENTED TO THE GRADUATE SCHOOL
OF THE UNIVERSITY OF FLORIDA IN PARTIAL FULFILLMENT
OF THE REQUIREMENTS FOR THE DEGREE OF
DOCTOR OF PHILOSOPHY

UNIVERSITY OF FLORIDA

1999

UMI Number: 9935208

UMI Microform 9935208
Copyright 1999, by UMI Company. All rights reserved.

This microform edition is protected against unauthorized copying under Title 17, United States Code.

UMI
300 North Zeeb Road
Ann Arbor, MI 48103

ACKNOWLEDGEMENTS

The author wishes to express his gratitude and appreciation for several people who have provided support. The satisfaction of the author with this research could not have been as great without the research advice of Dr. Mark E. Orazem. His insights into the research reported in this document were of tremendous assistance. Assistance was also provided by the many members (past and present) of the Electrochemical Engineering Research Group at the University of Florida. Discussions with Pankaj Agarwal that took place several years ago were one element of inspiration for the error analysis research. Many discussions with Madhav Durbha were also instrumental in progressing that work. Paul Wojcik and Mike Membrino were often sounding boards for the ideas of the author. Their comments on experimental design and the theoretical basis for experiments were of great help. Doug Riemer was instrumental in conducting any research that required a PC. His comments on the content of the research were also valuable. Dr. Luis H. Garcia-Rubio was invaluable with his advice on the development of the Rotational Electrophoretic Spectroscopy prototype. He and Dr. Oscar D. Crisalle provided several ideas that expanded the scope of the research on the propagation of errors. Dr. James Winefordner and Dr. Ben Smith also provided useful comments on the application of light-scattering measurements in the RES measurement. Dr. Chang Park also provided a useful perspective for the research on the propagation of errors. The three sets of data measured with combined techniques that are discussed in Chapter 5 were provided by

Prof. Andrzej Lasia of from the Department of Chemistry at the University of Sherbrooke.

The author would also like to thank those people who provided an outlet for his ideas in a more informal setting. Tracy Lambert provided technical assistance when needed. Peggy Dougherty, Janice Harris, Shirley Kelly, and Nancy Krell were of tremendous assistance in getting anything accomplished through the red tape. This document could not have been written without the support of Daryl Harrison, Wilbur Woo, Bill Epling, Aaron Gregory, Mike Norfleet, Sean McLauglin, John Bradshaw, Charlie Jacobson, and Brent Mayfield, all of whom helped keep this research in perspective. Helpful comments were also provided by friends outside the university, including Alex Densmore, Jim Radford, Carl Roth, June Carson, Louis Carson, and Greg Borgard.

The author would also like to state his appreciation for the financial support of the Engineering Research Center for Particle Science and Technology at the University of Florida.

TABLE OF CONTENTS

page

ACKNOWLEDGEMENTS ii

LIST OF TABLES viii

LIST OF FIGURES xii

ABSTRACT xxiv

CHAPTER

1 INTRODUCTION 1

2 LITERATURE REVIEW: ELECTROKINETIC PHENOMENA 7

2.1 The Beginnings of Electrokinetics 9
2.2 Recent Theoretical Developments 11
2.2.1 Macroscopic Behavior and Surface Charge 12
2.2.2 Electrohydrodynamic Models 15
2.2.3 Oscillating Electric Fields 21
2.3 Technical Innovations and Experimental Observations 23
2.3.1 New Measurement Technologies 24
2.3.2 Electrokinetic Standard 27
2.4 Summary 28

3 DEVELOPMENT OF ROTATIONAL ELECTROPHORETIC SPECTROSCOPY 29

3.1 Background 29
3.2 Concepts for Design 31
3.3 Accomplishments 35
3.4 Conclusions 39

4 WEIGHTING STRATEGIES FOR COMPLEX NONLINEAR LEAST SQUARES REGRESSION 51

5 INFLUENCE OF INSTRUMENTATION ON ERROR STRUCTURE 58

5.1 Motivation 58
5.2 Methods for Impedance Calculation 62
5.2.1 Frequency Response Analysis 63
5.2.2 Lissajous Parameterization 64
5.2.3 Phase Sensitive Detection 65
5.2.4 Peak Detection 67
5.3 Simulation of Impedance Systems 68
5.3.1 Time-Domain Noise 69
5.3.2 Application of Measurement Techniques 71
5.4 Results of Simulations 72
5.4.1 Simulations with Peak Detection 73
5.4.2 Simulations with Phase Sensitive Detection 74
5.4.2.1 Additive Noise 75
5.4.2.2 Proportional Noise 77
5.5 Discussion 79
5.5.1 Rectangular Coordinate Error Structure Due to Errors in Polar Measurement 80
5.5.2 Source of Bias Errors in Phase Sensitive Detection 82
5.5.3 Condition on Spectroscopy Errors by the Kramers-Kronig Relations 83
5.6 Conclusions 85

6 PROPAGATION OF ERRORS IN COMPLEX CURRENT AND VOLTAGE 106

6.1 Variance of Real and Imaginary Impedance from Complex Taylor Series Expansions of Complex Impedance 107
6.2 Variance of Real and Imaginary Impedance from the Real Taylor Series Expansions of the Impedance Components 112
6.3 Vector Representation of Variance in Impedance 117
6.4 Simulations Studies of Taylor Series Expansion for Variance of Complex Impedance in Rectangular Form 123
6.5 Taylor Series Expansion for Variance of Complex Impedance in Polar Form 128
6.6 Simulation Studies of Taylor Series Expansion for Variance of Complex Impedance in Polar Form 132
6.7 Conclusions 134

7 PROPAGATION OF COLORED NOISE IN TIME-DOMAIN SIGNALS 160

7.1 Simulated Measurement of Complex Impedance 161
7.2 Taylor Series 163
7.3 Discussion 166
7.4 Conclusions 167

8 TRANSFORMATION OF ADDITIVE TIME-DOMAIN NOISE INTO FREQUENCY-DOMAIN ERRORS 185

8.1 Variance as a Result of Frequency Response Analysis 187
8.1.1 Functional Variance Defined by Expectation Integral over Time 188
8.1.2 Simulation Studies of the Variance Defined by Expectation Integral over Time 190
8.1.2.1 CASE 1 191
8.1.2.2 CASE 2 192
8.1.2.3 CASE 3 192
8.1.2.4 Influence of System on Propagation of Errors 193
8.1.3 Sample Variance Based on Expectation of Discrete Measurements 200
8.1.4 Simulation Studies of Variance Based on Expectation in a Sampling Sense 201
8.2 Variance as a Result of Phase Sensitive Detection 202
8.2.1 Variance Defined by Expectation Integral over Time 203
8.2.2 Variance Based on Expectation in a Sampling Sense 206
8.3 Conclusions 207

9 CONVERGENCE OF THE STANDARD DEVIATION OF IMPEDANCE AT A SINGLE FREQUENCY 221

10 CONCLUSIONS 235

10.1 Rotational Electrophoretic Spectroscopy 235
10.2 Characterization of Frequency-Domain Errors 237

11 SUGGESTIONS FOR FUTURE WORK 241

11.1 Rotational Electrophoretic Spectroscopy 241
11.2 Propagation of Errors into Complex Spectra 242

APPENDICES

A TAYLOR SERIES EXPANSION OF VARIANCE 244

A.1 Variance of Real and Imaginary Impedance from Complex Taylor Series Expansion of Complex Impedance 244
A.2 Variance of Real and Imaginary Impedance from the Real Taylor Series Expansions of the Impedance Components 245
A.3 Vector Representation of Variance in Impedance 249

B DERIVATION OF VARIANCE IN FREQUENCY-DOMAN ERRORS FROM ADDITIVE ERRORS IN TIME-DOMAIN 257

B.1 Variance for Frequency Response Analysis 257
B.1.1 Variance Defined by Expectation Integral over Time 258
B.1.2 Variance Based on Expectation in a Sampling Sense 264
B.2 Sample Variance as a Result of Phase Sensitive Detection 272

BIBLIOGRAPHY 278

BIOGRAPHICAL SKETCH 286

LIST OF TABLES

Table page

5.1. Student t-test ratio for impedance spectra measured with a combination of techniques. 88

5.2. Student t-test values for matrix of simulations and assessment techniques. Additive noise level was 10% of input signal amplitude unless otherwise noted. 88

5.3. Range of values of variance in stochastic errors for matrix of simulations and assessment techniques. Additive noise level (INPUT and OUTPUT) was 10% of input signal amplitude unless otherwise noted. Transformed noise (Z*INPUT) was proportional to the impedance at the given frequency. 89

5.4. Student t-test (applied to ratio of variances in stochastic errors in the real and imaginary impedances) ratios for matrix of simulations and assessment techniques. Additive noise level was 10% of input signal amplitude unless otherwise noted. 89

5.5. Range of values of variance in stochastic errors for matrix of simulations and assessment techniques. Additive noise level (INPUT and OUTPUT) was 10% of input signal amplitude unless otherwise noted. Transformed noise (Z*INPUT) was proportional to the impedance at the given frequency. 90

5.6. Student t-test (applied to ratio of variances in stochastic errors in the real and imaginary impedances) ratios for matrix of simulations and assessment techniques. Additive noise level was 10% of input signal amplitude unless otherwise noted. 90

6.1. Student's t-tests for trivial solution conditions for equality of variance in the real and imaginary impedances described by the linear Taylor series expansion. Calculations were conducted for the CASE 1 scenario, noise added to the input and output signal, with output noise including input noise transformed by the system. 137

6.2. Student's t-tests for trivial solution conditions for equality of variance in the real and imaginary impedances described by the linear Taylor series expansion. Calculations were conducted for the CASE 2 scenario, noise added to the input and output signal, with output noise including input noise transformed by the system. Noise was not added to the current, so there was no variance in the complex current components. 138

6.3. Student's t-tests for trivial solution conditions for equality of variance in the real and imaginary impedances described by the linear Taylor series expansion. Calculations were conducted for the CASE 3 scenario, noise added to the input and output signal, with output noise including input noise transformed by the system. 139

6.4. Student's t-tests for difference in variances in impedance magnitude and phase angle and for the cross-covariance between the impedance magnitude and phase angle equal to zero 140

7.1. Range of values of variance in stochastic errors for matrix of simulations and assessment techniques. Additive noise level (INPUT and OUTPUT) was 10% of input signal amplitude unless otherwise noted. Transformed noise (Z*INPUT) was proportional to the impedance at the given frequency.
(T) Trapezoidal quadrature rule used in FRA calculation.
(B) Bode quadrature rule used in FRA calculation. 169

7.2. Student t-test (applied to ratio of variances in stochastic errors in the real and imaginary impedances) ratios for matrix of simulations and assessment techniques. Additive noise level was 10% of input signal amplitude unless otherwise noted.
(T) Trapezoidal quadrature rule used in FRA calculation.
(B) Bode quadrature rule used in FRA calculation.
* Variance of stochastic errors was often zero. 169

7.3. Student's t-test ratios for the conditions that satisfy the equality of variance in the real and imaginary impedances described by the linear Taylor series expansion. Calculations were conducted for all three cases, with the additive noise having a colored distribution (skewed with a non-zero mean) 170

8.1. Student's t-test results for ratio of variance in real impedance to variance in imaginary impedance calculated through Taylor series expansions for variance in complex components of the impedance. Variance vector was calculated as functional variance (F) through the integral equations and as sample variance (S) from observed replicate values of the complex components of the voltage and current signals 211

8.2. Student's t-tests for trivial solution conditions for equality of variance in the real and imaginary impedances described by the linear Taylor series expansion. Calculations were conducted for the CASE 1 scenario, noise added to the input and output signal, without input noise transformed by the system 212

8.3. Student's t-tests for trivial solution conditions for equality of variance in the real and imaginary impedances described by the linear Taylor series expansion. Calculations were conducted for the CASE 3 scenario, noise added to the input and output signal, with output noise including input noise transformed by the system 212

8.4. Student's t-test results for ratio of variance in real impedance to variance in imaginary impedance calculated through Taylor series expansions for variance in complex components of the impedance. Variance vector was calculated as the analytical sample variance (A) through the integral equations and as sample variance (S) from observed replicate values of the complex components of the voltage and current signals 213

8.5. Student's t-test results for the difference between and ratio of the ratio of variance in real impedance to variance in imaginary impedance calculated through Taylor series expansions for variance in complex components of the impedance. The variance vector was calculated as the analytical sample variance through the integral equations and as sample variance from observed replicate values of the complex components of the voltage and current signals 213

LIST OF FIGURES

Figure page

3.1. Schematic illustration of the influence of particle orientation on the light reaching a photo-detector 42

3.2. Expected photodiode responses at three representative frequencies of applied potential oscillating about zero. (a) high frequency. (b) characteristic frequency for rotation. (c) low frequency. 43

3.3. Expected photodiode responses at three representative frequencies of applied potential with imposed bias. (a) high frequency. (b) characteristic frequency for rotation. (c) low frequency. 44

3.4. Schematic illustration of the rotational electrophoretic spectroscopy system. 45

3.5. Borosilicate fibers 46

3.6. Ensemble of borosilicate fibers studied using the RES technique 46

3.7. Transient response in photodiode signal proportional to forward scatter from a suspension of the borosilicate fibers 47

3.8. Power spectrum of applied voltage signal at 784 mHz. 48

3.9. Power spectrum of responding photodiode signal. Primary peak is at 784 mHz. 48

3.10. Spectrum of magnitude of transfer function calculated for the single frequency sine wave of applied potential at 748 mHz. 49

3.11. Magnitude spectrum of the RES transfer function for a suspension of rod-like borosilicate fibers in water. 50

5.1. The ratio of variances in stochastic errors in the real impedance to those in the imaginary impedance as a function of frequency for the four cases of System 1: the FRA portion, the PSD portion, the entire spectrum, and the Kramers-Kronig consistent portion of the entire spectrum. The F-test probability limits are also plotted. The ratio for the PSD portion is not scattered about one, but generally falls within the 99% confidence limit. The ratios for the other three cases are scattered about one, and generally fall within the 99% confidence limit. The F-test suggest that the variances are equal for all four cases. The least confidence in that equality is for the PSD case..... 91

5.2. The ratio of variances in stochastic errors in the real impedance to those in the imaginary impedance as a function of frequency for the four cases of System 2: the FRA portion, the PSD portion, the entire spectrum, and the Kramers-Kronig consistent portion of the entire spectrum. The F-test probability limits are also plotted. The ratios for the all four cases are scattered about one, and generally fall within the 99% confidence limit. The F-test suggest that the variances are equal for all four cases. 92

5.3. The ratio of variances in stochastic errors in the real impedance to those in the imaginary impedance as a function of frequency for the four cases of System 1: the FRA portion, the PSD portion, the entire spectrum, and the Kramers-Kronig consistent portion of the entire spectrum. The F-test probability limits are also plotted. The ratio for the PSD portion is not scattered about one, but generally falls within the 99% confidence limit. The ratios for the other three cases are scattered about one, and generally fall within the 99% confidence limit. The F-test suggest that the variances are equal for all four cases. The least confidence in that equality is for the PSD case 93

5.4. Assessment of Fourier coefficients is achieved by integrating the in-phase and out-of-phase products of the voltage and current signals over each cycle. The impedance is calculated as the ratio of the complex representation of the voltage to the current..... 94

5.5. Phase sensitive detection maximizes the integral of the product of the measured signal and a square wave of the same frequency with respect to phase angle of the square wave. 95

5.6. Distribution of values for typical waveform of Gaussian white noise. Solid black line along middle of chart is equal to zero. 96

5.7: Distribution of frequency-domain errors of the real impedance calculated 500 times using the FRA technique at 1 kHz with Gaussian noise (see 5.6) added to the input signal and output signal in the time-domain. 97

5.8. Distribution of logarithm of ratio of variances of the stochastic errors in the real and imaginary impedance calculated using Lissajous parameterization, with Gaussian noise added to input signal and output signal (in time-domain). 98

5.9. Distribution of logarithm of ratio of variances of the stochastic errors in the real and imaginary impedance calculated using Phase Sensitive Detection with Gaussian noise added to input signal and output signal (in time-domain). 99

5.10. F-test for ratio of variance in real impedance to variance in imaginary impedance as a function of frequency. Impedance calculated using the FRA technique (Bode quadrature) with Gaussian noise added to both the input and output signals (CASE 3). The ratio is generally scattered around unity, and most points fall within the 1% level of significance. Thus, there is 99% confidence that the hypothesis that the variances are unequal is false. 100

5.11. F-test for ratio of variance in real impedance to variance in imaginary impedance as a function of frequency. Impedance calculated using the PSD technique with Gaussian noise added to both the input and output signals (CASE 3). The ratio is not scattered around unity, and most points fall outside the 1% level of significance. Thus, there is 99% confidence that the hypothesis that the variances are unequal is true. 101

5.12. F-test for ratio of variance in real impedance to variance in imaginary impedance as a function of frequency. Impedance calculated using the FRA technique (Bode quadrature) with Gaussian proportional noise added to both the input and output signals (CASE 3). The ratio is not scattered around unity. The ratio scaled by one-third, however, is scattered around unity, and falls within the 1% level of significance. 102

5.13. F-test for ratio of variance in real impedance to variance in imaginary impedance as a function of frequency. Impedance calculated using the PSD technique with Gaussian noise added to both the input and output signals (CASE 3). The ratio is generally scattered around unity, and most points fall inside the 1% level of significance. Thus, there is 99% confidence that the hypothesis that the variances are unequal is false. 103

5.14. Distribution of stochastic errors in the real impedance at 1 kHZ calculated using the PSD technique. The errors were calculated as the difference between the measured impedance and the theoretical impedance spectrum (used as the system in the simulation). The mean of this distribution is biased away from zero. The corresponding errors from the FRA calculated impedance are not distributed with a bias. 104

5.15. Distribution of errors in phase angle and distribution of the cosine of those errors. A Gaussian distribution is extremely skewed and biased through the cosine operation. 105

6.1. Ratio of Taylor series for variance in the real impedance to variance in the imaginary impedance when Phase Sensitive Detection is used to calculate the impedance. Note that in general the ratio does not satisfy the F-test for 5%. Therefore for all three cases, there is less than a 5% probability that the Taylor series for the variances are equal. 141

6.2. Ratio of Taylor series for variance in the real impedance to variance in the imaginary impedance when Frequency Response Analysis is used to calculate the impedance. Note that in general the ratio does satisfy the F-test for 5%. Therefore for all three cases, there is less than a 5% probability that the Taylor series for the variances are not equal. 142

6.3. Ratio of variance in the real voltage measurement to the variance in the imaginary voltage measurement. Calculation was made using the Phase Sensitive Detection technique. Note that the ratios for all three cases often fall outside the F-test 5% probability limits. Therefore, there is less than 95% probability that the variances are not equal. 143

6.4. Ratio of variance in the real voltage measurement to the variance in the imaginary voltage measurement. Calculation was made using the FRA technique. Note that the ratios for all three cases all fall inside the F-test 5% probability limits. Therefore, there is less than 5% probability that the variances are not equal. 144

6.5. Ratio of variance in the real current measurement to the variance in the imaginary current measurement. Calculation was made using the Phase Sensitive Detection technique. Note that the ratios for all three cases often fall outside the F-test 5% probability limits. Therefore, there is less than 95% probability that the variances are not equal. 145

6.6. Ratio of variance in the real current measurement to the variance in the imaginary current measurement. Calculation was made using the FRA technique. Note that the ratios for all three cases all fall inside the F-test 5% probability limits. Therefore, there is less than 5% probability that the variances are not equal. 146

6.7. Covariance between real and imaginary voltage components calculated using Phase Sensitive Detection. The trivial solution to the equality of variances in the complex impedance requires that this covariance be equal to zero. 147

6.8. Covariance between real and imaginary voltage components calculated using Frequency Response Analysis. The trivial solution to the equality of variances in the complex impedance requires that this covariance be equal to zero. 148

6.9. Covariance between real and imaginary current components calculated using Phase Sensitive Detection. The trivial solution to the equality of variances in the complex impedance requires that this covariance be equal to zero. 149

6.10. Covariance between real and imaginary current components calculated using Frequency Response Analysis. The trivial solution to the equality of variances in the complex impedance requires that this covariance be equal to zero. 150

6.11. Ratio of cross-covariances between real current and voltage to imaginary current and voltage components calculated using Phase Sensitive Detection. The trivial solution to the equality of variances in the complex impedance requires that this ratio be unity. For all three cases, the ratios generally fall outside the F-test 5% probability limits. There is 95% probability that these cross-covariances are not equal at those frequencies. 151

6.12. Ratio of cross-covariances between real current and voltage to imaginary current and voltage components calculated using Frequency Response Analysis. The trivial solution to the equality of variances in the complex impedance requires that this ratio be unity. For all three cases, the ratios generally fall inside the F-test 5% probability limits. There is 5% probability that these cross-covariances are not equal at those frequencies. 152

6.13. Ratio of cross-covariance between real voltage and imaginary current to cross-covariance between imaginary voltage and real current components calculated using Phase Sensitive Detection. The trivial solution to the equality of variances in the complex impedance requires that this ratio be the negative of the other. For all three cases, the ratios generally fall outside the F-test 5% probability limits. There is 95% probability that these cross-covariances are not equal at those frequencies. 153

6.14. Ratio of cross-covariance between real voltage and imaginary current to cross-covariance between imaginary voltage and real current components calculated using Frequency Response Analysis. The trivial solution to the equality of variances in the complex impedance requires that this ratio be the negative of the other. For all three cases, the ratios generally fall outside the F-test 5% probability limits. There is 95% probability that these cross-covariances are not equal at those frequencies. 154

6.15. Ratios of variances in voltage components for CASE 2 to variances in voltage components for CASE 1, in which Gaussian noise was introduced into the signals. These are the ratios of additive noise to noise transformed by the system. The ratios are clearly frequency dependent, and correlated to the reciprocal of the square of the impedance magnitude. The ratios scaled by the reciprocal of the square of the impedance magnitude are generally scattered about unity 155

6.16. Difference in variances of impedance magnitude and phase angle for PSD calculation. The difference should be equal to zero over the spectrum. 156

6.17. Difference in variances of impedance magnitude and phase angle for FRA calculation. The differences are scattered about zero over the spectrum. 157

6.18. Cross-covariance between impedance magnitude and phase angle for PSD calculation. The cross-covariance should be equal to zero over the spectrum for the imaginary part of the Taylor series expansion for variance in the real and imaginary impedance to be equal to zero. 158

6.19. Cross-covariance between impedance magnitude and phase angle for FRA calculation. The cross-covariance should be equal to zero over the spectrum for the imaginary part of the Taylor series expansion for variance in the real and imaginary impedance to be equal to zero. 159

7.1. Distribution of values for typical waveform of colored noise. Solid black line on left of chart is zero. 171

7.2. Distribution of frequency-domain errors of the real impedance calculated 500 times at 1 MHz with colored noise (see Figure 7.1) added to the input signal, output signal in the frequency-domain, and output signal in the time-domain. 172

7.3. F-test for ratio of variance in real impedance to variance in imaginary impedance as a function of frequency. Impedance calculated using the FRA technique (Bode quadrature) with colored noise added to both the input and output signals (CASE 3). The ratio is generally scattered around unity, and most points fall within the 1% level of significance. Thus, there is 99% confidence that the hypothesis that the variances are unequal is false. 173

7.4. Distribution of the logarithm of the ratio of the variance in the real impedance to the variance in the imaginary impedance calculated for CASE 3. This ratio is normally distributed about zero. Thus, the expectations of the variances over the spectrum are equivalent for the FRA measurement technique. 174

7.5. F-test for ratio of variance in real impedance to variance in imaginary impedance as a function of frequency. Impedance calculated using the PSD technique with colored noise added to both the input and output signals (CASE 3). The ratio is not scattered around unity, and most points fall outside the 1% level of significance. Thus, there is 99% confidence that the hypothesis that the variances are unequal is true. 175

7.6. Distribution of the logarithm of the ratio of the variance in the real impedance to the variance in the imaginary impedance calculated for CASE 3. This ratio is normally distributed, but not about zero. Thus, the expectations of the variances over the spectrum are not equivalent for the PSD measurement technique. 176

7.7. Ratio of Taylor series for variance in the real impedance to variance in the imaginary impedance when Frequency Response Analysis is used to calculate the impedance and when the introduced noise in the time-domain had a colored, or skewed distribution. Note that in general the ratio does satisfy the F-test for 5%. Therefore for all three cases, there is less than a 5% probability that the Taylor series for the variances are not equal. 177

7.8. Ratio of variance in the real voltage measurement to the variance in the imaginary voltage measurement when colored noise was added to the time-domain signals. Calculation was made using the FRA technique. Note that the ratios for all three cases all fall inside the F-test 5% probability limits. Therefore, there is less than 5% probability that the variances are not equal. 178

7.9. Ratio of variance in the real current measurement to the variance in the imaginary current measurement when colored noise was added to the time-domain signals. Calculation was made using the FRA technique. Note that the ratios for all three cases all fall inside the F-test 5% probability limits. Therefore, there is less than 5% probability that the variances are not equal. 179

7.10. Covariance between real and imaginary voltage components when colored noise was added to the time-domain signals. Impedance was calculated using Frequency Response Analysis. The trivial solution to the equality of variances in the complex impedance requires that this covariance be zero. 180

7.11. Covariance between real and imaginary current components when colored noise was added to the time-domain signals. Impedance was calculated using Frequency Response Analysis. The trivial solution to the equality of variances in the complex impedance requires that this covariance be zero. 181

7.12. Ratio of cross-covariances between real current and voltage to imaginary current and voltage components calculated using Frequency Response Analysis. Noise introduced in the time-domain had a colored, or skewed, distribution. The condition for the equality of variances in the complex impedance requires that this ratio be unity. For all three cases, the ratios generally fall inside the F-test 5% probability limits. There is 5% probability that these cross-covariances are not equal at those frequencies. 182

7.13. Ratio of cross-covariances between imaginary current and real voltage to real current and imaginary voltage components calculated using Frequency Response Analysis. Noise introduced in the time-domain had a colored, or skewed, distribution. The condition for the equality of variances in the complex impedance requires that this ratio be unity. The ratio is generally scattered around one. 183

7.14. Ratios of variances in voltage components for CASE 2 to variances in voltage components for CASE 1, in which colored, or skewed, noise was introduced into the signals. These are the ratios of additive noise to noise transformed by the system. The ratios are clearly frequency dependent, and correlated to the reciprocal of the square of the impedance magnitude. The ratios scaled by the reciprocal of the square of the impedance magnitude are generally scattered about unity. 184

8.1. F-test for CASE 1, in which noise was added to input and output signals and not transformed through system. Functional variance is calculated through the derived integral equations, while the sample variance was calculated by sample expectation of the observed replicate calculations of the complex components of the voltage and current signals. 214

8.2. F-test for CASE 2, in which noise was added to input signal and transformed through system. Functional variance is calculated through the derived integral equations, while the sample variance was calculated by sample expectation of the observed replicate calculations of the complex components of the voltage and current signals. 215

8.3. F-test for CASE 3, in which noise was added to input and output signals and transformed through system. Functional variance was calculated through the derived integral equations, while the sample variance was calculated by sample expectation of the observed replicate calculations of the complex components of the voltage and current signals. 216

8.4. Auto-correlation function for noise in current signal when frequency was 10 kHz. 217

8.5. Auto-correlation function for noise in voltage signal when frequency was 10 kHz. Noise in voltage signal was transformed by the system from the noise in the current signal. 218

8.6. Integrands functions for the variance in real and imaginary voltage and real and imaginary current. (a) Integrand in voltage is significantly different than integrand in current. (b) Integrand for real voltage is different that integrand for imaginary voltage. 219

8.7. F-test for sample variance simulation, in which noise was added to input and output signals and transformed through system. The integral form of the sample variance was calculated through the derived integral equations, while the sample variance was calculated by sample expectation of the observed replicate calculations of the complex components of the voltage and current signals. 220

9.1. Convergence of impedance calculated using the FRA algorithm as a function of cycle number as defined by equation (9.1). At a given frequency, the average value of the impedance was calculated over all cycles up to the value of n. The plotted mean, median, maximum, and minimum was then calculated at each cycle number n over all frequencies in the spectrum. 225

9.2. Convergence of impedance calculated using the PSD algorithm as a function of cycle number as defined by equation (9.1). At a given frequency, the average value of the impedance was calculated over all cycles up to the value of n. The plotted mean, median, maximum, and minimum was then calculated at each cycle number n over all frequencies in the spectrum. 226

9.3. Convergence of impedance calculated using the FRA algorithm as a function of cycle number as defined by equation (9.2). At a given frequency, the average value of the impedance was calculated over all cycles up to the value of n. The plotted mean, median, maximum, and minimum was then calculated at each cycle number n over all frequencies in the spectrum. 227

9.4. Convergence of impedance calculated using the PSD algorithm as a function of cycle number as defined by equation (9.2). At a given frequency, the average value of the impedance was calculated over all cycles up to the value of n. The plotted mean, median, maximum, and minimum was then calculated at each cycle number n over all frequencies in the spectrum. 228

9.5. Convergence of impedance calculated using the FRA equation (9.3). At a given frequency, the average value of the impedance was calculated over all cycles up to the value of n. The plotted mean, median, maximum, and minimum was then calculated at each cycle number n over all frequencies in the spectrum. 229

9.6. Convergence of impedance calculated using the PSD equation (9.3). At a given frequency, the average value of the impedance was calculated over all cycles up to the value of n. The plotted mean, median, maximum, and minimum was then calculated at each cycle number n over all frequencies in the spectrum. 230

9.7. Convergence of impedance calculated using the FRA equation (9.6). At a given frequency, the average value of the impedance was calculated over all cycles up to the value of n. The plotted mean, median, maximum, and minimum was then calculated at each cycle number n over all frequencies in the spectrum. 231

9.8. Convergence of impedance calculated using the FRA equation (9.7). At a given frequency, the average value of the impedance was calculated over all cycles up to the value of n. The plotted mean, median, maximum, and minimum was then calculated at each cycle number n over all frequencies in the spectrum 232

9.9. Convergence of impedance calculated using the PSD equation (9.6). At a given frequency, the average value of the impedance was calculated over all cycles up to the value of n. The plotted mean, median, maximum, and minimum was then calculated at each cycle number n over all frequencies in the spectrum 233

9.10. Convergence of impedance calculated using the PSD equation (9.7). At a given frequency, the average value of the impedance was calculated over all cycles up to the value of n. The plotted mean, median, maximum, and minimum was then calculated at each cycle number n over all frequencies in the spectrum 234

Abstract of Dissertation Presented to the Graduate School
of the University of Florida in Partial Fulfillment of the
Requirements for the Degree of Doctor of Philosophy

APPLICATION OF COMPLEX SPECTROSCOPIC TECHNIQUES TO THE CHARACTERIZATION OF PARTICLES IN SUSPENSION

By

Steven L. Carson

May, 1999

Chairman: Professor Mark E. Orazem
Major Department: Chemical Engineering

A new complex spectroscopy technique for the characterization of particles in suspension was developed which integrates electrochemical impedance spectroscopy and UV/Vis light scattering. The technique was designed to characterize the particle size distribution, shape, and surface charge heterogeneity. Rotational electrophoretic spectroscopy (RES) measures the rotational electrophoretic response to an applied potential perturbation. Light-scattering measurements were demonstrated to be a reasonable method for capturing the change of orientation of particles due to their rotational electrophoretic mobility. An oscillatory light-scattering response was measured

for a ensemble of borosilicate fibers rotating in response to an applied oscillatory electric field. The two AC signals were analyzed to determine the magnitude of a complex transfer function describing the relationship between the light scattered by rotating non-spherical particles and the perturbing alternating electric field.

In support of the development of RES, infrastructure was developed for the assessment and characterization of errors in spectroscopy measurements. The propagation of errors from the time domain into the frequency domain was studied by numerical simulation and by a formal statistical analysis. The variance of stochastic errors in spectroscopy measurements was defined by a Taylor series of integral transforms of random noise in the constituent time-domain signals. The statistical analysis was conducted for four spectroscopy measurement techniques. This work demonstrated that, while the error structure of complex impedance measurements was dependent upon the employed measurement technology, the errors were always normally distributed in the frequency domain. This result, seen even for colored noise in the time domain signals, can be regarded to be a consequence of the central limit theorem. With the exception of measurement techniques that introduced a bias in the error structure, the variance for real and imaginary parts of the spectrum were found to be equal. These results are general and can be applied to any spectroscopy measurement of stationary and causal systems. This work supports the concept that the correlations between errors in complex spectroscopy measurements are a condition of the Kramers-Kronig relations.

CHAPTER 1
INTRODUCTION

Complex spectroscopy techniques are employed in a diverse range of disciplines for a broad array of applications. In comparison to time-domain measurements with a single measurement at a single time, the complex measurement contains two pieces of information at each frequency. As a result, the real and imaginary components of a spectrum can be tested for consistency with each other via the Kramers-Kronig relations. This consistency test provides a means for quantitative indication of reliability of data.

Complex spectroscopic measurements are becoming more popular for characterization of particles in suspension. For example, state-of-the-art techniques such as dielectric spectroscopy[1] and acoustophoresis[2] are spectroscopy techniques. Current commercial particle sensing technology typically provides the user with information about the distribution of one particle property, *e.g.* particle size.[3] There are other property distributions which are of interest. Particle shape, surface charge (zeta potential), and dielectric properties are currently determined independently of other properties. Surface charge heterogeneity of particles in suspension can not currently be measured *in-situ* with commercially available sensor technology. A rotational electrophoretic spectroscopic sensor is under development that integrates electrochemical impedance spectroscopy with UV/Vis light scattering measurements. This is accomplished by developing a spectroscopy (or transfer function technique) that is based on perturbations to an applied electric field in a suspension of particles. The measured potential response in the

suspension and the response of a UV/Vis light signal measured at various angles around the sample volume are related to the applied perturbation in potential as a complex transfer function.

Charge heterogeneity may play a significant role for a variety of industrial processes, including control of particle dispersions for stability, viscosity, and applicability.[4] The long-range Coulombic forces that act between particles or between the particles and a surface are influenced by the manner in which charge is distributed on the particle surface. The goal of this effort is to develop a characterization technique that can determine accurately *in-situ* the distribution of size and shape in conjunction with the nature of charge heterogeneity on particles. While SEM can provide some of this information, currently available technology cannot provide such information for particles in suspension. The proposal is to employ light-scattering measurements to determine the rotational electrophoretic response of suspensions of particles responding to oscillating electric fields. The term "Rotational Electrophoretic Spectroscopy" has been coined to describe the new technique.

The rotational electrophoretic spectra must satisfy the Kramers-Kronig relations if they are to satisfy the conditions of causality, stability, stationarity, and linearity.[5] Consistency can be tested using the measurement model tools developed in the laboratory of Dr. Mark E. Orazem.[6-9] To determine the consistent range of the spectrum, the spectral errors must be classified and quantified. The stochastic errors can be used to weight the measurement model regression. This weighting strategy can provide improved filtering of Kramers-Kronig inconsistent data.

The form of these errors (the error structure) has been a matter of some controversy. Descriptions of the stochastic error structure have been based upon observation for a variety of measurements and systems. Macdonald *et al.* have suggested that the standard deviations are roughly proportional to the complex impedance at each frequency.[10-13] Researchers in Orazem's laboratory[6-9,14-1516] have demonstrated experimentally that the variances of the stochastic error contributions to the real and imaginary impedance are equal. They proposed an error structure that defined the equivalent standard deviations in the stochastic errors in the real and imaginary impedances to be a function of frequency. Both groups have supported their arguments by demonstrating that the relationship between the standard deviations in the real and imaginary impedances is constrained by the Kramers-Kronig relations. However, two very different sets of constraints have been reported. The different constraints are the result of divergent assumptions about the distributions of stochastic noise in impedance spectra. Durbha *et al.*[9] found that the variances in the stochastic errors in the real and imaginary impedances were equal with the assumption that stochastic noise is distributed normally. Macdonald and Piterbarg[17] did not find that equality, but they assumed that stochastic noise could have a skewed distribution.

An effort is made in this work to illustrate that the crucial issue surrounding the form of the stochastic error structure is the spectroscopy measurement technique. The Kramers-Kronig relations do not transform errors; frequency-domain errors exist because they are propagated through the measurement technology. The stochastic errors over time are transformed uniquely into stochastic errors over frequency by each measurement technique. Each measurement technology can be simulated on computer and studied to

determine the mechanisms by which time-domain errors propagate into the frequency-domain. Also, frequency-domain errors in the complex impedance are the result of the ratio of frequency-domain errors in the complex current and voltage signals. Integral transforms can be determined that describe the propagation of time-domain stochastic errors into the complex current and voltage.

The focus of this document is divided between discussions on the RES technique and error analysis. The Rotational Electrophoretic Spectroscopy technique is described in Chapters 2 and 3. Rotational electrophoresis is one form of electrokinetic phenomena. Electrokinetic phenomena refer to the physics that relate fluid motion, charged surfaces, and electric fields. A review of electrokinetic phenomena and how they apply to alternating electric fields is provided in Chapter 2. The Rotational Electrophoretic Spectroscopy technique is described in Chapter 3. In this chapter, the visual observation of rotational electrophoresis is discussed. Proof of a light-scattering response to the application of the rotational electrophoretic driving force (electric field) is provided. The state of the development of the method is discussed.

The propagation of time-domain noise into frequency-domain errors is discussed in Chapters 4 through 9. A thorough review of the controversy surrounding the error structure of impedance measurements is provided in Chapter 4. A historical perspective of complex nonlinear least squares (CNLS) regression is provided. The introduction of various weighting strategies is discussed. Unanswered questions about the structure of errors in complex spectroscopy measurements are raised.

Those questions are answered in the next five chapters. The influence of specific measurement technologies on the error structure of impedance spectroscopy

measurements is demonstrated in Chapter 5. Questions about the universality of weighting a regression of complex spectroscopy data by the variance in the measurement have been raised in the literature. The results of the simulations reported in Chapter 5 demonstrate that the variance of the real and imaginary parts of the complex impedance are equal as long as the measurement technique does not introduce bias error into the spectrum.

The relationship between the errors in complex impedance and the errors in the respective complex current and voltage signals is determined in Chapter 6. Taylor series expansions for the variances of the real and imaginary impedances as a function of the complex current and voltage signals are derived. The variances of the components of the complex impedance are demonstrated to be a function of the variances in the complex voltage and current signals and the six cross-correlations between the four components.

The propagation of skewed distributions of time-domain noise into the frequency-domain measurement is discussed in Chapter 7. This work shows that, independent of the distribution function for stochastic errors in the time-domain, stochastic errors in the frequency-domain have a normal distribution. This result is shown to be a consequence of the Central Limit Theorem applied to the methodology used to measure the complex impedance. Durbha *et al.* determined that, in an expectation sense, the variance of the stochastic errors in the real impedance is equal to the variance of the stochastic errors in the imaginary impedance as a result of satisfaction of the conditions necessary for the application of the Kramers-Kronig transforms.[9] A necessary assumption for constraint of the errors in the complex impedance through the Kramers-Kronig relations is the normal distribution of frequency-domain errors.[9]

The mechanism by which noise in the time-domain is transformed into the frequency-domain is derived in Chapter 8. The Taylor series derived in Chapter 6 is determined as integral transforms of the noise in the current and voltage signals. These transforms are expressed for two commonly used measurement technologies. The errors in the real and imaginary impedance are shown to be uncorrelated. This result supports the experimentally determined finding that errors in the real impedance are uncorrelated to errors in the imaginary impedance when the impedance does not include a bias error contribution.

Auto-integration is a convergence condition employed in impedance spectroscopy measurements. The criterion is used to determine the termination point for the integration of the current and voltage signals that is required for the calculation of the complex impedance. In Chapter 9, it is demonstrated that the auto-integration criterion can not be set to an arbitrarily small value in order to minimize the magnitude of the errors in the complex impedance. It is also shown that the commonly used criteria are reasonable.

In Chapter 10, general conclusions about the research described in this document are drawn. The state of the development of the RES technique is discussed. The implications of the results of the numerical simulations and statistical analysis in Chapters 5-9 are presented. Possible directions for continuation of this work are listed in Chapter 11. Appendix A provides the details of the derivation that led to the results discussed in Chapter 6. The details of the derivations for the integral transforms describing the variances in the complex impedance components are provided in Appendix B.

CHAPTER 2
LITERATURE REVIEW: ELECTROKINETIC PHENOMENA

Electrokinetic phenomena were recognized for many years, but Smoluchowski first formalized a description of the phenomenon[18] in the late 19th century. After World War I, the field increasingly piqued the interest of researchers. Early researchers in the study of double layer phenomena were quite interested in the phenomena of electrophoresis, or cataphoresis as it was termed in that era. When an electric field is applied to a colloidal suspension of non-conducting particles, the particles will move with a certain velocity defined by the product of the electrophoretic mobility and the applied electric field. The problem that has faced researchers for over a century is the description of the electrophoretic mobility.

Electrophoresis, however, is not the only electrokinetic phenomenon.[19-21] Electroosmosis is the movement of fluid in a fixed non-conducting chamber under an applied electric field (it is electrophoresis with the particle frame of reference fixed). A streaming potential can be measured if the non-conducting solid is stationary while the liquid phase is in mechanically induced motion. If the non-conducting solid is in motion due to a mechanical driving force, i.e., particles under gravity, and the liquid phase is stationary, a sedimentation potential can be measured. Electrophoresis and sedimentation potentials are usually associated with colloidal suspensions. Electro-osmosis and streaming potentials are usually associated with liquid on large non-conducting surfaces (such as glass tubing).

Measurement techniques that utilize electrokinetic phenomena can provide a way of determining the surface charge of a non-conducting solid. The zeta-potential of a solid surface is the potential at the hydrodynamically immobile layer, or Stern layer. The zeta potential has a significant impact on colloid stability,[22,23] suspension viscosity,[24] and suspension conductivity.[25,26] Thus, the surface charge properties of particles can affect the macroscopic properties of the suspension. It is sometimes in the interest of industry to reach an understanding of the surface charge properties of the particles and powders with which they work.[27] *Research & Development* recently reported a survey of their readers that was taken to determine their needs in particle and powder characterization.[28] Seventeen percent measured suspension conductivity, ten percent were interested in suspension pH, and six percent focused on the particle surface charge as their primary concern.

A recent series of papers were published in *Chemical Engineering Progress* on the need for American researchers and engineering faculty to get more involved in particle science and technology. Enis *et al.*[29] described the need to catalog interparticle forces to understand the relation between surface energy and colloidal dispersion. One of the forces involved in colloidal dispersion is due to surface charge. Knowlton *et al.*[30] described the use of electric fields to more efficiently transport colloids. The understanding of surface charge would be useful in this utilization of electric fields. The surface charge properties of particulates and powders can be determined by measurement of electrokinetic phenomena. This can be achieved through integration of electrokinetic experiments and theory. In this chapter, a review of electrokinetics from the phenomenological and theoretical standpoints will be made. A description of recent

innovative models and measurement techniques will also be provided. Suggestions for future directions of research will also be included.

2.1 The Beginnings of Electrokinetics

The first calculation of the electrophoretic velocity of a non-conducting particle in an applied electric field is attributed to Smoluchowski in the late 19th century. Work on calculation of the effect of non-conducting particles on applied electric fields was first determined using a rigorous approach in which the particles were given a specific geometric arrangement.[31] The British scientist, Henry, expanded the calculation by relaxing one of the assumptions used by Smoluchowski in his derivation.[18,32] The original assumptions of Smoluchowski were that (1) the hydrodynamic equations of motion for a viscous fluid hold in the bulk fluid and in the electric double layer of the particle, (2) the inertia terms in the equation of motion can be neglected because the flow is relatively slow (that is, the Reynolds number is small with respect to unity), (3) the applied field can be superimposed on the field created by the field resulting from the particle double layer, and (4) the double layer thickness is small in comparison to the radius of the particle. The last assumption would now be described as $\kappa a >> 1$,[33] where a is the particle radius and κ is the reciprocal of the double layer thickness, namely, the debye length given by

$$\kappa = \left(\frac{1}{\varepsilon_r \varepsilon_0 kT} \sum_{i=1}^{N} z_i^2 e^2 n_i^{\infty} \right)^{1/2} \tag{2.1}$$

where ε_r is the relative permmittivity, ε_o is the permmittivity of a vacuum, k is Boltzmann's constant, T is the temperature, z_i is the valence number of ion i, e is the unit charge, and n_i^{∞} is the bulk concentration of the ith ion.

Henry[18] states that Debye and Hückel also attempted to determine the electrophoretic velocity as a function of the applied field, but found a different solution than that of Smoluchowski. However, the analysis of Debye and Hückel assumed that the applied field lines were always parallel, which is only possible in the particle is of conductivity equal to that of the fluid medium. Henry followed the analysis of Debye and Hückel except he allowed for the particle to be of a different dielectric property than the fluid. His analysis found solutions for the electrophoretic velocity without making use of the fourth assumption of Smoluchowski. However, when Henry made that assumption, his solution for the velocity, U, reduced to that determined by Smoluchowski:[18]

$$U = \frac{\varepsilon E \zeta}{4\pi\mu} \tag{2.2}$$

where ε is the dielectric constant, E is the applied field, ζ is the zeta potential, and μ is the viscosity of the medium. At this point, it was believed that the shape of the particle would not affect the value of the electrophoretic velocity, as long as the radius of curvature was much greater than the Debye length. Henry also determined that equation (2.2) should also apply to electroosmosis calculations.

Even in 1931, Henry[18] realized that the third Smoluchowski assumption (that the particle field would remain undistorted in the presence of the applied field) was unlikely. A new generation of papers on correction of Smoluchowski's equation (2.2) with relaxation of the third assumption began to appear soon after World War II. Henry[34] corrected the Smoluchowski equation (2.2) for the distortion to the applied electric field due to surface conductivity on the particle. Booth[35] took relaxation effects in the diffuse double layer cloud into account. Accounting for the distortion in the diffuse cloud (using

the Debye and Hückel double layer model), he was able to determine the charge on the particles. This work contributed a major departure from the solution of Smoluchowski, in that Booth rewrote the electrophoretic mobility as a power series in the particle surface charge.

Researchers began to concentrate on the fourth assumption of Smoluchowski in the 1960s. It was found that for moderate values of κa ($0.2 < \kappa a < 50$), relaxation effects required significant correction to the Smoluchowski equation.[36] Also, in this era, researchers began to exploit the computational power available with digital computers. The assumptions of Overbeek[36] were applied to these models which were solved through numerical computation. The two most significant assumptions included in this model were that (1) the applied field distorts the double layer, and that (2) only terms linear in the electric field are considered. These early models also limited consideration of the ions in the fluid and the magnitude of the applied field. These simple assumptions have provided an avenue for further theoretical development in the theory of electrokinetics.

2.2 Recent Theoretical Developments

As the understanding of electrophoresis improved, the importance of the surface charge on macroscopic properties became better understood. Many researchers began to model the influence of zeta potential on the macroscopic behavior of colloidal suspensions. Others attempted to improve the correlation between the electrohydrodynamical model describing electrokinetic phenomena and experimental observation. Another movement has been to ascertain theoretically the response of colloidal suspensions to an applied oscillatory electric field. In this section, these efforts will be described.

2.2.1 Macroscopic Behavior and Surface Charge

The most easily understood dependency of a macroscopic property on surface charge is most like suspension conductivity. It is well understood that water containing mobile ions will have an electrical conductivity; [20,21] salt water allows the passage of electricity more easily than most fresh waters, for example. It is therefore not surprising that the addition of charged particles would affect the conductivity of a suspension. First, particles which have an electrophoretic mobility are non-conducting,[18] therefore the inclusion of these dielectric solids will affect the current lines through the fluid.[25,26] The double layer of each particle can also affect current lines. None of the models described in Section 2 allowed for the polarization of the particles. Polarization of the disperse phase would be expected to affect the conductivity of the suspension.

The effective conductivity of a suspension comprises contributions from the conductivity of the bulk medium, polarization of the applied field by the dielectric disperse phase, polarization of the particles, distortion in the distribution of ions in the double layer, and transport of ions due to electroosmosis of the fluid, and electrophoresis of particles.[37,38] Saville[37] approached the problem by defining a particle surface conductivity. He was able to determine analytical solutions for symmetrical electrolytes. The analytical solution was correct to second order in the zeta potential. Numerical results for the same model verified that polarization, electroosmosis, and surface conductivity can significantly affect the suspension conductivity. In further studies he included the addition of counter-ions created in the particle charging process and changes in the bulk concentrations due to nonspecific adsorption in his model.[39] These inclusions greatly improved the agreement with conductivity data.

O'Brien also considered the problem of the addition of particles to suspension conductivity. It was his belief that each particle contributed to the effective conductivity through the solution for the electric potential and ionic concentrations far from the particle.[40] As in the derivation of the Saville model,[37] an approximate solution was determined that was correct to order ζ^2. Numerical solutions were also calculated and they agreed within a few per cent at low surface charge (low zeta potential). The discrepancy increased dramatically as the zeta potential increased. This model was not in good agreement with conductivity data. The author attributed the discrepancy to an inappropriate model for the particle and the electrolyte. The model was later tested on data collected on a porous plug system consisting of closely packed spheres.[41] The equations of the model were the same, but the boundary conditions were changed to accommodate the plug system. The numerical solutions to the model for the closely packed system were in good agreement with measured conductivities. The zeta potential was calculated and was in good agreement between estimates using the closely packed conductivity and the conductivity of a dilute suspension using the same spheres. However, when the estimate was made using the electrophoretic mobility of the spheres, the zeta potential was much smaller. While the first and second estimated zeta potentials decreased with decreasing Debye length, the third estimate increased with decreasing Debye length.

Ohshima[42,43] derived a conductivity formula based on the prior described O'Brien solution.[40] He claimed that his formula was valid for insulating and conducting particles alike as long as two assertions held - (1) that the applied field is small with respect to the field of the potential, that is, that $E << \kappa\zeta$; and (2) that there is no flux of material into

the particle, that is, that $\bar{v} \cdot \bar{n} = 0$ at the particle surface, where $\bar{v}$ is the velocity of either ion, and $\bar{n}$ is the unit normal at the surface.[42] His approximate formula and numerical solution are both in agreement with the same formula and solution derived by O'Brien.[40] Both are also correct to the same order.

One failure of all of these models is that they do not account for the induced dipole moment that occurs under disequilibration of the double layer under applied field.[44] In his review paper, Dukhin[44] derived a model for the induced dipole moment created when the diffuse cloud of the double layer is distorted. The simplest way to visualize the induced dipole moment is to consider the diffuse cloud under the imposed field. If the co-ions in a colloidal system are positively charged, then under an electric field, the co-ions will migrate towards the negative electrode. Thus, more positive charge exists on one hemisphere of the particle than on the other. A dipole moment has been induced because of the antisymmetry of the diffuse cloud.[45] It is shown by electrostatic theory that a set of closed field lines results.[46] Classical double layer theory assumes that a particle and its double layer is electrically neutral and would not have any long rang field lines. The field resulting from the induced dipole moment were expected to interfere with a field applied to a colloidal suspension and thereby to affect the suspension conductivity. Dukhin and Shilov[45] derived the effective conductivity of a suspension when induced dipole moments form. Dukhin[45] also points out that conductometric measurements are difficult in the presence of polarized electrodes and suggests that such measurements be performed under alternating current conditions. This will be discussed further in Section 3.3.

Another macroscopic property that is widely held to be dependent upon surface charge is suspension viscosity. In fact, applied electric fields have been used to affect the

viscosity of suspensions. The term *electroviscosity* was created to describe the increase in viscosity due to the fixing of ions in the double layer of the disperse phase. In the 1950s, Booth[24] derived a formula for the effective viscosity of a suspension of particles and electrolyte. He found that the electroviscous effect increased with the debye length. Dukhin[44] discussed the effect that the field of the diffuse double layer will fix the dipole of water molecules and affect the location of the shear plane near the particles surface. Recent work described in his review paper[44] suggest that the displacement of the slipping plane is probably no more that one water molecule in thickness, but at high surface charge values, the displacement seems to increase, thereby increasing the effective viscosity.

2.2.2 Electrohydrodynamic Models

Redefinition of Smoluchowski's equation (2.2) gives

$$U = \mu E \tag{2.3}$$

where U is the electrophoretic velocity, E is the applied field, and μ is the electrophoretic mobility. In order to understand better the electrophoretic mobility and its dependence on the applied field, the zeta potential, and the fluid viscosity, many researchers have developed electrohydrodynamic models to solve for the velocity of the fluid around a particle when the particle is undergoing electrophoretic motion, but is held in a fixed coordinate frame. The fixing of the coordinate system means that the fluid at the particle surface is still (no-slip), while the velocity of the fluid far from the particle is equal to $-U$.

The electrohydrodynamic models usually consist of the same set of equations but use slightly different boundary conditions, assumptions necessary for an analytical solution,

or numerical solution technique. The equations in the fluid include the equation of motion and the continuity equation. These can be written as

$$\mu \nabla^2 \mathbf{u} - \nabla p = \rho \nabla \Psi \tag{2.4}$$

and

$$\nabla \cdot \mathbf{u} = 0 \tag{2.5}$$

where p is the pressure field, $\mathbf{u}$ is the fluid velocity vector, and Ψ is the electrostatic potential field in the fluid. The basic assumptions in these equations are that the inertial terms can be neglected (Re small), and that the fluid is incompressible.

O'Brien and White developed a model to describe the electrophoretic mobility of a spherical colloidal particle that coupled the above equations with the determined ionic distribution and potential around a colloidal particle.[47] They calculated the required force to move a particle at the velocity U and the force required to hold the particle fixed under the applied field E. The sum of these forces must be equal to zero which allowed for determination of the electrophoretic mobility. The Poisson-Boltzmann equation[20] was used to describe the potential field with the boundary condition that the gradient of the potential is equal to the electric field strength far from the particle. The boundary conditions for the velocity consisted of the no-slip condition at the surface (the hydrodynamically immobile layer was assumed to be approximately the particle surface) and that the velocity is the negative electrophoretic velocity far from the particle. Conservation of species equations were used to determine the ionic concentration profile for each ion:

$$\nabla \cdot (kT\nabla n_i + z_i e n_i \nabla \Psi - \lambda_i n_i \mathbf{u}) = 0 \tag{2.6}$$

where n_i is the concentration of each ion and λ_i is the ionic drag coefficient. The boundary conditions for these equations required that far from the particle, the concentration of each ion is the bulk concentration of that ion, and that at the surface, there was no ionic flux into the particle. To determine the approximate solution to the model, the equations were linearized under the assumption that the applied field was much weaker than the field created by the zeta potential. The results of his study were that the mobility is a monotonically increasing function at low values of the zeta potential. At low values of the κa product, the mobility plateaus at high zeta potentials. At higher values of the product, the mobility shows a maximum (although this maximum occurs at zeta potentials that are difficult to reach in experiments). The maximum was found for both symmetric and asymmetric electrolytes. The approximate solution[48] was compared to both the numerical solution and an earlier approximate formula derived by Dukhin.[44,45] The approximate O'Brien formula was simpler than the Dukhin formula and in better agreement with the numerical solution. O'Brien,[49] to allow for a general electrolyte (as compared to a symmetric electrolyte), later redeveloped the Dukhin formula. The approximate formula was again in good agreement with the numerical solution to the redeveloped model. The electrochemical potential was included in the model to allow for changes in the ion density in the double layer of a spheroid particle with a debye length much smaller than the radius of curvature.[50] This work illustrated that the Smoluchowski equation was not suitable for description of the electrophoretic mobility for non-spherical particles. O'Brien also noted that for the non-spherical particle, rotation may occur upon the application of an external field.

Anderson also worked on the issue of particle rotation. It has been shown that the Smoluchowski equation (2.2) holds for a nonconducting rigid particle of any shape if the four assumptions of Smoluchowski hold.[51] Also, the particle will not rotate no matter what its shape.[51] The focus of his early work was on particles which had discrete surface charge distributions but on a scale consistent with the particle size. [51] Using essentially the same model as O'Brien,[47-50] the problem was simplified by describing an inner region near the particle and an outer region outside the double layer. In the inner region, the Poissan-Boltzmann equation[20] held, and in the outer region, Laplace's equation[20] held. As a condition at the boundary between the inner and outer regions, a slip velocity was defined as the sum of the electrophoretic velocity, the velocity transform of the angular velocity due to rotation, and the negative mobility calculated using the field at the particle surface. Through this model, the linear velocity and angular velocity were determined as functions of the monopole, dipole, and quadrapole moments of the particle. No experimental data was available for confirmation of the model results. The model was expanded to be valid for particles with a surface charge that is an arbitrary function of the surface position.[52] The solution was again determined as a function of the three polar moments. Formulas were developed explicitly for spheroidal particles with axisymmetric charge distribution. The result shows that while the particle will orient in a certain direction, the particle may translate in a direction skew to the orientation angle. It was also determined that a particle with a net neutral charge, but with a definite charge distribution, can have a nonzero electrophoretic mobility. The model was also applied to kaolinite clay to determine the unique zeta potentials on the faces and edges of the clay particle. The translational and rotational velocities of dumbbell-like particles were

similarly calculated except that not only were the forces on the net particle determined, but the forces on the individual spheres of the dumbbell were determined.[53] This study found again that the translational velocity direction angle may be skew to the direction of particle orientation. It also determined that the particle would align itself in the field even if the difference in the zeta potentials of the two dumbbell spheres was small. A true dipole does not need to exist for the dumbbell like particle to rotate, a gradient in the zeta potential down the axis of the connector is simply required. Similar studies have performed for nonuniformly charged particles of geometric descriptions-slender and chain of spheres.[54] The findings of the models for these geometry were similar to the findings for the other geometries. A final addition to the model accounted for both symmetric nonuniform charge and polarization of (flux of ions into) the double layer of a spherical particle.[55] Under these assumptions, it was determined that even a spherical particle could have an angular velocity component, and the particle may move skew to the angle of the charge symmetry axis. The dependence of the electrophoretic mobility of a nonuniformly charge spherical particle on the monopole and quadrapole moments has been independently verified.[56]

Ohshima followed closely the path that O'Brien followed in using electrohydrodynamic models to improve the correlation between measured electrophoretic mobility and theory. Using a similar model to the first model of O'Brien,[47] an approximate formula and numerical solution for the electrophoretic mobility of spherical colloidal particles were determined by introducing the electrochemical potential.[57] The results were in good agreement with other researchers and the approximate formula and numerical solution provided similar results. The

electrophoretic mobility was found to have a maximum at large values of κa. A similar approach was taken to determine the sedimentation velocity and potential of charged spherical particles in a dilute suspension.[58] Both the numerical and approximate model to the solution showed that both the sedimentation velocity and potential had a saddle point in a 3D plot of velocity or potential versus the zeta potential and the product κa.

An attempt was made to better correlate electrophoretic mobility data with electrokinetic models by introducing a new model for the Stern layer. Earlier measurements had shown that zeta potentials measured via mobility and conductivity were in disagreement.[1] In order to bring these two values into agreement, a dynamic Stern layer model was introduced which allowed for transport of ions in the Stern layer.[59] Adsorption-desorption processes and lateral movement of ions in the layer was allowed. The lateral movement is described by the effects of electromigration and diffusion caused by the application of an external electric field. Plots of the numerical solution of the model for the mobility against the ionic strength showed local maxima and minima for a given number of binding sites and for a given value of the ion surface mobility. Plots of the mobility against the number of binding sites and ionic straight suggested the possible presence of saddle points. The mobility increased as the ion surface mobility decreased. The calculated mobilities were in good agreement with the measured mobilities of two types of latex particle suspensions.[60] Other researchers have taken the inability to correlate zeta potential values determined by the electrokinetic models with other measurements and have moved toward characterization of the charged surface through other properties.[61]

The shear plane of a particle can be moved with respect to the particle radius by creation of surface charge layer such as adsorbed polymer chains or polyelectrolytes.[62,63] In one study, the electrophoretic mobility increased as the shear plane was placed deeper into the charge layer.[62] Numerical solutions for the mobility showed a maximum with respect to the shear plane depth and increased with the fixed charge in the surface layer when the Donnan potential was included in the model.[64] An approximate analytic solution to the same model was also developed and showed similar behavior to the numerical solution at low charge in the surface layer.[65] The model was further modified to allow liquid flow through the surface layer and an analytic solution was derived.[66] Surface charge layer effects were also determined for electroosmosis and streaming potentials along plane walls with a surface layer,[67] and as an approximation, the surface layer does not effect the streaming potential or electroosmotic fluid velocity.

2.2.3 Oscillating Electric Fields

The application of an oscillatory electric field can affect a colloidal dispersion in two ways: (1) the particle will respond in a kinetic movement and (2) the suspension conductivity may be frequency dependent. The first way is quite simple to describe. If a positive field is applied in a coordinate system fixed for the observer, a charged particle in a colloid will show an electrophoretic mobility. They will translate and they may rotate[68] into alignment with the field. If the field is turned off, the particles will relax. If the field is reversed, the electrophoretic mobility would be in the opposite direction and the particles may rotate into a reverse orientation. Recent studies have determined that in an oscillating electric field, the oscillatory movement of colloidal particles will create a propagating sound wave. Likewise, if an ultrasonic beam is directed into a colloid,

alternating electric fields will be produced.[2] This phenomenon has been described as *electroacoustics* or *acoustophoresis*.

O'Brien was one of the first researchers to formalize the phenomenon. The phenomenon occurs because the oscillatory electrophoretic movement created by the imposed oscillatory field creates oscillatory pressure fields on the opposing sides of particles in a suspension. The alternating pressure fields propagate as sound waves. The applied field and resulting sound wave bring about a complex transfer function known as the dynamic mobility. The dynamic mobility is complex because there is a phase lag between the applied field wave and the sound wave. The value of the dynamic mobility is a function of the applied frequency, the zeta potential, the kinematic viscosity of the fluid, and the size of the particle.[69] An extensive study of the acoustophoretic response of non-spherical particles was accomplished by using a traditional electrohydrodynamic model while accounting for the electroosmotic flow field surrounding the particle. Dynamic mobility spectra were calculated for several aspect ratios of prolate particles and for several ratios of the density of the particle to the fluid density.[70]

The more common use of alternating electric fields is in the measurement of the frequency dependent dielectric properties of a colloid. In the early years of the century, AC technology was implemented to measure the complex admittance of colloidal suspension. The real and imaginary parts of the admittance are related to the conductivity and dielectric constant of the suspension. The high frequency asymptotic value of the dielectric constant was associated with the suspended and suspending phases, and the difference between the measured dielectric constant and this asymptotic value was believed to give the value of the dielectric constant associated with the interface.[71]

With the improved ability to measure frequency dependent phenomena, more focus has been placed on the dielectric properties in recent years. The dipole formation of a particle in the presence of an applied oscillatory field will effect the conductivity of a colloidal suspension.[44] O'Brien has formulated an expression for a complex dipole coefficient that describes how the dielectric properties of the particle and its dipole moment will distort the external field.[72] The admittance has also been revealed to be a more cumbersome function of the conductivity and dielectric constant than had earlier been believed. The conductivity is frequency dependent, and the dielectric constant is complex and frequency dependent.[73] Electrohydrodynamic models have been used to calculate the admittance of a colloidal suspension. The real part of the dielectric coefficient has two plateaus, increases from one to the other as frequency decreases, and has a nonzero derivative with respect to frequency at roughly 10-100 kHz. The magnitude increases with increasing zeta potential.[73] The effective conductance is constant at low frequency and monotonically increasing at high frequency. [73] The imaginary part of the dielectric response behaves like the imaginary impedance response of a Voigt circuit element,[74] and its magnitude increases with increasing zeta potential. These calculations for the conductivity and dielectric response have been independently verified through another modeling effort.[75]

2.3 Technical Innovations and Experimental Observations

The development of more sophisticated models in the field of electrokinetics has inspired a great deal of new measurement technologies. An increased effort has also been made to describe the electrokinetic properties of a greater catalog of particulate materials. These recent advances will be described in this section.

2.3.1 New Measurement Technologies

Classical electrophoretic measurements have been adapted to changing needs. Its usage in DNA analysis (gel electrophoresis) is well known (O.J. Simpson). Microelectrophoresis has been commonplace for several years.[76,77] Hewlett Packard has recently developed an instrument making use of capillary electrophoresis.[78] It is primarily being used to separate and detect biopolymer particles.[79] Free solution capillary electrophoresis (FSCE) makes use of three driving forces: the electrophoresis of the particles, the electroosmosis of fluid along the capillary wall, and the drag of the particle in the fluid. An external flow field can also be imposed to introduce another force.[79] These forces in conjunction create a greater separation of particles than could be accomplished with traditional electrophoresis. Detection is accomplished using UV/Vis absorption spectroscopy.[80] The small currents required for the technique generate less heat than the traditional current requirements.[79] The approach has certain difficulties. For the detection and analysis of biopolymers and proteins to be accomplished, the capillary wall needs to be suitable for the substance in study.[81] This in itself is no trivial task. The system also requires a more complex sample injection system than traditional electrophoresis.[82] However, the small volume required for sample measurement is a benefit for the small amounts of biomaterial available.

Electrophoretic fingerprinting is another technique which has very recently been developed.[83] The electrophoretic mobility of a colloidal particle is measured and plotted against pH and pλ (the negative log of the specific conductance). The three dimensional plot is converted into a two dimensional topographic plot where the mobility is the

contour variable, resulting in an electrophoretic fingerprint. The technique could be used to assess particle composition, charge, and colloid stability.

A truly visual method has been developed to determine the zeta potential based on 3D tracking of individual particles.[84] A sample chamber rests on a piezoelectric actuator that keeps a particle in the focal plane of a CCD microscope using a sophisticated control algorithm. Particles can be tracked when moving under Brownian motion or under an applied field. The technique allows the user to actually sample what each individual particle is doing, and average after all the measurements. Traditional electrophoretic detectors use light-scattering methods that are averaged in the measurement.

Coulter® has recently made use of the discovery of particle rotation in a new instrument. Rotation of particles was just recently verified.[68] The Coulter® Delsa 440SX uses a pulsed electric field to align particles and then allow them to relax when the pulse is in the off state.[85] It is also equipped with multiangle detectors to get a variety of perspectives on the particles in a colloid sample. The alignment and relaxation of non-spherical particles can provide information on the surface charge and the particle shape. Analysis of the data can remove the influence of Brownian motion from the electrophoretic mobility spectrum, thus providing a more accurate assessment of the zeta potential.

The development of acoustophoretic theory inspired the construction of the Matec Applied Sciences Acoustosizer.[2] A sample chamber consists of two electrodes opposite each other. Each electrode is connected to a transducer. An oscillatory potential signal is transmitted across the electrodes and the transducers sense the resulting sound wave. Likewise, an oscillatory potential signal can be transmitted across the transducers,

emitting a sound wave, which will result in a measured oscillatory potential between the electrodes. Either technique can provide an assessment of the dynamic mobility as a function of the frequency of the applied signal. Analysis of the data can provide values for the zeta potential and the particle size distribution.[2] Determination of the dynamic mobility can be difficult if the particles aggregate; another measurement technique is required to determine the particle size independent of aggregation formation.[69] However, the limiting dynamic mobility has been shown to correspond with dc mobility in the case of polystyrene latex particles.[86] Studies have been completed on silicon nitride suspensions to characterize the technique. The technique was determined to provide a good assessment of the surface charge on the particle independently by two research groups on the ceramic material.[87,88]

An increasing popular electrokinetic technique is dielectric spectroscopy.[89] The design of the dielectric spectrometer is quite similar to the design of an electrochemical impedance spectroscopy experiment. A chamber is filled with a colloidal suspension.[90] Two electrodes are placed at opposite walls to drive an oscillatory field through the chamber. Polarization of the electrodes can create a non-uniform field in the colloid,[91] therefore selection of the driving electrodes is important. Two reference, or sensing, electrodes are placed in a line normal to the faces of the other two electrodes. An oscillatory potential is driven between the external electrodes and is sensed between the reference electrodes. A phase lag may exist between the two signal, thus yields the measurement of a complex admittance. The analysis follows in a different manner than that described before,[73] but the admittance can be converted into an expression for the conductivity and the dielectric constant at any frequency.[90] The model derived by Saville

for the frequency dependent conductivity and dielectric constant are in extremely good agreement with experimental data.[92,93] Measurements on colloidal hematite using the technique discovered a previously inaccessible phenomenon in the dielectric spectra.[94]

2.3.2 Electrokinetic Standard

An effort has been made to identify a reasonable electrokinetic standard, in order that electrokinetic property determination can be better correlated between experimentalists and between techniques. While polystyrene latex serves as a good mechanical model for a spherical particle, it has been found to be troublesome as an electrokinetic standard.[95] There have been difficulties in relating the measured zeta potential with the surface charge on latex particles,[96,97] and a modified description of the Stern layer has been suggested. Latex suspension preparation has also been shown to effect zeta potential measurements.[98] Charging phenomena on hydrocarbon particles is poorly understood. For a hydrocarbon particle to carry charges that have been reported,[99] ions would have to adsorb to a hydrocarbon surface out of the aqueous phase. Ions should favor the aqueous phase over the hydrocarbon phase.

In response to the need for the standard, some researchers have suggested that goethite be used. A series of studies on several inexpensive materials have been performed to get replicate measurements of the electrophoretic mobility under a variety of experimental preparation and measurement conditions.[95] Red blood cells, silica, latex, and goethite were all considered. Goethite particles can be produced with a very narrow size distribution. The addition of phosphate can control the IEP of a goethite suspension. Also, goethite suspensions age with little decomposition of the particles as compared to the organic species.

2.4 Summary

Electrokinetic models have been developing rapidly for the last twenty years. While general models can be developed for broad classifications of systems, in application, models must be specific to the application that is being considered. This is especially true in the case of biosystems and non-rigid particles that demonstrate non-stationary behavior. The development of increasingly sophisticated models has allowed development of new characterization instrumentation. Frequency dependent phenomena, electrosonic amplitude effects, and better sensitivity are being utilized in new measurement techniques.

The science of electrokinetics can be extended to include mobility differences between fluid and solid phases that result from the application of other fields. Electric fields are not the only driving forces that can create the phenomena associated with electrokinetics. Both the theories of diffusiophoresis and thermophoresis are derived from the theory of electrophoresis.[100] The research community can also utilize these phenomena in development of new measurement technologies.

Although electrokinetic phenomena have been under study for over a century, the general electrokinetic model is still incomplete. Theory and experimental observation do not always agree. Instrumentation will become more powerful as on-line computational ability improves. And as computational power increases, researchers will be better able to solve more sophisticated models. The improvements in ability to assess electrokinetic phenomena experimentally and via numerical simulation will provide an avenue for improvement of the general electrokinetic model.

CHAPTER 3
DEVELOPMENT OF ROTATIONAL ELECTROPHORETIC SPECTROSCOPY

Charge heterogeneity may play a significant role for a variety of industrial processes, including control of particle dispersions and the use of slurries for chemical mechanical polishing of silicon wafers. The long-range Coulombic forces that act between particles or between the particles and a surface are influenced by the manner in which charge is distributed on the particle surface.[4] The goal of this effort was to develop a characterization technique that can determine accurately *in-situ* the distribution of size and shape in conjunction with the nature of charge heterogeneity on particles. While SEM can provide some of this information, currently available technology cannot provide such information for particles in suspension. Technology was under development that employed light-scattering measurements to determine the rotational electrophoretic response of suspensions of particles responding to oscillating electric fields. The term "Rotational Electrophoretic Spectroscopy" was coined to describe the new technique.

3.1 Background

Charge heterogeneity refers to the distribution of charge on the surface of individual particles. Three types of charge heterogeneity are typically discussed in the literature: random heterogeneity, isolated patches of charge, and interacting patches of charge.[101] The most common colloidal particles that have non-uniform distributions of charge are soil clays.[4] Clay particles are composed of sheets of silicon-based lattices.[4] Bentonite clay lattices tend to have a different base or ion exchange capacity on the edges and faces of

the sheets.[4] At an acidic pH, the edges of the sheets will usually be positively charged while the exposed faces will be negatively charged.[4] This property is utilized in the drilling of oil wells.[4] Bentonite clays are used as drilling mud for cooling and lubricating drilling bits, removing debris, and sealing the walls of drilled holes. If drilling is stopped, the clay solidifies. Polyvalent ions are added to the mud to neutralize the positive charge on the edges of the lattice. The removal of positive charge inhibits the formation of three-dimensional solid structures, reducing the amount of work required to re-liquefy the mud.[4] The combined properties of particle charge heterogeneity, shape, and size influence the packing structure of concentrated suspensions, and thereby influence the associated rheological properties.[3]

The rotational moment of the electrophoretic mobility of particles in suspension is utilized in this technique to focus on phenomena associated with surface charge heterogeneity, non-spherical shape, and induced dipole formation. Translational electrophoretic measurements can provide erroneous results for particles with heterogeneous surface charge. For example, a non-uniformly charged, spheroidal particle with a net zero zeta potential can still have a non-zero electrophoretic zeta potential.[52] Non-uniform surface charge distribution has also been shown to create a component of the translational electrophoretic mobility that is skewed toward the direction of the applied electrophoretic field.[55] Rotational electrophoretic mobility occurs as a response by particles with non-uniformly distributed surface charge to an applied electric field. Non-spherical particles may also align themselves in an applied electric field due to formation of an induced dipole.[102] Focus on the rotation of particles in suspension in an

oscillating electric field will provide information on relaxation phenomena associated with surface charge heterogeneity and diffuse double layer polarization.

The combined properties of particle charge heterogeneity, shape, and size influence the packing structure of concentrated suspensions, and thereby influence the associated rheological properties.[4,101] Charge heterogeneity is generally overlooked because its measurement is difficult. Most models for patchy charge transform the heterogeneous charge into a smeared surface potential.[103] Charge heterogeneity has also been described in terms of the permanent dipole or multipole moment of a particle.[102] The translational and rotational moments of the electrophoretic mobility have been described with respect to monopolar, dipolar, and quadrapolar moments. Models have been presented for doublets of dissimilar particles,[68] dumbbell-like particles,[53] non-uniformly charged ellipsoidal particles,[52] and "slender" particles.[54]

3.2 Concepts for Design

The electrochemical component of rotational electrophoretic spectroscopy takes advantage of the tendency of non-spherical particles to rotate to reach a preferred alignment when an electric field is applied. If the field is applied in an oscillatory manner, the particle will rotate in an oscillatory manner to achieve its preferred alignment.[70] Light scattering techniques can sense the rotation of the particle as illustrated in a simplistic manner in Figure 3.1. The intensity of the photodetector response will vary in accordance with the amount of light blocked by the particle. In an end-on configuration, the light intensity reaching the photodetector will be at a maximum, and in a parallel configuration, the light intensity reaching the photodetector will be at a minimum. As indicated in Figure 1d, rotation of a spherical particle will have no effect on the photodetector, thus the technique will be sensitive to departures from a

spherical particle shape. Note that, since the technique allows measurement of potential and current, the more standard dielectric spectroscopy can be used to complement the interpretation of the photodetector response.

The rotation of a particle is determined by the electrohydrodynamics of the fluid surrounding the particle and is opposed by the viscous drag of the fluid on the particle. The rotational electrophoretic mobility is dependent on the applied field and the heterogeneity of charge on the surface. For example, John Anderson and his coworkers at Carnegie Mellon determined that the angular velocity of a particle is dependent on its dipole and quadrapole moments of charge.[52-55,68] Also, the particle can have an angular velocity because of its tendency to align in an applied field.[102] Due to polarization of the diffuse double layer around the particle in an applied field, a dipole moment for the particle and its diffuse double layer can be induced. This induced dipole will draw the particle into alignment with the field. Therefore, sensing the oscillating particle orientations employs light scattering measurements lagging behind the applied alternating electric field. An oscillating scatter signal can be measured because we are controlling particle orientation and placement of the photodetector. The field measurement is much simpler. The electric field is proportional to the current. And since the voltage drop is measured between the reference electrodes, the field can be calculated as the gradient of the potential.

The scattering intensity from a single particle is proportional to the wavelength of light and a scattering function that is dependent on particle orientation and scattering angle.[104] Thus, the orientation of a single particle will affect the scattering intensity. The scattering function can be approximated by the summation of the scattering functions for

n identical particles. This description can be extended to a volume-averaged description of the scattering. From this perspective, the system-described scattering function should be different for a system of particles in random orientations or for a system of particle in identical orientation or for a system with distributions of orientations.

The response of the photodetector to an oscillating electric field is a function of frequency. At high frequency, the particle cannot change its alignment to conform to the rapidly changing electric field, and the photodiode response is constant. At a frequency characteristic for the particle shape and dipole moment and the fluid viscosity, the particle will rotate at the frequency of the field, but this signal lags the field by a constant amount. The phase lag itself also contains information concerning the particle shape and dipole moment and the fluid viscosity. At very low frequencies, the particle will orient with the field, but, once aligned, the particle will stay in alignment until the field strength reduces sufficiently to allow relaxation. This will yield a maximum in the photodiode response.

A zero-biased signal applied to the suspension would avoid translational electrophoresis. At high frequencies, particles do not have sufficient time to respond to the field, and therefore no scattering signal is expected as shown in Figure 3.2a. As the field frequency is reduced and approaches the inverse of the time constant for particle rotation, some particles would begin to cyclically rotate with the field. At some critical frequency, all the particles would be oscillating in the field. The output signal would have a phase lag with respect to the applied voltage signal, but it would not be purely sinusoidal. Because the field is at full strength twice each cycle, the particles can align twice each cycle. For forward scattering, an axially symmetric particle (with respect to

the dipole moment) would be aligned in the light whether the field is positive or negative in orientation. Therefore the photodiode signal is fully rectified. The applied voltage and photodiode signals would look like those plotted in Figure 3.2b. As the frequency decreases, a point would be reached where the particles would be aligned in the field before the field reached its maximum. Since the particles would maintain the same orientation as the field continued to increase, the scatter signal would appear to be not only rectified, but clipped with respect to the applied field (Figure 3.2c). As a first approximation, when the particles are mostly aligned, the optical signal should be strongest (less projected area by the particles). When the particles are mostly relaxed, the optical signal should be at its weakest (more projected area by the particles). The photodiode response is expected to look like the absolute value of a sine wave. This has been experimentally observed.

The Fourier series expansion in harmonics of the fundamental signal for that signal is an even series of cosine harmonics.

$$|\sin(\omega t)| = \frac{2}{\pi} + \sum_{n=1}^{\infty} \frac{4}{\pi} \cdot \frac{1}{1-(2n)^2} \cdot \cos(2n\omega t) \tag{3.1}$$

The impedance transfer function can not be directly measured from the applied voltage and photodiode response signals, because the generator signal is a "pure" sinusoid while the photodiode signal is a summation of harmonic sinusoids. This problem could be solved by fully rectifying the applied signal from the generator would provide an applied signal which also looked like the absolute value of a sine wave. Both the input signal and the output signal would have the same structure defined by the Fourier series of equation (3.1). The clipping phenomenon is nonlinear and does not lend itself to frequency domain measurement, thus, the frequency range for the measurement is limited.

To avoid harmonic analysis a bias is added to the alternating electric field so that either the maximum or the minimum value of the field is null. Under this condition, no oscillation in the scattering signal at high applied field frequencies would be observed (Figure 3.3a). But as the frequency is reduced towards the characteristic frequency, a scatter response (Figure 3.3b) that is purely sinusoidal would be observed. This results because the particles only aligned once per cycle of the applied electric field. At low frequencies, the clipping effect would still be present (Figure 3.3c). The transfer function describing this set of perturbation and response signals could be directly calculated without the necessity of signal conditioning. However, a bias is applied, and there is a net translational electrophoretic mobility. But, with short enough measurements, and occasional mixing of the system, this measurement strategy is reasonable and preferable for this preliminary assessment of the technology.

3.3 Accomplishments

A schematic illustration of the rotational electrophoretic spectrometer system is given in Figure 3.4. The RES prototype consisted of a cell with an optically clear chamber exposed to monochromatic light scattered off a diffraction grating from a Xenon white light source. A single wavelength of light was passed through the sampling chamber to a photodetector, which recorded scattering intensity. The photodiode measured the forward scatter of particles in suspension. After the particulate suspension was added to the cell, working electrodes were placed in the upper chambers of the cell to apply a field across the optical chamber. Micro-reference electrodes were inserted to just above the optical chamber to measure the field in the suspension. A sinusoidal electric field was generated by a Solartron 1254 Frequency Response Analyzer amplified by a KEPCO BOP 500M Power Supply.

The experiment was controlled *via* a personal computer. The frequency response analyzer provided a signal used to drive the power supply to generate the oscillating electric field across the sample volume. The potential difference across the reference electrodes was monitored using a high-input-impedance voltage follower. The current provided by the power supply could also be monitored. The photodetector signal was returned to the frequency response analyzer either *via* a high impedance current-follower or through the current follower and matched analog low-pass filters (not shown). The frequency response analyzer provided an impedance measurement corresponding to the ratio of any two signals. Thus, the system shown here could be used to measure impedance corresponding to dielectric spectroscopy or to rotational electrophoretic spectroscopy. At high frequency, the applied current signal and measured voltage drop across the paired reference electrodes could be transformed into the dielectric spectroscopy transfer function. The Rotational electrophoretic spectra were obtained for arbitrarily selected wavelengths of light. A key feature of this approach was the coupling of two very different frequencies to sample the suspension. The characteristic frequency for light scattering is very large as compared to the characteristic frequency for particle rotation. Thus, changes in light scattering signals can be used to monitor rotation of suspended particles without hindering the interpretation of the light scattering signals in terms of size, shape, concentration, and chemical composition.

The RES technique was applied to suspensions of borosilicate fibers. These fibers had a large aspect ratio as their length was much greater than their diameter (Figure 3.5). Video microscopy was used to verify that these fibers would respond to an oscillating electric field with cyclical rotation. An ensemble of fibers was observed (Figure 3.6)

while an oscillating electric field was applied to the suspension. The particles were observed to align with an applied field and relax when no field was applied. The particles rotated in a cyclical fashion when an oscillating electric field was applied.

A transient in the light scattering signal was measured (Figure 3.7) when a step change in the electric field was applied. From an initially relaxed state, a field of approximately 25 volts per centimeter was applied. The potential drop across the optical chamber relaxed slowly over time because of the relaxation of the current resulting from the onset of the potential between the working electrodes. A transient was visible in the photodiode response. However, the signal change was on the order of a couple of millivolts. The signal to noise is very low. FFT analysis of the transient showed that the noise masked the low frequency features of the spectrum.

The experimental approach was deconstructed into its component measurements in order to verify the measurement approach of the rotational electrophoretic spectroscopy prototype. At several frequencies, the voltage perturbation and resulting light scattering signal were captured using a DAQ-board. At each frequency, a rigorous signal processing protocol was performed to determine the RES transfer function. An FFT was performed on each signal (Figure 3.8 is the applied voltage and Figure 3.9 is the responding photodiode signal) to verify that the primary frequency component of the signal was the frequency of the applied perturbation. Thus, linearity of the measurement was demonstrated. Once the existence of the response was verified, the transfer function for the system at the applied frequency was calculated. The system transfer function was determined by calculating the power spectra of the raw signals and the cross-correlation of the two signals. The reciprocal of the magnitude is plotted against frequency in Figure

3.10. The reciprocal is shown because the input signal is several orders of magnitude larger than the output signal. A clear peak is located at approximately 784 mHz, which was the frequency of the applied voltage signal. The cross-covariance of the input perturbation and output signals was used to measure the modulus and phase angle of the RES transfer function at the frequency of the applied perturbation. The magnitude spectrum of the RES transfer function for a suspension of rod-like borosilicate fibers is shown in Figure 3.11.

The magnitude spectrum for the system was calculated using the FFT technique at each frequency of the applied electric field. This is the set of data that is connected by a line. At this point the out-of-phase component has not been independently assessed. In fact, determination of the out-of-phase component was difficult through the FFT technique because the phase lag fluctuated greatly over frequency. An explicit calculation for the phase lag at the forcing frequency was difficult because the analysis was conducted on discrete data. The accurate phase angle might not have been detectable within the constraints of the signal sampling frequency. The phase lags can only be determined by interpolation between the calculated phase angles at the closest discretized frequencies. The inability to measure the out-of-phase component of the transfer function was also the result of the low signal to noise ratio of the out-of-phase signal. The out-of-phase signal was smaller than in-phase signal & the noise levels of the two signals should be equal when the transfer function is calculated using the FFT analysis or an analog Frequency Response Analyzer. This equality will be thoroughly discussed in Chapters 4-8.

To assess the out-of-phase component with greater confidence, the real and imaginary parts of the transfer function were measured using the analog frequency response analyzer. This method of calculation is described in Chapter 5. Several values of the complex transfer function were measured at the same frequency. The two components were converted into magnitude values to check for consistency with the FFT-determined spectrum. The values were reasonably consistent (the two FRA points in Figure 3.11). Only two points could be determined before the instrumentation broke down.

3.4 Conclusions

Interpretation of these results in terms of rotation of rod-like particles was confirmed by observation through video microscopy of frequency-dependent rotation of suspended particles under an alternating applied field. The assumption that the rotation of particles was a reversible process was verified by using an oscilloscope to monitor the photodiode response. Relaxation processes in response to a square wave potential input were observed to be repeatable. The rotation of particles was observed in the presence of a superimposed flow field, which confirms the suitability of this approach for on-line sensing.

Measurement of the Rotational Electrophoretic Spectroscopy transfer function was accomplished using Fast Fourier Transforms on digitally stored pairs of applied voltage and photodiode response signals. The magnitude of the transfer function was determined at the frequency of the applied voltage signal. Power spectral analysis of the perturbation and response signals provided evidence of a linear response of the light scattering signal to a perturbation in the rotational electrophoretic driving force. The out-of-phase component was not independently assessed because of the low signal-to-noise level in that component.

The RES measurement was extremely difficult to conduct. Oscillations in the light-scattering signal have the same signal level as the noise in that signal. Thus, visual verification of sinusoidal oscillations in the photodiode signal on an oscilloscope could not be made; FFT analysis was required for that verification. The measurement technique was unable to conduct reliable and repeatable measurements of the borosilicate suspension using the RES system. However, the particulate response was observed several times using video microscopy, and the transient response in the photodiode signal was observed on several occasions although it could not be reliably reproduced.

The technique shows promise as a tool for characterization of particles in suspension, since the RES transfer function could be measured, and that the rotational electrophoretic phenomena was repeatedly observed. The biggest hurdle to overcome is improving the signal-to-noise ratio of the measurement. One contributing issue to the signal-to-noise problem is that, in the current implementation, a single wavelength of light is used for the scattering measurement. The appropriate choice of that single wavelength has not been determined. One approach to avoid an inappropriate choice is to expose the system to white light and sense the scattered spectrum of light. Thus, a spectrum of scattered wavelengths could be measured over time, and the FFT analysis could be applied to each wavelength. The wavelength associated with the optimal signal-to-noise could then be determined. This approach would also provide a determination of the rotational electrophoretic spectral surface that described the RES transfer function for each frequency of applied field and wavelength of light.

Another problem that might have led to reduced signal-to-noise is the superposition of imposed fields in the sample volume of the measurement. While the

particles responded to the electric field, the fluid in the sampling chamber experienced an electroosmotic response to that same imposed field. The electroosmotic flow of the fluid exerted drag on the particles. The particles were also mobile via translational electrophoretic. The application of an electric field resulted in a current across the resistive suspension that experienced a heat dissipation associated with resistive heating. The heat dissipation also introduced natural convection into the suspension. The signal-to-noise ratio of the measurement might be improved by introducing a Pouiselle flow to the system with an average velocity that was much larger than the other velocities imposed by the other fields. Application of the electric field in a direction normal to the imposed flow field might result in rotation of the ensemble particles from one aligned state to another aligned state, thereby improving the signal-to-noise.

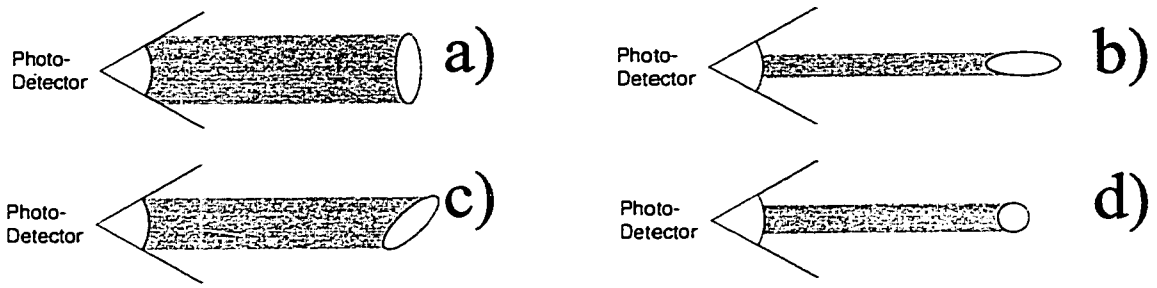

Figure 3.1: Schematic illustration of the influence of particle orientation on the light reaching a photo-detector.

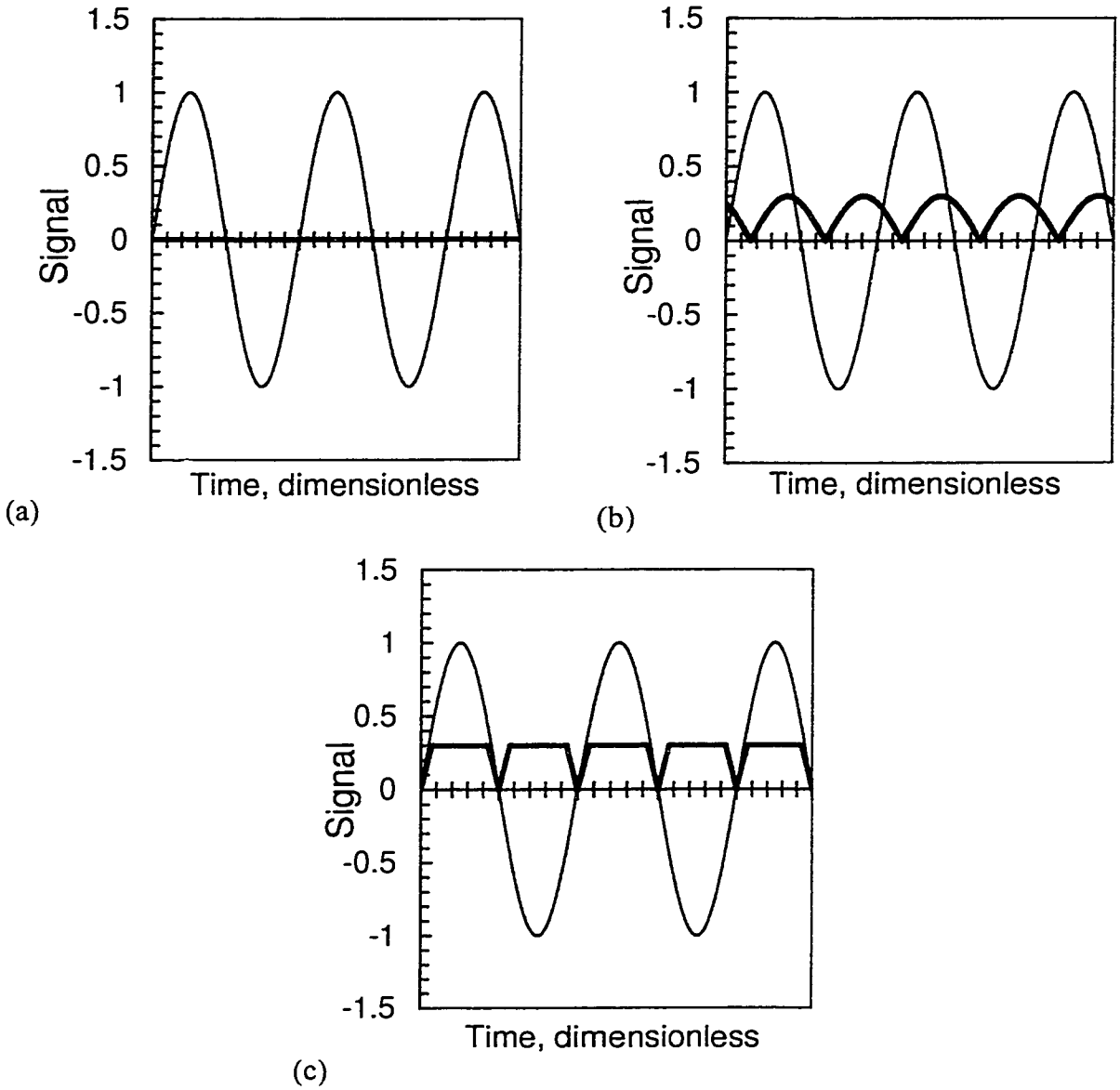

Figure 3.2: Expected photodiode responses at three representative frequencies of applied potential oscillating about zero. (a) high frequency. (b) characteristic frequency for rotation. (c) low frequency.

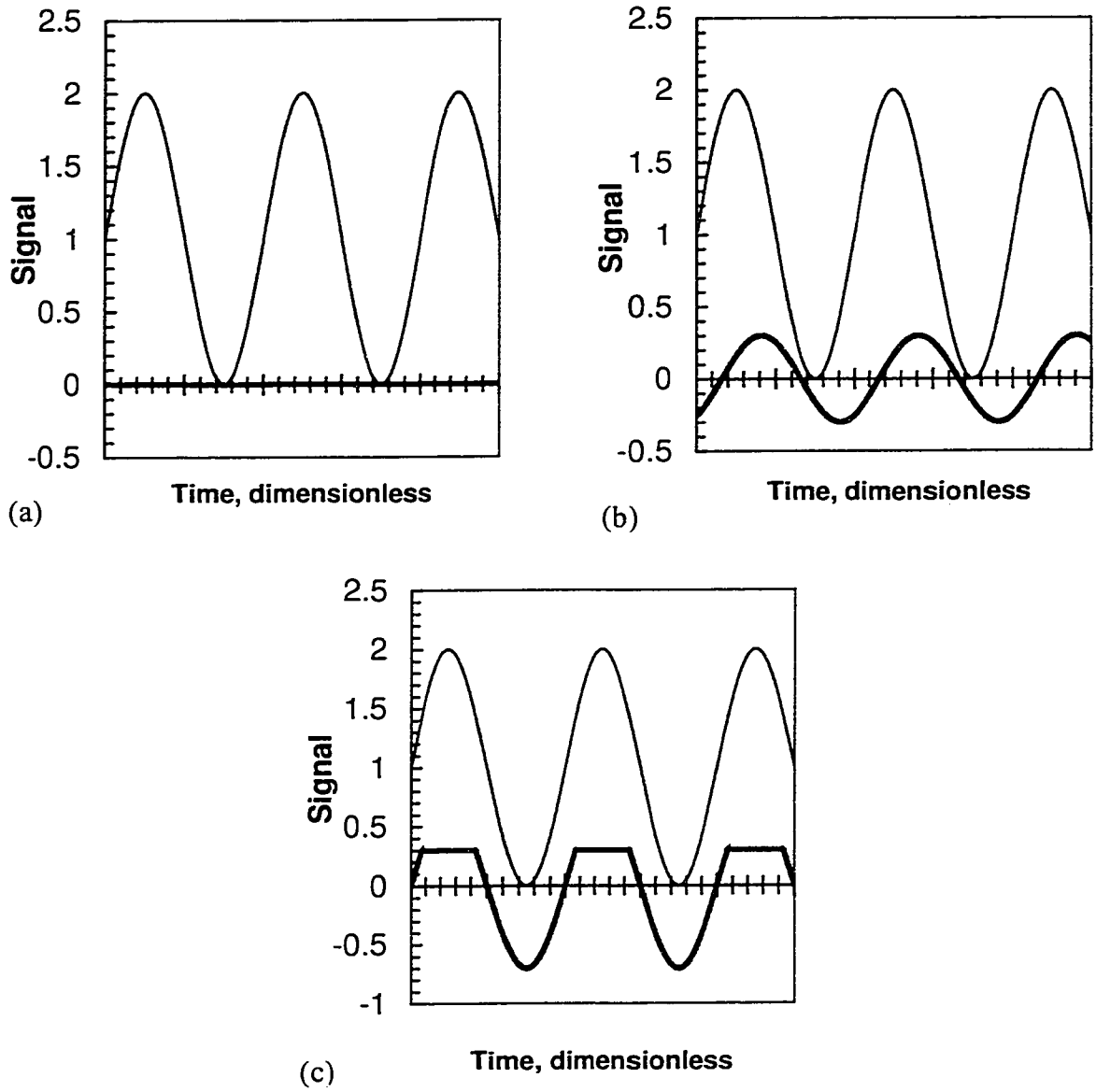

Figure 3.3: Expected photodiode responses at three representative frequencies of applied potential with imposed bias. (a) high frequency. (b) characteristic frequency for rotation. (c) low frequency.

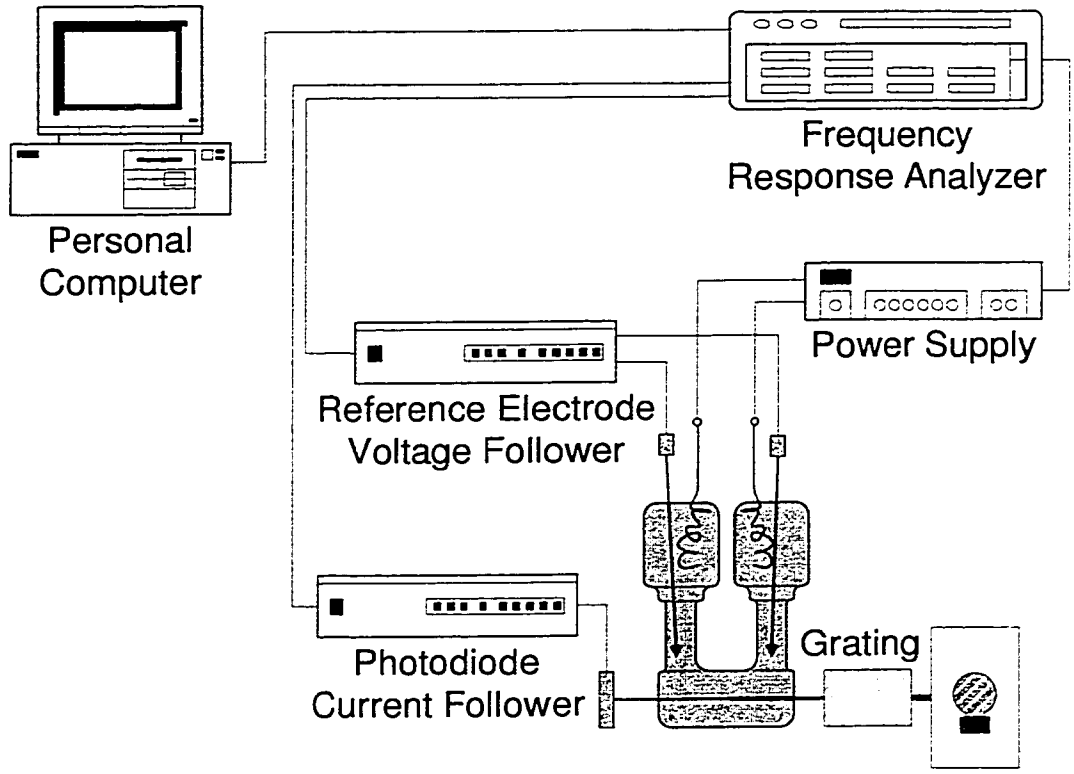

Figure 3.4: Schematic illustration of the rotational electrophoretic spectroscopy system.

Figure 3.5: Borosilicate fibers.

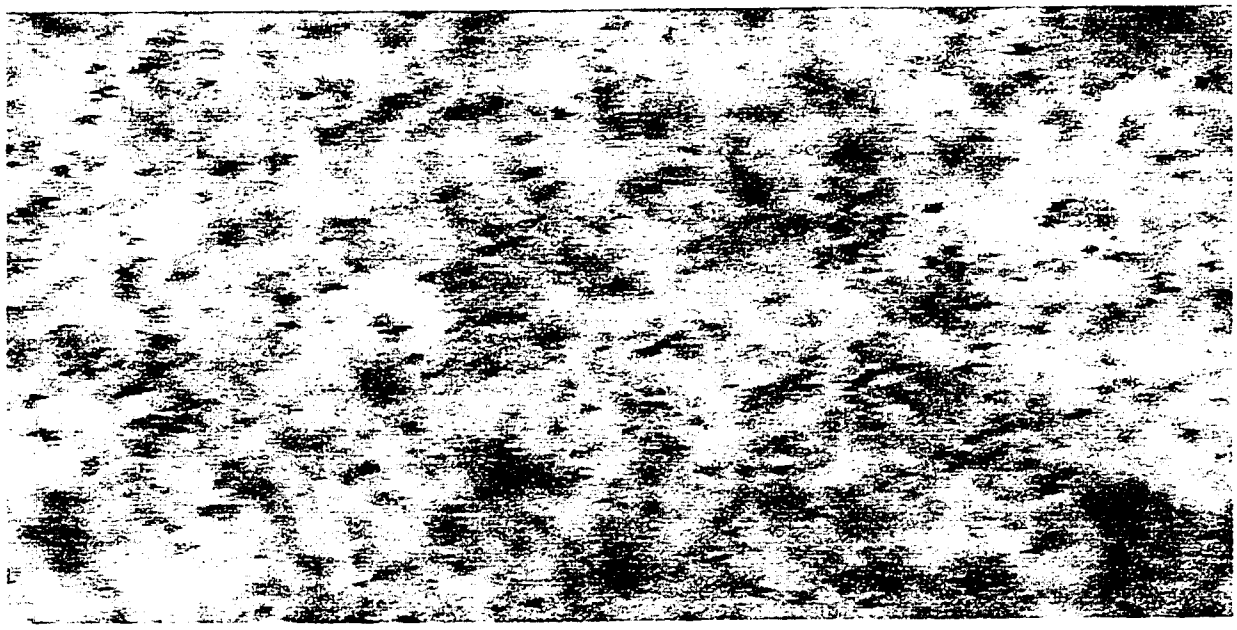

Figure 3.6: Ensemble of borosilicate fibers studied using the RES technique. Long strands are the borosilicate fibers that were closest to the focal plane.

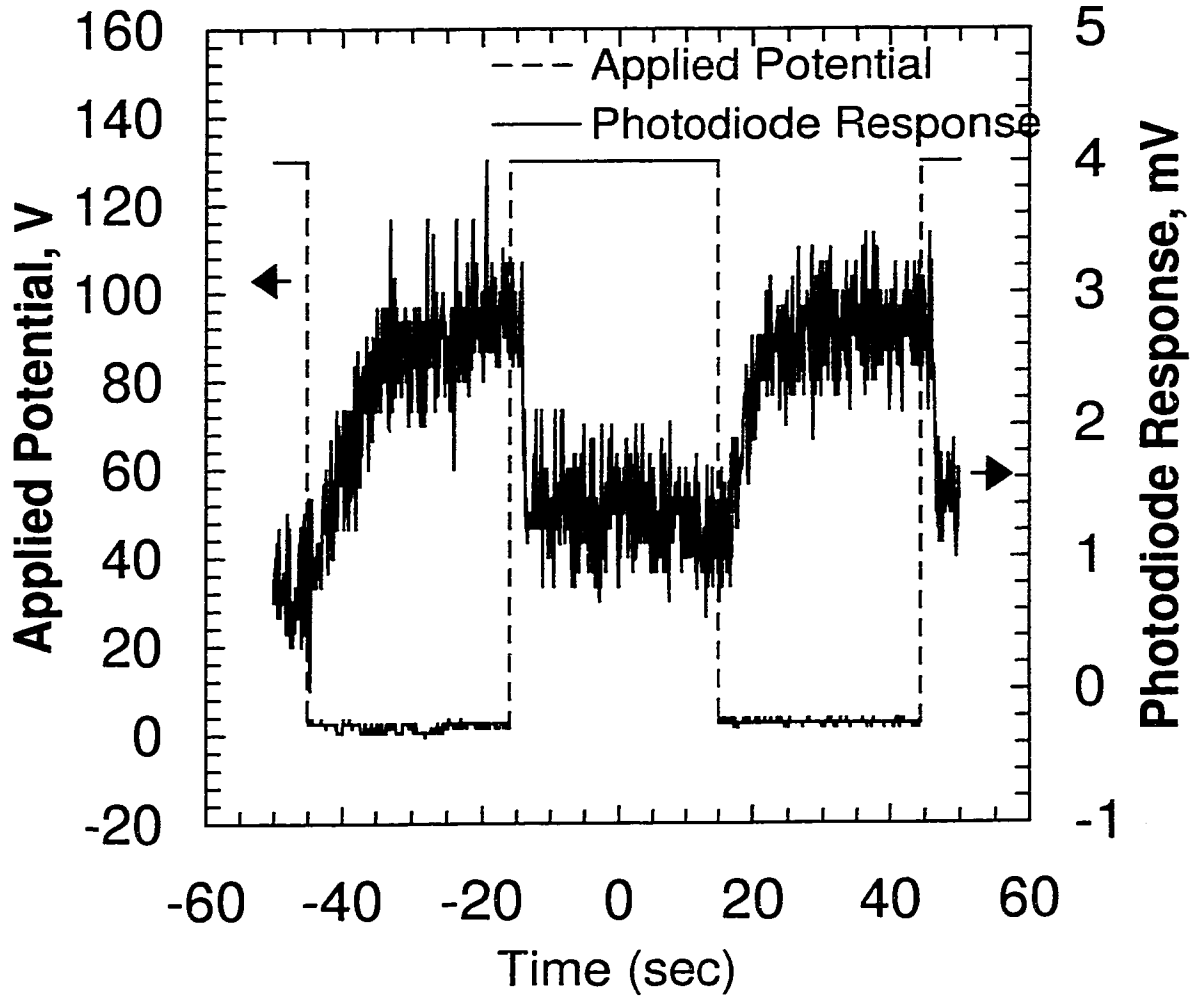

Figure 3.7: Transient response in photodiode signal proportional to forward scatter from a suspension of the borosilicate fibers.

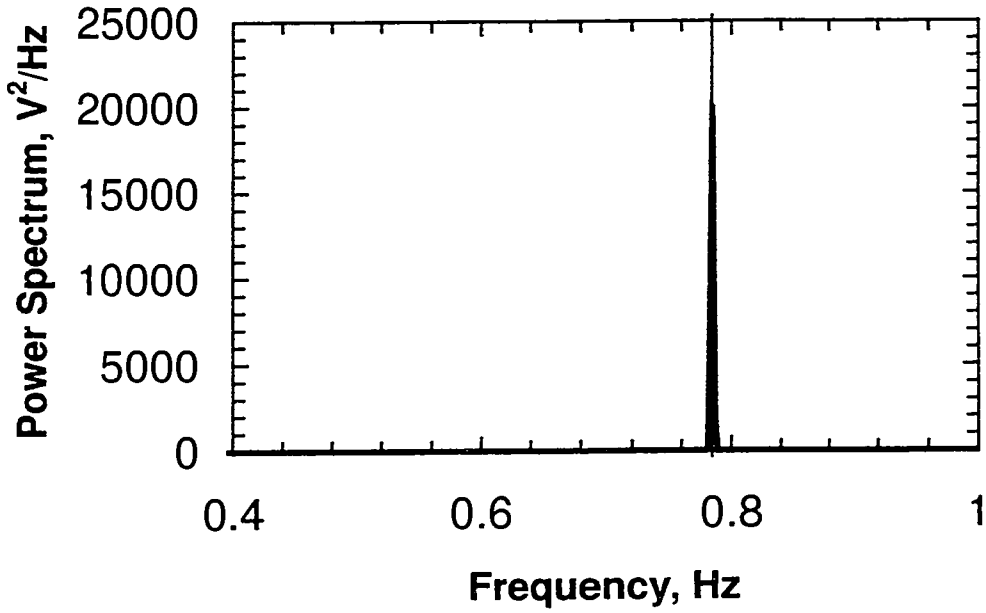

Figure 3.8: Power spectrum of applied voltage signal at 784 mHz.

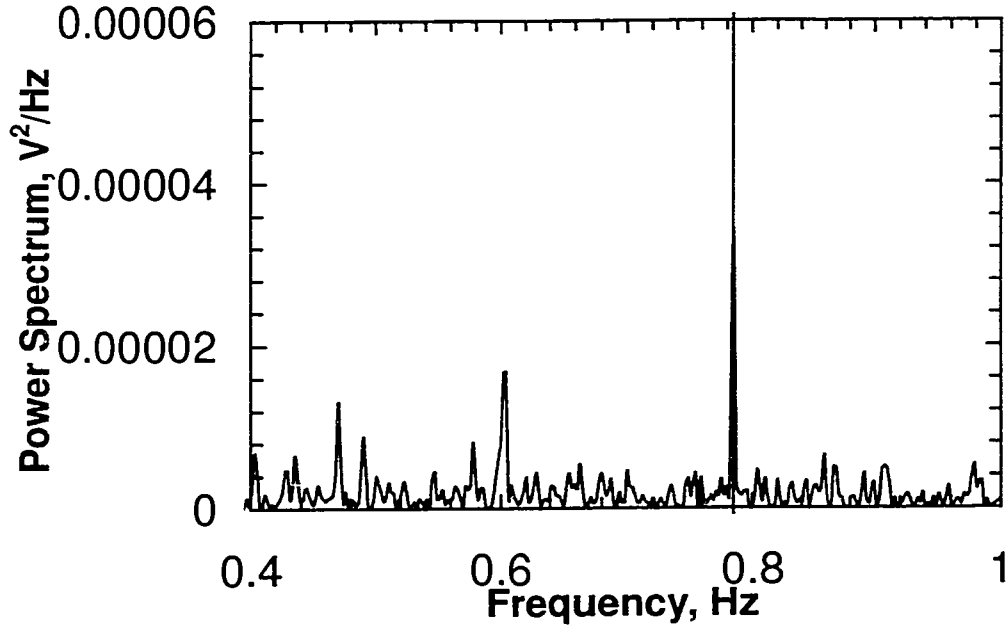

Figure 3.9: Power spectrum of responding photodiode signal. Primary peak is at 784 mHz.

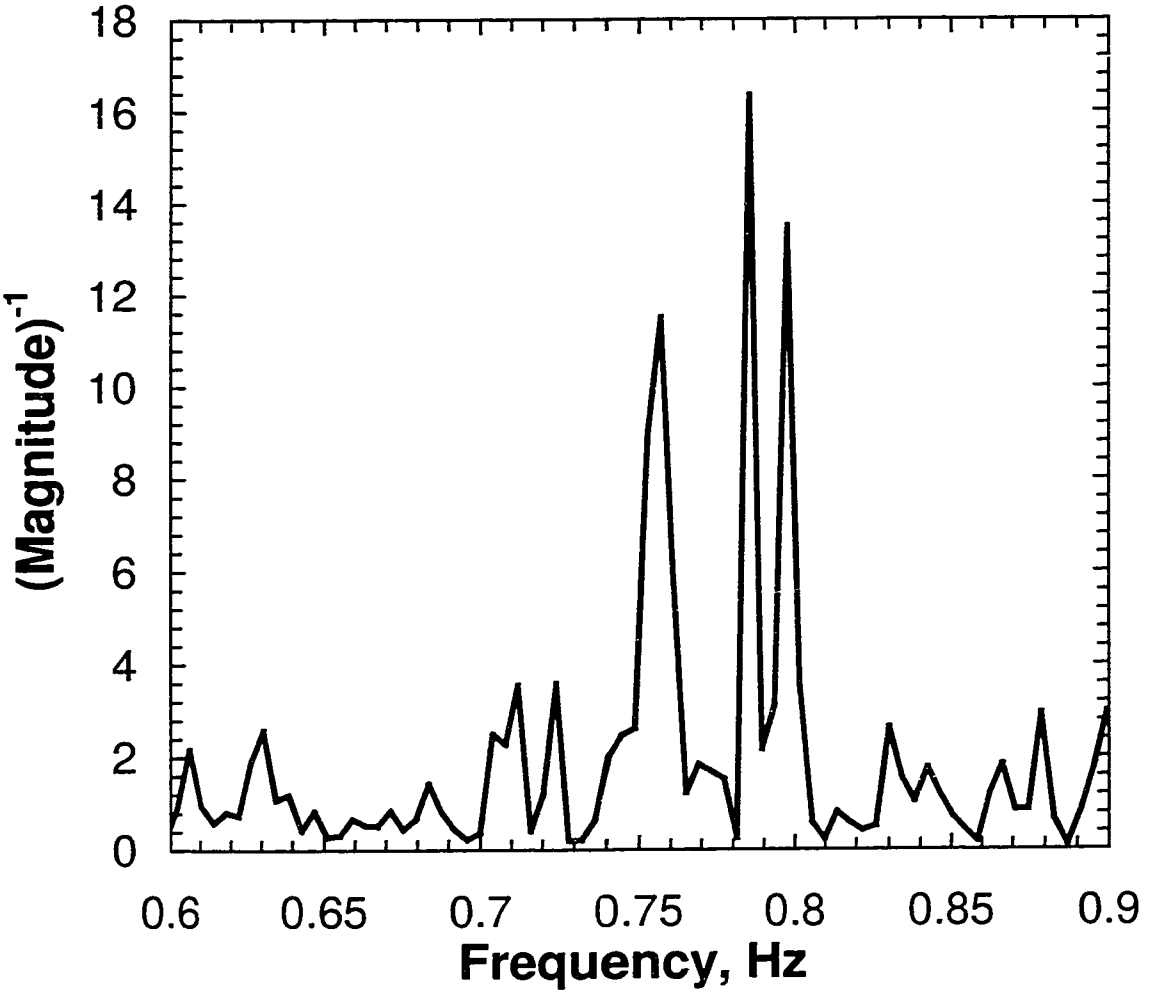

Figure 3.10: Spectrum of magnitude of transfer function calculated for the single frequency sine wave of applied potential at 748 mHz.

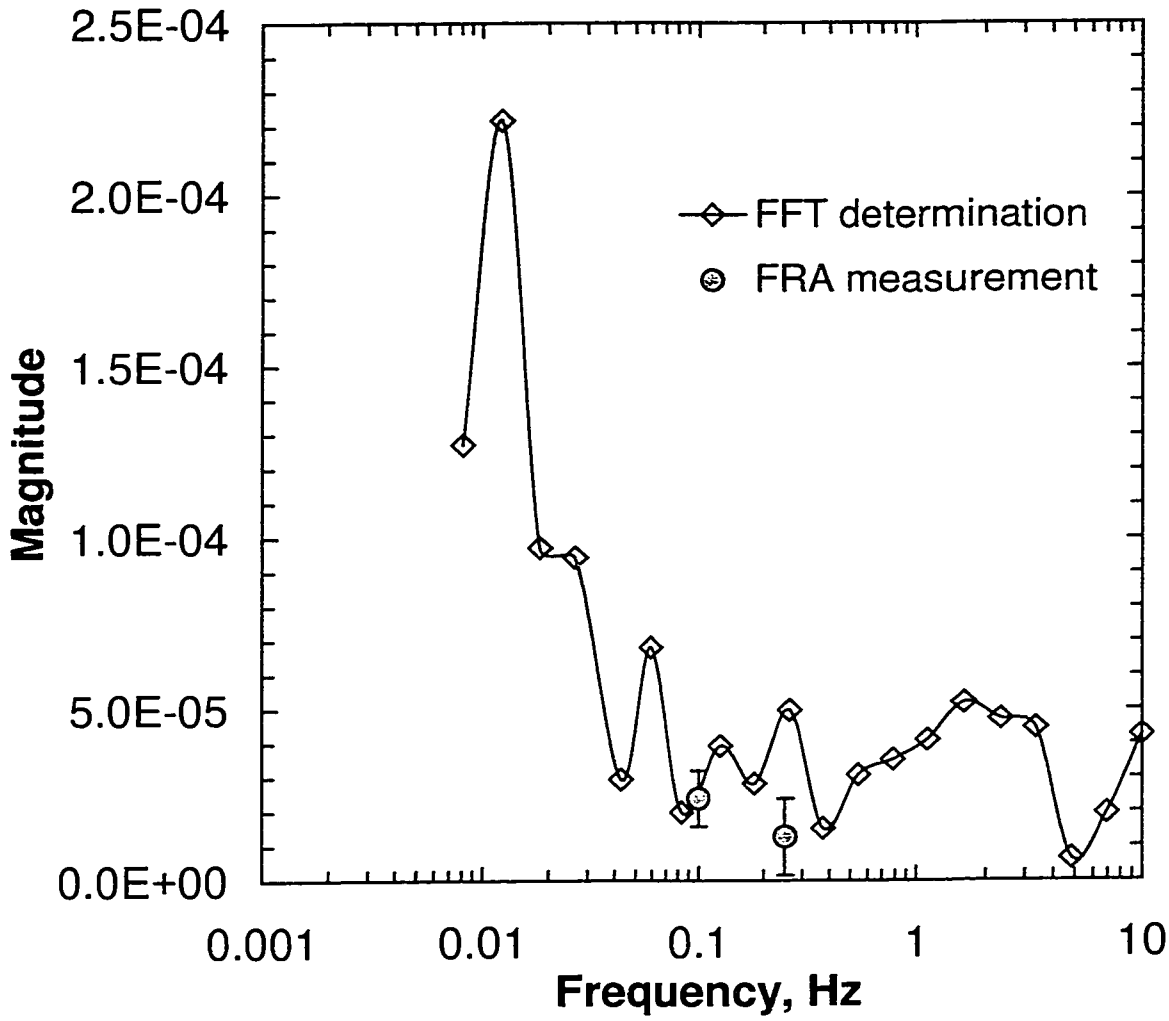

Figure 3.11: Magnitude spectrum of the RES transfer function for a suspension of rod-like borosilicate fibers in water.

CHAPTER 4
WEIGHTING STRATEGIES FOR COMPLEX NONLINEAR LEAST SQUARES REGRESSION

Regression of complex impedance spectra to complex models presents challenges that are not observed with the regression of real data to real models. Since the real and imaginary parts of the complex quantity are correlated by the Kramers-Kronig Relations (KKR),[11,105] an appropriate regression strategy should allow for the correlation of the real and imaginary parts of the complex model through the KKR. Nonlinear Least Squares (NLS)[106] regression techniques have been employed to estimate the parameters of complex impedance models.

Complex nonlinear least squares (CNLS) regression techniques were developed in the late 1960's. The CNLS approach is an improvement over NLS techniques because a combined model parameter set is estimated by simultaneous regression of the model to both real and imaginary data.[11] The CNLS objective function can be derived through a Taylor series expansion of the complex objective function to be

$$\sum_k w_k (Z(\omega_k) - \hat{Z}(\omega_k))^2 \tag{4.1}$$

where $\hat{Z}(\omega_k)$ is the model value of the impedance at the kth frequency and w_k is a weighting factor (or function) at that frequency.[107]

The first derivation of the CNLS objective function did not consider any form of weighting except the inherent choice of unity weighting.[107] Regression weighting is important in improving the ability of the minimization algorithm to provide tight

confidence intervals on the parameters of the model.[108] A weighting matrix was introduced into the CNLS objective function in its matrix form.[108] The weights were complex and, therefore, the real and imaginary impedance could be given independent weighting in a regression. While the weights could be independent, the form was suggested to be the inverse of the variance of the measurement.

Current papers[11,109,110] refer to the Macdonald and Garber paper[105] of 1977 as the original derivation of the CNLS technique as it applies to impedance spectroscopy. The CNLS objective function is applied to impedance models and complex spectra. At this point, the authors did not make any conclusions as to the most appropriate weighting strategy for the regression. They observed that the most appropriate strategy would be to use the inverse of the variance in the measurement as the weight at each frequency, but that at low frequency, time-constraints prevents the measurement of replicate spectra. The authors then suggested an approximation of the inverse of the variance of quantity X as a proportionality function, where the standard deviation, s, of quantity X can be written as

$$s_k^X = a|X_k|^n \tag{4.2}$$

where a is a proportionality constant and the exponent n satisfies $1 \geq n \geq -4$. The authors tested the proportional weighting scheme and unity weighting (in which the exponent is zero and that proportionality constant is unity), and found that the standard deviations of the parameter estimates were smallest when $n \leq -1$.

Since that paper, several categories of weighting strategy have been proposed. The first strategy was unity weighting, or no weighting, which is appropriate if the impedance is relatively constant over frequency ($(1/3)\overline{Z}_X \leq Z_X \leq 3\overline{Z}_X$). Zoltowski suggested a modulus weighting scheme in which the weighting function is the inverse of the modulus

of the impedance at that frequency.[110,111,112,113] Zoltowski argued that the modulus weighting scheme is appropriate when errors in the real and imaginary impedance are correlated. Macdonald refuted the choice of modulus weighting on the grounds that correlation between the errors in the real and imaginary impedance were presumed to be the result of instrumentation, as opposed a result of transformation through the KKR.[105] Another strategy is the proportional scheme suggested by Macdonald and others. [5,105,109] Proportionality weighting is considered to be the weighting scheme in which the standard deviation of a component in the measurement is approximately equal to the magnitude of the measurement of that component. The strategy is appropriate when the data range is large.[105] Two other weighting strategies have been suggested which can be reduced to the proportional weighting scheme. The first is called VWT[105] and is the form described in equation (4.2). The second is termed CWT[105] and can be written as

$$s_k^X = 1 + B_w |X_k|^n \tag{4.3}$$

where B_w is a proportionality constant. Another weighting scheme is termed residual iteration weighting (RWT)[105], in which each term in the objective function is weighted by the residual error between the model prediction and observed value at the kth frequency at the last iteration. Finally, all authors recommend that the regression be weighted by the inverse of the variance of the measurement at each frequency. [6-8,105,106,108-112] Macdonald and his co-authors have suggested that the standard deviation can be approximated as being proportional to the magnitude of the measurement.[105,109] Orazem and others have suggested that a measurement model be used to estimate the standard deviation of the measurement at each frequency.[6-8] Durbha *et al.* and Agarwal *et al.* have shown that the variance in the stochastic error in the real and imaginary impedance is statistically equivalent and can therefore be represented by an error structure model over frequency.[6-9]

Obviously, a contradiction exists between the descriptions of the standard deviation of the impedance made by the Macdonald and Orazem camps. If the variances in the errors of the real and imaginary impedances are equal, then the variances of the real and imaginary impedances cannot be equal to the squares of the magnitudes of the real and imaginary impedances. Both camps have studied the errors associated with impedance measurements to illustrate the behavior of those errors over frequency. Macdonald and his co-authors have studied both experimental and simulated data, but their focus has been on simulated data.[5,105,109] Orazem and his co-authors,[6-9] along with Dygas and his co-authors,[114] have observed the equality of the variances in the stochastic errors of the real and imaginary complex spectra on several classifications of experimentally-determined complex spectra such as electrochemical impedance spectra, electrohydrodynamic impedance spectra, and complex rheological spectra. It has been suggested that the observed equality of the variances is the result of the instrumentation in use. Thus, it is fair to determine how the errors that are characterized in these studies are, first, introduced into the spectra, and second, ascertained from the spectra.

The errors in simulated spectra generated by Macdonald and co-authors[105,109] were introduced in two ways. First, a spectrum was calculated with 13 significant digits. These "exact" results were then rounded to n significant digits where $n \leq 4$.[105,109] The authors realized that the rounding error was "not really a simulation of real experimental error."[109] The other approach was to add random noise to the exact (13 significant digit) spectrum.[105,109] The random noise had a Gaussian distribution around zero with standard deviation proportional to the exact value of the impedance.[109] The distribution was calculated using a seeded generator. Other distributions have been studied such as

colored noise, but in all cases, the noise is added directly to the frequency domain quantity and in a manner that is proportional to the exact value of the impedance. If the noise that is introduced into the spectra is proportional to the impedance, then it is obvious that the proportional weighting strategy is the most appropriate choice, as Macdonald and his co-authors have suggested.[5,105,109] Such simulations do not, however, provide any evidence on the nature of errors in experimental spectra.

The errors are ascertained by Macdonald and his co-authors to be the residuals between a model and a spectrum. Unlike Orazem and his co-authors, no filtering for non-stochastic errors is done (unless an obvious outlyer is present). This is obvious through an assertion that has been made[109] which refutes a suggestion made by Zoltowski:[110] a model should be fit to the form of the impedance (rectangular or polar) in which it is measured; transformation of the impedance will result in the generation of bias errors. That algebraic transformation would introduce bias errors only in the manner that machine errors are propagated through numerical calculations. Those bias errors would be, in general, orders of magnitudes smaller than experimentally determined stochastic errors[7] for double-precision calculations.[115]

Different researchers have taken extremely different stances on the nature of errors in impedance spectra. While Durbha *et al.* have considered the stochastic errors in impedance spectra to be normally distributed, other researchers have considered other distributions of noise in the spectra. Macdonald and Piterbarg have studied the transformation of colored random noise by the Kramers-Kronig transforms.[17] The authors have focused on the distribution of errors propagated through the KKR as a result of the numerical quadrature procedure that is used for integration of the transforms. This effort

is only useful if only one component of the complex impedance is measured, or if one wishes to predict the other component as a consistency test. However, the authors determined the dependence of the transformed errors on the quadrature procedure used to calculate the KKR error transform; they did not determine any physical reasons for the forms of distribution of errors in the spectra that they claimed to observe.

In that same paper,[17] Macdonald and Piterbarg present criticisms of the work of Durbha *et al* that have inspired the research that will be presented in the following chapters. In their criticism, they state that both groups have focused on numerical integration of the KKR to determine transformed errors.[17] They also claim that both groups recognize "that output stochastic errors are generated in the immediate neighborhood of the pole"[17] of the appropriate KK-transform. The paper[9] in contention was not intended to illustrate that the level or distribution of the stochastic errors "output," or more appropriately, transformed by the KKR were influenced by the implemented quadrature scheme. Rather, the authors intended to illustrate that a natural condition existed between the variances in the stochastic errors of the real and imaginary impedances. The conditions of the Kramers-Kronig relations were shown to lead to the equality of the variances in the stochastic errors of the complex impedance components.

An important point that has been missed in this controversy, however, is the evolution of the noise in impedance spectra. It is not the poles associated with the KKR that cause errors in measured spectra. The errors in measured spectra are the result of errors in the measurement technique and errors that have been transformed from the measured time-domain signals to the calculated frequency-domain quantities. Little discussion of this process has been made in the literature on impedance spectroscopy.

Some researchers[116,117] have looked at the issue of noise propagation from the time-domain into the frequency-domain, and their work will be discussed in the following chapters. The research that will be presented in the following chapters is a result of a desire to answer important questions raised by this controversy that have not yet been addressed. Thus, studies will be discussed that focus on the distribution of frequency-domain errors, the relationship between the variances in the complex impedance components, and the relationship between the frequency-domain errors and the noise associated with the time-domain signals under study and with the employed measurement technique.

CHAPTER 5
INFLUENCE OF INSTRUMENTATION ON ERROR STRUCTURE

Model transfer functions can be regressed to impedance spectra to assess information on the physics or chemistry of the system. The ability to regress the model to the spectra is enhanced by choice of an appropriate weighting strategy. One approach is to weight the regression by some function of the standard deviations of the complex errors in the data. Much controversy has been generated over defining the functionality of the standard deviations of the errors. Agarwal *et al.* and Durbha *et al.*[6-9] have found that the variances of the stochastic error contribution to the real and imaginary impedance are equal, and therefore, an error structure that defines the equivalent standard deviations as a function of frequency can be determined. Macdonald *et al.* have suggested that the standard deviations are roughly proportional ($\sigma_{Xi} / |X_i| = \text{constant}$) to the complex impedance at each frequency.[10-13] The findings of Agarwal *et al.* and Durbha *et al.* have been verified experimentally[6-8] and analytically.[9] Critics[17] of this finding have suggested that the equivalence of variances in the stochastic errors in the real and imaginary impedance is a result of the instrumentation used to measure the impedance spectra.

5.1 Motivation

Equivalence of the variances of the real and imaginary parts of the spectra has also been verified experimentally for electrohydrodynamic impedance spectroscopy,[74] rheology of viscoelastic fluids such as suspensions of particles (a purely mechanical

measurement of frequency-dependent stress-strain relations),[118] and dielectric spectroscopy (in which heterogeneous media disperse high frequency electric fields).[119] The measurement model infrastructure[6-9,74,75,119] developed for enhanced interpretation of electrochemical impedance spectroscopy was shown to be directly applicable to spectroscopic measurements that are important in the area of characterization of particulate suspensions. This infrastructure can be used to identify the degree of consistency of spectra to the Kramers-Kronig relations; thus, portions of the spectra that are corrupted by instrumental or other artifacts can be identified and rejected. The variances of the components of the complex stochastic errors of acoustophoretic spectra[75] were shown to be equal at most frequencies through the acceptance of the hypothesis that the variances were equal via the F-test. The variances of the real and imaginary parts of the stochastic error of the complex transfer functions were found to be equal for rheological and dielectric spectroscopy data that satisfied the Kramers-Kronig relations.

The arguments made by all parties have been mostly based on simulated spectra or analysis of experimental measurements (impedance spectroscopy, electrohydrodynamic impedance spectroscopy,[74] acoustophoresis,[75] dielectric spectroscopy,[119] or complex viscometry).[75] Recently, the aforementioned groups have independently produced papers with differing views on the propagation of complex impedance errors through the Kramers-Kronig relations (KKR).[9,17]

Throughout these works, the manner in which these frequency-domain errors develop from time-domain measurements has been largely uninvestigated.[120] While the focus on previous work has been on assembling a database of physico-chemical systems and various spectroscopic techniques, the full commonality of these measurements has

not been identified. There are various analog and digital methods for the measurement of complex spectra from time-domain signals. The spectroscopic techniques mentioned here (viscometry, EHD, etc) must use the same basic technologies for measuring complex quantities.

Some researchers combine the measurement techniques of Fourier analysis and phase-sensitive detection in order to measure a larger frequency range. Both techniques will be described fully in the next section of this chapter, but it should be noted that these two techniques measure complex electrochemical impedance through significantly different algorithms. Sets of data that were measured using the two techniques in conjunction were analyzed to determine the error structure of the measurement and the consistency of these measurements with the Kramers-Kronig relations. Sets of impedance spectra in which the low frequency spectrum was measured using the Fourier technique and the high frequency portion was measured using phase-sensitive detection were collected for three different systems.[1] System descriptions were not provided with the data. This was preferable, in that the purpose of this analysis was to determine the dependency of error structure and the Kramers-Kronig consistency on measurement technique. The spectra were analyzed with the Measurement Model Tool[6-8] set developed in the research group of Dr. Mark E. Orazem. The collected data were organized in four ways for study: the portion measured with the Fourier technique, the portion measured with phase-sensitive detection, the entire spectrum, and the portion of the entire spectrum that is Kramers-Kronig consistent. The student t-test ratio is presented for these systems

---

[1] Personal communication between Prof. Mark E. Orazem, Department of Chemical Engineering, University of Florida and Prof. Andrezj Lasia of the Department of Chemistry at the University of Sherbrooke, May 19, 1998.

in Table 5.1. The Fourier portion was found to produce errors in which the variances of the real and imaginary stochastic errors are equal. The PSD portion produces errors in which the variances of the real and imaginary stochastic errors were not necessarily equal. The variances of the errors determined for the sets of complete spectra were not necessarily equal. The variances of the errors determined for the KK-consistent portions of the sets of complete spectra might have been equal (Systems 2 and 3, in particular).

The ratio of the variance in the stochastic error in the real impedance to the variance in the stochastic error in the imaginary impedance is plotted as a function of frequency for all four cases of System 1 (Figure 5.1), System 2 (Figure 5.2), and System 3 (Figure 5.3). The F-test confidence limits are also plotted. For all three systems, the Fourier portion fell within the 99% confidence limit; and the entire spectrum and the Kramers-Kronig consistent part of the entire spectrum fell within the 99% confidence limit, but appear to be biased away from one at high frequency (the PSD portion). For all three systems, the PSD portion fell mostly within the 99% confidence limit, but the points were clearly scattered above unity, not around unity.

The character of the noise introduced into the signals in these experiments is unknown. And the nature of the systems is unknown. The FRA spectra were self-consistent with respect to the Kramers-Kronig transforms, while the PSD spectra were not. Also, the variance in the stochastic errors in the real impedance was equal to the variance in the stochastic errors in the imaginary impedance when the Fourier technique was employed, but the variances were not necessarily equal when the PSD technique was employed. Thus, experimental evidence suggests that the employed measurement technologies influence the stochastic errors in the complex impedance. The correlation

between the variances of the real and imaginary impedances is affected by the instrumentation used in the measurement of impedance spectra.

Software has been developed to simulate a variety of spectroscopic measurement techniques. The code is written so that the various techniques can be performed on the same signals. Different forms of time-domain stochastic and colored noise can be added to the signals. The various techniques are used to measure complex transfer functions. The frequency-domain errors can be determined and quantified to determine the influence of the measurement technique on the correlation between the variances of the real and imaginary stochastic errors.

The objective of this work is to apply the various complex spectral measurement techniques to a single pair of signals constructed with various additions of stochastic error. The simulated complex quantity is electrical impedance. Since the different technique algorithms for the same signals will calculate different impedance spectra, a direct comparison can be made of the error structure demonstrated by each technique. Another objective is to determine how the quality of time-domain noise is propagated into the frequency-domain. A quantitative means is required to test the equality of variances in stochastic errors and the Gaussian nature of the errors. While the F-test has been used as a means of testing for equality of variances, it is valid only at each frequency, not over the entire spectrum. The suitability of the student t-test will be assessed as means to test for equality of variances over the spectrum and to determine the form of distribution of errors.

5.2 Methods for Impedance Calculation

Complex impedance spectra are generally measured using one of three techniques.[5] Frequency Response Analysis (FRA)[5] makes use of the orthogonality of sines and

cosines to determine the complex impedance as the complex coefficients of a Fourier series representing the ratio of the response signal to the input signal. Lissajous Parameterization (LP) is the most classic technique in that it can be used if the only measurement instrument available is an oscilloscope.[5] Phase-sensitive detection (PSD)[5] is similar to FRA employing the orthogonality of sines and cosines along with the zero integral of these waves over an integer number of cycles. An additional technique can be envisioned which would simply relate the maximum and minimum of two signals as a relative magnitude and phase angle. This technique will be referred to a Peak Detection (PD).

5.2.1 Frequency Response Analysis

This method is used by the Solartron Instruments family of FRA's and gain/phase analyzers.[121] It is a specific application of Fourier analysis of signals. While Fourier analysis provides a spectral representation of a time-domain signal, frequency response analysis determines the coefficient of a specific term in the Fourier series representation of the signal. With the generation of the perturbation signal, an in-phase sine wave and a 90^0 out-of-phase sine wave are generated. The input signal (current for impedance) and the output signal (voltage) are multiplied with the in-phase and the out-of-phase sine waves producing four signals for analysis. Each product-of-signals is integrated over each cycle of the generated input signal. The current and voltage signals can be described by a complex representation where the real part of the current signal is

$$I_r(\omega) = \frac{1}{T}\int_0^T I_0 \sin(\omega t + \phi)\sin(\omega t)dt \tag{5.1}$$

the imaginary part of the current signal is

$$I_j(\omega)=\frac{1}{T}\int_0^T I_0\sin(\omega t+\phi)\cos(\omega t)dt \tag{5.2}$$

the real part of the voltage signal is

$$V_r(\omega)=\frac{1}{T}\int_0^T V_0\sin(\omega t+\phi)\sin(\omega t)dt \tag{5.3}$$

and the imaginary part of the voltage signal is

$$V_j(\omega)=\frac{1}{T}\int_0^T V_0\sin(\omega t+\phi)\cos(\omega t)dt \tag{5.4}$$

The real part is noted by the subscripted r and the imaginary part is denoted by the subscripted j. The constant coefficients of the integrands are the amplitudes of the respective signals. The current is the variable I and the voltage is the variable V. The difference between the limits of integration is an integral number of cycles. The impedance is calculated as the complex ratio of the complex representations of the output signal to the input signal as shown in Figure 5.4.

5.2.2 Lissajous Parameterization

A common technique that was used to determine the impedance prior to the development of fast microprocessors was the estimation of the peaks and axis-intercepts of the Lissajous representation of the input and output signals on an oscilloscope. The most robust manner to determine the impedance through the Lissajous plot would be regression of the data points to a curve. Similarly, a sine wave could be regressed to each signal to provide a regressed curve to the Lissajous figure.

If the input and output signals are regressed to the function

$$f(t) = A\sin(\omega t + \phi) \tag{5.5}$$

where A and ϕ are the estimated parameters, then any noise in the actual signal will be filtered by a Least Squares Minimization.[123] The ratio of the amplitude, A, for the voltage signal to the amplitude, A, for the current signal is taken to be the magnitude of the impedance transfer function at the given frequency. The difference between ϕ for the output signal and ϕ for the input signal is taken to be the phase angle of the transfer function at the same frequency.

5.2.3 Phase-Sensitive detection

A lock-in amplifier can also be used with a potentiostat to measure the complex impedance. The method of its use is fundamentally different than the method of a frequency response analyzer. Whereas the FRA performs an assessment of the Fourier coefficients of the input and output signals, the lock-in amplifier measures the amplitudes of the two signals and the phase angle of each signal with respect to some reference signal. Thus, the impedance is measured in polar, rather than Cartesian, form.

A general signal can be written as

$$A = A_0 \sin(\omega t + \phi_A)\,. \tag{5.6}$$

A reference square wave of unity amplitude is generated at the same frequency as the sinusoidal perturbation. It can be approximated by the Fourier series[5]

$$S = \frac{4}{\pi}\sum_{n=0}^{\infty}\frac{1}{2n+1}\sin[(2n+1)\omega t + \phi_S]. \tag{5.7}$$

As was done in the Fourier assessment technique, the measured signal and reference signal are multiplied, resulting in a product signal

$$AS = \frac{4A_0}{\pi}\sum_{n=0}^{\infty}\frac{1}{2n+1}\sin(\omega t+\phi_A)\sin[(2n+1)\omega t+\phi_S]. \tag{5.8}$$

This can be rewritten using trigonometric identities to be[5]

$$AS = \sum_{n=0}^{\infty}\frac{2A_0}{(2n+1)\pi}\left\{\begin{array}{l}\cos[-2n\omega+\phi_A-(2n+1)\phi_S] \\ -\cos[(2n+2)\omega t+\phi_A+(2n+1)\phi_S]\end{array}\right\}. \tag{5.9}$$

The product of the signals can be expanded via the trigonometric identity for the cosine of the sum of two angles to be[5]

$$AS = \frac{2A_0}{\pi}\left[\begin{array}{l}\cos(\phi_A-\phi_S)-\cos(2\omega t+\phi_A+\phi_S) \\ +\frac{1}{3}\cos(-2\omega t+\phi_A-3\phi_S)-\frac{1}{3}\cos(4\omega t+\phi_A+3\phi_S) \\ +\frac{1}{5}\cos(-4\omega t+\phi_A-5\phi_S)-\frac{1}{5}\cos(6\omega t+\phi_A+5\phi_S)+\cdots\end{array}\right]. \tag{5.10}$$

If the product signal is integrated over each cycle, it is clear that only the leading term of the series will have a non-zero value, thus,[5]

$$\frac{\omega}{2\pi}\int_0^{2\pi/\omega} AS\,dt = \frac{2A_0}{\pi}\cos(\phi_A-\phi_S). \tag{5.11}$$

The integral (5.11) will have a maximum value when the phase angle of the square wave is equal to the phase angle of the measured signal. In practice, the phase angle of the generated square wave is adjusted such that the integral is maximized. The phase angle of the square wave at the maximum value of the integral yields the phase angle of the measured signal. The maximum value of the integral provides the amplitude of the measured signal. This procedure is used on both signals such that the amplitude and phase angle of each signal is measured as shown in Figure 5.5. The ratio of the voltage amplitude to the current amplitude is the impedance magnitude and the difference between the phase angles of the output and input signals is the impedance phase angle.[5]

5.2.4 Peak Detection

This method is expected to be the least robust method for measurement of the complex impedance because its lack of an averaging algorithm makes it sensitive to random noise. Each cycle of the input and output signals is stored as one-dimensional arrays of data $\mathbf{V}$ and $\mathbf{I}$. The maximum and minimum values of each array is determined (see equations (5.12) and (5.13)); the average of the maximum and absolute value of the minimum (equations (5.14) and (5.15)) are taken to be the amplitude of the signal.

$$\max(\mathbf{V}) = \mathbf{V}(k), \quad \min(\mathbf{V}) = \mathbf{V}(l) \tag{5.12}$$

$$\max(\mathbf{I}) = \mathbf{I}(m), \quad \min(\mathbf{I}) = \mathbf{I}(n) \tag{5.13}$$

$$\tilde{V} = \frac{\left(|\mathbf{V}(k)| + |\mathbf{V}(l)|\right)}{2} \tag{5.14}$$

$$\tilde{I} = \frac{\left(|\mathbf{I}(m)| + |\mathbf{I}(n)|\right)}{2} \tag{5.15}$$

The index of the maximum element of the input array is subtracted from the index of the maximum element of the output array. The same difference is calculated between the indices of the minimum elements of the two arrays. The average of the difference is divided by the number of samples per cycle, p, and multiplied by 2π to give the phase angle of the transfer function at the given frequency. If the input signal is the current perturbation, then

$$\phi = \frac{2\pi\left[(k-m)+(l-n)\right]}{2p}. \tag{5.16}$$

The ratio of the amplitude of the voltage signal to the amplitude of the current signal is taken as the magnitude of the transfer function at the same frequency.

5.3 Simulation of Impedance Systems

Code was written in the LabView® G Language. The program was designed to simulate an actual impedance experiment. The parameters of the simulation mimicked the experimental parameters of the Solartron Instruments family of frequency response and gain/phase analyzers, *i.e.*, SI 1250, SI 1254, and SI 1260 instruments. The interactive panel of the program provided a choice of the number of replicate scans to be made, the frequency range of the scan, the number of points in the scan, the auto-integration channel, the auto-integration mode, the delay before enforcing the auto-integration criterion, and the maximum time for integration.

A choice of transfer functions, or systems, to study was also provided. In this work, a simple single Voigt element was chosen. The Voigt element consisted of a 1 Ω resistor, R_{sol}, in series with a 1 Ω resistor, R, and a 100 μF capacitor, C, in parallel. The transfer function was written as

$$Z(\omega) = Z_r + jZ_j = R_{sol} + \frac{R}{1+\omega^2 R^2 C^2} + j\frac{-\omega RC}{1+\omega^2 R^2 C^2}. \tag{5.17}$$

Since this was a digital simulation, a sampling number, p, was an option also provided to the user. In the simulations discussed here, each cycle of each sine wave was sampled at 1024 samples/cycle. The effective digital sample rate, s, is related to the sine wave frequency, ω, by

$$s = p \cdot \omega \tag{5.18}$$

where s provides the upper frequency limit on the FFT of the sampled signal. Finally, the option of adding Gaussian-white noise to the input signal, the output signal, or both signals was provided with. The noise level was set as a percentage of the input signal

amplitude. In these simulations the Gaussian-noise level was 10% of the input signal amplitude unless otherwise noted.

Each technique was applied to each cycle of the input and output signal. The impedance estimation was completed when the auto integration criterion was met on the chosen channel. For short integration, convergence was achieved when the ratio of the standard deviation of the estimation of the magnitude to the magnitude over all cycles on the selected channel was less than 0.10. For long integration, convergence was achieved when the same ratio was less than 0.1. The simulation could be run without an auto integration criterion; the impedance at each frequency was measured until the auto integration time elapsed. The impedance was taken to be the mean of the impedances calculated at all cycles.

5.3.1 Time-domain Noise

Two forms of time-domain noise were proposed. The first was a stochastic error signal added to the signals or the system. Thus, for galvanostatic impedance measurements, the signals could be described by

$$\tilde{V}(t) = V(\omega)\sin(\omega t + \phi_V) + \varepsilon_V \tag{5.19}$$

$$\tilde{I}(t) = I_{applied}\sin(\omega t + \phi_I) + \varepsilon_I \tag{5.20}$$

where ε_V and ε_I are stochastic additive errors to the "true" value of the potential and current signals, respectively.

The second type of noise was a stochastic error with a standard deviation that was proportional to the instantaneous value of the signal. This noise distribution was not intended to represent an experimentally observed noise distribution. Proportional noise was a mathematical construct in which stochastic error was added at each point in time to

each signal amplitude and phase angle (or instantaneous value of the frequency). However, this type of error could be viewed as describing noise in the frequency control, because the error in the phase angle could be rewritten as the product of an error in frequency and time. For galvanostatically controlled impedance measurements, the signals could be described by

$$\tilde{V}(t) = \left(\hat{V}(\omega) + \varepsilon_V\right)\sin\left(\omega t + \hat{\phi}_V + \varepsilon_{\phi_V}\right) \tag{5.21}$$

$$\tilde{I}(t) = \left(I_{applied} + \varepsilon_I\right)\sin\left(\omega t + \hat{\phi}_I + \varepsilon_{\phi_I}\right). \tag{5.22}$$

Of course, the two types of errors could be combined to provide a general form for a signal with error by

$$\tilde{A}(t) = \left(\hat{A} + \varepsilon_A\right)\sin\left(\omega t + \hat{\phi}_A + \varepsilon_{\phi_A}\right) + \varepsilon_1. \tag{5.23}$$

This was rewritten such that

$$\begin{aligned}\tilde{A}(t) = {} & \hat{A}\sin\left(\omega t + \hat{\phi}\right) + \hat{A}\cos\left(\omega t + \hat{\phi}\right) \\ & + \varepsilon_1 + \varepsilon_2 \sin\left(\omega t + \hat{\phi}\right) + \varepsilon_3 \cos\left(\omega t + \hat{\phi}\right)\end{aligned}. \tag{5.24}$$

where

$$\varepsilon_2 = \varepsilon_A \cos\left(\varepsilon_{\phi_A}\right) + A\left(\cos\left(\varepsilon_{\phi_A}\right) - 1\right) \tag{5.25}$$

$$\varepsilon_3 = \varepsilon_A \sin\left(\varepsilon_{\phi_A}\right) + A\left(\sin\left(\varepsilon_{\phi_A}\right) - 1\right). \tag{5.26}$$

In general, a noisy sinusoidal signal could contain the true sinusoid plus an out-of-phase component plus error proportional to the true sinusoid plus error proportional to the out-of-phase component plus additive error. The noise introduced in this chapter was Gaussian, or normal, white noise. The values of this noise waveform had mean of zero and were evenly distributed around the mean.[122] A histogram of this type of error can be found in Figure 5.6. In Chapter 7, a second noise distribution will be discussed.

5.3.2 Application of Measurement Techniques

The impedance spectra could be calculated using any set of the four techniques to calculate the impedance: assessment of the real and imaginary Fourier coefficients using trapezoidal quadrature, detection of peaks, regression to the individual waveforms, and phase-sensitive detection. For each technique, a separate file was saved for each scan. Thus, one input signal was correlated to one output signal simultaneously using up to four different techniques.

One cycle of the (clean or noisy) perturbation signal was constructed. The Fast Fourier Transform of the signal was then determined. The response signal was determined as the real inverse FFT of the product of the FFT of the perturbation signal and the impedance transfer function. A second random noise signal could be added to the response signal. Thus, if noise were added only to the input, then the response signal would contain noise transformed from noise in the perturbation via the impedance transfer function. If noise was added to the perturbation and response signals, then the response signal contained transformed noise and additive noise. It should be noted that this algorithm was tested on a perturbation impulse, and the response of the first order transfer function showed the expected transient behavior that would be associated with analytical Fourier transformation of the same impulse.

The pair of single cycles of the perturbation and response signals was then passed to the calculation techniques. The complex impedance was calculated for that cycle of the two signals. After three cycles of measurement, the auto-integration criterion was tested. The calculations were performed over enough cycles for the auto-integration criterion to be achieved by all the techniques.

5.4 Results of Simulations

The error analysis tools used for electrochemical impedance spectroscopy were applied to the simulated impedance spectra. The measurement techniques corresponding to measurement with a frequency response analyzer or Lissajous parameterization provided data in which the variance in the real and imaginary parts of the stochastic error contributions were equal. The peak detection method provided data that contained a large bias error contribution. The technique corresponding to measurement using a lock-in amplifier was found to provide data in which the variances in the real and imaginary components of the stochastic error were not equal.

It was necessary to establish an acceptable means to test for equality of variances over the spectrum and to determine the form of distribution of errors. Noise was characterized using two standard statistical parameters. The ratio of the variances of the stochastic errors in the real and imaginary parts of the impedance was compared to the F-test and student t-test.[122] The F-test is a means of accepting or rejecting the hypothesis of equality of the variances in the real and imaginary impedances at each frequency of the scan. Several plots of this test follow for each simulation and measurement technique. The student t-test provides a method for testing the equality over the entire spectrum, and verification of the normal distribution of errors. Because the t-test parameter is dependent upon the number of samples, the ratio has been calculated of the measured t-test parameter and the critical t-test parameter, $t_{0.025/90}$.

The t-test parameter is appropriate for characterization of the frequency-domain errors because, in each case studied, the impedance values at each frequency are distributed in a Gaussian form (for example, Figure 5.7). The distribution of errors shown in this plot were calculated for impedance spectra determined using the FRA

technique. The errors were normally distributed at each frequency for all the commercially available techniques (FRA, PSD, and LP). The t-test ratios for the distributions of replicate impedance calculations at each frequency are less than one. Thus, one aspect of this work is to determine the effectiveness of the student t-test for qualification of the mean value and form of error distributions.

5.4.1 Simulations with Peak Detection

The different technique algorithms applied to the same signals resulted in the calculation of different impedance spectra. The results of the FRA technique and the Lissajous Parameterization technique were, in general, very similar. The peak detection technique failed as an impedance measurement technique because it introduced a significant bias error contribution to the measurement. The spectra were not at all representative of the relaxation phenomena associated with the Voigt element. This bias error contribution was filtered from the stochastic error contribution, though. The variances of the real and imaginary stochastic errors were never equal. This is not a surprising result in that noise in the signal would be directly propagated into the value of the impedance calculated for each cycle at each frequency.

The t-test ratios of the logarithm of the ratio of the variances of the stochastic errors in the real and imaginary impedance are shown in Table 5.2 for three of the measurement techniques and several simulation conditions. The t-test ratio was less than one for systems in which noise was added only to the output signal or to both the current and voltage signals and the impedance was calculated via the FRA or Lissajous Parameterization algorithms. The Peak Detection method never produced errors for which the ratio of the variances was one. This was a result of the technique not using averaging for impedance calculation. The t-test ratios were greater than one for the

systems in which noise was added only to the input signal. In these cases, the calculated errors were on the order of machine error, and loss of significance in the calculated variances resulted. Two plots are provided to illustrate the effectiveness of the t-test ratio for qualification of the distribution of errors. In Figure 5.8, in which Lissajous Parameterization was employed, and Gaussian noise was added to the input and response signals, the log of the ratio appears to be distributed around zero as a Gaussian, and the t-test ratio is less than one. The same result was found for the calculation of the impedance using the FRA technique and either quadrature scheme.

5.4.2 Simulations with Phase-Sensitive detection

The phase-sensitive detection simulation was developed. An algorithm was introduced to calculate the complex impedance with a level of precision associated with the calculation via frequency response analysis. The integral of the product of the test signal (perturbation or response) and reference square wave was calculated for 16 evenly spaced values of square wave phase angle. The process was repeated using 16 values of phase angle over the four intervals of the preceding iteration around the phase angle at which the maximum value of the integrals occurred. Since the signals are digital, this process is repeated until the phase angle is not smaller than 2π radians divided by the number of points in each cycle of the signal. Once this level has been reached, the integral-phase angle points are fit to a second order polynomial. The phase angle at which this polynomial is maximized is determined with the appropriate numerical precision. The process is repeated over several cycles until the standard deviation of the calculated impedance magnitudes satisfies the auto-integration criterion. In Figure 5.9, the log of the ratio of the variances in the real and imaginary impedances calculated using the PSD

technique is plotted. The log of the ratio may be Gaussian but it is not distributed around zero, and the t-test ratio is much greater than one. The t-test was not satisfied for this simulation. The variance in the real impedance was less than the variance in the imaginary impedance calculated via PSD, thus one component of the impedance was biased with respect to the other. The student's t-test ratio demonstrated this inequality of the variances.

With the development of the PSD calculation technique, the simulations were run again with the PSD, Lissajous parameterization, and frequency response analysis calculation techniques applied to the same set of perturbation and response signals. The FRA technique was applied twice. In one case, the trapezoidal quadrature rule was used to integrate the signals.[123] In the other case, Bode quadrature was employed for signal integration.[123] Two quadrature schemes were employed to determine the effect of quadrature error on the impedance calculations. The Bode quadrature rule is a higher order rule, and therefore generates a smaller error than the trapezoidal rule (order h^7 as compared to h^3, where h is the step-size of integration, $2\pi/1024$).[123]

5.4.2.1 Additive Noise

Four categories of simulations were conducted - CASE 0: adding no noise (a test of precision for each technique), CASE 1: adding noise only to the perturbation signal, CASE 2: adding noise only to the response signal, and CASE 3: adding noise to both the perturbation and response signals. The range of values for the variances in the real and imaginary impedance is listed in Table 5.3. The student's t-test results for equality of variances of the stochastic errors in the real and imaginary impedance are reported in Table 5.4. The noise in each case was Gaussian with a standard deviation of 10% of the

input perturbation. Thus the standard deviation of the additive noise to the response varied between 5% and 10% of the signal depending on the frequency of the measurement, since the impedance varied between one and two ohms.

The test case of calculating the impedance from clean perturbation and response signals provided verification that each technique generated only deterministic errors, namely those associated with the numerical technique employed. This is a crucial result in that it allows for the comparison of frequency domain stochastic errors to time-domain stochastic noise introduced into the clean signals. The deterministic errors were on the order of the level of precision associated with the code compiler and microprocessor-set (see Table 5.3).

Frequency-domain stochastic errors were on the machine level of precision for the simulation cases in which noise was added only to the input perturbation and the impedance was calculated using either the FRA or Lissajous parameterization techniques (see Table 5.3). The PSD calculation for the same simulated signal set resulted in frequency-domain stochastic errors that were significant. The variance of these errors in the real impedance were not equal to the variance of the errors in the imaginary impedance as qualified by the F-test and student's t-test (See Table 5.4).

The errors in the impedance determined from the other two simulation cases were of significant order (see Table 5.3). For the two FRA and the Lissajous parameterization calculations, the variance in the stochastic errors in the real impedance were equal to the variance in the stochastic errors in the imaginary impedance. The variances were not equal when the PSD calculation was applied to the same set of perturbation-response signals. Figure 5.10 is the ratio of variance in the real impedance to variance in the

imaginary impedance as a function of frequency. The impedance was calculated using the FRA technique with Bode quadrature. The ratio is generally distributed around one and most points fall within the 99% probability level. Therefore, the hypothesis that the variances are not equal can be dismissed with 99% confidence. Figure 5.11 is the ratio of variance in the real impedance to variance in the imaginary impedance as a function of frequency where the impedance was calculated using the PSD technique with Bode quadrature. The ratio is not distributed around one and most points fall outside the 99% probability level. Therefore, the hypothesis that the variances are not equal can be accepted with 99% confidence. The equality was tested for each case and for each measurement technique at each frequency using the F-test, and over the spectrum using the student's t-test. The results of the student's t-test ratio are consistent with the results of the F-test for each case.

5.4.2.2 Proportional Noise

Three categories of simulations were conducted - CASE 1: adding noise only to the perturbation signal (thereby introducing noise transformed by the system into the response signal), CASE 2: adding noise only to the response signal, and CASE 3: adding noise to both the perturbation and response signals. The range of values for the variances in the real and imaginary impedance is listed in Table 5.3. The student's t-test results for equality of variances of the stochastic errors in the real and imaginary impedance are reported in Table 5.4. The noise in each case was Gaussian with a standard deviation of 10% of the parameter to which the noise was added (amplitude or phase angle).

Frequency-domain stochastic errors were on the machine level of precision for the simulation cases in which noise was added only to the input perturbation and the impedance was calculated using either the FRA or Lissajous parameterization techniques.

The PSD calculation for the same simulated signal set resulted in frequency-domain stochastic errors that were significant. The variance of these errors in the real impedance were not equal to the variance of the errors in the imaginary impedance as qualified by the F-test and student's t-test (See Table 5.4).

The errors in the impedance determined from the other two simulation cases were of significant order. For the two FRA and the Lissajous parameterization calculations, the variance in the stochastic errors in the real impedance were equal to the variance in the stochastic errors in the imaginary impedance. The variances were not equal when the PSD calculation was applied to the same set of perturbation-response signals. Figure 5.12 is the ratio of variance in the real impedance to variance in the imaginary impedance as a function of frequency. The impedance was calculated using the FRA technique with Bode quadrature. The ratio is not distributed around one and most points fall on the 99% probability limit. Therefore, the hypothesis that the variances are not equal cannot be dismissed. Figure 5.13 is the ratio of variance in the real impedance to variance in the imaginary impedance as a function of frequency where the impedance was calculated using the PSD technique with Bode quadrature. The ratio is generally distributed around one and most points fall within the 99% probability level. Therefore, the hypothesis that the variances are not equal can be rejected with 99% confidence. The results of the student's t-test ratio are consistent with the results of the F-test for each case. The equality for each case and for each measurement technique was tested at each frequency using the F-test, and over the spectrum using the student's t-test.

The ratio of variances divided by three is also plotted in Figure 5.12. It is generally distributed about one, and falls within the 99% probability limit. Therefore, the

hypothesis that the variance in the real impedance is not equal to three times the variance in the imaginary impedance can be rejected with 99% confidence. This factor of three may be the result of the skewness of frequency domain errors that will result from the bias introduced by this type of time-domain error. The error added to the phase angle introduces the problems associated with measurement using phase-sensitive detection. No analytical reason could be found for the factor of three. One explanation for this result is that the introduction of noise in the phase angle offset the errors in phase angle measurement due to the PSD calculation. The noise in phase angle also could be considered as noise in the frequency control. As a result, the Kramers-Kronig transforms could not be expected to hold, and this might account for the inequality of the variances in the complex impedance components when the impedance was measured using the FRA or Lissajous parameterization techniques.

5.5 Discussion

As the experimental evidence suggested, these simulations verify that the instrumentation used to conduct impedance spectroscopy measurements will influence the correlation between the variance in the stochastic errors in the real impedance and the variance in the stochastic errors in the imaginary impedance. The distributions of the errors in the components of the complex impedance are Gaussian, and can therefore be defined by variances, but the variances of the distributions may not be equal. For additive errors, it was shown that the variances were equal when the FRA technique was used, but not when the PSD technique was used. For proportional errors, the opposite was found to be true.

5.5.1 Rectangular Coordinate Error Structure Due to Errors in Polar Measurement

If the phase angle is measured independently of the magnitude, then, the error in measurement of the phase angle is independent of the error in measurement of the magnitude. The accuracy of the measurement of the phase angle and signal amplitude may not necessarily be the same. In this case, one may not expect the variance in the real and imaginary stochastic errors to be equal. This can be shown explicitly.

Let $\hat{Z}_r$, $\hat{Z}_j$, $|\hat{Z}|$, and $\hat{\phi}$ be the true values of the complex impedance in real and imaginary and modulus and phase angle forms, respectively. Then, the measured values of the same components can be written as

$$Z_{r,meas} = \hat{Z}_r + \varepsilon_r \tag{5.27}$$

$$Z_{j,meas} = \hat{Z}_j + \varepsilon_j \tag{5.28}$$

$$|Z_{meas}| = |\hat{Z}| + \varepsilon_m \tag{5.29}$$

$$\phi_{meas} = \hat{\phi} + \varepsilon_\phi \tag{5.30}$$

if bias errors are neglected. By solving (5.27)-(5.30) for the true values of each component, the measured impedance in Cartesian form can be found to be

$$Z_{r,meas} = \sqrt{\frac{\left(|\hat{Z}| - \varepsilon_m\right)^2}{1 + \tan^2\left(\hat{\phi} - \varepsilon_\phi\right)}} \tag{5.31}$$

$$Z_{j,meas} = \sqrt{\frac{\left(|\hat{Z}| - \varepsilon_m\right)^2 \tan^2\left(\hat{\phi} - \varepsilon\right)}{1 + \tan^2\left(\hat{\phi} - \varepsilon_\phi\right)}} \tag{5.32}$$

From (5.27) and (5.28), the error in the measurement of the real and imaginary impedance can be found by subtracting (5.31) and (5.32) from the true values of the real

and imaginary impedance, respectively. For N measurements of the impedance in polar form, the corresponding errors in the measurement of the Cartesian form can be derived as

$$\sigma_r^2 = \hat{Z}_r^2 - \frac{2\hat{Z}_r}{N}\sum_{n=1}^{N}\sqrt{\frac{\left(\left|\hat{Z}\right| - \varepsilon_{n,m}\right)^2}{1+\tan^2\left(\hat{\phi} - \varepsilon_{\phi,n}\right)}} + \frac{1}{N}\sum_{n=1}^{N}\left[\frac{\left(\left|\hat{Z}\right| - \varepsilon_{n,m}\right)^2}{1+\tan^2\left(\hat{\phi} - \varepsilon_{\phi,n}\right)}\right] \tag{5.33}$$

$$\sigma_j^2 = \hat{Z}_j^2 - \frac{2\hat{Z}_j}{N}\sum_{n=1}^{N}\sqrt{\frac{\left(\left|\hat{Z}\right| - \varepsilon_{n,m}\right)^2 \tan^2\left(\hat{\phi} - \varepsilon_{\phi,n}\right)}{1+\tan^2\left(\hat{\phi} - \varepsilon_{\phi,n}\right)}} + \frac{1}{N}\sum_{n=1}^{N}\left[\frac{\left(\left|\hat{Z}\right| - \varepsilon_{n,m}\right)^2 \tan^2\left(\hat{\phi} - \varepsilon_{\phi,n}\right)}{1+\tan^2\left(\hat{\phi} - \varepsilon_{\phi,n}\right)}\right] \tag{5.34}$$

It is clear from (5.33) and (5.34) that for $\sigma_r^2 = \sigma_j^2$ there must be a curve that relates the vector of errors in the magnitude to the vector of errors in the phase angle measurement as a function of the true Cartesian and polar forms of the impedance.

The equality of variance in the Cartesian errors mapped from the polar form was tested using a variety of forms of noise added to calculated impedance spectra of a single Voigt element. Two tests were used to check for equality of the variances. For every form (proportional to the magnitude, proportional to the component, and absolute error), the variances were found to differ with respect to the F-test and student t-test. This result would be most representative of the FRA testing signals with proportional errors. The errors in the signal phase angles would be independent of the errors in signal magnitudes (and thus error in the impedance phase angle would be independent of the error in impedance magnitude). Thus, equations (5.33) and (5.34) support the result (see Section

3.2.2) that the variances in the real and imaginary impedance are not necessarily equal for the cases where the FRA was used to measure the impedance from signals with proportional noise.

5.5.2 Source of Bias Errors in Phase-Sensitive detection

Figure 5.14 shows the distribution of errors in the real impedance calculated via the PSD technique on current and voltage signals with additive Gaussian noise introduced into the input and output signals with respect to the theoretical impedance spectrum. It is clear that a bias exists; the mean value of the distribution is not equal to zero. This bias is a result of errors introduced by the PSD measurement.

If error is present in the PSD measurement of the impedance magnitude, then the integral of the product of signals in equation (5.11) can be rewritten to be

$$e_{out} = \frac{\omega}{2\pi}\int_0^{2\pi/\omega} ASdt = \frac{2A_0}{\pi}\cos\left(\phi_A - \phi_S + \varepsilon_\phi\right) + \varepsilon_X . \tag{5.35}$$

where ε_X is the error in the integration (an additive error) and ε_ϕ is the error in the phase angle measurement (due to error in the phase angle controller). If the difference in phase angles is equal to zero, then the observed value of the signal amplitude will be

$$A_{0,ob} = \frac{\pi}{2\cos\left(\varepsilon_\phi\right)}\left(e_{out} - \varepsilon_X\right). \tag{5.36}$$

The error in magnitude estimate, ε_A, can be written as the difference between the observed value of the magnitude and the expectation value

$$\varepsilon_A = A_{0,ob} - E\left(A_0\right) = \frac{\pi}{2}e_{out} - \frac{\pi}{2\cos\left(\varepsilon_\phi\right)}\left(e_{out} - \varepsilon_X\right). \tag{5.37}$$

Therefore, the error in the magnitude is a function of the integral, the error in the phase angle controller and error in the integral

$$\varepsilon_A = \frac{\pi}{2} e_{out}\left(1 - \frac{1}{\cos(\varepsilon_\phi)}\right) + \frac{\pi}{2}\left(\frac{\varepsilon_X}{\cos(\varepsilon_\phi)}\right). \tag{5.38}$$

Note that the error in phase angle propagates into the magnitude through a cosine. Thus, while the error in phase angle may be distributed normally about zero, the cosine of those errors will not be normally distributed since the cosine of a negative number is the same as the cosine of the absolute value of that number (see Figure 5.15). The skewness of the distribution of the cosine of the errors in phase angle that are normally distributed about zero is quite negative. As a result of this cosine, the error in amplitude will be biased away from zero. This is the cause for the inequality of variances in the real and imaginary impedances calculated via PSD. The bias in the frequency-domain errors is therefore not characteristic of the error distribution. The bias is caused by the PSD instrumentation.

If the error in phase angle control in equation (5.38) is equal to zero, then the errors in magnitude are distributed like the errors in integration (additive errors). In the case where PSD is employed on signals with proportional noise, the errors in phase angle control and phase angle noise (through the introduction of the proportional noise) may cancel. If this were to occur, and the additive error in equation (5.38) is equal for both current and voltage signals, then the impedance determined via the PSD technique would have variance in the real stochastic errors that would be equal to the variance in the imaginary stochastic error. This could explain the results of Section 3.2.2 in which the variances in the real impedance were equal to the variances in the imaginary impedance only when the PSD method was used (Figure 5.13).

5.5.3 Condition on Spectroscopy Errors by the Kramers-Kronig Relations

Durbha *et al.*[9] determined that the variance of the stochastic errors in the real impedance is equal to the variance of the stochastic errors in the imaginary impedance.

This equality held as a statistical expectation. Three fundamental assumptions were associated with their derivation. First, the expectation of the frequency-domain errors was assumed to be equal to zero. Second, it was assumed that the errors were distributed normally. Finally, the derivation held for complex spectra in which the real and imaginary parts were determined simultaneously. For example, the equality of the variances would not be expected for measurements of the complex refractive index because the real and imaginary parts are determined independently.

The results of the simulations on the systems for which Gaussian additive noise was introduced into the signals and the impedance was calculated using the FRA or LP techniques satisfied the assumptions made by Durbha *et al.*[9] The spectral errors were distributed normally about zero. The real and imaginary parts of the spectrum were calculated simultaneously by these two methods. The equality of the variances was not observed for impedance calculated using the PSD technique on the same systems. It was shown in the previous section that the expectation of the errors would not be equal to zero. One of the assumptions made by Durbha *et al.*[9] was not satisfied, therefore, the variances were not equal.

The results of the simulations on the systems with proportional noise was introduced into the signals were quite different. When the FRA or LP techniques were employed for impedance calculation, the equality of the variances was not observed. When the PSD technique was used for the calculation, the equality of the variances was observed. Possible reasons for this were presented in Section 5.5.1. One possible reason was that the error in phase angle could be considered as an error in the frequency control. When the frequency was not stationary, the FRA and LP methods determined impedances

containing errors that did not satisfy the conditions of the Kramers-Kronig relations. Thus, an unstated assumption in the derivation of Durbha *et al.*[9] may be that the frequency of the measured impedance must be free of error. The PSD method may minimize the affect of the error in frequency control with error in the phase shift control.

5.6 Conclusions

Replicate impedance spectra were provided for three different physical systems. Each spectrum was measured using a combination of techniques: PSD at high frequency, FRA at low frequency. The variance in the stochastic error in the real impedance was equal to the variance in the stochastic error in the imaginary impedance when the FRA technique was employed; the same equality did not necessarily hold when the PSD method was used. The PSD spectra could be transformed via the Kramers-Kronig relations with 95% confidence, but a residual bias error was always present. This bias error could be associated with the independent measurements of magnitude and phase angle for PSD.

To better understand the influence of measurement technique on the error structure of impedance measurements, three commercially available impedance spectroscopy measurement techniques were simulated using LabView® programs. Frequency response analysis, phase-sensitive detection, and Lissajous parameterization were applied simultaneously to an identical pair of perturbation and response signals associated with a given transfer function. Different forms of error were introduced into these signals in various combinations to determine the dependence of frequency-domain errors in impedance spectra on the noise in the constituent time-domain current and voltage signals. Two forms of time-domain noise with three means of introduction were

considered. The two forms of noise were Gaussian additive and Gaussian proportional types. For each type of noise, three sets of simulations were conducted, namely, noise introduced into the input signal and transformed by the system into the voltage signal, noise introduced only into the voltage (response) signal, and noise introduced into the current and voltage signals.

The variance in the stochastic error in the real impedance was equal to the variance in the imaginary impedance for the cases where the additive noise types were introduced into the signals, and the impedance was measured using the FRA or Lissajous parameterization techniques. Impedances with equivalent variances in the real and imaginary impedances were not calculated by the PSD technique applied to the same pairs of signals. This inequality was a result of the independent measurements of phase angle and magnitude associated with the PSD technique. However, in the proportional noise cases, impedances with equivalent variances in the complex impedance components were determined using the PSD technique, while the other two techniques failed to generate that result. The only explanation for this result is that the introduction of noise in the phase angle associated with the proportional noise type offset the errors in phase angle measurement due to the PSD calculation. The noise in phase angle also could be considered as noise in the frequency control. As a result, the Kramers-Kronig transforms could not be expected to hold, and this might account for the inequality of the variances in the complex impedance components when the impedance was measured using the FRA or Lissajous parameterization techniques.[9]

The equivalence of the variances in the stochastic errors in the real and imaginary impedances is a condition of the Kramers-Kronig relations if the necessary conditions of

the KKR hold and the errors are normally distributed and have an expectation value of zero.[9] The stochastic errors in impedance calculated using the PSD technique were normally distributed, but the mean value of the distribution was not zero. Therefore, criticism of the equivalence of the variances as a result of instrumentation has some basis. However, the bias of the stochastic errors is caused by the PSD instrumentation; the bias is not characteristic of the stochastic error distribution.

Table 5.1: Student t-test ratio for impedance spectra measured with a combination of techniques.

	System 1	System 2	System 3
Fourier Analysis	0.46	0.46	0.20
Phase-Sensitive Detection	1.50	0.47	1.40
Entire Spectrum	1.10	1.34	1.22
KK-consistent Spectrum	1.36	0.47	0.89

Table 5.2: Student t-test values for matrix of simulations and assessment techniques. Additive noise level was 10% of input signal amplitude unless otherwise noted.

	Fourier Assessment	Peak Detection	Signal Regression
Input - 10%	4.67 (2e-5)**	5.71 (0.03)**	---
Input - 20%	4.63 (3e-5)**	3.13 (0.04)**	---
Input - 50%	4.31 (8e-5)**	3.02 (0.06)**	---
Output	0.544	14.3	0.614
All	0.0685	14.9	0.0232
Colored Noise - All	0.196	15.7	0.197

* FD indicates FFT of noise signal added to FFT of output signal; TD indicates noise signal added to output signal in the time-domain.

** Term in parentheses is the inverse of the signal-to-noise ratio.

Table 5.3: Range of values of variance in stochastic errors for matrix of simulations and assessment techniques. Additive noise level (INPUT and OUTPUT) was 10% of input signal amplitude unless otherwise noted. Transformed noise (Z*INPUT) was proportional to the impedance at the given frequency.

NOISE ADDED						
INPUT	Z*INPUT	OUTPUT	FRA(T)	FRA(B)	LP	PSD
☐	☐	☐	$0 \Leftrightarrow 10^{-44}$	$0 \Leftrightarrow 10^{-14}$	$0 \Leftrightarrow 10^{-40}$	$0 \Leftrightarrow 10^{-42}$
☒	☒	☐	$10^{-14} \Leftrightarrow 10^{-8}$	$10^{-12} \Leftrightarrow 10^{-6}$	$0 \Leftrightarrow 10^{-20}$	$10^{-8} \Leftrightarrow 10^{-2}$
☐	☐	☒	$10^{-8} \Leftrightarrow 10^{-6}$	$10^{-8} \Leftrightarrow 10^{-6}$	$10^{-8} \Leftrightarrow 10^{-6}$	$10^{-6} \Leftrightarrow 10^{-4}$
☒	☒	☒	$10^{-8} \Leftrightarrow 10^{-4}$	$10^{-8} \Leftrightarrow 10^{-4}$	$10^{-8} \Leftrightarrow 10^{-4}$	$10^{-6} \Leftrightarrow 10^{-2}$

(T) Trapezoidal quadrature rule used in FRA calculation.

(B) Bode quadrature rule used in FRA calculation.

Table 5.4: Student t-test (applied to ratio of variances in stochastic errors in the real and imaginary impedances) ratios for matrix of simulations and assessment techniques. Additive noise level was 10% of input signal amplitude unless otherwise noted.

NOISE ADDED						
INPUT	Z*INPUT	OUTPUT	FRA(T)	FRA(B)	LP	PSD
☒	☒	☐	4.99	2.35	---*	8.16
☐	☐	☒	0.0526	0.000858	0.0901	15.03
☒	☒	☒	0.0781	0.636	0.142	16.35

(T) Trapezoidal quadrature rule used in FRA calculation.

(B) Bode quadrature rule used in FRA calculation.

* Variance of stochastic errors was often zero.

Table 5.5: Range of values of variance in stochastic errors for matrix of simulations and assessment techniques. Additive noise level (INPUT and OUTPUT) was 10% of input signal amplitude unless otherwise noted. Transformed noise (Z*INPUT) was proportional to the impedance at the given frequency.

NOISE ADDED						
INPUT	Z*INPUT	OUTPUT	FRA(T)	FRA(B)	LP	PSD
☒	☒	☐	$10^{-8} \Leftrightarrow 10^{-5}$	$10^{-8} \Leftrightarrow 10^{-5}$	$10^{-8} \Leftrightarrow 10^{-5}$	$10^{-8} \Leftrightarrow 10^{-5}$
☐	☐	☒	$10^{-7} \Leftrightarrow 10^{-5}$	$10^{-7} \Leftrightarrow 10^{-5}$	$10^{-7} \Leftrightarrow 10^{-5}$	$10^{-8} \Leftrightarrow 10^{-5}$
☒	☒	☒	$10^{-7} \Leftrightarrow 10^{-4}$	$10^{-7} \Leftrightarrow 10^{-4}$	$10^{-7} \Leftrightarrow 10^{-4}$	$10^{-7} \Leftrightarrow 10^{-4}$

(T) Trapezoidal quadrature rule used in FRA calculation.

(B) Bode quadrature rule used in FRA calculation.

Table 5.6: Student t-test (applied to ratio of variances in stochastic errors in the real and imaginary impedances) ratios for matrix of simulations and assessment techniques. Additive noise level was 10% of input signal amplitude unless otherwise noted.

NOISE ADDED						
INPUT	Z*INPUT	OUTPUT	FRA(T)	FRA(B)	LP	PSD
☒	☒	☐	4.59	4.98	4.59	1.00
☐	☐	☒	4.80	4.63	4.78	1.91
☒	☒	☒	5.58	5.75	5.58	1.85

(T) Trapezoidal quadrature rule used in FRA calculation.

(B) Bode quadrature rule used in FRA calculation.

* Variance of stochastic errors was often zero.

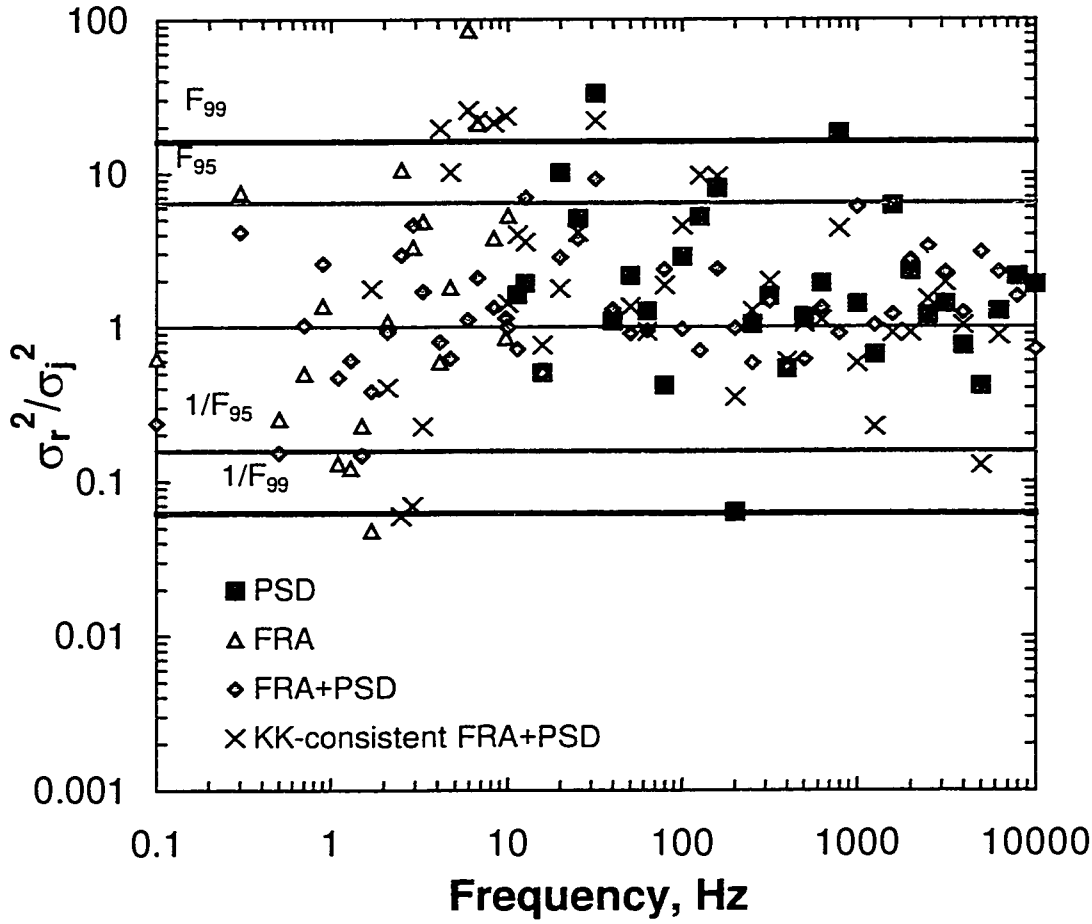

Figure 5.1: The ratio of variances in stochastic errors in the real impedance to those in the imaginary impedance as a function of frequency for the four cases of System 1: the FRA portion, the PSD portion, the entire spectrum, and the Kramers-Kronig consistent portion of the entire spectrum. The F-test probability limits are also plotted. The ratio for the PSD portion is not scattered about one, but generally falls within the 99% confidence limit. The ratios for the other three cases are scattered about one, and generally fall within the 99% confidence limit. The F-test suggest that the variances are equal for all four cases. The least confidence in that equality is for the PSD case.

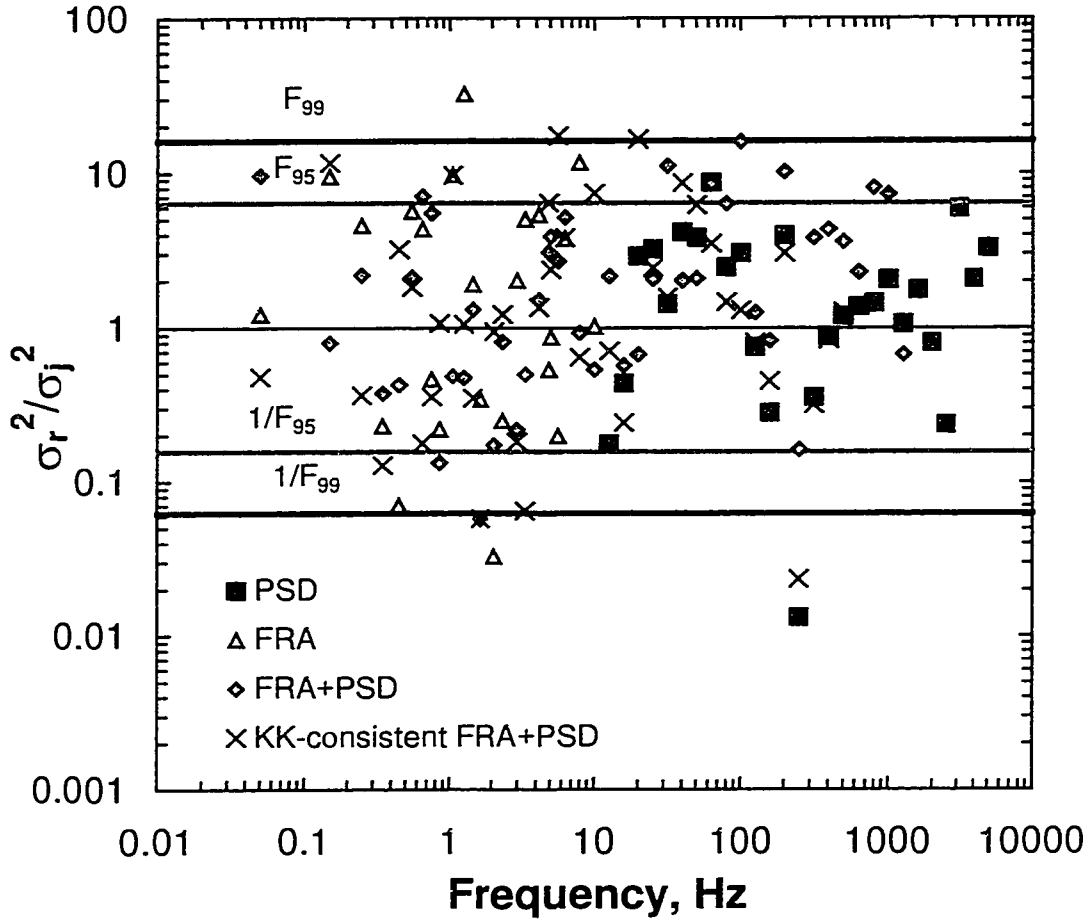

Figure 5.2: The ratio of variances in stochastic errors in the real impedance to those in the imaginary impedance as a function of frequency for the four cases of System 2: the FRA portion, the PSD portion, the entire spectrum, and the Kramers-Kronig consistent portion of the entire spectrum. The F-test probability limits are also plotted. The ratios for the all four cases are scattered about one, and generally fall within the 99% confidence limit. The F-test suggest that the variances are equal for all four cases.

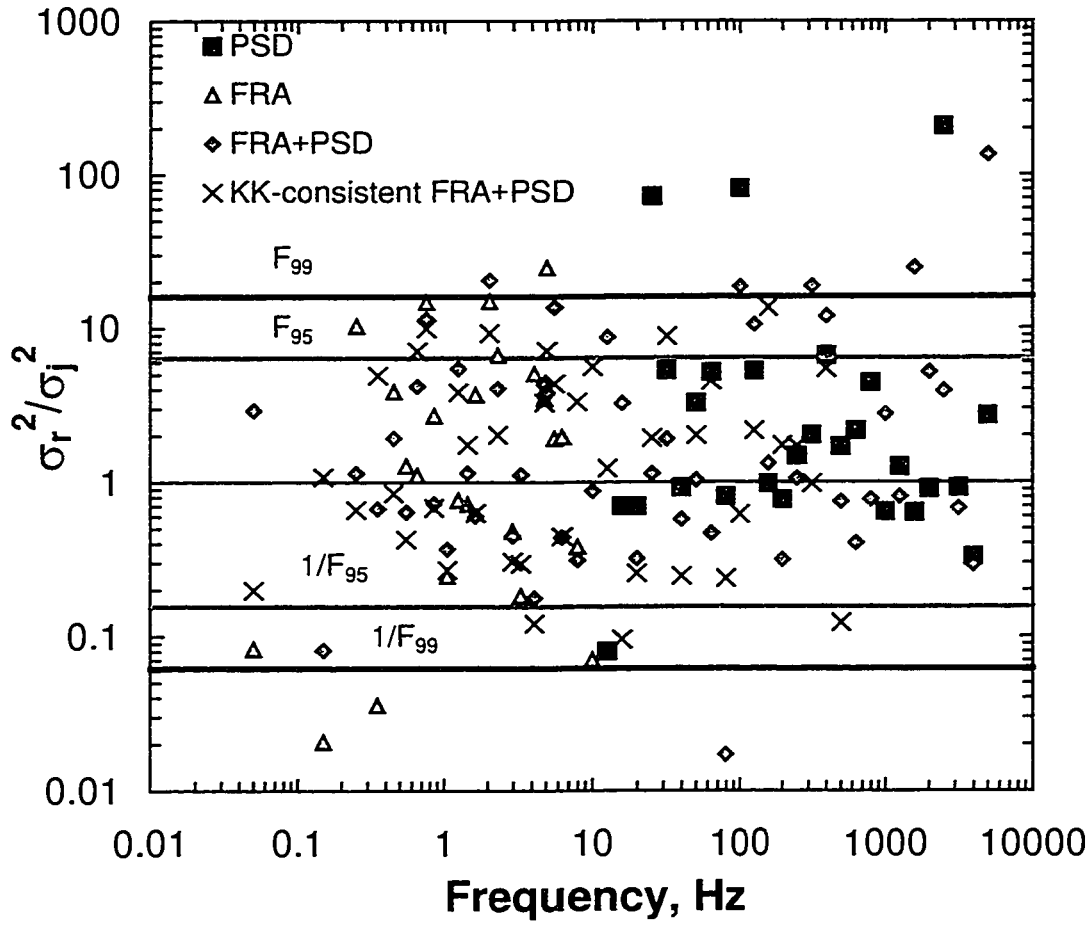

Figure 5.3: The ratio of variances in stochastic errors in the real impedance to those in the imaginary impedance as a function of frequency for the four cases of System 1: the FRA portion, the PSD portion, the entire spectrum, and the Kramers-Kronig consistent portion of the entire spectrum. The F-test probability limits are also plotted. The ratio for the PSD portion is not scattered about one, but generally falls within the 99% confidence limit. The ratios for the other three cases are scattered about one, and generally fall within the 99% confidence limit. The F-test suggest that the variances are equal for all four cases. The least confidence in that equality is for the PSD case.

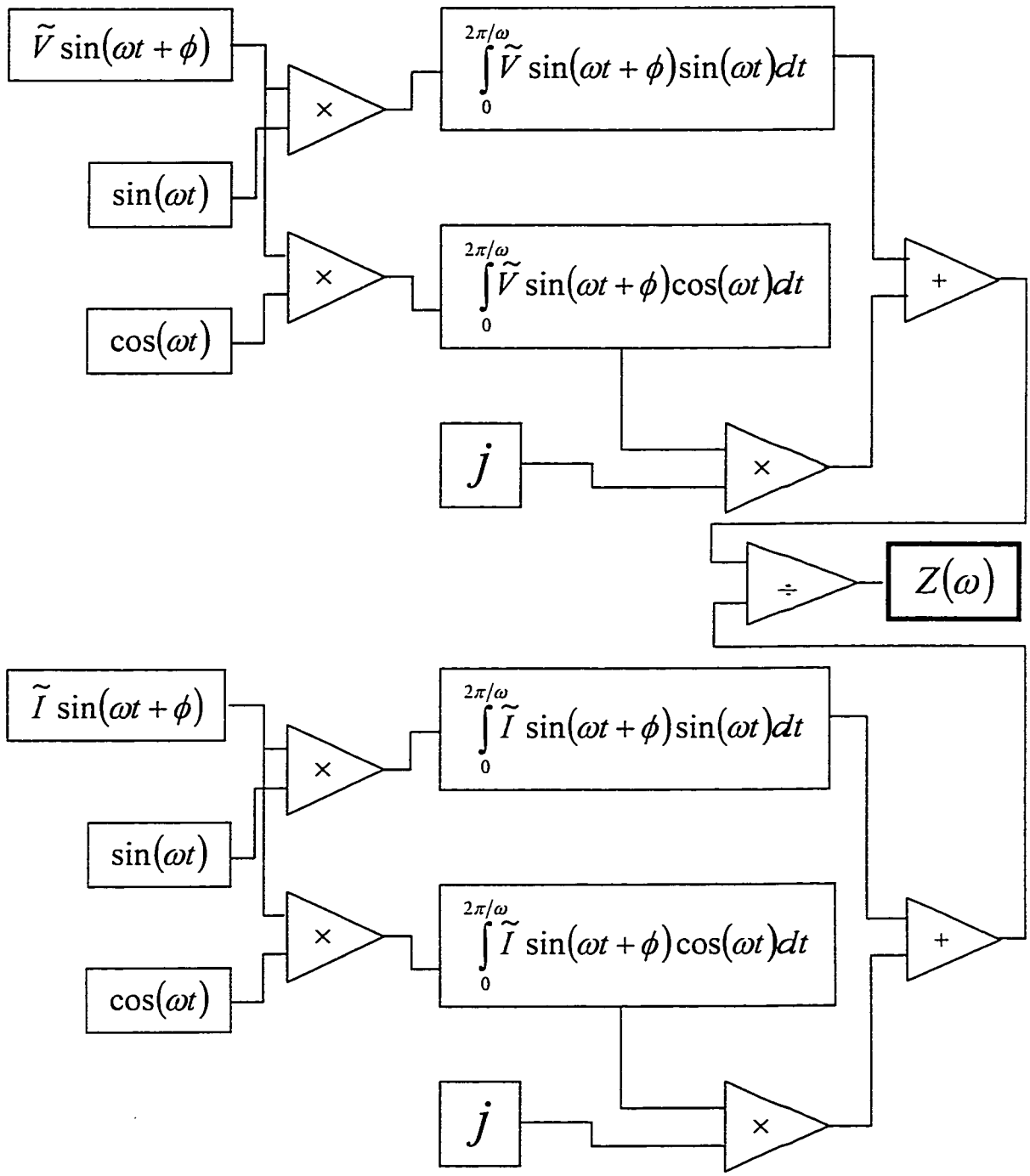

Figure 5.4: Assessment of Fourier coefficients is achieved by integrating the in-phase and out-of-phase products of the voltage and current signals over each cycle. The impedance is calculated as the ratio of the complex representation of the voltage to the current.

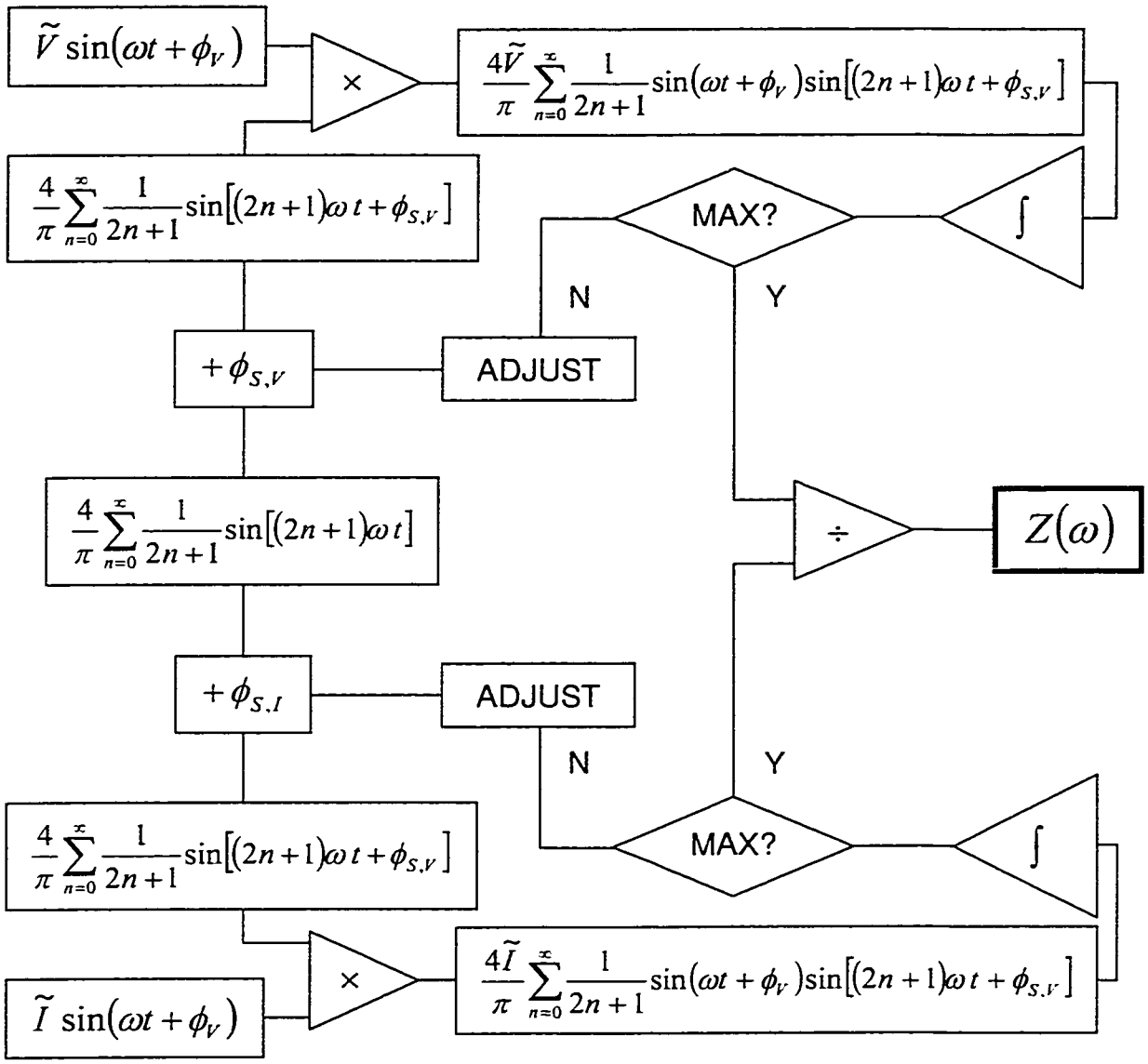

Figure 5.5: Phase-sensitive detection maximizes the integral of the product of the measured signal and a square wave of the same frequency with respect to phase angle of the square wave.

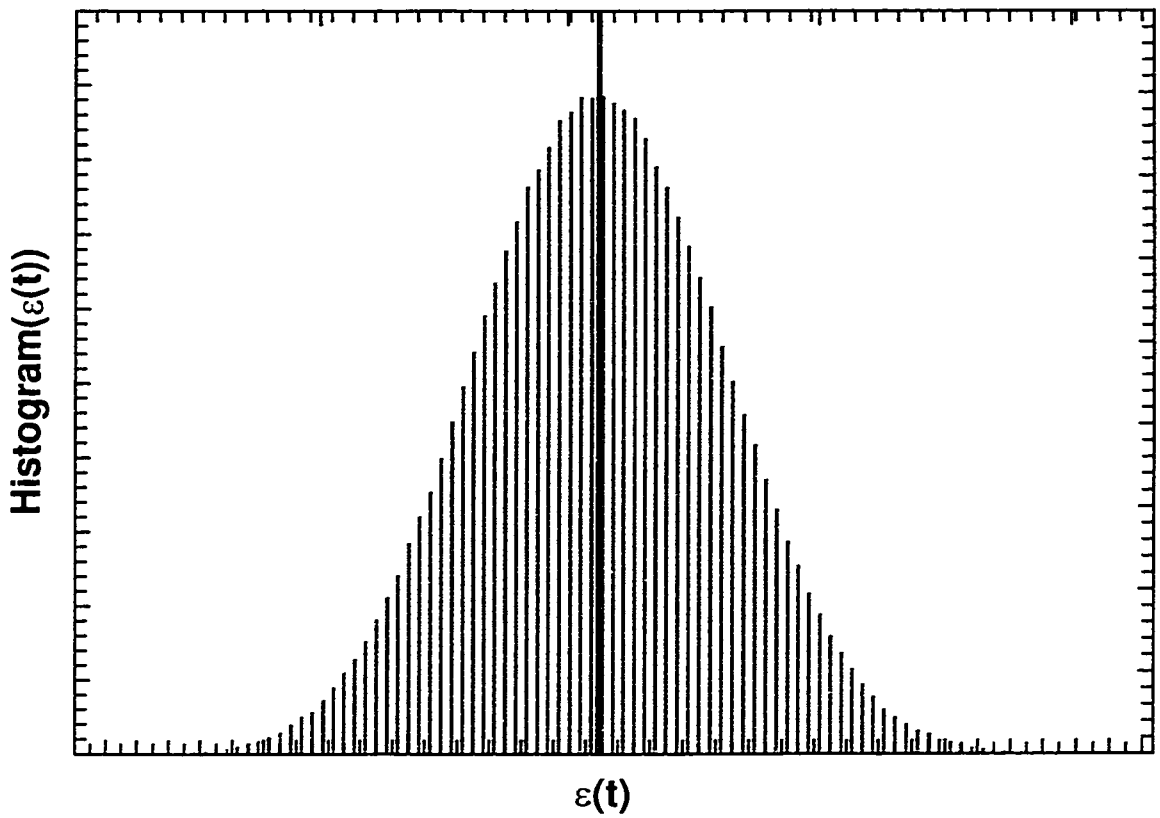

Figure 5.6: Distribution of values for typical waveform of Gaussian white noise. Solid black line along middle of chart is equal to zero.

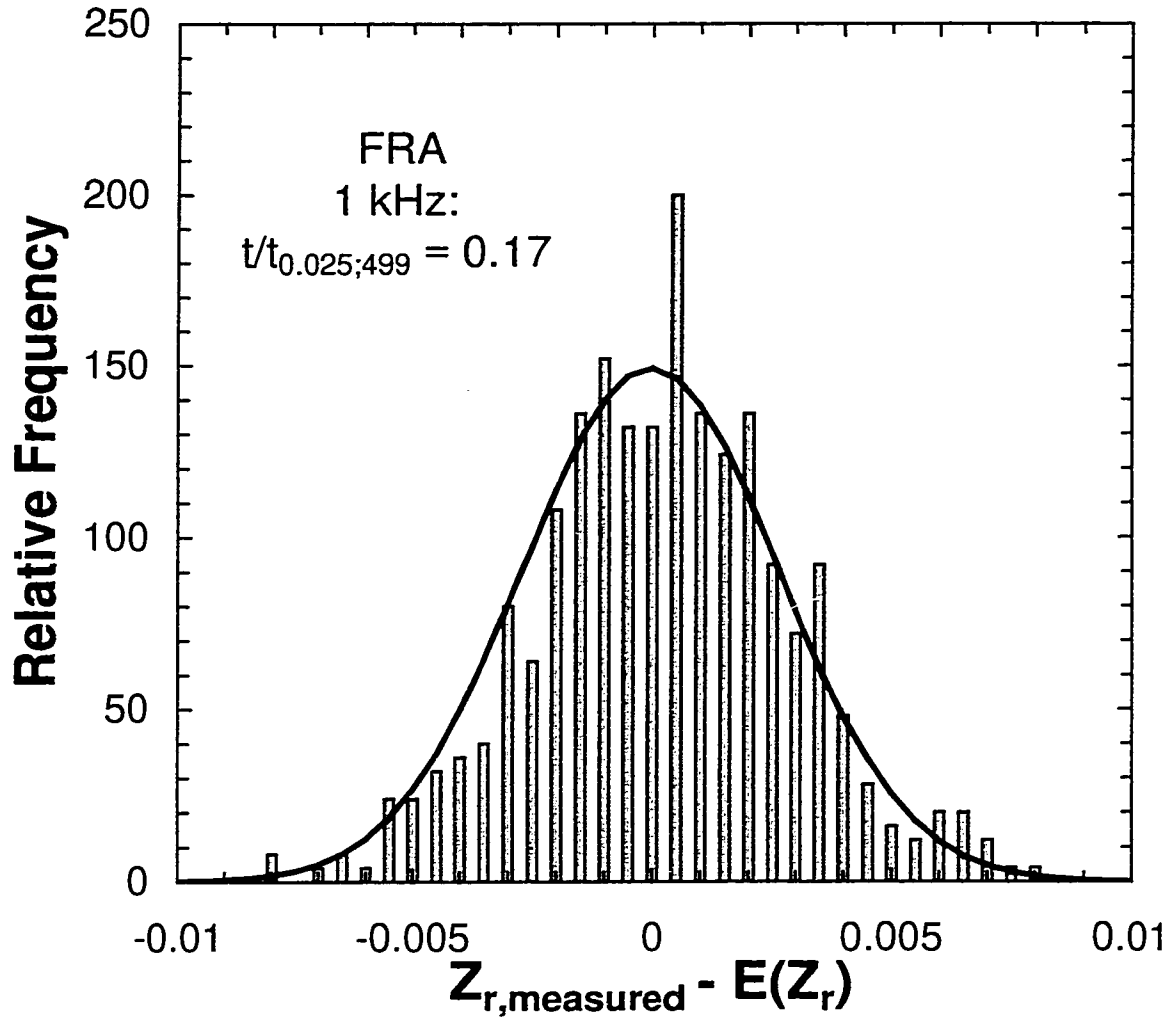

Figure 5.7: Distribution of frequency-domain errors of the real impedance calculated 500 times using the FRA technique at 1 kHz with Gaussian noise (see Figure 5.6) added to the input signal and output signal in the time-domain.

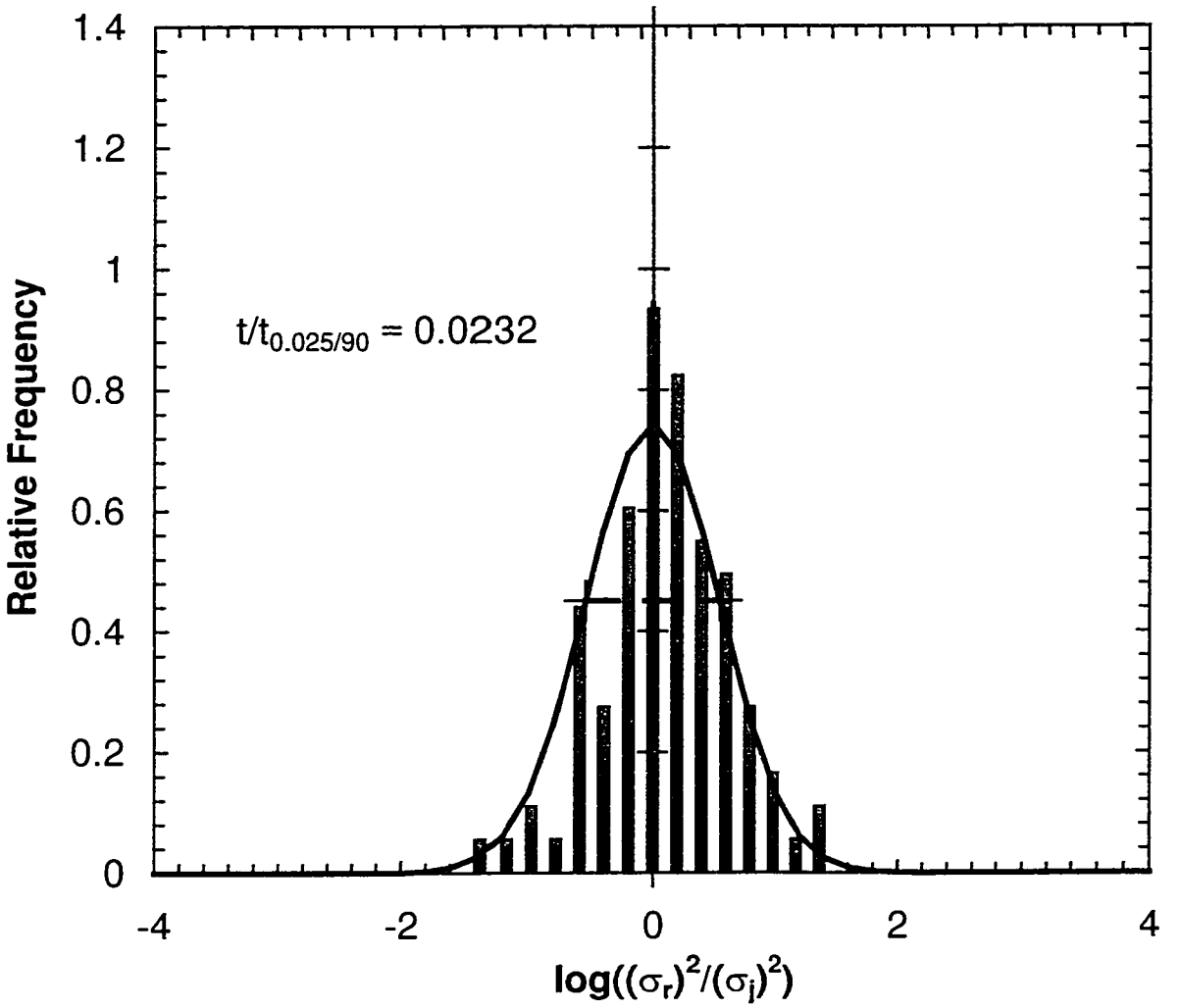

Figure 5.8: Distribution of logarithm of ratio of variances of the stochastic errors in the real and imaginary impedance calculated using Lissajous parameterization, with Gaussian noise added to input signal and output signal (in time-domain).

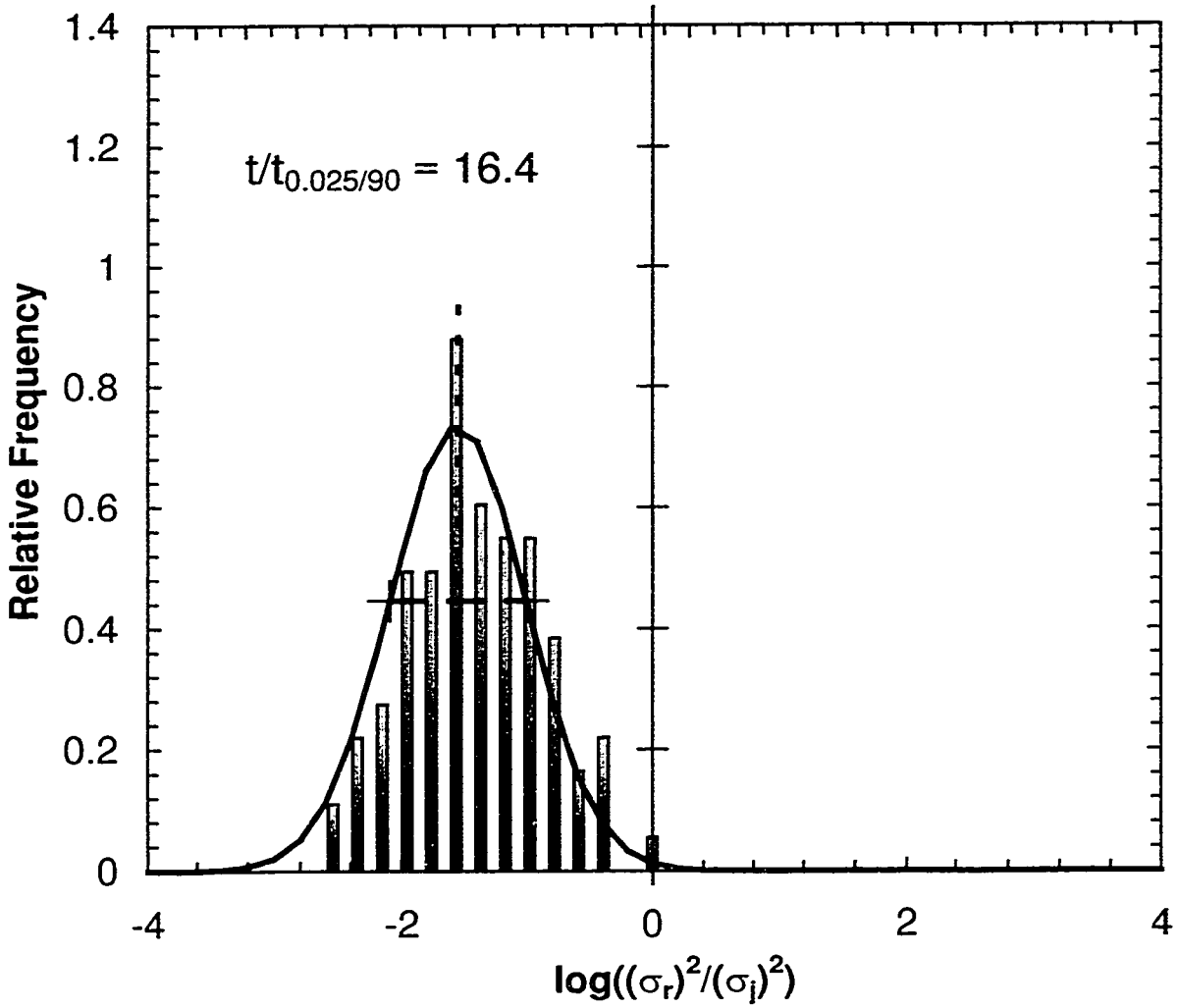

Figure 5.9: Distribution of logarithm of ratio of variances of the stochastic errors in the real and imaginary impedance calculated using phase-sensitive detection with Gaussian noise added to input signal and output signal (in time-domain).

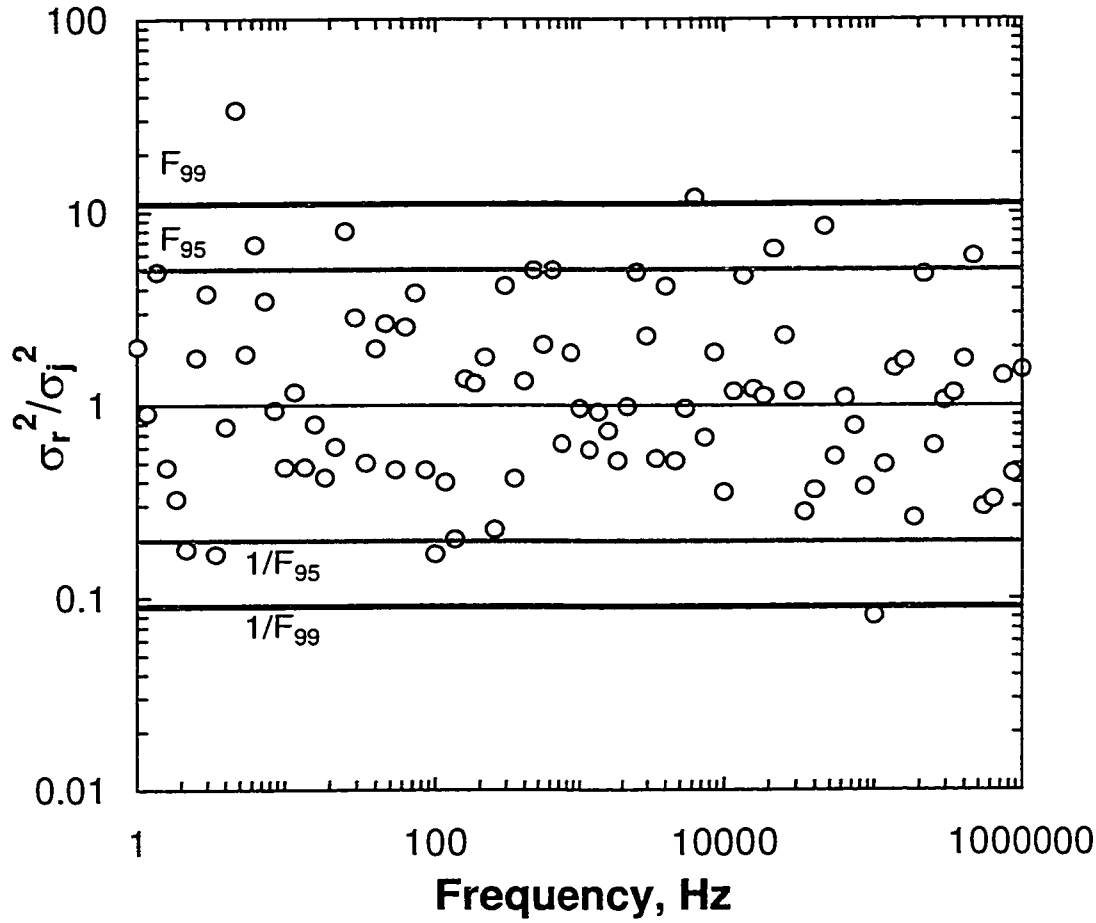

Figure 5.10: F-test for ratio of variance in real impedance to variance in imaginary impedance as a function of frequency. Impedance calculated using the FRA technique (Bode quadrature) with Gaussian noise added to both the input and output signals (CASE 3). The ratio is generally scattered around unity, and most points fall within the 1% level of significance. Thus, there is 99% confidence that the hypothesis that the variances are unequal is false.

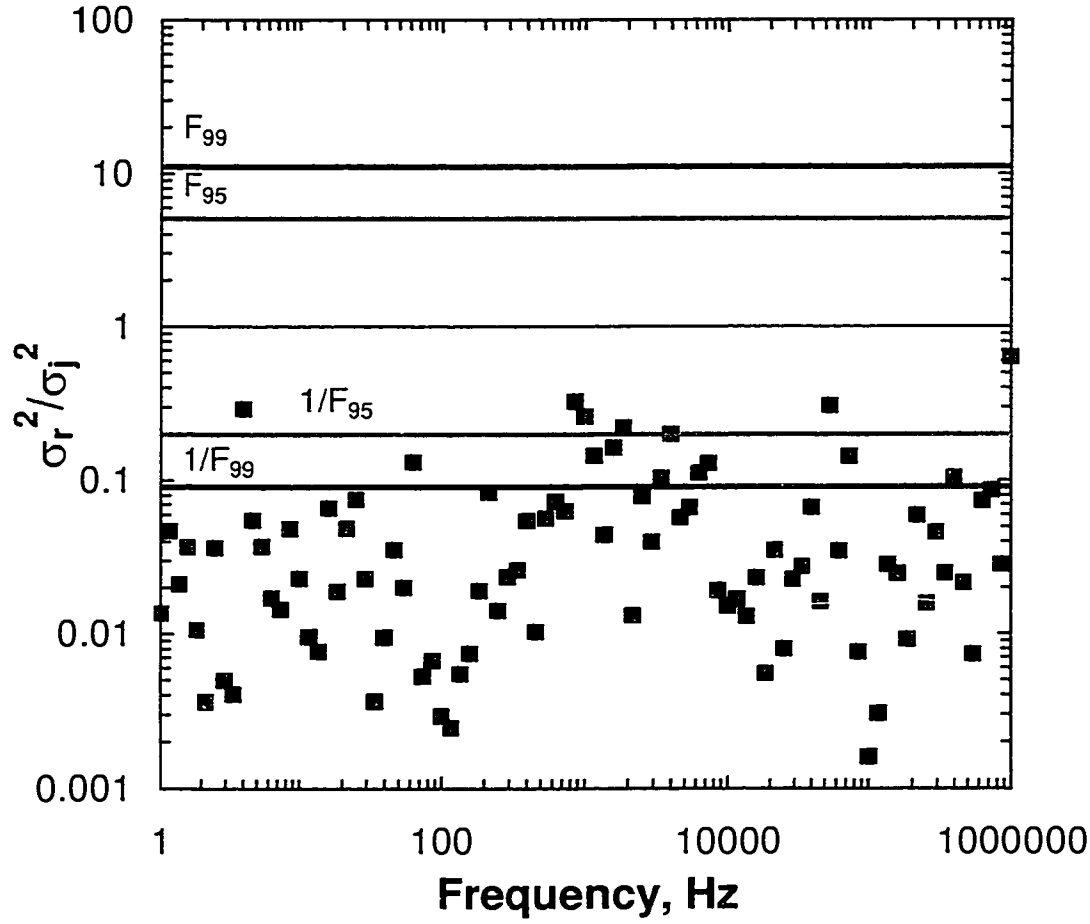

Figure 5.11: F-test for ratio of variance in real impedance to variance in imaginary impedance as a function of frequency. Impedance calculated using the PSD technique with Gaussian noise added to both the input and output signals (CASE 3). The ratio is not scattered around unity, and most points fall outside the 1% level of significance. Thus, there is 99% confidence that the hypothesis that the variances are unequal is true.

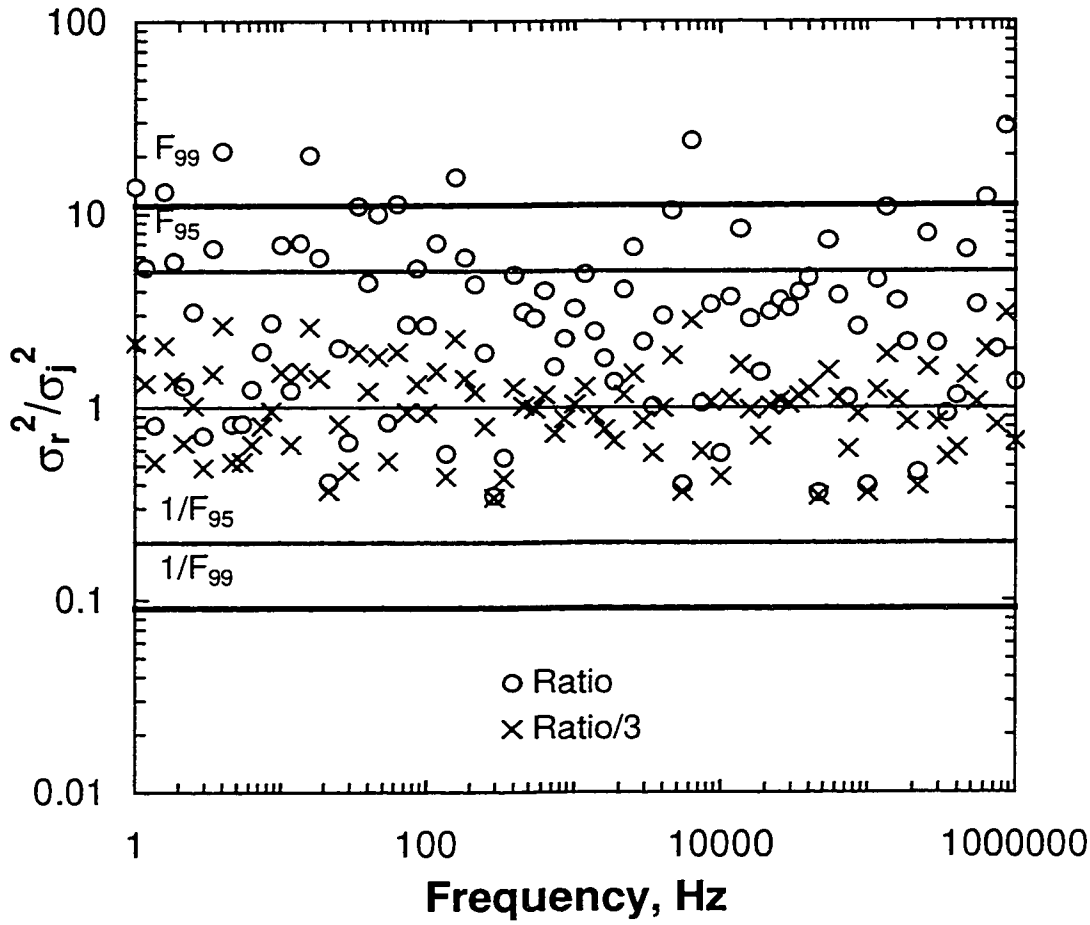

Figure 5.12: F-test for ratio of variance in real impedance to variance in imaginary impedance as a function of frequency. Impedance calculated using the FRA technique (Bode quadrature) with Gaussian proportional noise added to both the input and output signals (CASE 3). The ratio is not scattered around unity. The ratio scaled by one-third, however, is scattered around unity, and falls within the 1% level of significance.

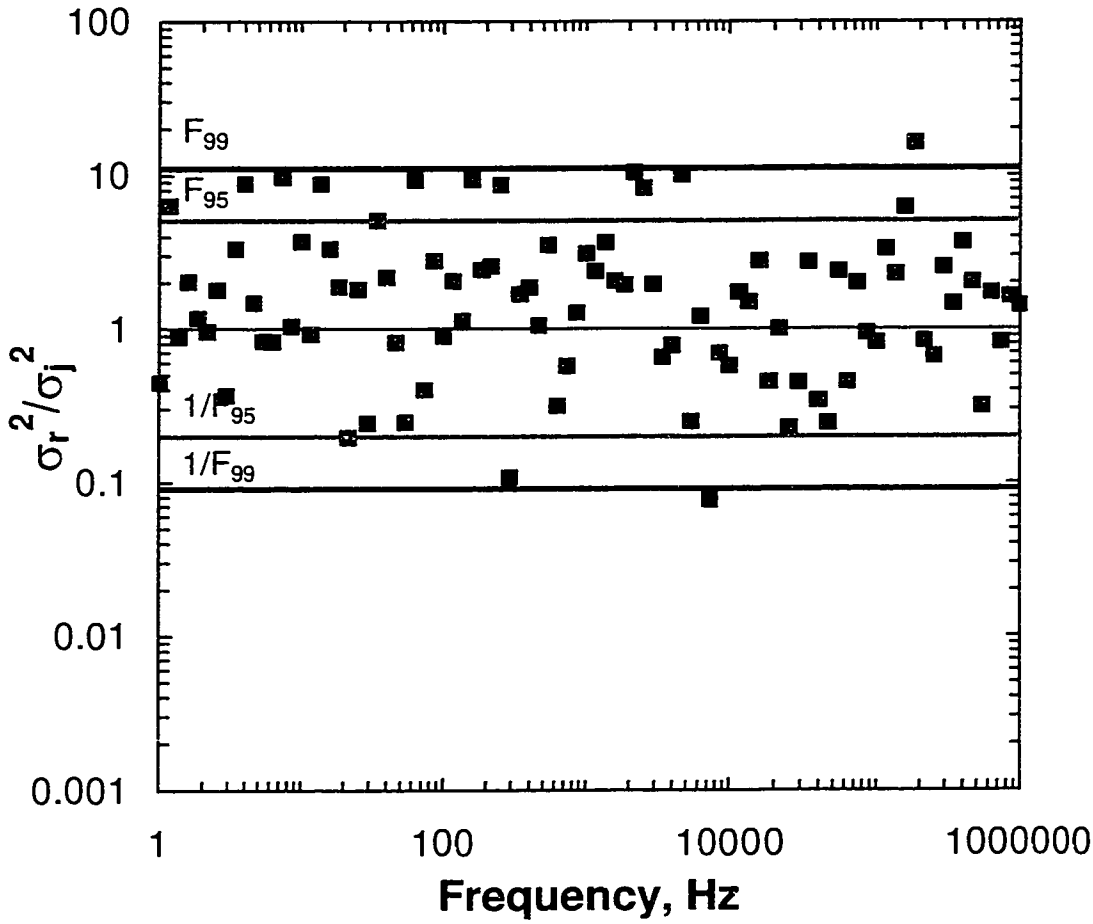

Figure 5.13: F-test for ratio of variance in real impedance to variance in imaginary impedance as a function of frequency. Impedance calculated using the PSD technique with Gaussian noise added to both the input and output signals (CASE 3). The ratio is generally scattered around unity, and most points fall inside the 1% level of significance. Thus, there is 99% confidence that the hypothesis that the variances are unequal is false.

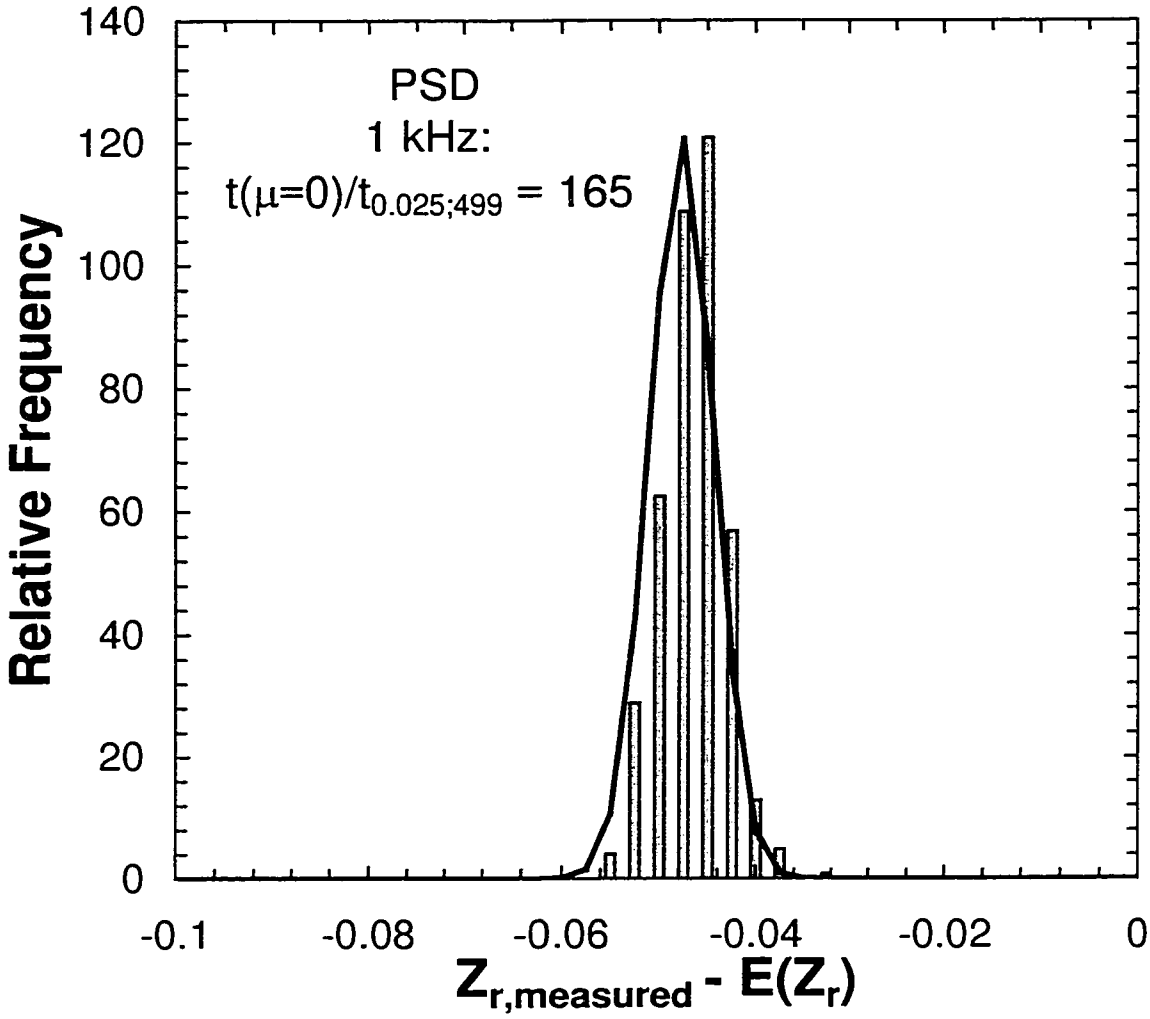

Figure 5.14: Distribution of stochastic errors in the real impedance at 1 kHZ calculated using the PSD technique. The errors were calculated as the difference between the measured impedance and the theoretical impedance spectrum (used as the system in the simulation). The mean of this distribution is biased away from zero. The corresponding errors from the FRA calculated impedance are not distributed with a bias.

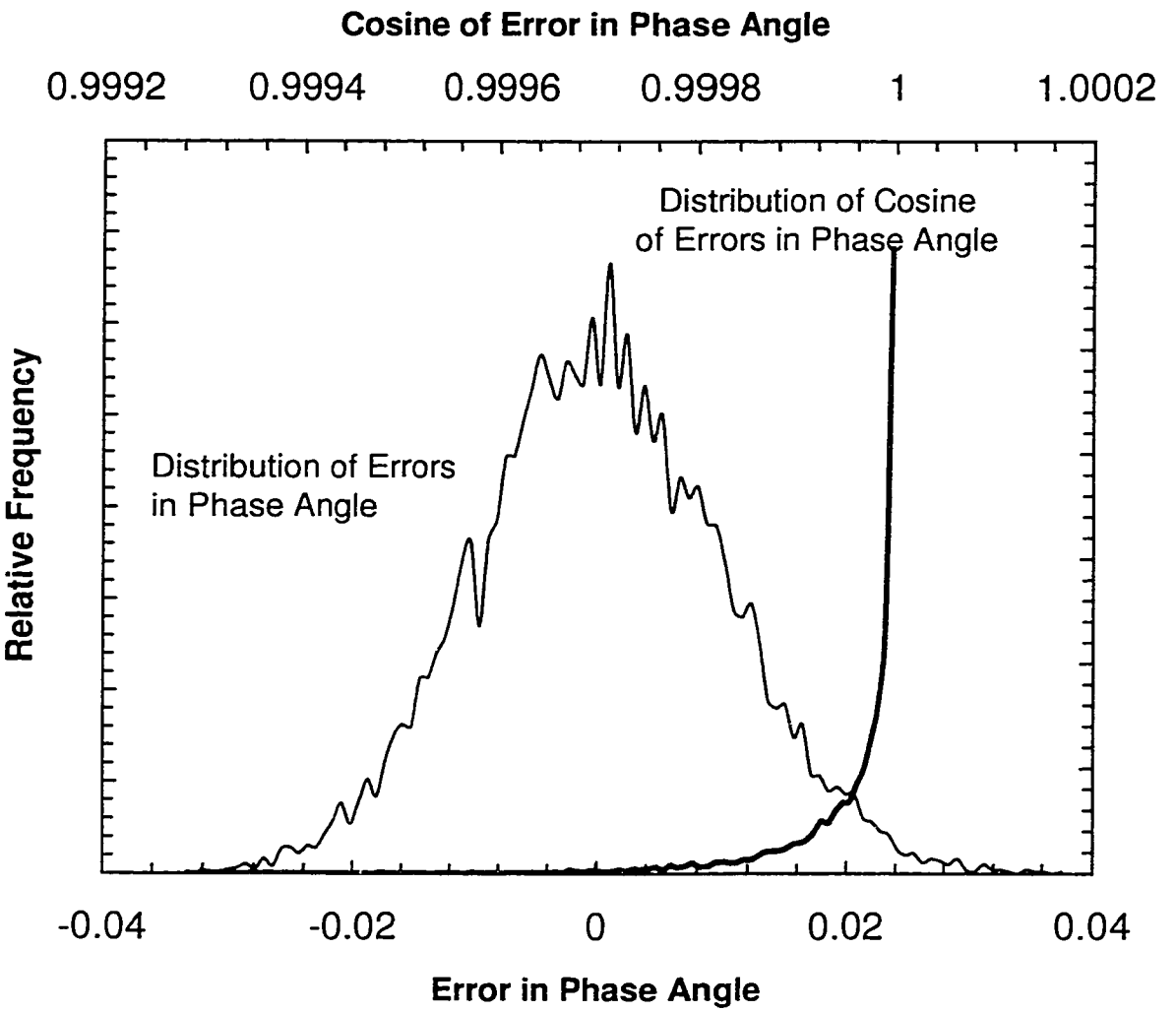

Figure 5.15: Distribution of errors in phase angle and distribution of the cosine of those errors. A Gaussian distribution is extremely skewed and biased through the cosine operation.

CHAPTER 6
PROPAGATION OF ERRORS IN COMPLEX CURRENT AND VOLTAGE

Time-domain noise in the current and voltage signals propagates into the frequency-domain quantities that are measured, namely, the complex current and voltage. To understand better the nature and sources of errors in the complex impedance, the manner in which errors in the current and voltage signals propagate into the complex impedance must be determined. While it is straightforward to describe the complex impedance in terms of the complex signals, it is difficult to characterize explicitly the noise in the complex impedance in terms of noise in the complex current and voltage. If the errors in the components of the complex signals are considered to be small with respect to the mean values of the components, the variance in the impedance can be linearized around the mean values of the components of the complex current and voltage. This linearization can be accomplished through derivation of the Taylor series for the variance in the impedance in terms of the signal components. The result provides a means of assessing the character of the errors in the impedance in terms of the errors in the current and voltage.

Thus, this chapter will address several issues. First, the correlation between the variance in the complex impedance and the variances in the complex current and voltage will be determined. Second, a condition for equality of variance in the real impedance and variance in the imaginary impedance will be observed. This equality has been

observed experimentally by Orazem and co-workers[6-9,74] and Dygas *et al.*[114] It was also demonstrated in the previous chapter for simulated data calculated using the FRA technique. This condition for equality of variances in the real and imaginary impedances will be verified as the reason for equality of variances in the complex impedance components. Finally, the frequency dependent error structure will be shown to be a result of the manner in which noise is introduced into the signals. The introduction of noise into different signals influences the error structure of the impedance measurement.

If a quantity X is sampled repeatedly, then the expectation value of X can be described as the mean value of X

$$E(X)=\frac{1}{n}\sum_{k=1}^{n}X_k\,. \tag{6.1}$$

The variance (the square of the standard deviation) is then

$$\sigma_X^2=\frac{n}{n-1}E\left[(X-E(X))^2\right]. \tag{6.2}$$

It should be noted that these definitions for standard deviation and variance still hold if the definition of expectation is adjusted for a continuous population rather than a discrete sampling of the population. If the quantity X is a continuous function with a probability distribution defined by p, then the expectation of X will be

$$E(X)=\int_{-\infty}^{\infty}p(t)X(t)dt\,. \tag{6.3}$$

The first definition of expectation (equation (6.1)) will be the one considered in this chapter, but the second definition (equation (6.3)) will be employed in a later chapter.

6.1 Variance of Real and Imaginary Impedance from Complex Taylor Series Expansion of Complex Impedance

The complex impedance at a given frequency is the ratio of a resulting complex voltage signal at that frequency to a perturbing complex current signal. The Fourier

transform of the signals are complex and the phase angle of each signal is defined with respect to a reference sinusoid at the same frequency. The impedance can be written

$$\tilde{Z}(\omega)=\frac{\tilde{V}(\omega)}{\tilde{I}(\omega)} \tag{6.4}$$

where ω is the frequency and the tilde represents a complex quantity. If the impedance at a given frequency is sampled several times, then an expectation value can be determined via equation (6.1). The complex impedance can be linearized about the expectation value by a Taylor series expansion

$$\tilde{Z}(\omega)\approx E\left(\frac{\tilde{V}}{\tilde{I}}\right)+\left[E\left(\frac{\partial\tilde{Z}}{\partial\tilde{V}}\right)\right]\left(\tilde{V}-E\left(\tilde{V}\right)\right)+\left[E\left(\frac{\partial\tilde{Z}}{\partial\tilde{I}}\right)\right]\left(\tilde{I}-E\left(\tilde{I}\right)\right) \tag{6.5}$$

Therefore the expectation of the linearized impedance can be written as

$$E\left(\tilde{Z}(\omega)\right)=E\left(\frac{\tilde{V}}{\tilde{I}}\right)+\left[E\left(\frac{\partial\tilde{Z}}{\partial\tilde{V}}\right)\right]E\left(\tilde{V}-E\left(\tilde{V}\right)\right)+\left[E\left(\frac{\partial\tilde{Z}}{\partial\tilde{I}}\right)\right]E\left(\tilde{I}-E\left(\tilde{I}\right)\right) \tag{6.6}$$

The variance in the impedance can then be written in terms of the linearized description of the impedance as

$$E\left[\tilde{Z}(\omega)-E\left(\tilde{Z}(\omega)\right)\right]^2=E\left\{\begin{array}{l}\left[E\left(\frac{\partial\tilde{Z}}{\partial\tilde{V}}\right)\right]\left[\left(\tilde{V}-E\left(\tilde{V}\right)\right)-E\left(\tilde{V}-E\left(\tilde{V}\right)\right)\right]\\+\left[E\left(\frac{\partial\tilde{Z}}{\partial\tilde{I}}\right)\right]\left[\left(\tilde{I}-E\left(\tilde{I}\right)\right)-E\left(\tilde{I}-E\left(\tilde{I}\right)\right)\right]\end{array}\right\}^2. \tag{6.7}$$

The right hand side of equation (6.7) can be expanded to give

$$\begin{aligned}E\left[\tilde{Z}(\omega)-E\left(\tilde{Z}(\omega)\right)\right]^2=&\left[E\left(\frac{\partial\tilde{Z}}{\partial\tilde{V}}\right)\right]^2E\left(\tilde{V}-E\left(\tilde{V}\right)\right)^2+\left[E\left(\frac{\partial\tilde{Z}}{\partial\tilde{I}}\right)\right]^2E\left(\tilde{I}-E\left(\tilde{I}\right)\right)^2\\&+\left[E\left(\frac{\partial\tilde{Z}}{\partial\tilde{V}}\right)\right]\left[E\left(\frac{\partial\tilde{Z}}{\partial\tilde{I}}\right)\right]E\left(\tilde{V}-E\left(\tilde{V}\right)\right)E\left(\tilde{I}-E\left(\tilde{I}\right)\right)\end{aligned}. \tag{6.8}$$

This can be written in terms of variances and co-variances as

$$\sigma_{\tilde{Z}}^2 = \left[E\left(\frac{\partial \tilde{Z}}{\partial \tilde{V}}\right)\right]^2 \sigma_{\tilde{V}}^2 + \left[E\left(\frac{\partial \tilde{Z}}{\partial \tilde{I}}\right)\right]^2 \sigma_{\tilde{I}}^2 + \left[E\left(\frac{\partial \tilde{Z}}{\partial \tilde{V}}\right)\right]\left[E\left(\frac{\partial \tilde{Z}}{\partial \tilde{I}}\right)\right]\sigma_{\tilde{I}\tilde{V}}. \tag{6.9}$$

To simplify notation of the expectation values of the derivatives, the caret will represent evaluation at the expectation, and the subscript zero will represent the expectation value. Then, the derivatives in equation (6.9) are

$$\left(\frac{\partial \hat{Z}}{\partial V}\right) = \frac{1}{\tilde{I}_0}, \tag{6.10}$$

and

$$\left(\frac{\partial \hat{Z}}{\partial I}\right) = -\frac{\tilde{Z}_0}{\tilde{I}_0}. \tag{6.11}$$

Then the variance in the complex impedance is

$$\sigma_Z^2 = \left(\frac{1}{\tilde{I}_0^2}\right)\sigma_V^2 + \left(\frac{\tilde{Z}_0^2}{\tilde{I}_0^2}\right)\sigma_I^2 - 2\left(\frac{\tilde{Z}_0}{\tilde{I}_0^2}\right)\sigma_{IV} \tag{6.12}$$

The variance in the complex impedance can be written in terms of real and imaginary components as

$$\begin{aligned}\sigma_Z^2 &= E\left(Z - \hat{Z}\right)^2 \\ &= E\left(Z_r + jZ_j - \hat{Z}_r - j\hat{Z}_j\right)^2 \\ &= E\left(Z_r - \hat{Z}_r\right)^2 - E\left(Z_j - \hat{Z}_j\right)^2 + 2jE\left(Z_r - \hat{Z}_r\right)E\left(Z_j - \hat{Z}_j\right) \\ &= \sigma_{Z_r}^2 - \sigma_{Z_j}^2 + 2j\sigma_{Z_r Z_j}\end{aligned} \tag{6.13}$$

Therefore the variance in the impedance can be rewritten in terms of the real and imaginary components of all the signals

$$\sigma_{Z_r}^2 - \sigma_{Z_j}^2 + 2j\sigma_{Z_rZ_j} = \left(\frac{1}{\tilde{I}_0^2}\right)\left(\sigma_{V_r}^2 - \sigma_{V_j}^2 + 2j\sigma_{V_rV_j}\right) + \left(\frac{\tilde{Z}_0^2}{\tilde{I}_0^2}\right)\left(\sigma_{I_r}^2 - \sigma_{I_j}^2 + 2j\sigma_{I_rI_j}\right) - 2\left(\frac{\tilde{Z}_0}{\tilde{I}_0^2}\right)\left(\sigma_{V_rI_r} - \sigma_{V_jI_j} + j\left(\sigma_{V_rI_j} + \sigma_{V_jI_r}\right)\right) \tag{6.14}$$

The complex components of the coefficients in equation (6.14) are derived in Appendix A. Substituting those expressions into the Taylor series expansion in equation (6.14), the variance in the complex impedance can be written as

$$\begin{aligned}\sigma_{Z_r}^2 - \sigma_{Z_j}^2 + 2j\sigma_{Z_rZ_j} = {} & E\left(\frac{I_r^2 - I_j^2 - 2jI_rI_j}{\left(I_r^2 + I_j^2\right)^2}\right)\left(\sigma_{V_r}^2 - \sigma_{V_j}^2 + 2j\sigma_{V_rV_j}\right) \\ & + \left\{E\left(\frac{\left\{\begin{array}{l}\left[\left(I_r^2 - I_j^2\right)\left(Z_r^2 - Z_j^2\right) + 4\left(I_rI_j\right)\left(Z_rZ_j\right)\right] \\ + 2j\left[\left(I_r^2 - I_j^2\right)\left(Z_rZ_j\right) - \left(I_rI_j\right)\left(Z_r^2 - Z_j^2\right)\right]\end{array}\right\}}{\left(I_r^2 + I_j^2\right)^2}\right)\left(\sigma_{I_r}^2 - \sigma_{I_j}^2 + 2j\sigma_{I_rI_j}\right)\right\} \\ & - 2\left\{E\left(\frac{\left\{\begin{array}{l}\left[\left(I_r^2 - I_j^2\right)\left(Z_r\right) + 2\left(I_rI_j\right)\left(Z_j\right)\right] \\ + j\left[\left(I_r^2 - I_j^2\right)\left(Z_j\right) - 2\left(I_rI_j\right)\left(Z_r\right)\right]\end{array}\right\}}{\left(I_r^2 + I_j^2\right)^2}\right)\left(\sigma_{V_rI_r} - \sigma_{V_jI_j} + j\left(\sigma_{V_rI_j} + \sigma_{V_jI_r}\right)\right)\right\}\end{aligned} \tag{6.15}$$

The real part of this equation gives

$$\left[\sigma_{Z_r}^2 - \sigma_{Z_j}^2\right] E\left(I_r^{\,2} + I_j^{\,2}\right)^2 = \left\{\begin{matrix} E\left(I_r^{\,2} - I_j^{\,2}\right)\left(\sigma_{V_r}^2 - \sigma_{V_j}^2\right) \\ +4E\left(I_r I_j\right)\left(\sigma_{V_r V_j}\right) \end{matrix}\right\} + \left\{\begin{matrix} E\left[\begin{matrix}\left(I_r^{\,2} - I_j^{\,2}\right)\left(Z_r^{\,2} - Z_j^{\,2}\right) \\ +4E\left(I_r I_j\right)\left(Z_r Z_j\right)\end{matrix}\right]\left(\sigma_{I_r}^2 - \sigma_{I_j}^2\right) \\ -4E\left[\begin{matrix}\left(I_r^{\,2} - I_j^{\,2}\right)\left(Z_r Z_j\right) \\ -\left(I_r I_j\right)\left(Z_r^{\,2} - Z_j^{\,2}\right)\end{matrix}\right]\left(\sigma_{I_r I_j}\right) \end{matrix}\right\} - 2\left\{\begin{matrix} E\left[\begin{matrix}\left(I_r^{\,2} - I_j^{\,2}\right)\left(Z_r\right) \\ +2\left(I_r I_j\right)\left(Z_j\right)\end{matrix}\right]\left(\sigma_{V_r I_r} - \sigma_{V_j I_j}\right) \\ -E\left[\begin{matrix}\left(I_r^{\,2} - I_j^{\,2}\right)\left(Z_j\right) \\ -2\left(I_r I_j\right)\left(Z_r\right)\end{matrix}\right]\left(\sigma_{V_r I_j} + \sigma_{V_j I_r}\right) \end{matrix}\right\} \tag{6.16}$$

The imaginary part of this equation gives

$$\left[\sigma_{Z_r Z_j}\right] E\left(I_r^{\,2} + I_j^{\,2}\right)^2 = \left\{\begin{matrix} E\left(I_r^{\,2} - I_j^{\,2}\right)\left(\sigma_{V_r V_j}\right) \\ -E\left(I_r I_j\right)\left(\sigma_{V_r}^2 - \sigma_{V_j}^2\right) \end{matrix}\right\} + \left\{\begin{matrix} E\left[\left(I_r^{\,2} - I_j^{\,2}\right)\left(Z_r^{\,2} - Z_j^{\,2}\right) + 4\left(I_r I_j\right)\left(Z_r Z_j\right)\right]\left(\sigma_{I_r I_j}\right) \\ +E\left[\left(I_r^{\,2} - I_j^{\,2}\right)\left(Z_r Z_j\right) - \left(I_r I_j\right)\left(Z_r^{\,2} - Z_j^{\,2}\right)\right]\left(\sigma_{I_r}^2 - \sigma_{I_j}^2\right) \end{matrix}\right\} - \left\{\begin{matrix} E\left[\left(I_r^{\,2} - I_j^{\,2}\right)\left(Z_r\right) + 2\left(I_r I_j\right)\left(Z_j\right)\right]\left(\sigma_{V_r I_j} + \sigma_{V_j I_r}\right) \\ +E\left[\left(I_r^{\,2} - I_j^{\,2}\right)\left(Z_j\right) - 2\left(I_r I_j\right)\left(Z_r\right)\right]\left(\sigma_{V_r I_r} - \sigma_{V_j I_j}\right) \end{matrix}\right\} \tag{6.17}$$

The ten variance components in equations (6.16) and (6.17) are grouped such that if the variance terms in parentheses on the right-hand-side of equations (6.16) and (6.17) are equal to zero, the variances in the real and imaginary impedances are equal, and the covariance between the real and imaginary impedances is equal to zero. This condition also requires that there is no correlation between the real and imaginary impedances, because the covariance between them would be equal to zero.

6.2 Variance of the Real and Imaginary Impedance from the Real Taylor Series Expansions of the Impedance Components

If the impedance in equation (6.1) was measured several times, then the expectation value of the impedance, and the variance in the impedance could be calculated. Equation (6.9) provides a means of calculating the variance in the complex impedance as a function of the variances in the complex current and voltage signals. However, to determine independently the behavior of each of the variances in the real and imaginary impedances, the variances of the real and imaginary impedance must be derived as independent functions of the real and imaginary components of the complex current and voltage signals. (Note that since the only error contribution being considered here is stochastic in nature, the variance in the impedance is equivalent to the variance in the stochastic errors if the expectation value of the stochastic errors is equal to zero.)

The Taylor series expansion for the variances of the real and imaginary impedance can be derived in the same manner as was done for the complex impedance.

$$Z_r + jZ_j = \frac{V_r + jV_j}{I_r + jI_j} \tag{6.18}$$

Rationalization of the fraction by multiplication of the numerator and denominator by the complex conjugate of the leads to

$$Z_r = \frac{V_r I_r + V_j I_j}{I_r^{\,2} + I_j^{\,2}}, \tag{6.19}$$

and

$$Z_j = \frac{V_j I_r - V_r I_j}{I_r^{\,2} + I_j^{\,2}}. \tag{6.20}$$

The variances in Z_r and Z_j at each frequency can be written in terms of the linearized Taylor series expansion of (6.19) and (6.20).

Equation (6.9) is derived for the impedance as a function of two variables. The Taylor series could have been written in terms of the four components in equations (6.19) and (6.20). Equation (6.5) would be rewritten as

$$Z_r \approx E\left(\frac{V_r I_r + V_j I_j}{I_r^2 + I_j^2}\right) + \left[E\left(\frac{\partial Z_r}{\partial V_r}\right)\right](V_r - E(V_r)) + \left[E\left(\frac{\partial Z_r}{\partial V_j}\right)\right](V_j - E(V_j)) + \left[E\left(\frac{\partial Z_r}{\partial I_r}\right)\right](I_r - E(I_r)) + \left[E\left(\frac{\partial Z_r}{\partial I_j}\right)\right](I_j - E(I_j)) \tag{6.21}$$

and

$$Z_j \approx E\left(\frac{V_j I_r - V_r I_j}{I_r^2 + I_j^2}\right) + \left[E\left(\frac{\partial Z_j}{\partial V_r}\right)\right](V_r - E(V_r)) + \left[E\left(\frac{\partial Z_j}{\partial V_j}\right)\right](V_j - E(V_j)) + \left[E\left(\frac{\partial Z_j}{\partial I_r}\right)\right](I_r - E(I_r)) + \left[E\left(\frac{\partial Z_j}{\partial I_j}\right)\right](I_j - E(I_j)) \tag{6.22}$$

The variance can be written as

$$\sigma_{Z_r}^2 = \left\{ \begin{array}{l} \left[E\left(\frac{\partial Z_r}{\partial V_r}\right)\right](V_r - E(V_r)) + \left[E\left(\frac{\partial Z_r}{\partial V_j}\right)\right](V_j - E(V_j)) \\ + \left[E\left(\frac{\partial Z_r}{\partial I_r}\right)\right](I_r - E(I_r)) + \left[E\left(\frac{\partial Z_r}{\partial I_j}\right)\right](I_j - E(I_j)) \end{array} \right\}^2 \tag{6.23}$$

and

$$\sigma_{Z_j}^2 = \left\{ \begin{array}{l} \left[E\left(\frac{\partial Z_j}{\partial V_r}\right)\right](V_r - E(V_r)) + \left[E\left(\frac{\partial Z_j}{\partial V_j}\right)\right](V_j - E(V_j)) \\ + \left[E\left(\frac{\partial Z_j}{\partial I_r}\right)\right](I_r - E(I_r)) + \left[E\left(\frac{\partial Z_j}{\partial I_j}\right)\right](I_j - E(I_j)) \end{array} \right\}^2 \tag{6.24}$$

The variance in the real and imaginary impedance can be written as a function of the variances of and covariances between the complex components of the current and voltage signals

$$\sigma_{Z_r}^2 = \left(\frac{\partial \hat{Z}_r}{\partial V_r}\right)^2 \sigma_{V_r}^2 + \left(\frac{\partial \hat{Z}_r}{\partial Vj}\right)^2 \sigma_{V_j}^2 + \left(\frac{\partial \hat{Z}_r}{\partial I_r}\right)^2 \sigma_{I_r}^2 + \left(\frac{\partial \hat{Z}_r}{\partial I_j}\right)^2 \sigma_{I_j}^2$$
$$+ 2\left(\frac{\partial \hat{Z}_r}{\partial V_r}\right)\left(\frac{\partial \hat{Z}_r}{\partial Vj}\right)\sigma_{V_rV_j} + 2\left(\frac{\partial \hat{Z}_r}{\partial V_r}\right)\left(\frac{\partial \hat{Z}_r}{\partial I_r}\right)\sigma_{V_rI_r} + 2\left(\frac{\partial \hat{Z}_r}{\partial V_r}\right)\left(\frac{\partial \hat{Z}_r}{\partial I_j}\right)\sigma_{V_rI_j}$$
$$+ 2\left(\frac{\partial \hat{Z}_r}{\partial V_j}\right)\left(\frac{\partial \hat{Z}_r}{\partial I_r}\right)\sigma_{V_jI_r} + 2\left(\frac{\partial \hat{Z}_r}{\partial V_j}\right)\left(\frac{\partial \hat{Z}_r}{\partial I_j}\right)\sigma_{V_jI_j} + 2\left(\frac{\partial \hat{Z}_r}{\partial I_r}\right)\left(\frac{\partial \hat{Z}_r}{\partial I_j}\right)\sigma_{I_rI_j} \tag{6.25}$$

$$\sigma_{Z_j}^2 = \left(\frac{\partial \hat{Z}_j}{\partial V_r}\right)^2 \sigma_{V_r}^2 + \left(\frac{\partial \hat{Z}_j}{\partial Vj}\right)^2 \sigma_{V_j}^2 + \left(\frac{\partial \hat{Z}_j}{\partial I_r}\right)^2 \sigma_{I_r}^2 + \left(\frac{\partial \hat{Z}_j}{\partial I_j}\right)^2 \sigma_{I_j}^2$$
$$+ 2\left(\frac{\partial \hat{Z}_j}{\partial V_r}\right)\left(\frac{\partial \hat{Z}_j}{\partial V_j}\right)\sigma_{V_rV_j} + 2\left(\frac{\partial \hat{Z}_j}{\partial V_r}\right)\left(\frac{\partial \hat{Z}_j}{\partial I_r}\right)\sigma_{V_rI_r} + 2\left(\frac{\partial \hat{Z}_j}{\partial V_r}\right)\left(\frac{\partial \hat{Z}_j}{\partial I_j}\right)\sigma_{V_rI_j}$$
$$+ 2\left(\frac{\partial \hat{Z}_j}{\partial V_j}\right)\left(\frac{\partial \hat{Z}_j}{\partial I_r}\right)\sigma_{V_jI_r} + 2\left(\frac{\partial \hat{Z}_j}{\partial V_j}\right)\left(\frac{\partial \hat{Z}_j}{\partial I_j}\right)\sigma_{V_jI_j} + 2\left(\frac{\partial \hat{Z}_j}{\partial I_r}\right)\left(\frac{\partial \hat{Z}_j}{\partial I_j}\right)\sigma_{I_rI_j} \tag{6.26}$$

where $\hat{Z}_n$ represents the expectation value of the impedance.

The derivations of the coefficients in the Taylor series of equations (6.25) and (6.26) are reported in Appendix A. Substitution of these determined coefficients into equations (6.25) and (6.26) leads to the variance in the real impedance as

$$
\begin{aligned}
\sigma_{Z_r}^2 = {} & E\left(\frac{I_r^2}{\left(I_r^{\,2}+I_j^{\,2}\right)^2}\right)\sigma_{V_r}^2 + E\left(\frac{I_j^2}{\left(I_r^{\,2}+I_j^{\,2}\right)^2}\right)\sigma_{V_j}^2 + 2E\left(\frac{I_rI_j}{\left(I_r^{\,2}+I_j^{\,2}\right)^2}\right)\sigma_{V_rV_j} \\
& + E\left[\frac{V_r^2}{\left(I_r^{\,2}+I_j^{\,2}\right)^2} - \frac{4(I_r)(V_r)[V_rI_r+V_jI_j]}{\left(I_r^{\,2}+I_j^{\,2}\right)^3} + \frac{4\left(I_r^2\right)[V_rI_r+V_jI_j]^2}{\left(I_r^{\,2}+I_j^{\,2}\right)^4}\right]\sigma_{I_r}^2 \\
& + E\left[\frac{V_j^2}{\left(I_r^{\,2}+I_j^{\,2}\right)^2} - \frac{4(I_j)(V_j)[V_rI_r+V_jI_j]}{\left(I_r^{\,2}+I_j^{\,2}\right)^3} + \frac{4\left(I_j^{\,2}\right)[V_rI_r+V_jI_j]^2}{\left(I_r^{\,2}+I_j^{\,2}\right)^4}\right]\sigma_{I_j}^2 \\
& + 2E\left[\frac{V_rI_r}{\left(I_r^{\,2}+I_j^{\,2}\right)^2} - \frac{2\left(I_r^{\,2}\right)[V_rI_r+V_jI_j]}{\left(I_r^{\,2}+I_j^{\,2}\right)^3}\right]\sigma_{V_rI_r} \\
& + 2E\left[\frac{V_jI_r}{\left(I_r^{\,2}+I_j^{\,2}\right)^2} - \frac{2(I_j)(I_r)[V_rI_r+V_jI_j]}{\left(I_r^{\,2}+I_j^{\,2}\right)^3}\right]\sigma_{V_rI_j} \\
& + 2E\left[\frac{V_rI_j}{\left(I_r^{\,2}+I_j^{\,2}\right)^2} - \frac{2(I_r)(I_j)[V_rI_r+V_jI_j]}{\left(I_r^{\,2}+I_j^{\,2}\right)^3}\right]\sigma_{V_jI_r} \\
& + 2E\left[\frac{V_jI_j}{\left(I_r^{\,2}+I_j^{\,2}\right)^2} - \frac{2\left(I_j^{\,2}\right)[V_rI_r+V_jI_j]}{\left(I_r^{\,2}+I_j^{\,2}\right)^3}\right]\sigma_{V_jI_j} \\
& + 2E\left[\begin{array}{l}\dfrac{V_rV_j}{\left(I_r^{\,2}+I_j^{\,2}\right)^2} - \dfrac{2[V_jI_r+V_rI_j][V_rI_r+V_jI_j]}{\left(I_r^{\,2}+I_j^{\,2}\right)^3} \\ + \dfrac{4(I_r)(I_j)[V_rI_r+V_jI_j]^2}{\left(I_r^{\,2}+I_j^{\,2}\right)^4}\end{array}\right]\sigma_{I_rI_j}
\end{aligned}
\tag{6.27}
$$

and the variance of the imaginary impedance as

$$
\begin{aligned}
\sigma_{Z_j}^2 = {} & E\left(\frac{I_j^{\,2}}{\left(I_r^{\,2}+I_j^{\,2}\right)^2}\right)\sigma_{V_r}^2 + E\left(\frac{I_r^{\,2}}{\left(I_r^{\,2}+I_j^{\,2}\right)^2}\right)\sigma_{V_j}^2 - 2E\left(\frac{I_r I_j}{\left(I_r^{\,2}+I_j^{\,2}\right)^2}\right)\sigma_{V_r V_j} \\
& + E\left[\frac{V_j^2}{\left(I_r^{\,2}+I_j^{\,2}\right)^2} - \frac{4(I_r)(V_j)\left[V_j I_r - V_r I_j\right]}{\left(I_r^{\,2}+I_j^{\,2}\right)^3} + \frac{4\left(I_r^{\,2}\right)\left[V_j I_r - V_r I_j\right]^2}{\left(I_r^{\,2}+I_j^{\,2}\right)^4}\right]\sigma_{I_r}^2 \\
& + E\left[\frac{V_r^2}{\left(I_r^{\,2}+I_j^{\,2}\right)^2} + \frac{4(I_j)(V_r)\left[V_j I_r - V_r I_j\right]}{\left(I_r^{\,2}+I_j^{\,2}\right)^3} + \frac{4\left(I_j^{\,2}\right)\left[V_j I_r - V_r I_j\right]^2}{\left(I_r^{\,2}+I_j^{\,2}\right)^4}\right]\sigma_{I_j}^2 \\
& + 2E\left[\frac{2(I_r)(I_j)\left[V_j I_r - V_r I_j\right]}{\left(I_r^{\,2}+I_j^{\,2}\right)^3} - \frac{V_j I_j}{\left(I_r^{\,2}+I_j^{\,2}\right)^2}\right]\sigma_{V_r I_r} \\
& + 2E\left[\frac{V_r I_j}{I_r^{\,2}+I_j^{\,2}} + \frac{2\left(I_j^{\,2}\right)\left[V_j I_r - V_r I_j\right]}{\left(I_r^{\,2}+I_j^{\,2}\right)^3}\right]\sigma_{V_r I_j} \\
& + 2E\left[\frac{V_j I_r}{I_r^{\,2}+I_j^{\,2}} - \frac{2\left(I_r^{\,2}\right)\left[V_j I_r - V_r I_j\right]}{\left(I_r^{\,2}+I_j^{\,2}\right)^3}\right]\sigma_{V_j I_r} \\
& - 2E\left[\frac{V_r I_r}{I_r^{\,2}+I_j^{\,2}} + \frac{2(I_r)(I_j)\left[V_j I_r - V_r I_j\right]}{\left(I_r^{\,2}+I_j^{\,2}\right)^3}\right]\sigma_{V_j I_j} \\
& + 2E\left[\begin{array}{l}\dfrac{4(I_r)(I_j)\left[V_j I_r - V_r I_j\right]^2}{\left(I_r^{\,2}+I_j^{\,2}\right)^4} + \dfrac{2\left[V_r I_r - V_j I_j\right]\left[V_j I_r - V_r I_j\right]}{\left(I_r^{\,2}+I_j^{\,2}\right)^3} \\ -\dfrac{V_r V_j}{\left(I_r^{\,2}+I_j^{\,2}\right)^2}\end{array}\right]\sigma_{I_r I_j}
\end{aligned}
\tag{6.28}
$$

This method for determination of the Taylor series expansions for the variances in the real and imaginary impedances does not provide a means of assessing the covariance between the two components as a function of the variance in the constituent current and voltage signals. However, by isolating the two impedance variances, the equality of the variances in the real and imaginary impedances can be tested through the ratio of the two, rather than the difference of the two. As a result, the statistical F-test and student's t-test

can be used to qualify the relationship between the variances in the complex components of the impedance.

6.3 Vector Representation of Variance in Impedance

Equations (6.27) and (6.28) can be considered to be the inner-product of a coefficient vector and a vector of variances, covariances, and cross-covariances. The vectors

$$\mathbf{A}_r = E\begin{bmatrix} \dfrac{I_r^2}{\left(I_r^{\,2}+I_j^{\,2}\right)^2} \\ \dfrac{I_j^2}{\left(I_r^{\,2}+I_j^{\,2}\right)^2} \\ \dfrac{V_r^2}{\left(I_r^{\,2}+I_j^{\,2}\right)^2} - \dfrac{4(I_r)(V_r)\left[V_rI_r+V_jI_j\right]}{\left(I_r^{\,2}+I_j^{\,2}\right)^3} + \dfrac{4\left(I_r^2\right)\left[V_rI_r+V_jI_j\right]^2}{\left(I_r^{\,2}+I_j^{\,2}\right)^4} \\ \dfrac{V_j^2}{\left(I_r^{\,2}+I_j^{\,2}\right)^2} - \dfrac{4(I_j)(V_j)\left[V_rI_r+V_jI_j\right]}{\left(I_r^{\,2}+I_j^{\,2}\right)^3} + \dfrac{4\left(I_j^{\,2}\right)\left[V_rI_r+V_jI_j\right]^2}{\left(I_r^{\,2}+I_j^{\,2}\right)^4} \\ \dfrac{2I_rI_j}{\left(I_r^{\,2}+I_j^{\,2}\right)^2} \\ \dfrac{2V_rV_j}{\left(I_r^{\,2}+I_j^{\,2}\right)^2} - \dfrac{4\left[V_jI_r+V_rI_j\right]\left[V_rI_r+V_jI_j\right]}{\left(I_r^{\,2}+I_j^{\,2}\right)^3} + \dfrac{8(I_r)(I_j)\left[V_rI_r+V_jI_j\right]^2}{\left(I_r^{\,2}+I_j^{\,2}\right)^4} \\ \dfrac{2V_rI_r}{\left(I_r^{\,2}+I_j^{\,2}\right)^2} - \dfrac{4\left(I_r^{\,2}\right)\left[V_rI_r+V_jI_j\right]}{\left(I_r^{\,2}+I_j^{\,2}\right)^3} \\ \dfrac{2V_jI_r}{\left(I_r^{\,2}+I_j^{\,2}\right)^2} - \dfrac{4(I_j)(I_r)\left[V_rI_r+V_jI_j\right]}{\left(I_r^{\,2}+I_j^{\,2}\right)^3} \\ \dfrac{2V_rI_j}{\left(I_r^{\,2}+I_j^{\,2}\right)^2} - \dfrac{4(I_r)(I_j)\left[V_rI_r+V_jI_j\right]}{\left(I_r^{\,2}+I_j^{\,2}\right)^3} \\ \dfrac{2V_jI_j}{\left(I_r^{\,2}+I_j^{\,2}\right)^2} - \dfrac{4\left(I_j^{\,2}\right)\left[V_rI_r+V_jI_j\right]}{\left(I_r^{\,2}+I_j^{\,2}\right)^3} \end{bmatrix}, \tag{6.29}$$

$$
\mathbf{A}_j = E\begin{bmatrix}
\dfrac{I_j^{\,2}}{\left(I_r^{\,2}+I_j^{\,2}\right)^2} \\
\dfrac{I_r^{\,2}}{\left(I_r^{\,2}+I_j^{\,2}\right)^2} \\
\dfrac{V_j^2}{\left(I_r^{\,2}+I_j^{\,2}\right)^2} - \dfrac{4(I_r)(V_j)\left[V_jI_r - V_rI_j\right]}{\left(I_r^{\,2}+I_j^{\,2}\right)^3} + \dfrac{4\left(I_r^{\,2}\right)\left[V_jI_r - V_rI_j\right]^2}{\left(I_r^{\,2}+I_j^{\,2}\right)^4} \\
\dfrac{V_r^2}{\left(I_r^{\,2}+I_j^{\,2}\right)^2} + \dfrac{4(I_j)(V_r)\left[V_jI_r - V_rI_j\right]}{\left(I_r^{\,2}+I_j^{\,2}\right)^3} + \dfrac{4\left(I_j^{\,2}\right)\left[V_jI_r - V_rI_j\right]^2}{\left(I_r^{\,2}+I_j^{\,2}\right)^4} \\
-\dfrac{2I_rI_j}{\left(I_r^{\,2}+I_j^{\,2}\right)^2} \\
\dfrac{8(I_r)(I_j)\left[V_jI_r - V_rI_j\right]^2}{\left(I_r^{\,2}+I_j^{\,2}\right)^4} + \dfrac{4\left[V_rI_r - V_jI_j\right]\left[V_jI_r - V_rI_j\right]}{\left(I_r^{\,2}+I_j^{\,2}\right)^3} - \dfrac{2V_rV_j}{\left(I_r^{\,2}+I_j^{\,2}\right)^2} \\
\dfrac{4(I_r)(I_j)\left[V_jI_r - V_rI_j\right]}{\left(I_r^{\,2}+I_j^{\,2}\right)^3} - \dfrac{2V_jI_j}{\left(I_r^{\,2}+I_j^{\,2}\right)^2} \\
\dfrac{2V_rI_j}{I_r^{\,2}+I_j^{\,2}} + \dfrac{4\left(I_j^{\,2}\right)\left[V_jI_r - V_rI_j\right]}{\left(I_r^{\,2}+I_j^{\,2}\right)^3} \\
\dfrac{2V_jI_r}{I_r^{\,2}+I_j^{\,2}} - \dfrac{4\left(I_r^{\,2}\right)\left[V_jI_r - V_rI_j\right]}{\left(I_r^{\,2}+I_j^{\,2}\right)^3} \\
-\left[\dfrac{2V_rI_r}{I_r^{\,2}+I_j^{\,2}} + \dfrac{4(I_r)(I_j)\left[V_jI_r - V_rI_j\right]}{\left(I_r^{\,2}+I_j^{\,2}\right)^3}\right]
\end{bmatrix}, \tag{6.30}
$$

and

$$\mathbf{V} = \begin{bmatrix} \sigma_{V_r}^2 \\ \sigma_{V_j}^2 \\ \sigma_{I_r}^2 \\ \sigma_{I_j}^2 \\ \sigma_{V_r V_j} \\ \sigma_{I_r I_j} \\ \sigma_{V_r I_r} \\ \sigma_{V_r I_j} \\ \sigma_{V_j I_r} \\ \sigma_{V_j I_j} \end{bmatrix}, \tag{6.31}$$

are related through equations (6.27) and (6.28) by

$$\sigma_{Z_r}^2 = \mathbf{A}_r^{\mathrm{T}} \mathbf{V} \tag{6.32}$$

and

$$\sigma_{Z_j}^2 = \mathbf{A}_j^{\mathrm{T}} \mathbf{V}, \tag{6.33}$$

respectively

If another two vectors are defined to be

$$\mathbf{D} = E\left\{ \frac{1}{\left(I_r^2 + I_j^2\right)^2} \begin{bmatrix} \left(I_r^2 - I_j^2\right) \\ -\left(I_r^2 - I_j^2\right) \\ \left[\left(I_r^2 - I_j^2\right)\left(Z_r^2 - Z_j^2\right) + 4\left(I_r I_j\right)\left(Z_r Z_j\right)\right] \\ -\left[\left(I_r^2 - I_j^2\right)\left(Z_r^2 - Z_j^2\right) + 4\left(I_r I_j\right)\left(Z_r Z_j\right)\right] \\ 4\left(I_r I_j\right) \\ -4\left[\left(I_r^2 - I_j^2\right)\left(Z_r Z_j\right) - \left(I_r I_j\right)\left(Z_r^2 - Z_j^2\right)\right] \\ -2\left[\left(I_r^2 - I_j^2\right)\left(Z_r\right) + 2\left(I_r I_j\right)\left(Z_j\right)\right] \\ 2\left[\left(I_r^2 - I_j^2\right)\left(Z_j\right) - 2\left(I_r I_j\right)\left(Z_r\right)\right] \\ 2\left[\left(I_r^2 - I_j^2\right)\left(Z_j\right) - 2\left(I_r I_j\right)\left(Z_r\right)\right] \\ 2\left[\left(I_r^2 - I_j^2\right)\left(Z_r\right) + 2\left(I_r I_j\right)\left(Z_j\right)\right] \end{bmatrix} \right\} \tag{6.34}$$

and

$$\mathbf{C} = E\left\{\frac{1}{\left(I_r^{\,2} + I_j^{\,2}\right)^2}\begin{bmatrix} -\left(I_r I_j\right) \\ \left(I_r I_j\right) \\ \left[\left(I_r^{\,2} - I_j^{\,2}\right)\left(Z_r Z_j\right) - \left(I_r I_j\right)\left(Z_r^{\,2} - Z_j^{\,2}\right)\right] \\ -\left[\left(I_r^{\,2} - I_j^{\,2}\right)\left(Z_r Z_j\right) - \left(I_r I_j\right)\left(Z_r^{\,2} - Z_j^{\,2}\right)\right] \\ \left(I_r^{\,2} - I_j^{\,2}\right) \\ \left[\left(I_r^{\,2} - I_j^{\,2}\right)\left(Z_r^{\,2} - Z_j^{\,2}\right) + 4\left(I_r I_j\right)\left(Z_r Z_j\right)\right] \\ -\left[\left(I_r^{\,2} - I_j^{\,2}\right)\left(Z_j\right) - 2\left(I_r I_j\right)\left(Z_r\right)\right] \\ -\left[\left(I_r^{\,2} - I_j^{\,2}\right)\left(Z_r\right) + 2\left(I_r I_j\right)\left(Z_j\right)\right] \\ -\left[\left(I_r^{\,2} - I_j^{\,2}\right)\left(Z_r\right) + 2\left(I_r I_j\right)\left(Z_j\right)\right] \\ \left[\left(I_r^{\,2} - I_j^{\,2}\right)\left(Z_j\right) - 2\left(I_r I_j\right)\left(Z_r\right)\right] \end{bmatrix}\right\}, \tag{6.35}$$

then, equations (6.16) and (6.17) can be rewritten as

$$\sigma_{Z_r}^2 - \sigma_{Z_j}^2 = \mathbf{D}^{\mathrm{T}}\mathbf{V} \tag{6.36}$$

and

$$\sigma_{Z_r Z_j} = \mathbf{C}^{\mathrm{T}}\mathbf{V}. \tag{6.37}$$

The coefficient vectors can be correlated by substitution of equations (6.32) and (6.33) into equation (6.36) as

$$\mathbf{D} = \mathbf{A}_r - \mathbf{A}_j. \tag{6.38}$$

The difference between equations (6.29) and (6.30) can be written as

$$
\mathbf{A}_r - \mathbf{A}_j = E \begin{bmatrix}
\dfrac{I_r^2 - I_j^{\,2}}{\left(I_r^{\,2} + I_j^{\,2}\right)^2} \\
\dfrac{I_j^2 - I_r^{\,2}}{\left(I_r^{\,2} + I_j^{\,2}\right)^2} \\
\begin{bmatrix} \dfrac{V_r^2 - V_j^2}{\left(I_r^{\,2} + I_j^{\,2}\right)^2} - \dfrac{4(I_r)(V_r)\left[V_r I_r + V_j I_j\right] - 4(I_r)(V_j)\left[V_j I_r - V_r I_j\right]}{\left(I_r^{\,2} + I_j^{\,2}\right)^3} \\ + \dfrac{4\left(I_r^2\right)\left[V_r I_r + V_j I_j\right]^2 - 4\left(I_r^{\,2}\right)\left[V_j I_r - V_r I_j\right]^2}{\left(I_r^{\,2} + I_j^{\,2}\right)^4} \end{bmatrix} \\
\begin{bmatrix} \dfrac{V_j^2 - V_r^2}{\left(I_r^{\,2} + I_j^{\,2}\right)^2} - \dfrac{4(I_j)(V_j)\left[V_r I_r + V_j I_j\right] + 4(I_j)(V_r)\left[V_j I_r - V_r I_j\right]}{\left(I_r^{\,2} + I_j^{\,2}\right)^3} \\ + \dfrac{4\left(I_j^{\,2}\right)\left[V_r I_r + V_j I_j\right]^2 - 4\left(I_j^{\,2}\right)\left[V_j I_r - V_r I_j\right]^2}{\left(I_r^{\,2} + I_j^{\,2}\right)^4} \end{bmatrix} \\
\dfrac{4 I_r I_j}{\left(I_r^{\,2} + I_j^{\,2}\right)^2} \\
\begin{bmatrix} \dfrac{4 V_r V_j}{\left(I_r^{\,2} + I_j^{\,2}\right)^2} \\ - \dfrac{4\left[V_j I_r + V_r I_j\right]\left[V_r I_r + V_j I_j\right] + 4\left[V_r I_r - V_j I_j\right]\left[V_j I_r - V_r I_j\right]}{\left(I_r^{\,2} + I_j^{\,2}\right)^3} \\ + \dfrac{8(I_r)(I_j)\left[V_r I_r + V_j I_j\right]^2 - 8(I_r)(I_j)\left[V_j I_r - V_r I_j\right]}{\left(I_r^{\,2} + I_j^{\,2}\right)^4} \end{bmatrix} \\
\dfrac{2V_r I_r + 2V_j I_j}{\left(I_r^{\,2} + I_j^{\,2}\right)^2} - \dfrac{4\left(I_r^{\,2}\right)\left[V_r I_r + V_j I_j\right] + 4(I_r)(I_j)\left[V_j I_r - V_r I_j\right]}{\left(I_r^{\,2} + I_j^{\,2}\right)^3} \\
\dfrac{2V_j I_r - 2V_r I_j}{\left(I_r^{\,2} + I_j^{\,2}\right)^2} - \dfrac{4(I_j)(I_r)\left[V_r I_r + V_j I_j\right] + 4\left(I_j^{\,2}\right)\left[V_j I_r - V_r I_j\right]}{\left(I_r^{\,2} + I_j^{\,2}\right)^3} \\
\dfrac{2V_r I_j - 2V_j I_r}{\left(I_r^{\,2} + I_j^{\,2}\right)^2} - \dfrac{4(I_r)(I_j)\left[V_r I_r + V_j I_j\right] - 4\left(I_r^{\,2}\right)\left[V_j I_r - V_r I_j\right]}{\left(I_r^{\,2} + I_j^{\,2}\right)^3} \\
\dfrac{2V_j I_j + 2V_r I_r}{\left(I_r^{\,2} + I_j^{\,2}\right)^2} - \dfrac{4\left(I_j^{\,2}\right)\left[V_r I_r + V_j I_j\right] - 4(I_r)(I_j)\left[V_j I_r - V_r I_j\right]}{\left(I_r^{\,2} + I_j^{\,2}\right)^3}
\end{bmatrix}
\tag{6.39}
$$

The ten components of the vector in equation (6.39) were expanded, and then simplified. The results are presented in Appendix A. The simplified components were introduced into equation (6.39) that can be rewritten as

$$\mathbf{A}_r - \mathbf{A}_j = \frac{1}{\left(I_r^{\,2} + I_j^{\,2}\right)^2}\begin{bmatrix} \left(I_r^{\,2} - I_j^{\,2}\right) \\ -\left(I_r^{\,2} - I_j^{\,2}\right) \\ \left[\left(I_r^{\,2} - I_j^{\,2}\right)\left(Z_r^{\,2} - Z_j^{\,2}\right) + 4\left(I_r I_j\right)\left(Z_r Z_j\right)\right] \\ -\left[\left(I_r^{\,2} - I_j^{\,2}\right)\left(Z_r^{\,2} - Z_j^{\,2}\right) + 4\left(I_r I_j\right)\left(Z_r Z_j\right)\right] \\ 4\left(I_r I_j\right) \\ -4\left[\left(I_r^{\,2} - I_j^{\,2}\right)\left(Z_r Z_j\right) - \left(I_r I_j\right)\left(Z_r^{\,2} - Z_j^{\,2}\right)\right] \\ -2\left[\left(I_r^{\,2} - I_j^{\,2}\right)\left(Z_r\right) + 2\left(I_r I_j\right)\left(Z_j\right)\right] \\ 2\left[\left(I_r^{\,2} - I_j^{\,2}\right)\left(Z_j\right) - 2\left(I_r I_j\right)\left(Z_r\right)\right] \\ 2\left[\left(I_r^{\,2} - I_j^{\,2}\right)\left(Z_j\right) - 2\left(I_r I_j\right)\left(Z_r\right)\right] \\ 2\left[\left(I_r^{\,2} - I_j^{\,2}\right)\left(Z_r\right) + 2\left(I_r I_j\right)\left(Z_j\right)\right] \end{bmatrix} \tag{6.40}$$

Comparison with equation (6.34) leads to the verification of

$$\mathbf{A}_r - \mathbf{A}_j = \mathbf{D} \tag{6.41}$$

As a result of this equality, the test for the equality of the variance in the real impedance to the variance in the imaginary impedance can be accomplished in two ways. First, the difference between the two can be set to be equal to zero and the relationship between $\mathbf{D}$ and $\mathbf{V}$ can be determined. Second, the variances can be set to be equal and the relationship between $\mathbf{A}_r$ and $\mathbf{A}_j$ can be determined.

If equation (6.36) is rewritten such that the difference between the variances is set equal to zero,

$$\sigma_{Z_r}^2 - \sigma_{Z_j}^2 = \mathbf{D}^{\mathrm{T}}\mathbf{V} = 0 \tag{6.42}$$

then it is apparent that the transpose of the difference vector $\mathbf{D}$ must be orthogonal to the variance vector $\mathbf{V}$. Equations (6.32) and (6.33) can also be set to be equal such that

$$\mathbf{A}_r^{\mathrm{T}}\mathbf{V} = \mathbf{A}_j^{\mathrm{T}}\mathbf{V} \tag{6.43}$$

The tests for equality, equations (6.42) and (6.43), defined for the Taylor series descriptions of the variances in the real and imaginary impedances have been written such that they hold at a single frequency.

6.4 Simulation Studies of Taylor Series Expansion for Variance of Complex Impedance in Rectangular Form

One possible solution to equations (6.42) and (6.43) is obtained under the condition that the variances in voltage be equal, the variances in current be equal, the real cross-covariance and imaginary cross-covariance be equal, the other two cross-covariances be the negative value of the other, and, finally, that the two covariances be equal to zero.

$$\sigma_{V_r}^2(\omega) = \sigma_{V_j}^2(\omega). \tag{6.44}$$

$$\sigma_{I_r}^2(\omega) = \sigma_{I_j}^2(\omega) \tag{6.45}$$

$$\sigma_{V_r V_j}(\omega) = \sigma_{I_r I_j}(\omega) = 0 \tag{6.46}$$

$$\sigma_{V_r I_r}(\omega) = \sigma_{V_j I_j}(\omega) \tag{6.47}$$

$$\sigma_{V_j I_r}(\omega) = -\sigma_{V_r I_j}(\omega). \tag{6.48}$$

This solution also satisfies the condition that the errors in the real and imaginary impedance are uncorrelated, or that the covariance, equation (6.37), between the real and imaginary impedance is equal to zero. Simulation studies were conducted to determine if this solution to the equality of variances in the real and imaginary impedances could be found.

Whereas the simulations discussed in the previous chapter were conducted to mimic the actual impedance measurement that only reported the complex impedance, these

simulations were conducted to determine the complex components of the current and voltage signals as well as the complex impedance. Each component was time-averaged until the auto-integration criterion for the impedance calculation was satisfied. The single Voigt element, first order, transfer function studied in the previous chapter was employed here. The measurement of the complex components of impedance, current, and voltage were repeated 500 times at each frequency. The spectrum consisted of the same 91 frequencies ranging from 1 Hz to 1 MHz that were used in the simulations of the previous chapter. From the six replicate complex components, the variances and covariance in real and imaginary impedances and the variances and covariances of cross-covariances between the real and imaginary currents and voltages were calculated. The expectation value (sample mean) of each complex component was calculated for substitution into the Taylor series coefficient vectors $\mathbf{A}_r$, $\mathbf{A}_j$, and $\mathbf{D}$.

The simulations were conducted using the frequency response analysis calculation and phase-sensitive detection calculation. The Bode quadrature rule was employed in both impedance calculation techniques. Three simulation cases were conducted. In one case (CASE 1), Gaussian noise was added to the input and this noise was transformed by the system into the output signal. The distribution of this noise was defined by a standard deviation that was 10% of the input signal amplitude. Thus, the signal to noise level in the input signal was 10 at all frequencies. The next case (CASE 2) consisted of adding noise only to the output, such that one signal was clean while the other was noisy. The distribution of the noise added to the output signal also was defined by a standard deviation that was 10% of the input signal amplitude. Thus, in this simulation the signal to noise ratio was 10 at high frequency at 20 at low frequency. The final case (CASE 3)

was the combination of the first two in that the same distribution of Gaussian noise was added to the input and output, and the input noise was transformed into the output signal.

For all three cases in which the FRA calculation was employed, the condition of the variance vector by which equation (6.43) can be observed was satisfied. The ratio of the Taylor series for variance in the real impedance to the Taylor series for variance in the imaginary impedance are plotted in Figure 6.1 (for PSD calculation) and Figure 6.2 (for FRA determination). The variances in real and imaginary impedance are generally equal when the complex signal components are calculated using the FRA technique. The ratio does not appear to be unity at high frequency for CASE 1. In fact, the ratio is scattered widely at high frequency, but this may be a result of loss-of-significance machine errors or of the lack of higher order terms in the Taylor series expansions. The variances in the real and imaginary impedances are not equal in all three cases when the complex signal components are measured using phase-sensitive detection. The correlation between the real and imaginary impedance was also calculated, and was determined to be equal to zero on average over the spectrum for both measurement techniques for CASE 1 and CASE 2. The errors were correlated to a very small level in CASE 3 when the PSD technique was used. The errors were uncorrelated in CASE 3 when frequency response analysis was employed. This was verified using the student's t-test over the spectrum of correlation coefficients associated with the covariance between the components and the standard deviation of each component.

Each condition on the variance vector by which equation (6.43) can be observed, defined by equations (6.44)-(6.48), was tested. The ratio of variances in the complex voltage is shown in Figure 6.3 for the PSD measurement and in Figure 6.4 for the FRA

measurement as a function of frequency. The ratio of variances in the complex current is shown in Figure 6.5 for the PSD measurement and in Figure 6.6 for the FRA measurement as a function of frequency. The F-test probability lines are also plotted. The covariances in voltage are shown in Figure 6.7 and Figure 6.8, respectively, for PSD and FRA calculations, and in current, for PSD and FRA calculations, respectively, are shown in Figure 6.9 and Figure 6.10. The ratio of real cross-covariance to imaginary cross-covariance are plotted as a function of frequency in Figure 6.11 for the PSD measurement and in Figure 6.12 for the FRA measurement. Finally, the ratios of cross-covariances between the real voltage and imaginary current and imaginary voltage and real current are shown in Figure 6.13 and Figure 6.14, respectively, for PSD and FRA calculations.

Nearly all of the conditions of the conditions defined by equations (6.44)-(6.48) were satisfied when the FRA technique was used to calculate the impedance. Not all of the conditions were satisfied when the PSD technique was employed. Tables Table 6.1-6.2Table 6.3 provide student's t-test results applied to the equality of the calculated variance vector and the trivial solution for the respective case numbers. The ratio of voltage variances falls well within the middle of the F-test limits for the PSD calculation (Figure 6.3), but the same ratio for the FRA calculation (Figure 6.4) shows trending and falls outside the limits. The ratio of current variances falls well within the middle of the F-test limits for the PSD calculation (Figure 6.5), but the same ratio for the FRA calculation (Figure 6.6) is distributed to the lower limit. PSD calculated covariances in voltage and current are widely scattered about zero (Figure 6.7 and Figure 6.9); the corresponding covariances calculated using frequency response analysis are scattered

tightly around zero (Figure 6.8 and Figure 6.10). The ratio of the cross-covariances between the real current and voltage and the imaginary current and voltage calculated via the PSD technique (Figure 6.11) are scattered widely about one, and fall well outside the F-test limit, while the same ratio calculated through the FRA technique (Figure 6.12) fall well within the F-test limits. The final cross-covariance ratio is distributed widely about -1 for both calculation methods (Figure 6.13 and Figure 6.14). The calculated cross-covariances are scattered more widely when the impedance is calculated via the PSD technique than via the FRA technique. The wide scatter of these values leads to the failure of the ratio of the variances of the PSD measured impedances to generally satisfy the F-test.

Another interesting result from these simulations is that the noise level in the constituent signals was frequency-dependent due to the method of introduction of noise into those signals. The noise level in the current was the same for the two of the three cases in which noise was added to the current. However, the noise level in the complex voltage was highly dependent upon the manner in which noise is introduced. In Figure 6.15, the ratio of the variances in the real and imaginary voltage for CASE 1 with Gaussian noise to the same variances for CASE 2 with Gaussian noise are plotted as functions of frequency. The ratio was a function of frequency. This may seem an obvious result in that, the noise level introduced into the voltage signal was constant over frequency in CASE 2, but the noise level introduced into the voltage signal in CASE 1 was scaled by the impedance. The impedance magnitude, and the reciprocal of the square of the impedance magnitude are also plotted as a function of frequency. The ratio was a function of the impedance magnitude, and was scaled by the reciprocal of the square of

the impedance magnitude. This scaling was applied to the ratios, and they are also plotted. Both ratios were generally scattered about unity. Therefore, the nature of the frequency dependent error structure of impedance measurements is a function of the manner in which noise is introduced in the time-domain.

6.5 Taylor Series Expansion for Variance of Complex Impedance in Polar Form

The Taylor series for variance in the complex impedance can also be derived for a polar coordinate description of the impedance. Thus, the general Taylor series for the variance will be given by

$$\begin{aligned}\sigma_Z^2 = &\left(\frac{\partial Z}{\partial |V|}\right)^2 \sigma_{|V|}^2 + \left(\frac{\partial Z}{\partial |I|}\right)^2 \sigma_{|I|}^2 + \left(\frac{\partial Z}{\partial \phi_V}\right)^2 \sigma_{\phi_V}^2 + \left(\frac{\partial Z}{\partial \phi_I}\right)^2 \sigma_{\phi_I}^2 \\ &+ 2\left(\frac{\partial Z}{\partial |V|}\right)\left(\frac{\partial Z}{\partial |I|}\right)\sigma_{|V||I|} + 2\left(\frac{\partial Z}{\partial |V|}\right)\left(\frac{\partial Z}{\partial \phi_V}\right)\sigma_{|V|\phi_V} + 2\left(\frac{\partial Z}{\partial |V|}\right)\left(\frac{\partial Z}{\partial \phi_I}\right)\sigma_{|V|\phi_I} \\ &+ 2\left(\frac{\partial Z}{\partial |I|}\right)\left(\frac{\partial Z}{\partial \phi_I}\right)\sigma_{|I|\phi_I} + 2\left(\frac{\partial Z}{\partial |I|}\right)\left(\frac{\partial Z}{\partial \phi_V}\right)\sigma_{|I|\phi_V} + 2\left(\frac{\partial Z}{\partial \phi_I}\right)\left(\frac{\partial Z}{\partial \phi_V}\right)\sigma_{\phi_I\phi_V}\end{aligned} \tag{6.49}$$

where the polar form of impedance is defined by

$$Z = \frac{|V|e^{j\phi_V}}{|I|e^{j\phi_I}}. \tag{6.50}$$

The four derivatives can be calculated as

$$\left(\frac{\partial Z}{\partial |V|}\right) = \frac{1}{|I|}e^{j(\phi_V - \phi_I)} \tag{6.51}$$

$$\left(\frac{\partial Z}{\partial |I|}\right) = -\frac{|Z|}{|I|^2}e^{j(\phi_V - \phi_I)} \tag{6.52}$$

$$\left(\frac{\partial Z}{\partial \phi_V}\right) = j\frac{|V|}{|I|}e^{j(\phi_V - \phi_I)} \tag{6.53}$$

$$\left(\frac{\partial Z}{\partial \phi_I}\right) = -j\frac{|V|}{|I|}e^{j(\phi_V - \phi_I)} \tag{6.54}$$

The variance in the complex impedance, in terms of its magnitude and phase angle, can be written as

$$\sigma_Z^2 = \left(\frac{\partial Z}{\partial |Z|}\right)^2 \sigma_{|Z|}^2 + +\left(\frac{\partial Z}{\partial \phi}\right)^2 \sigma_\phi^2 + 2\left(\frac{\partial Z}{\partial |Z|}\right)\left(\frac{\partial Z}{\partial \phi}\right)\sigma_{|Z|\phi} \tag{6.55}$$

$$\sigma_Z^2 = e^{2j\phi}\sigma_{|Z|}^2 - |Z|^2 e^{2j\phi}\sigma_\phi^2 + 2j|Z|e^{2j\phi}\sigma_{|Z|\phi} \tag{6.56}$$

where

$$\phi = \phi_V - \phi_I \tag{6.57}$$

By combining equations (6.49) and (6.56) and substituting equations (6.51)-(6.54) for the partial derivatives, the Taylor series can be written as

$$\begin{aligned} & e^{2j\phi}\sigma_{|Z|}^2 - |Z|^2 e^{2j\phi}\sigma_\phi^2 + 2j|Z|e^{2j\phi}\sigma_{|Z|\phi} \\ & = \frac{1}{|I|^2}e^{2j\phi}\sigma_{|V|}^2 + \frac{|V|^2}{|I|^4}e^{2j\phi}\sigma_{|I|}^2 - \frac{|V|^2}{|I|^2}e^{2j\phi}\sigma_{\phi_V}^2 - \frac{|V|^2}{|I|^2}e^{2j\phi}\sigma_{\phi_I}^2 \\ & -2 - \frac{|V|}{|I|^3}e^{2j\phi}\sigma_{|V||I|} + 2j\frac{|V|}{|I|^2}e^{2j\phi}\sigma_{|V|\phi_V} - 2j\frac{|V|}{|I|^2}e^{2j\phi}\sigma_{|V|\phi_I} \\ & +2j\frac{|V|^2}{|I|^3}e^{2j\phi}\sigma_{|I|\phi_I} - 2j\frac{|V|^2}{|I|^3}e^{2j\phi}\sigma_{|I|\phi_V} + 2\frac{|V|^2}{|I|^2}e^{2j\phi}\sigma_{\phi_I\phi_V} \end{aligned} \tag{6.58}$$

The common exponential can be cancelled and the ratio of voltage to current magnitudes can be replaced with magnitude in impedance. Equation (6.58) then becomes

$$\sigma_{|Z|}^2 - |Z|^2\sigma_\phi^2 + 2j|Z|\sigma_{|Z|\phi} = \frac{1}{|I|^2}\sigma_{|V|}^2 + \frac{|Z|^2}{|I|^2}\sigma_{|I|}^2 - |Z|^2\sigma_{\phi_V}^2 - |Z|^2\sigma_{\phi_I}^2$$
$$-2 - \frac{|Z|}{|I|^2}\sigma_{|V||I|} + 2j\frac{|Z|}{|I|}\sigma_{|V|\phi_V} - 2j\frac{|Z|}{|I|}\sigma_{|V|\phi_I} \,.$$
$$+2j\frac{|Z|^2}{|I|}\sigma_{|I|\phi_I} - 2j\frac{|Z|^2}{|I|}\sigma_{|I|\phi_V} + 2|Z|^2\sigma_{\phi_I\phi_V} \tag{6.59}$$

The real and imaginary parts can then be separated, leaving

$$\sigma_{|Z|}^2 - |Z|^2\sigma_\phi^2 = \frac{1}{|I|^2}\sigma_{|V|}^2 + \frac{|Z|^2}{|I|^2}\sigma_{|I|}^2 - |Z|^2\sigma_{\phi_V}^2 - |Z|^2\sigma_{\phi_I}^2 - 2 - \frac{|Z|}{|I|^2}\sigma_{|V||I|} + 2|Z|^2\sigma_{\phi_I\phi_V} \tag{6.60}$$

$$\sigma_{|Z|\phi} = \frac{1}{|I|}\sigma_{|V|\phi_V} - \frac{1}{|I|}\sigma_{|V|\phi_I} + \frac{|Z|}{|I|}\sigma_{|I|\phi_I} - \frac{|Z|}{|I|}\sigma_{|I|\phi_V} \,. \tag{6.61}$$

These two equations can be expressed in vector form as

$$\sigma_{|Z|}^2 - |Z|^2\sigma_\phi^2 = \mathbf{D_p}^{\mathbf{T}}\mathbf{V_p} \tag{6.62}$$

$$\sigma_{|Z|\phi} = \mathbf{C_p}^{\mathbf{T}}\mathbf{V_p} \,. \tag{6.63}$$

where the vectors components are

$$\mathbf{D_p} = \begin{bmatrix} 1/|I|^2 \\ |Z|^2/|I|^2 \\ -|Z|^2 \\ -|Z|^2 \\ 0 \\ 0 \\ -2|Z|/|I|^2 \\ 0 \\ 0 \\ 2|Z|^2 \end{bmatrix} \tag{6.64}$$

$$\mathbf{C}_{\mathrm{p}} = \begin{bmatrix} 0 \\ 0 \\ 0 \\ 0 \\ 1/|I| \\ |Z|/|I| \\ 0 \\ -1/|I| \\ -|Z|/|I| \\ 0 \end{bmatrix} \tag{6.65}$$

$$\mathbf{V}_{\mathrm{p}} = \begin{bmatrix} \sigma^2_{|V|} \\ \sigma^2_{|I|} \\ \sigma^2_{\phi_V} \\ \sigma^2_{\phi_I} \\ \sigma_{|V|\phi_V} \\ \sigma_{|I|\phi_I} \\ \sigma_{|V||I|} \\ \sigma_{|V|\phi_I} \\ \sigma_{|I|\phi_V} \\ \sigma_{\phi_I\phi_V} \end{bmatrix}. \tag{6.66}$$

This method for determination of the Taylor series expansions for the variances in the magnitude and phase angle of the impedance provides a means of assessing the covariance between the two components as a function of the variance in the constituent current and voltage signals. However, the statistical F-test can not be used to qualify the relationship between the variances in the complex components of the impedance. The student's t-test can be used to determine if the difference defined by equation (6.62) and the covariance defined by equation (6.63) is equal to zero.

6.6 Simulation Studies of Taylor Series Expansion for Variance of Complex Impedance in Polar Form

Whereas the LabView simulations conducted to mimic the actual impedance measurement only reported the complex impedance, these simulations were conducted to determine the complex components of the current and voltage signal along with the complex impedance. Each component was time-averaged until the auto-integration criterion was satisfied. The measurement of the complex components of impedance, current, and voltage were repeated 500 times at each frequency. The complex components were all reported in polar form. The spectrum consisted of 91 frequencies. From the six replicate complex components, the variances and covariance in real and imaginary impedances and the variances and covariances of cross-covariances between the real and imaginary currents and voltages were calculated. The expectation value (sample mean) of each complex component was calculated for substitution into the Taylor series coefficient vectors $\mathbf{C}$, and $\mathbf{D}$.

A set of simulations patterned after the three cases of Section 4 were conducted. The simulations were performed using the frequency response analysis calculation and phase-sensitive detection calculation. The Bode quadrature rule was employed in both impedance calculation techniques. The same three simulation cases were conducted: CASE 1 in which noise was added to the input and this noise was transformed by the system into the output signal, CASE 2 in which noise was added only to the output, such that one signal was clean while the other was noisy, CASE 3 in which noise was added to the input and output, and the input noise was transformed into the output signal.

The difference in variance in impedance magnitude and scaled phase angle as defined by equation (6.62) are plotted for all three cases in Figure 6.16 for PSD

calculation and in Figure 6.17 for FRA calculations. The cross-covariance between the impedance magnitude and phase angle defined by equation (6.63) is plotted for all three cases in Figure 6.18 for PSD determination and in Figure 6.19 for FRA determination. The differences and cross-covariances for the three cases are scattered tightly around zero for the impedance spectra measured using the FRA technique. The differences and cross-covariances are distributed over frequency for all three cases when the impedance spectra were calculated using the PSD method.

The t-test for the differences between variances in impedance magnitude and phase angle and the impedance cross-covariance being equal to zero is shown in Table 6.4. When the FRA technique was used to calculate the impedance, the hypothesis that the difference between the two variances was equal to zero can be accepted for CASES 2 and 3. The hypothesis that the mean of the difference determined over the spectrum was equal to zero can be rejected for the FRA calculation in CASE 1 since the calculated *t*-parameter is greater than the critical value with 5% level of significance. The noise level in the impedance measurement was extremely small for the CASE 1 simulation, since very little noise was in the response signal. When frequency response analysis was used, the noise level was on the order of the machine (computer) error - 10^{-8} for these simulations. The hypothesis that the difference was equal to zero when the impedance was calculated via the PSD technique can be rejected for all three cases. The hypothesis that the impedance cross-covariance defined by equation (6.63) was equal to zero can be accepted for all three cases in which frequency response analysis was employed, while the hypothesis that the cross-covariance was equal to zero for the three cases in which phase-sensitive detection was used can be rejected. The test parameter is greater than the

critical value for 5% level of significance (almost greater for CASE 1, but the parameter will be greater than the critical value when the level of significance is greater).

6.7 Conclusions

The variance in the real and imaginary impedance was estimated by a ten-term linear Taylor series expansion with respect to the variances and covariances of and cross-covariances between the complex components of the current and voltage signals. The Taylor series expansion was derived in both rectangular and polar complex coordinates. Choice of the rectangular coordinate expansion derived for the individual impedance components allowed equality of the variance in the real and imaginary impedance to be tested through a ratio rather than a difference. The rectangular coordinate ratio accommodated the F-test as a test of equality of the variances at each frequency, and accommodated the student's t-test as a test of equality of the variances over the spectrum. Also, by using the rectangular coordinate expansion, a condition on the variance vector for the equality of the variances in the real and imaginary impedances was determined. The rectangular coordinate expansion derived for the complex impedance and the polar coordinate expansion provided a means for testing the covariance between the real and imaginary impedance or impedance magnitude and phase angle. This analysis does not neglect, *a priori*, the correlations between the complex components of the current and voltage signals. Simulation studies confirmed that the complex components of the current and voltage signals were correlated even though the real and imaginary parts of each signal were not correlated.

Simulation studies were conducted to demonstrate that the Taylor series expansion could be used to describe the variances in the complex impedance components. The simulations conducted in the previous chapter intended to demonstrate the nature of the

stochastic errors associated with the employed spectroscopic calculation method. The errors in the real and imaginary impedance were not correlated when either technique was used to calculate the impedance and noise was added only to the input or output. The errors in the real and imaginary impedance were never correlated for the FRA calculation; they were correlated for the PSD calculation in the case in which noise was added to both the input and output. It was demonstrated in Chapter 5 that the PSD technique introduces a bias error into the real and imaginary impedances. These results are consistent with the experimental finding that errors in the real and imaginary impedance are uncorrelated if the impedances do not contain bias error contributions.[7] The variance in the real impedance was shown to be equal to the variance in the imaginary impedance for added Gaussian noise when the FRA technique was employed. The result was not found when the PSD method was used. Similarly, the Taylor series for variance in the real impedance was equal to the corresponding series for the imaginary impedance when the FRA technique was used to calculate the impedance spectra. The equality of the Taylor series for variances in the real and imaginary impedances did not hold when the PSD technique was employed. The condition on the rectangular coordinate variance vector for equality of the Taylor series for the impedance variances was observed when the measurement was made using the FRA technique. This condition was not observed when the phase-sensitive detection technique was used. The experimental evidence and the simulation results demonstrate that the variances in the real and imaginary impedances are equal when the FRA technique is employed in the simulation or experimental instrumentation. Therefore, the results of this chapter suggest that

equations (6.44)-(6.48) are satisfied when frequency response analysis is used to measure impedance spectra.

The frequency-dependent error structure of impedance spectra is a function of the manner in which noise is introduced into the integrated signals, not the distribution of noise introduced into them. The distribution of noise in the response signal will be a function of frequency if that noise has propagated through the system from the perturbation signal. In such a case, the distribution of noise in the response would be frequency dependent (or dependent upon the impedance), while the distribution of noise in the perturbation would be independent of the impedance. Thus, the distribution of noise in the complex impedance would have a frequency-dependent error structure because the ratio of a frequency-dependent function to a frequency-independent function would be frequency-dependent.

Table 6.1: Student's t-tests for trivial solution conditions for equality of variance in the real and imaginary impedances described by the linear Taylor series expansion. Calculations were conducted for the CASE 1 scenario, noise added to the input and output signal, with output noise including input noise transformed by the system.

			PSD		FRA	
RATIO	α	ν	t	$t/t_{\alpha/\nu,n-1}$	t	$t/t_{\alpha/\nu,n-1}$
$\sigma^2_{Z_r}/\sigma^2_{Z_j}=1$	0.05	2	0.739	0.372	0.559	0.281
$\sigma^2_{V_r}/\sigma^2_{V_j}=1$	0.05	2	1.08	0.546	0.612	0.308
$\sigma^2_{I_r}/\sigma^2_{I_j}=1$	0.05	2	24.7	12.4	0.219	0.110
$\sigma_{V_rI_r}/\sigma_{V_jI_j}=1$	0.05	2	5.07	2.55	0.089	0.045
$\sigma_{V_rI_j}/\sigma_{V_jI_r}=-1$	0.05	2	5.69	2.87	1.00	0.506
$\sigma_{V_rV_j}=0$	0.025	1	2.52	1.11	0.782	0.343
$\sigma_{I_rI_j}=0$	0.025	1	5.24	2.30	1.23	0.538

Table 6.2: Student's t-tests for trivial solution conditions for equality of variance in the real and imaginary impedances described by the linear Taylor series expansion. Calculations were conducted for the CASE 2 scenario, noise added to the input and output signal, with output noise including input noise transformed by the system. Noise was not added to the current, so there was no variance in the complex current components.

			PSD		FRA	
RATIO	α	ν	t	$t/\ t_{\alpha/\nu,n-1}$	t	$t/\ t_{\alpha/\nu,n-1}$
$\sigma^2_{Z_r}/\sigma^2_{Z_j}=1$	0.05	2	0.995	0.501	0.799	0.402
$\sigma^2_{V_r}/\sigma^2_{V_j}=1$	0.05	2	3.24	1.63	0.370	0.186
$\sigma^2_{I_r}/\sigma^2_{I_j}=1$	0.05	2	-	-	-	-
$\sigma_{V_rI_r}/\sigma_{V_jI_j}=1$	0.05	2	-	-	-	-
$\sigma_{V_rI_j}/\sigma_{V_jI_r}=-1$	0.05	2	-	-	-	-
$\sigma_{V_rV_j}=0$	0.025	1	3.63	1.59	1.227	0.538
$\sigma_{I_rI_j}=0$	0.025	1	-	-	-	-

Table 6.3: Student's t-tests for trivial solution conditions for equality of variance in the real and imaginary impedances described by the linear Taylor series expansion. Calculations were conducted for the CASE 3 scenario, noise added to the input and output signal, with output noise including input noise transformed by the system.

			PSD		FRA	
RATIO	α	ν	t	$t/t_{\alpha/\nu,n-1}$	t	$t/t_{\alpha/\nu,n-1}$
$\sigma^2_{Z_r}/\sigma^2_{Z_j}=1$	0.05	2	3.77	1.90	2.93	1.47
$\sigma^2_{V_r}/\sigma^2_{V_j}=1$	0.05	2	0.649	0.327	0.890	0.448
$\sigma^2_{I_r}/\sigma^2_{I_j}=1$	0.05	2	21.3	10.7	1.31	0.658
$\sigma_{V_rI_r}/\sigma_{V_jI_j}=1$	0.05	2	4.74	2.39	1.68	0.846
$\sigma_{V_rI_j}/\sigma_{V_jI_r}=-1$	0.05	2	4.55	2.29	.750	0.377
$\sigma_{V_rV_j}=0$	0.025	1	2.13	0.935	0.653	0.287
$\sigma_{I_rI_j}=0$	0.025	1	4.46	1.96	0.208	0.0913

Table 6.4: Student's t-tests for difference in variances in impedance magnitude and phase angle and for the cross-covariance between the impedance magnitude and phase angle equal to zero.

				PSD		FRA	
RATIO	CASE	α	ν	t	$t/t_{\alpha/\nu,n-1}$	t	$t/t_{\alpha/\nu,n-1}$
$\sigma^2_{\lvert Z\rvert}-\lvert Z\rvert^2\sigma^2_{\phi}=0$	1	0.05	2	11.0	5.54	2.41	1.21
$\sigma_{\lvert Z\rvert\phi}=0$	1	0.025	1	2.19	0.963	1.50	0.659
$\sigma^2_{\lvert Z\rvert}-\lvert Z\rvert^2\sigma^2_{\phi}=0$	2	0.05	2	23.6	11.9	0.702	0.353
$\sigma_{\lvert Z\rvert\phi}=0$	2	0.025	1	3.30	1.45	1.67	0.734
$\sigma^2_{\lvert Z\rvert}-\lvert Z\rvert^2\sigma^2_{\phi}=0$	3	0.05	2	22.6	11.4	1.03	0.307
$\sigma_{\lvert Z\rvert\phi}=0$	3	0.025	1	1.51	0.135	0.0321	0.0141

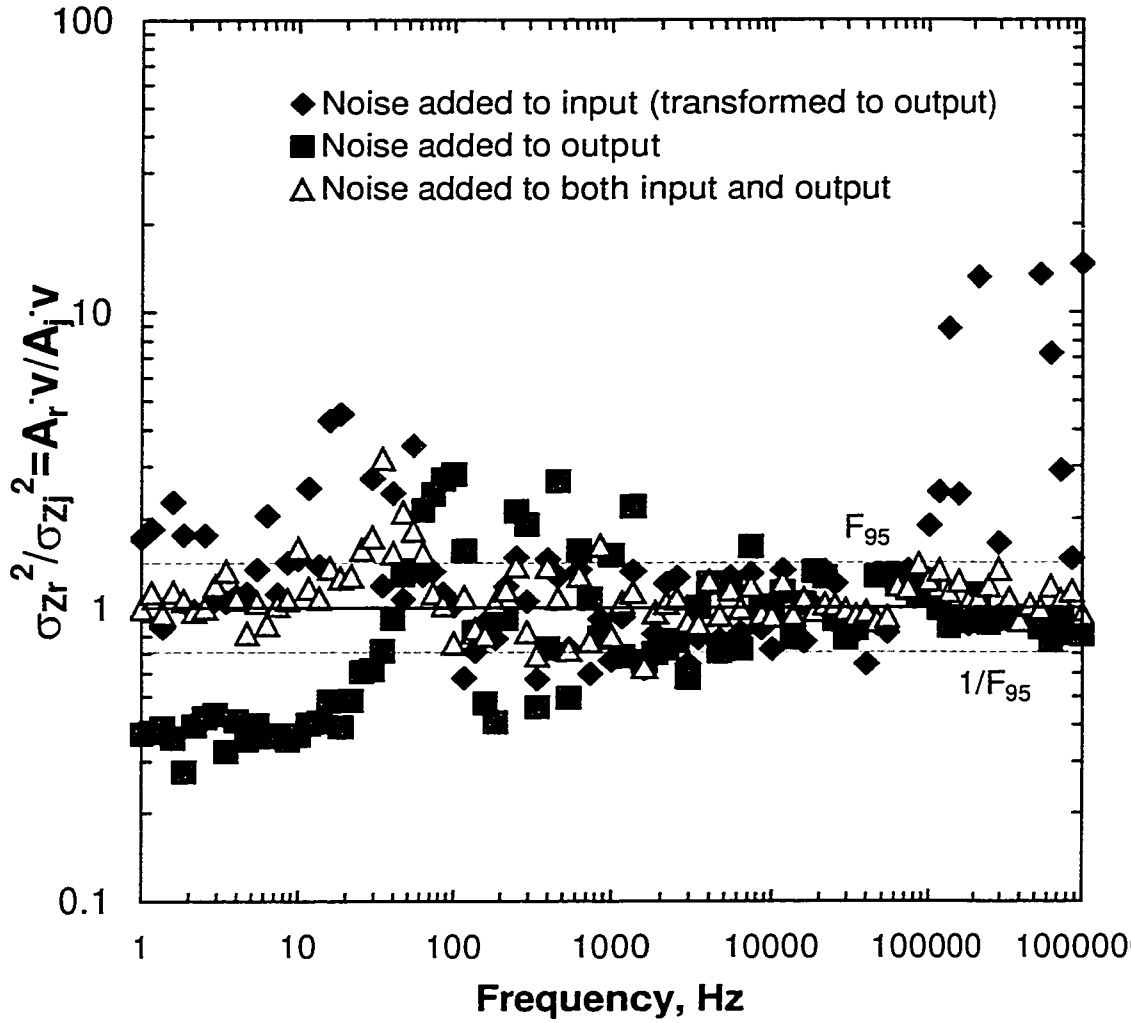

Figure 6.1: Ratio of Taylor series for variance in the real impedance to variance in the imaginary impedance when phase-sensitive detection is used to calculate the impedance. Note that in general the ratio does not satisfy the F-test for 5%. Therefore for all three cases, there is less than a 5% probability that the Taylor series for the variances are equal.

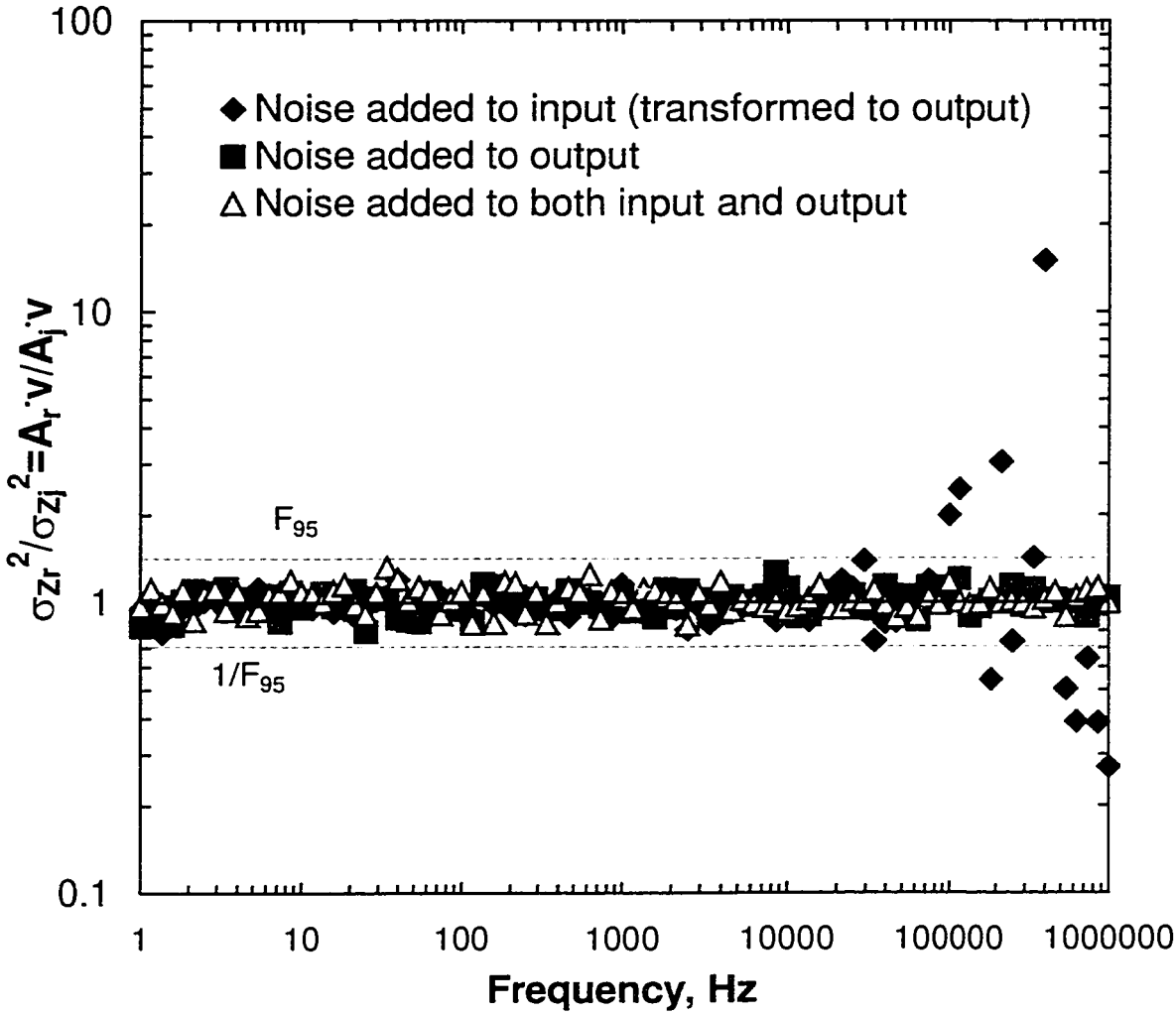

Figure 6.2: Ratio of Taylor series for variance in the real impedance to variance in the imaginary impedance when frequency response analysis is used to calculate the impedance. Note that in general the ratio does satisfy the F-test for 5%. Therefore for all three cases, there is less than a 5% probability that the Taylor series for the variances are not equal.

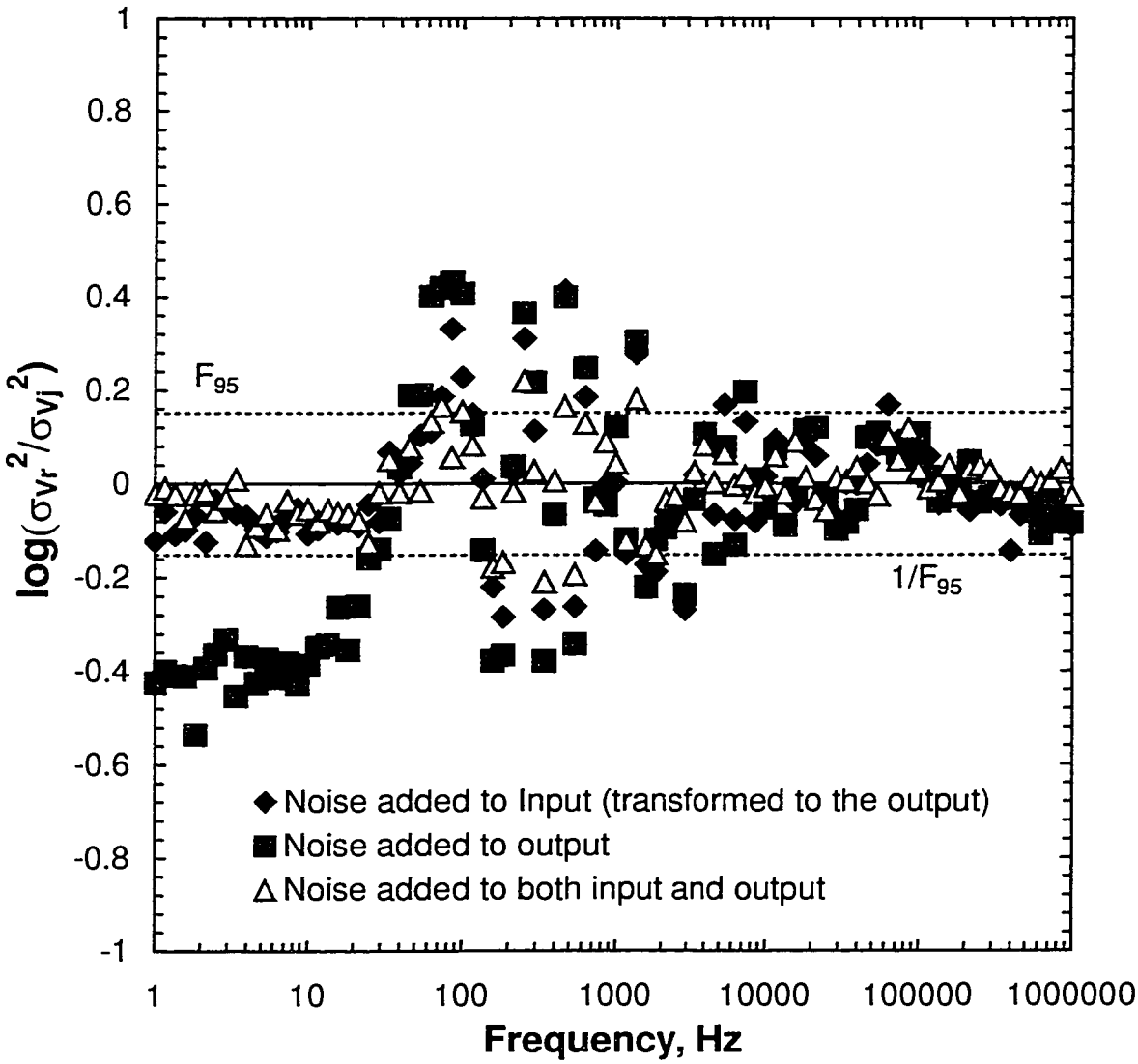

Figure 6.3: Ratio of variance in the real voltage measurement to the variance in the imaginary voltage measurement. Calculation was made using the phase-sensitive detection technique. Note that the ratios for all three cases often fall outside the F-test 5% probability limits. Therefore, there is less than 95% probability that the variances are not equal.

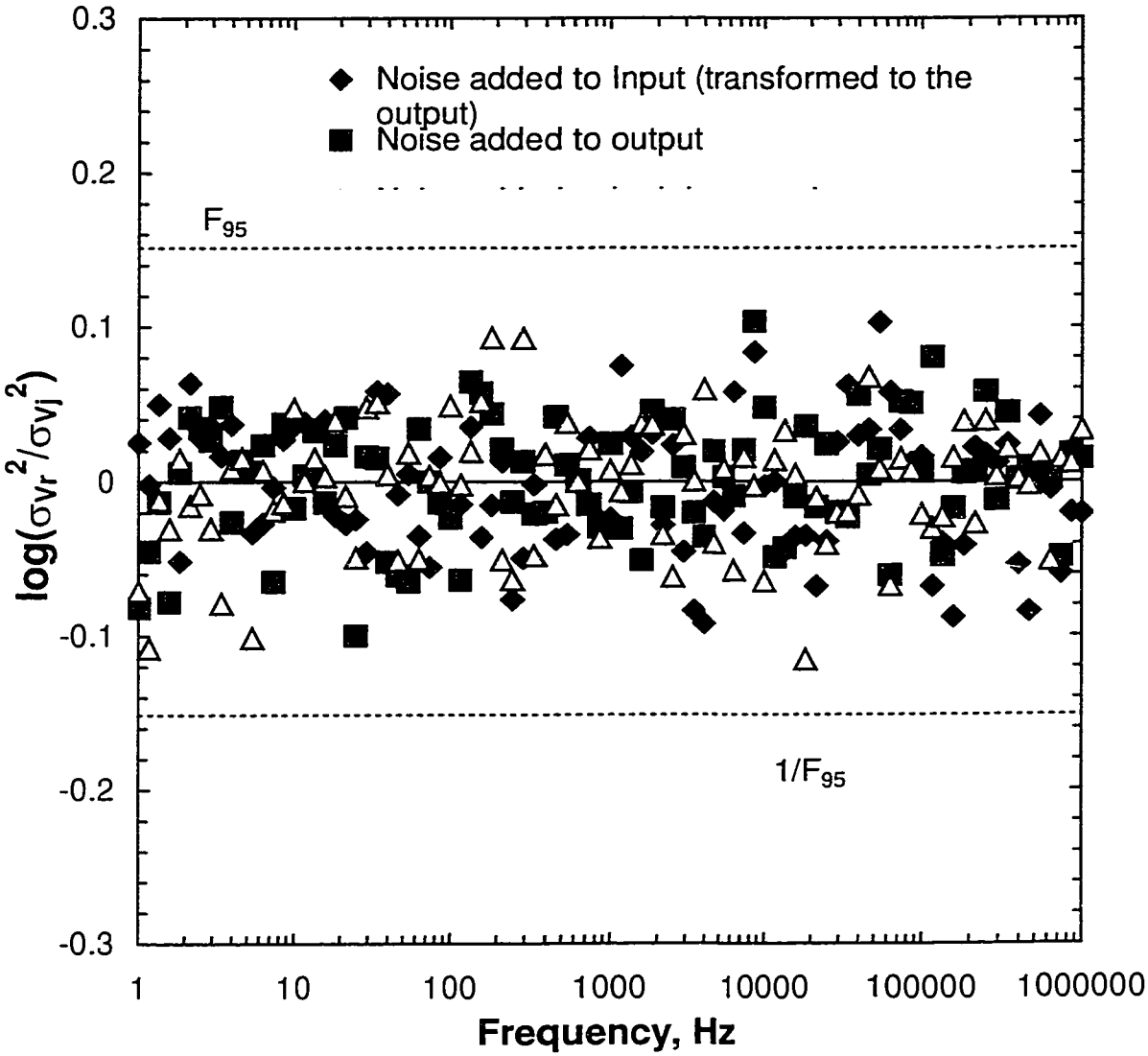

Figure 6.4: Ratio of variance in the real voltage measurement to the variance in the imaginary voltage measurement. Calculation was made using the FRA technique. Note that the ratios for all three cases all fall inside the F-test 5% probability limits. Therefore, there is less than 5% probability that the variances are not equal.

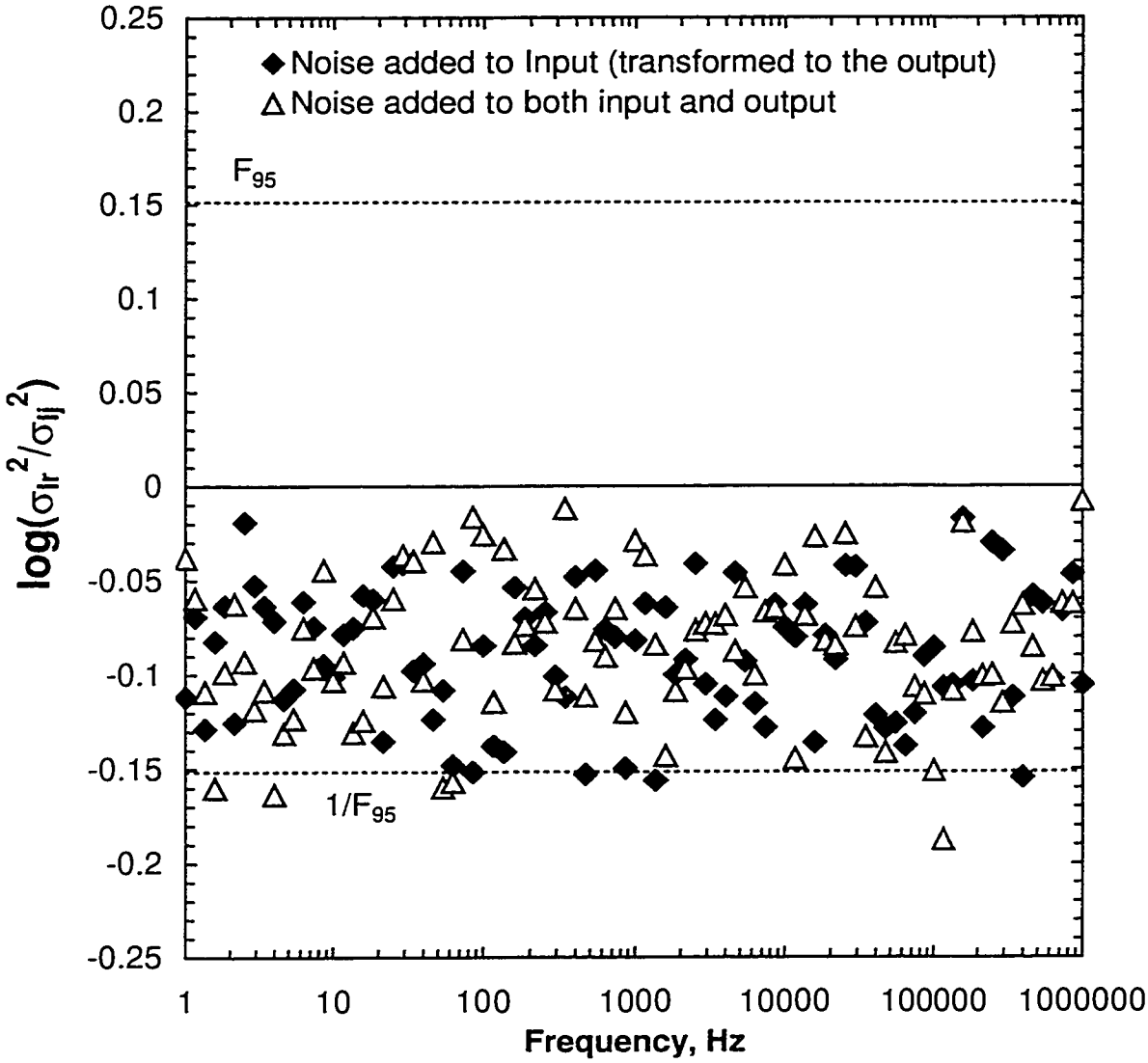

Figure 6.5: Ratio of variance in the real current measurement to the variance in the imaginary current measurement. Calculation was made using the phase-sensitive detection technique. Note that the ratios for all three cases often fall outside the F-test 5% probability limits. Therefore, there is less than 95% probability that the variances are not equal.

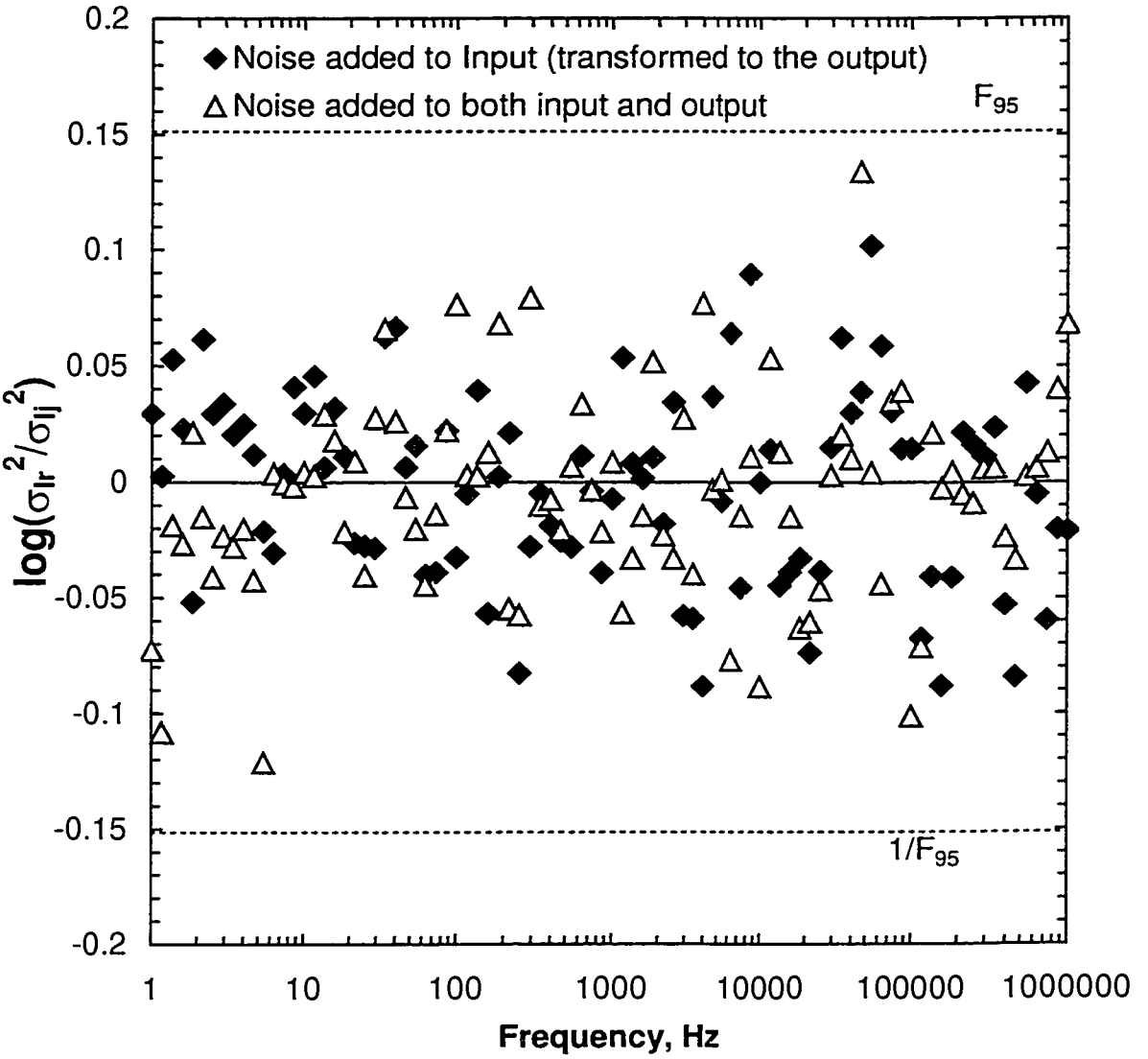

Figure 6.6: Ratio of variance in the real current measurement to the variance in the imaginary current measurement. Calculation was made using the FRA technique. Note that the ratios for all three cases all fall inside the F-test 5% probability limits. Therefore, there is less than 5% probability that the variances are not equal.

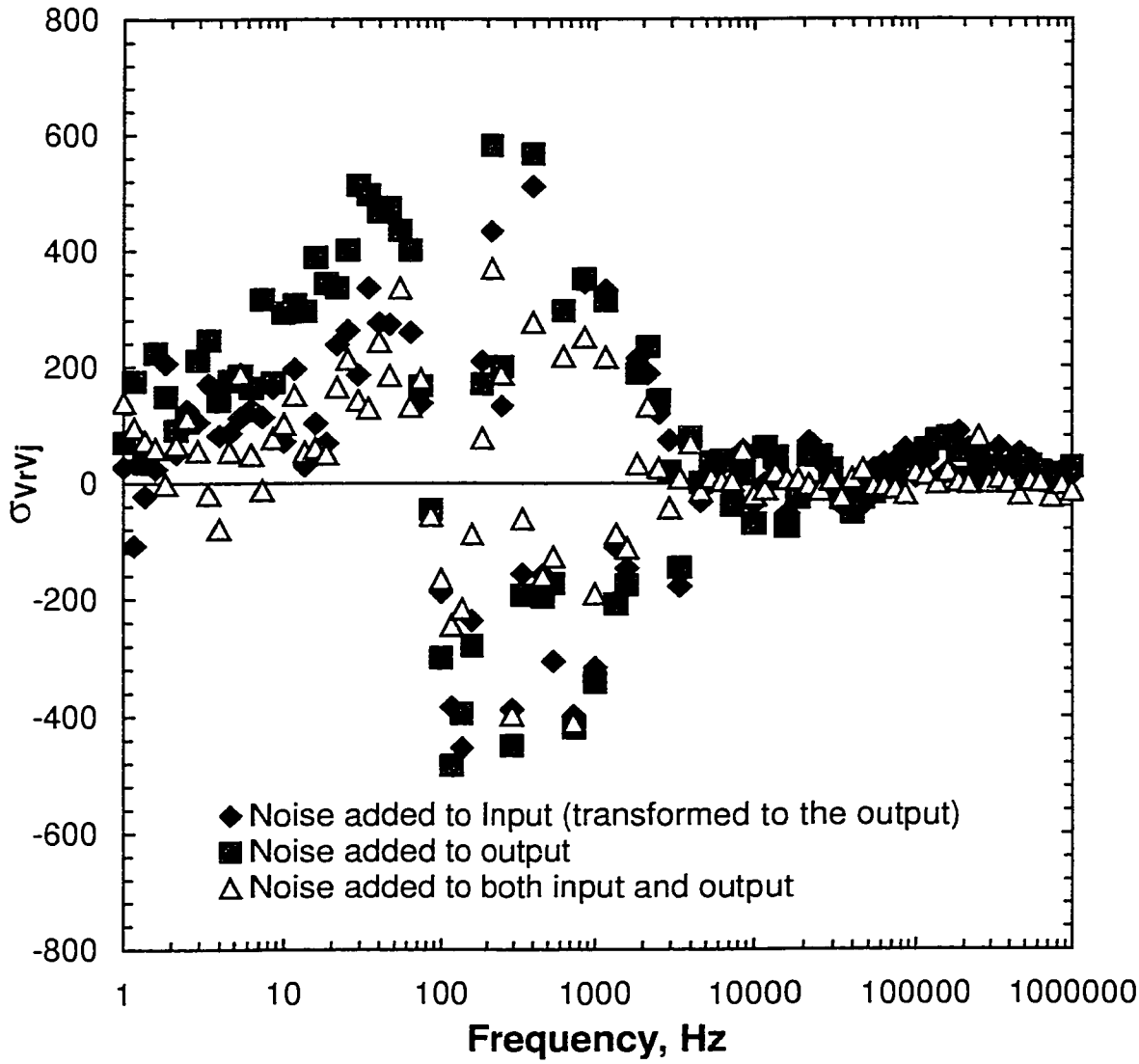

Figure 6.7: Covariance between real and imaginary voltage components calculated using phase-sensitive detection. The trivial solution to the equality of variances in the complex impedance requires that this covariance be equal to zero.

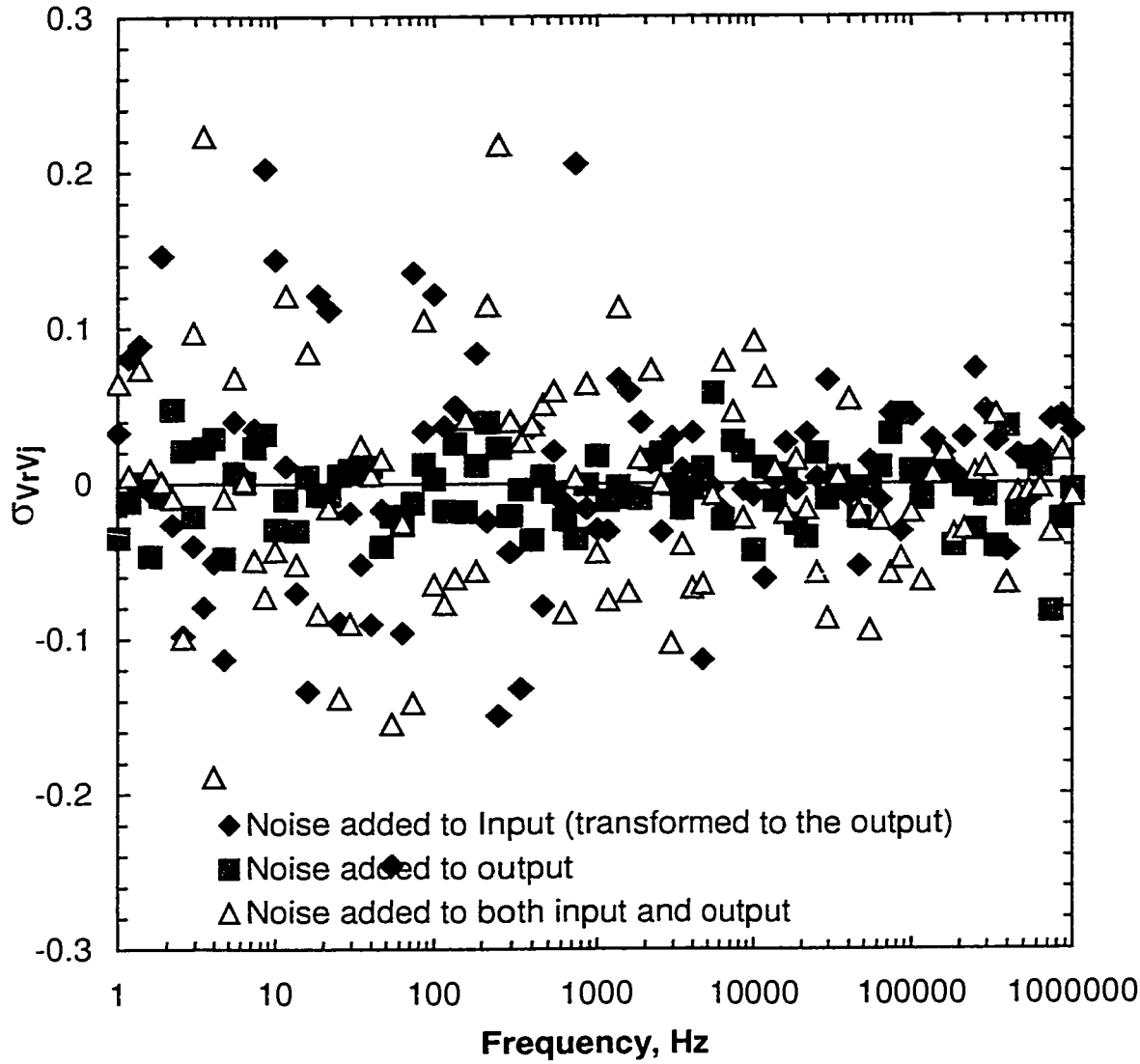

Figure 6.8: Covariance between real and imaginary voltage components calculated using frequency response analysis. The trivial solution to the equality of variances in the complex impedance requires that this covariance be equal to zero.

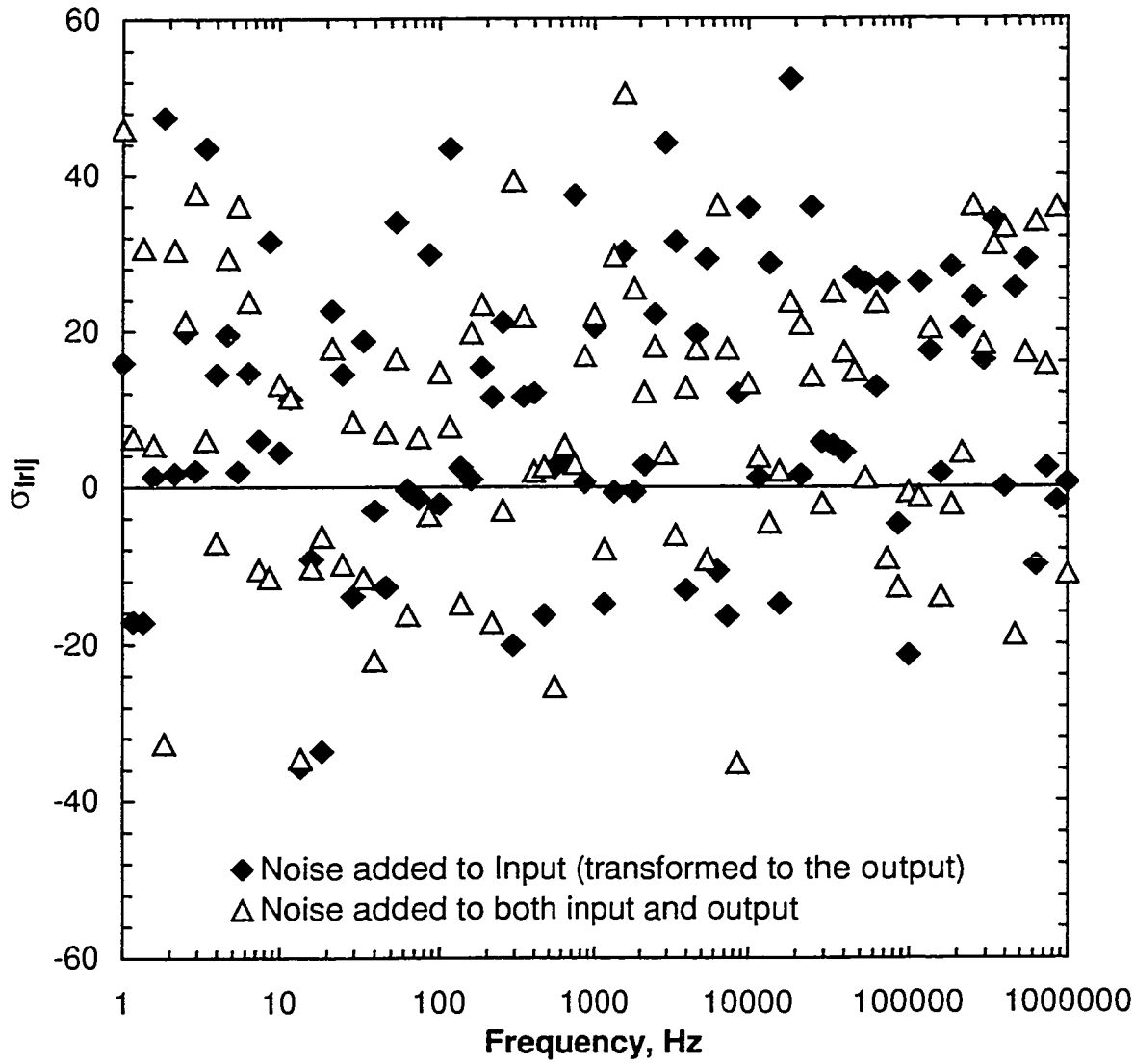

Figure 6.9: Covariance between real and imaginary current components calculated using phase-sensitive detection. The trivial solution to the equality of variances in the complex impedance requires that this covariance be equal to zero.

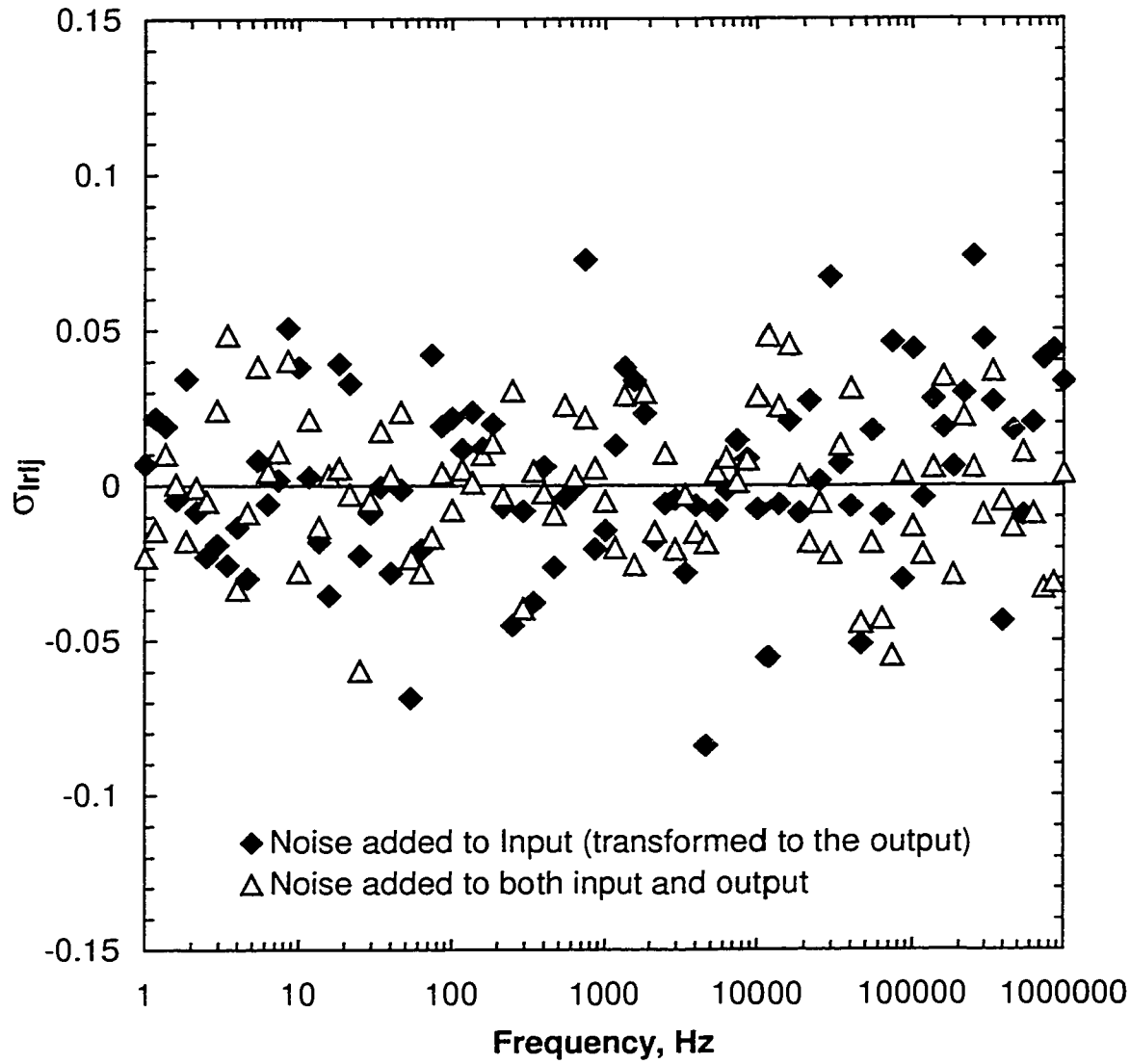

Figure 6.10: Covariance between real and imaginary current components calculated using frequency response analysis. The trivial solution to the equality of variances in the complex impedance requires that this covariance be equal to zero.

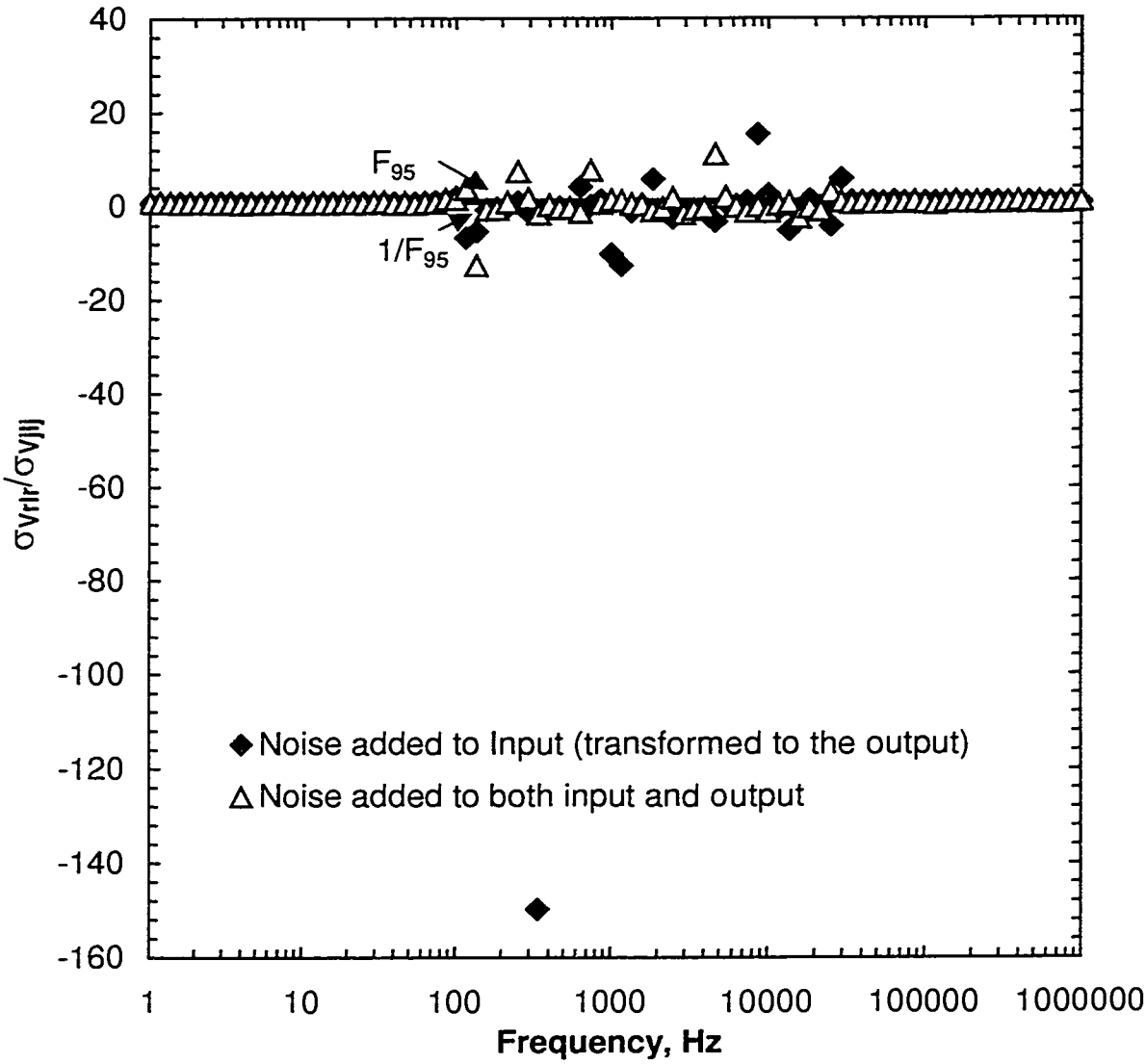

Figure 6.11: Ratio of cross-covariances between real current and voltage to imaginary current and voltage components calculated using phase-sensitive detection. The trivial solution to the equality of variances in the complex impedance requires that this ratio be unity. For all three cases, the ratios generally fall outside the F-test 5% probability limits. There is 95% probability that these cross-covariances are not equal at those frequencies.

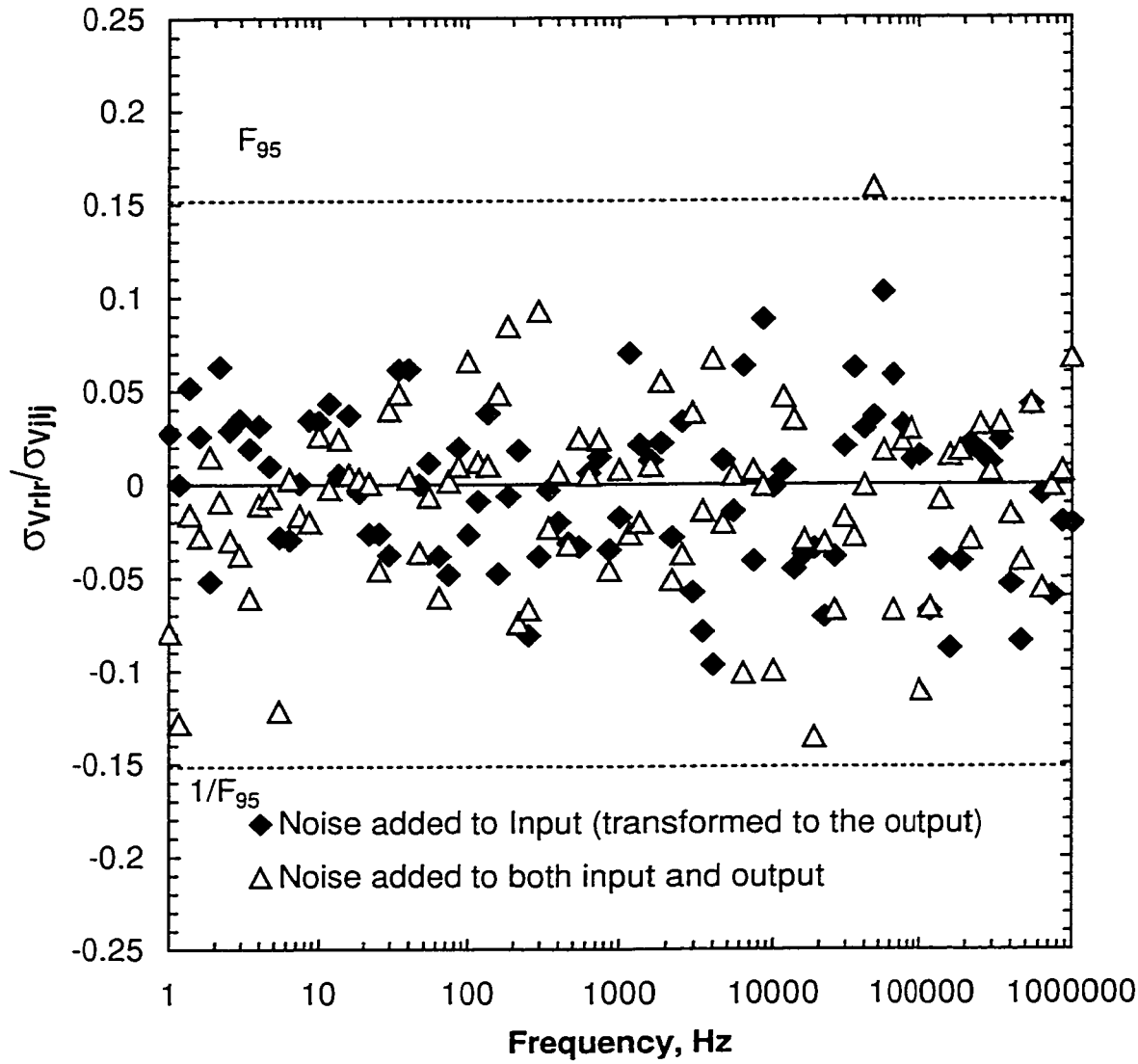

Figure 6.12: Ratio of cross-covariances between real current and voltage to imaginary current and voltage components calculated using frequency response analysis. The trivial solution to the equality of variances in the complex impedance requires that this ratio be unity. For all three cases, the ratios generally fall inside the F-test 5% probability limits. There is 5% probability that these cross-covariances are not equal at those frequencies.

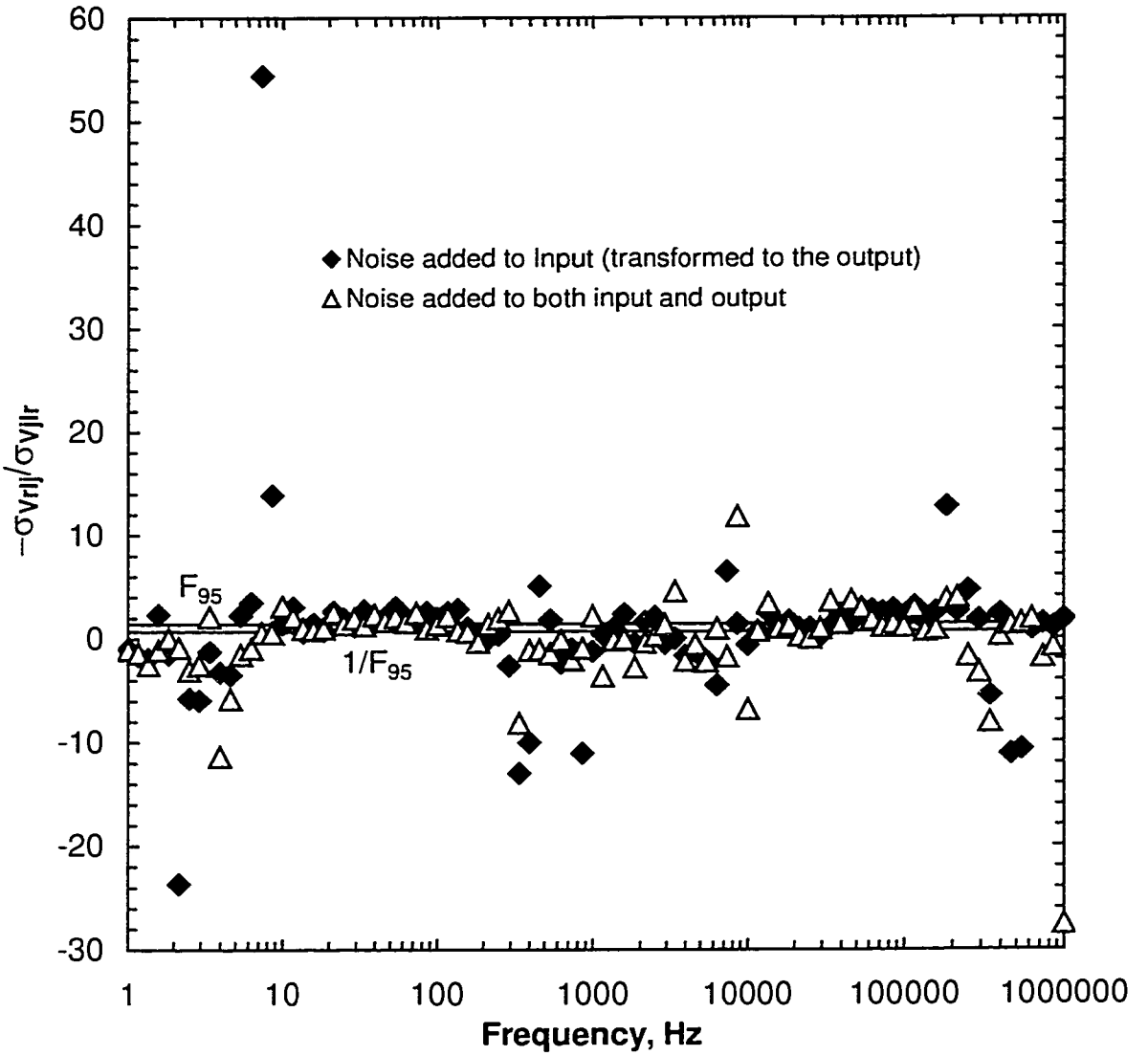

Figure 6.13: Ratio of cross-covariance between real voltage and imaginary current to cross-covariance between imaginary voltage and real current components calculated using phase-sensitive detection. The trivial solution to the equality of variances in the complex impedance requires that this ratio be the negative of the other. For all three cases, the ratios generally fall outside the F-test 5% probability limits. There is 95% probability that these cross-covariances are not equal at those frequencies.

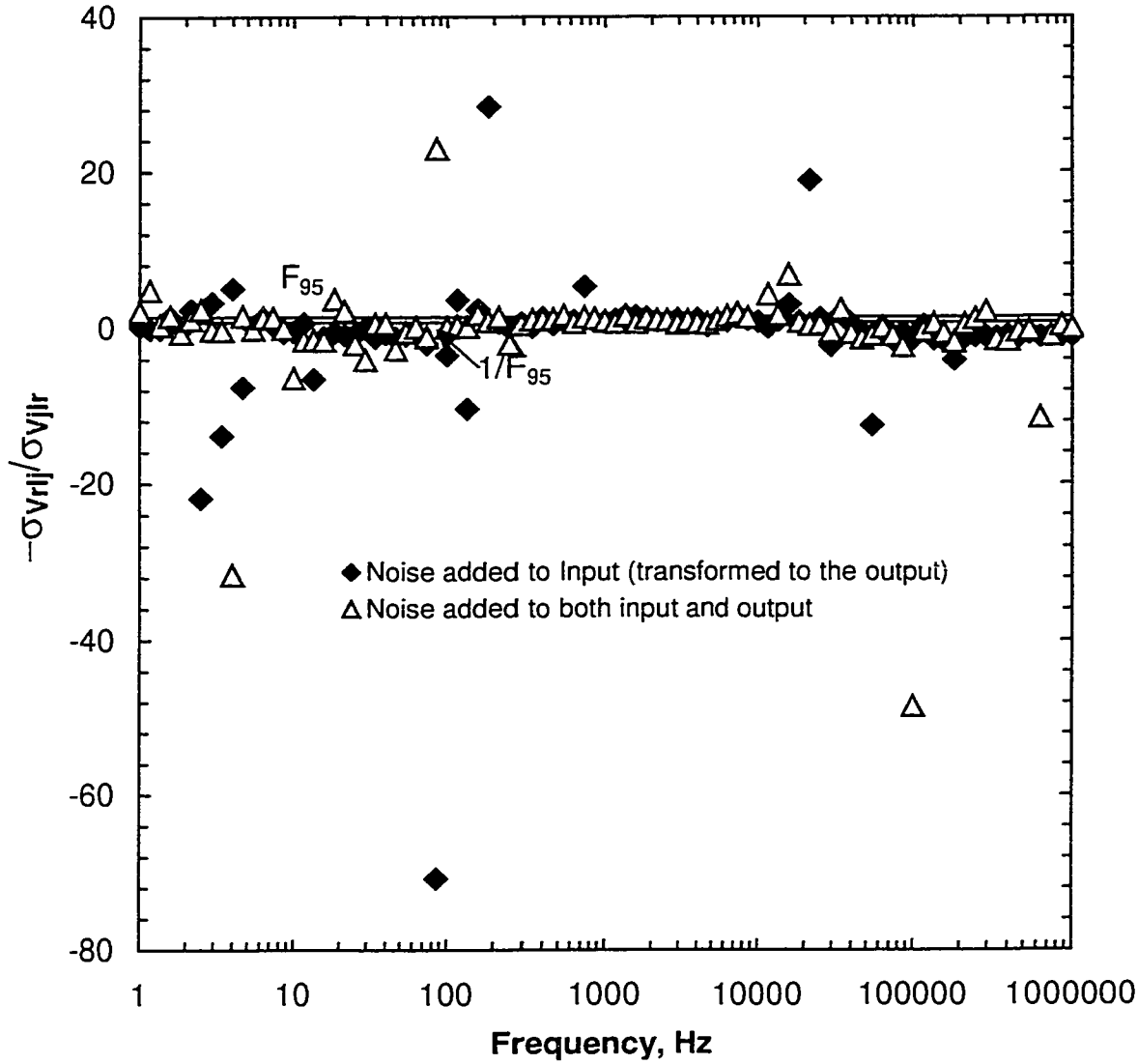

Figure 6.14: Ratio of cross-covariance between real voltage and imaginary current to cross-covariance between imaginary voltage and real current components calculated using frequency response analysis. The trivial solution to the equality of variances in the complex impedance requires that this ratio be the negative of the other. For all three cases, the ratios generally fall outside the F-test 5% probability limits. There is 95% probability that these cross-covariances are not equal at those frequencies.

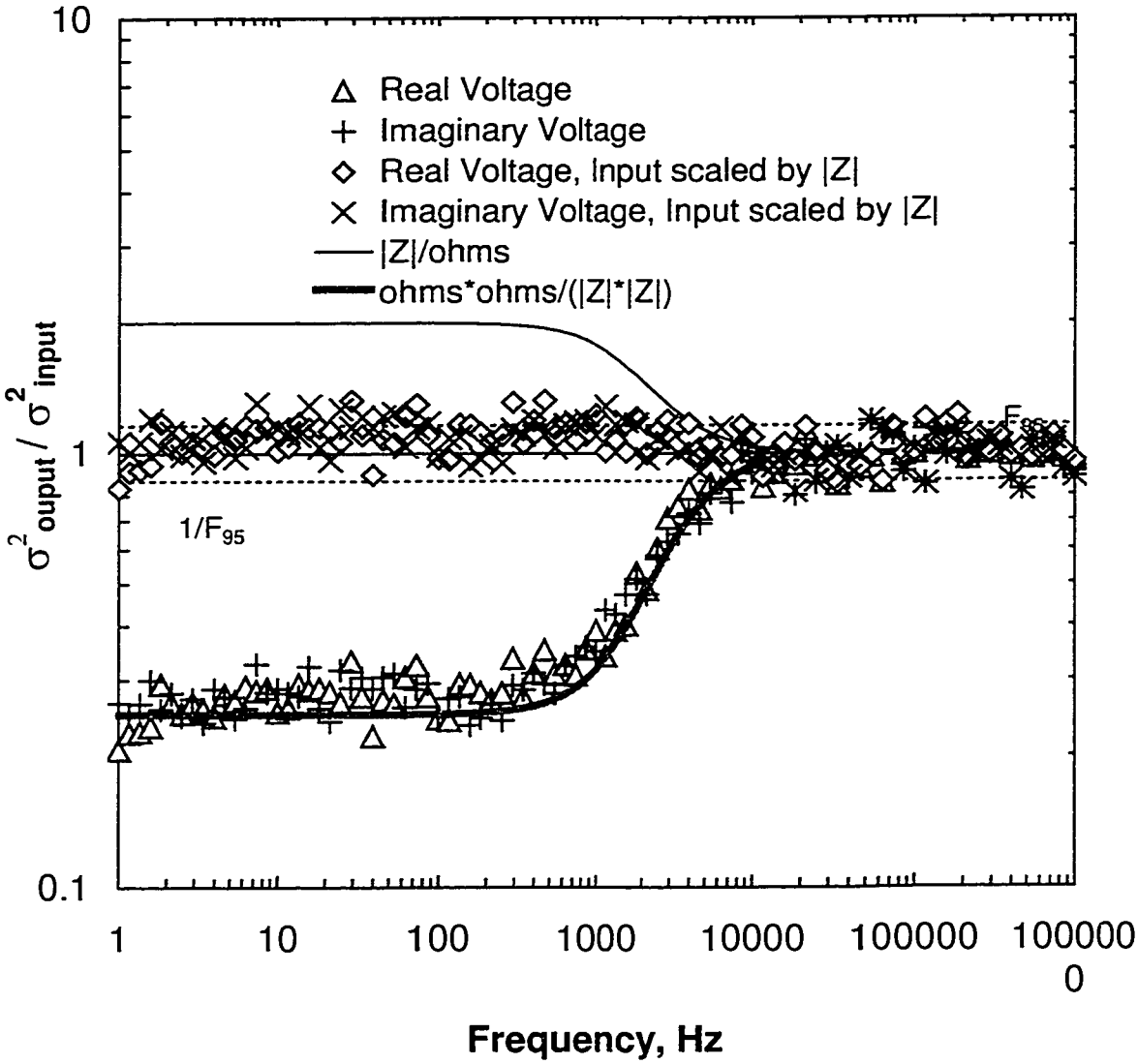

Figure 6.15: Ratios of variances in voltage components for CASE 2 to variances in voltage components for CASE 1, in which Gaussian noise was introduced into the signals. These are the ratios of additive noise to noise transformed by the system. The ratios are clearly frequency dependent, and correlated to the reciprocal of the square of the impedance magnitude. The ratios scaled by the reciprocal of the square of the impedance magnitude are generally scattered about unity.

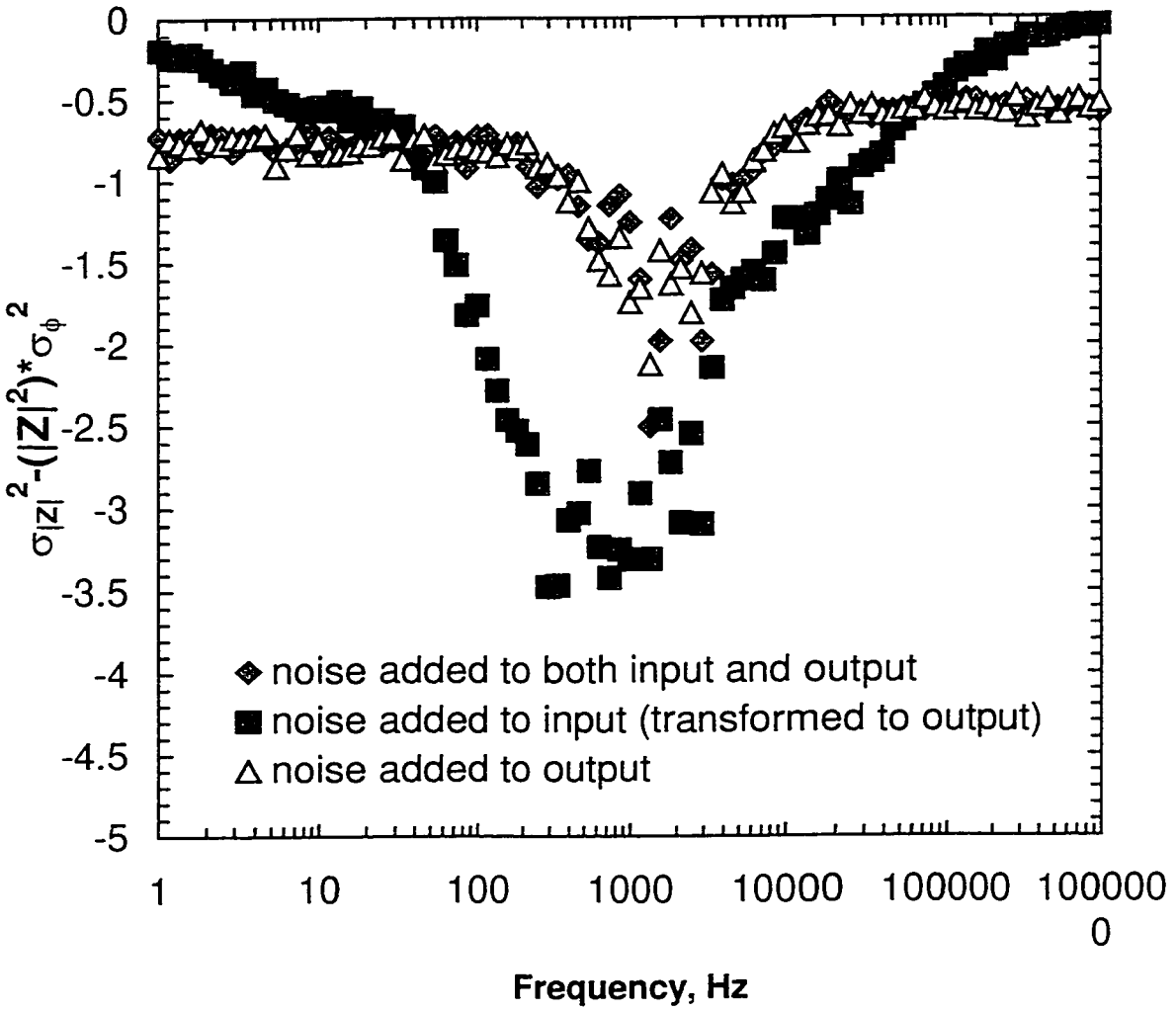

Figure 6.16: Difference in variances of impedance magnitude and phase angle for PSD calculation. The difference should be equal to zero over the spectrum.

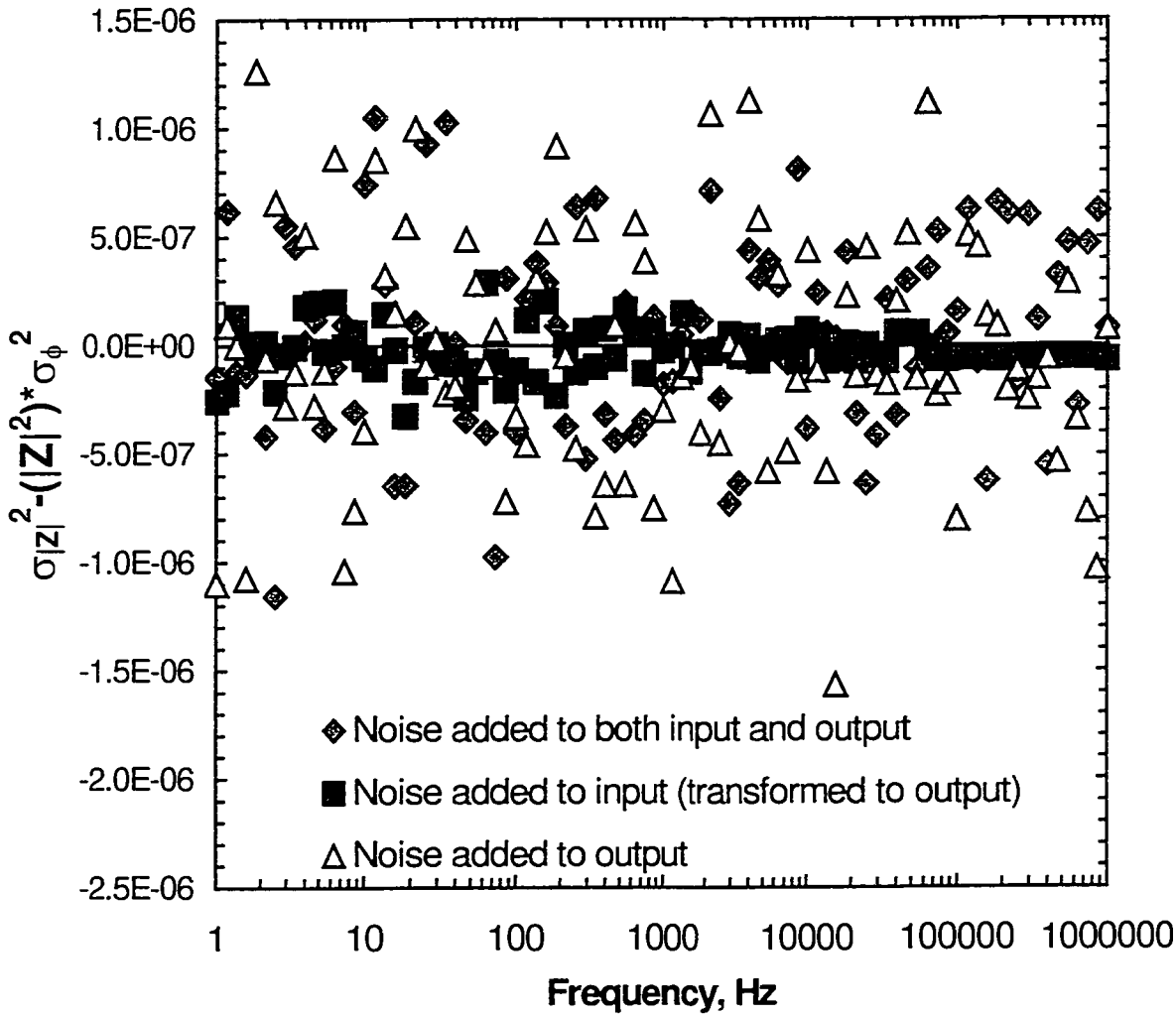

Figure 6.17: Difference in variances of impedance magnitude and phase angle for FRA calculation. The differences are scattered about zero over the spectrum.

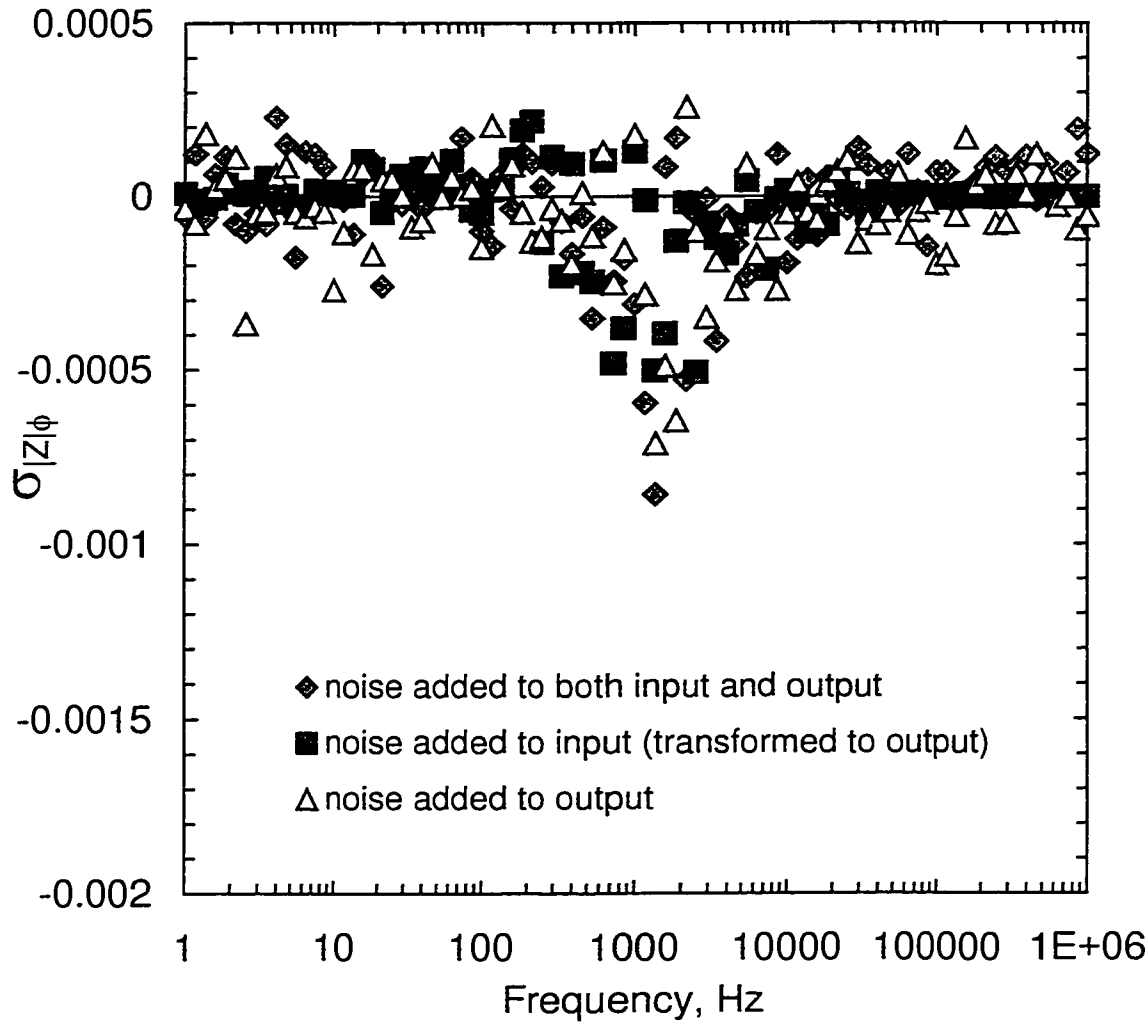

Figure 6.18: Cross-covariance between impedance magnitude and phase angle for PSD calculation. The cross-covariance should be equal to zero over the spectrum for the imaginary part of the Taylor series expansion for variance in the real and imaginary impedance to be equal to zero.

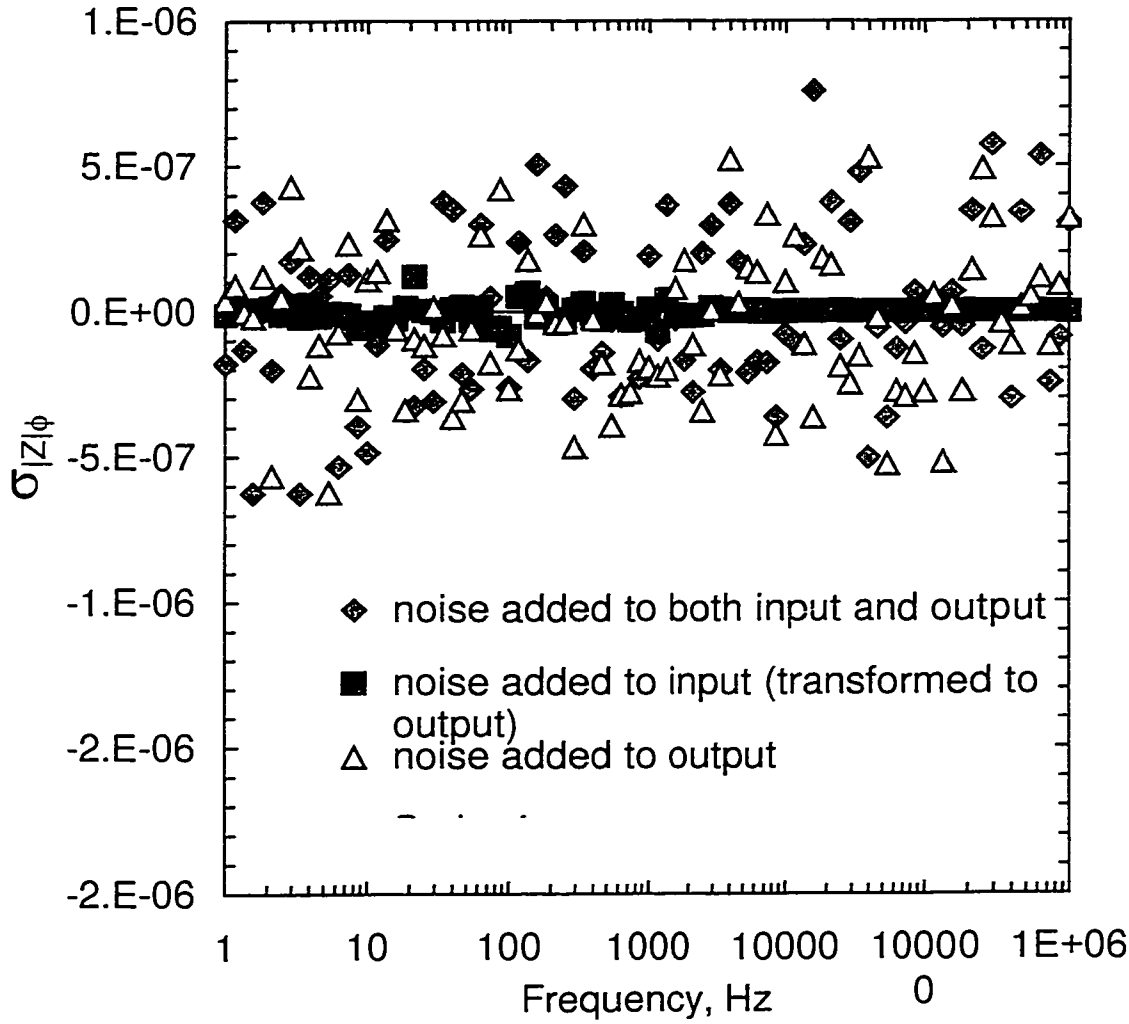

Figure 6.19: Cross-covariance between impedance magnitude and phase angle for FRA calculation. The cross-covariance should be equal to zero over the spectrum for the imaginary part of the Taylor series expansion for variance in the real and imaginary impedance to be equal to zero.

CHAPTER 7
PROPAGATION OF COLORED NOISE IN TIME-DOMAIN SIGNALS

Orazem and co-workers have demonstrated that as a result of the conditions necessary for the Kramers-Kronig Relations to apply to complex impedance spectra, the variance in stochastic errors in the real impedance is equal to the variance in the stochastic error in the imaginary impedance.[9] One assumption involved in that derivation is that the distribution of stochastic errors in the complex impedance is normal, or Gaussian.[9] Other researchers, however, have conducted research on the transformation of colored, or skewed, noise in the complex impedance components through the Kramers-Kronig relations.[17] If the distribution of frequency-domain errors can be non-Gaussian, then the derivation made by Durbha *et al.*[9] only holds for a subset of all impedance measurements. Also, if the distribution of errors in impedance spectra is not Gaussian, then the distribution is not fully defined by a mean and standard deviation. For such distributions of impedance errors, the variance in the impedance measurement would not be an appropriate choice of CNLS regression weighting strategy.[6-9,11,105,106,109-114,118]

Thus, it is necessary to determine if colored, or skewed, noise exists in impedance spectra. It has been shown in Chapter 5 that Gaussian noise in the time-domain propagates into Gaussian errors in the frequency-domain. If colored noise exists in the frequency-domain impedance measurements, then it must propagate from a non-Gaussian distribution of noise in the time-domain current and voltage signals. In this chapter, the

propagation of colored distributions of time-domain noise into the frequency-domain will be discussed. The equivalence of variances in the real and imaginary impedances[6-9,74,118] will be shown to hold for measurements conducted using the FRA technique on signals with colored noise. It will be shown that as a result of a fundamental theorem of statistics, frequency-domain errors will be normally distributed, even if the distribution of time-domain noise is not Gaussian.

7.1 Simulated Measurement of Complex Impedance

The calculation methodology described in Sections 1 and 2 of Chapter 5 was used to determine the complex impedance for signals with introduced colored, or skewed, additive noise. These errors were not uniformly distributed around the mean (see Figure 7.1). In this work, the time-domain colored noise contribution has a coefficient of skewness[122] on the order of 750. A Gaussian distribution would have a null coefficient of skewness.

A series of simulations were performed to attempt to map further the nature of the error structure of impedance measurements. Three categories of simulations were conducted - CASE 1: adding noise only to the perturbation signal (thereby introducing noise transformed by the system into the response signal), CASE 2: adding noise only to the response signal, and CASE 3: adding noise to both the perturbation and response signals. The range of values for the variances in the real and imaginary impedance is listed in Table 7.1. The student's t-test results for equality of variances of the stochastic errors in the real and imaginary impedance are reported in Table 7.2. The colored distribution was constructed by first calculating the absolute value of a normal distribution with a standard deviation of 4% of the input signal amplitude. A normal distribution with a standard deviation of 2% but with a mean of 2% of the input

amplitude was added to it. Finally a normal distribution with a standard deviation of 1% of the input amplitude with a mean of 1% of the input amplitude was added to the noise signal.

The frequency-domain errors were normally distributed for each calculation technique. An example of a distribution of frequency-domain errors at a single frequency of impedance measurement is presented in Figure 7.2. The errors in impedance at each frequency were normally distributed for each measurement technique.

As seen for simulations with normally distributed time-domain errors (presented in Chapter 5), frequency-domain stochastic errors were on the machine level of precision for the simulation cases in which noise was added only to the input perturbation (CASE 1) and the impedance was calculated using either the FRA or Lissajous parameterization techniques. The PSD calculation for the same simulated signal set resulted in frequency-domain stochastic errors that were significant. The variance of these errors in the real impedance were not equal to the variance of the errors in the imaginary impedance as qualified by the F-test and student's t-test (see Table 7.2).

The errors in the impedance determined from the other two simulation cases were of significant order. For the two FRA and the Lissajous parameterization calculations, the variance in the stochastic errors in the real impedance were equal to the variance in the stochastic errors in the imaginary impedance. The ratio of the variances is plotted for the FRA calculation of CASE 3 in Figure 7.3. The ratio is generally scattered around unity, and most points fall within the one-percent level of significance. Thus, there is 99% confidence that the hypothesis that the variances are unequal is false. The ratio is normally distributed over frequency as shown in Figure 7.4. Thus, the expectations of the

variances are equivalent over the spectrum for the FRA measurement technique. The variances were not equal when the PSD calculation was applied to the same set of perturbation-response signals. The ratio of the variances is plotted for the PSD calculation of CASE 3 in Figure 7.5. The ratio is not scattered around unity, and most points fall outside the one-percent level of significance. Thus, there is 99% confidence that the hypothesis that the variances are unequal is true. The ratio is normally distributed, as shown in Figure 7.6, but not about zero. Thus, the expectations of the variances are not equivalent over the spectrum for measurement using the PSD technique.

7.2 Taylor Series

In the previous chapter, the Taylor series expansions for variance in the components of the complex impedance in terms of the variances in the complex current and voltage were derived. The calculation methodology described in Section 4 of the Chapter 6 was repeated, but the distribution of noise introduced into the current and voltage signals was colored. This colored noise was constructed in the same manner that was described in the previous section. The Taylor series simulations were conducted for the same three cases of noise introduction described in the previous section. Only the FRA technique was tested, since the previous studies confirmed that the PSD method produced errors that were normally distributed although the variances of those real and imaginary errors were not equal.

In all three cases, the conditions defined by equations (6.44)-(6.48) of Chapter 6 were generally observed for the variance vector and equation (6.43) of the same chapter (equivalence of variances in real and imaginary impedances) was satisfied. Table 7.3 provides student's t-test ratio results applied to the observed condition for the equality of the calculated variance vector and for the respective case numbers. All of the ratios were

less than one, except for some in CASE 1, and some of the cross-covariance conditions. The CASE 1 exceptions were most likely the result of machine errors due to extremely small noise levels associated with the calculation. The cross-covariance exceptions were most likely also the result of machine errors.

The ratio of the Taylor series for variance in the real impedance to the Taylor series for variance in the imaginary impedance as a function of frequency is plotted in Figure 7.7. Note that in general the ratio does satisfy the F-test for a five-percent level of significance. Therefore for all three cases, there is less than a five-percent probability that the Taylor series for the variances are not equal. The ratio might not have been equal to unity at high frequency for CASE 3, since the ratio was widely scattered at high frequency. The extreme scatter at high frequency might be the result of loss-of-significance machine errors or of the lack of higher order terms in the Taylor series expansions. The ratio of variances in the complex voltage is shown in Figure 7.8 as a function of frequency. The ratio of variances in the complex current as a function of frequency is shown in Figure 7.9. The F-test probability lines (five-percent level of significance) are also plotted. For both voltage and current, the ratios generally fell within the F-test bounds. Therefore, the variances in the real and imaginary components of each signal were equal. The covariances in voltage are shown in Figure 7.10 and in the covariances in current are shown in Figure 7.11. Both covariances were scattered uniformly about zero. The student's t-test (see Table 7.3) was employed to verify that the mean values of these covariances were equal to zero. The ratio of real cross-covariance to imaginary cross-covariance is plotted as a function of frequency in Figure 7.12. For all three cases, the ratios generally fell inside the F-test 5% probability limits. Therefore,

there is a 5% probability that these cross-covariances are not equal at those frequencies. Finally, the ratios of cross-covariances between the real voltage and imaginary current and imaginary voltage and real current are shown in Figure 7.13. The ratio was generally scattered around one, although many values of the ratio fell outside the F-test 5% probability limits. Therefore, the probability that the two cross-covariances were not equal was greater than five-percent.

Another interesting result from these simulations is that, as was presented in Chapter 6, the noise level in the constituent signals was frequency-dependent due to the method of introduction of noise into those signals. The noise level in the current was the same for the two of the three cases in which noise was added to the current. However, the noise level in the complex voltage was highly dependent upon the manner in which noise is introduced. In Figure 7.14, the ratio of the variances in the real and imaginary voltage for CASE 1 with additive colored noise to the same variances for CASE 2 with additive colored noise are plotted as functions of frequency. The ratio was a function of frequency as was observed in Chapter 6 for signals with additive errors that were normally distributed. The impedance magnitude, and the reciprocal of the square of the impedance magnitude are also plotted as a function of frequency. The ratio was a function of the impedance magnitude, and was scaled by the reciprocal of the square of the impedance magnitude. This scaling was applied to the ratios, and they are also plotted. Both ratios were generally scattered about unity. Therefore, the nature of the frequency dependent error structure of impedance measurements is a function of the manner in which noise is introduced in the time-domain. The frequency-domain error structure in not dependent upon the distribution of the noise that is introduced into the signals.

7.3 Discussion

The Central Limit Theorem[124] states that the distribution of mean values calculated from random subsets of a population will approach normality as the number of selected subsets approaches infinity. As a result of the Central Limit Theorem, the distribution of errors in the impedance measured at a given frequency must be normal, independent of the distribution of errors in the time-domain signals. If the stochastic errors in impedance spectra are normally distributed and have an expectation of zero, then the variance in the real stochastic errors will be equal to the variance of the imaginary stochastic errors.[17]

The source of error in impedance spectroscopy measurements is time-domain noise associated with the analyzed signals. Each signal (system input and system output) is analyzed using any one of a variety of techniques (e.g., frequency response analysis). All of these techniques have one thing in common: they measure the complex impedance as an average value calculated over several cycles. In order to determine the error in the complex impedance at each frequency, replicate measurements have to be made.

The calculation of the complex impedance for each cycle can be considered to provide the samples of the subset of the overall population of complex impedance values. The mean value of the calculated complex impedances is kept as the observed value. Each replicate scan then provides a mean value of the complex impedance calculated from a different subset of the overall population of impedance values. Thus, by the Central Limit Theorem, the distribution of mean values of the impedance at each frequency should become normal as the number of replicates becomes large.

The integration of a signal over time when divided by the difference between the limits of integration is the average value of that signal. Thus, integration itself acts as the averaging of a small sample of the overall population of impedance values. Even if a

particular measurement technology does not measure over a multiple number of cycles, as long as it employs some form of integration (or regression as in the Lissajous parameterization technique described in Section 1 of Chapter 5), the distribution of replicate measurements of the real and imaginary impedance will be normal. Simulations were conducted in which 500 replicate calculations of the impedance were made at each frequency. Each calculation was made over a single cycle of the current and voltage signals. The replicate impedance values were normally distributed when the introduced noise in the time-domain signals had a Gaussian or colored distribution.

Observed errors at each frequency should be normally distributed. Even if the time domain noise has a colored distribution, the distribution of means of the subsets will be normal. Likewise, the natural distribution of impedance values may not be normal, but the experimentally determined distributions will always appear normal when commercially available measurement technology is employed.

7.4 Conclusions

The character of the noise added in the time-domain does not affect the distribution of noise in the complex spectra. Even if colored, or skewed, noise is introduced into the time-domain signals, the errors in the real and imaginary impedance will Gaussian, as long as replicate measurements of impedance averaged over multiple cycles are made. Thus, in practice, the FRA technique will measure spectra containing errors that are normally distributed and which have variances in the real and imaginary components that are equal. The PSD technique will also measure spectra containing errors that are normally distributed. But the variance of these errors in the real and imaginary components will not necessarily be equal. This is due to the independence of errors in the PSD integrator and phase shift controller.

The results presented in this chapter for propagation of colored time-domain noise further the argument that frequency-domain errors in the complex impedance will be Gaussian. There may be a frequency-dependent noise level in impedance measurements, but the errors will be normally distributed at each frequency and over the spectrum. The hypothesis is supported by the Central Limit Theorem (which holds to most any reasonable approach to conducting impedance spectroscopy measurements), the analysis of synthetic spectra using the Measurement Model Tools developed by Orazem and co-workers,[6-8,17,74,118] the results of Dygas *et al.*,[114] and the analysis of the components of the Taylor series variance vector. Since the variance vector solution to equation (6.43) of Chapter 6 holds for the colored-noise case, it is improbable that studies[17] need to be performed on impedance spectra containing frequency-domain colored noise. The normal distribution of stochastic errors in impedance spectra can be fully described by a mean value and standard deviation. As a result, weighting of CNLS regressions[5-17,74,105,106,109-114,118] by the variance of the measurement of the real and imaginary impedance[6-9,74,114,118] is a reasonable strategy.

Table 7.1: Range of values of variance in stochastic errors for matrix of simulations and assessment techniques. Additive noise level (INPUT and OUTPUT) was 10% of input signal amplitude unless otherwise noted. Transformed noise (Z*INPUT) was proportional to the impedance at the given frequency. (T) Trapezoidal quadrature rule used in FRA calculation. (B) Bode quadrature rule used in FRA calculation.

NOISE ADDED						
INPUT	Z*INPUT	OUTPUT	FRA(T)	FRA(B)	LP	PSD
☒	☒	☐	$10^{-13} \Leftrightarrow 10^{-7}$	$10^{-12} \Leftrightarrow 10^{-6}$	$0 \Leftrightarrow 10^{-15}$	$10^{-6} \Leftrightarrow 10^{-2}$
☐	☐	☒	$10^{-6} \Leftrightarrow 10^{-4}$	$10^{-6} \Leftrightarrow 10^{-4}$	$10^{-6} \Leftrightarrow 10^{-4}$	$10^{-6} \Leftrightarrow 10^{-2}$
☒	☒	☒	$10^{-7} \Leftrightarrow 10^{-4}$	$10^{-6} \Leftrightarrow 10^{-4}$	$10^{-6} \Leftrightarrow 10^{-4}$	$10^{-6} \Leftrightarrow 10^{-2}$

Table 7.2: Student t-test (applied to ratio of variances in stochastic errors in the real and imaginary impedances) ratios for matrix of simulations and assessment techniques. Additive noise level was 10% of input signal amplitude unless otherwise noted. (T) Trapezoidal quadrature rule used in FRA calculation. (B) Bode quadrature rule used in FRA calculation. * Variance of stochastic errors was often zero.

NOISE ADDED						
INPUT	Z*INPUT	OUTPUT	FRA(T)	FRA(B)	LP	PSD
☒	☒	☐	3.26	1.599	---*	9.05
☐	☐	☒	0.679	0.554	0.657	12.35
☒	☒	☒	0.901	1.402	1.005	12.43

Table 7.3: Student's t-test ratios for the conditions that satisfy the equality of variance in the real and imaginary impedances described by the linear Taylor series expansion. Calculations were conducted for all three cases, with the additive noise having a colored distribution (skewed with a non-zero mean).

			CASE 1	CASE 2	CASE 3
RATIO	α	ν	$t/t_{\alpha/\nu,n-1}$	$t/t_{\alpha/\nu,n-1}$	$t/t_{\alpha/\nu,n-1}$
$\sigma^2_{Z_r}/\sigma^2_{Z_j}=1$	0.05	2	0.416	0.470	0.623
$\sigma^2_{V_r}/\sigma^2_{V_j}=1$	0.05	2	0.412	0.353	0.220
$\sigma^2_{I_r}/\sigma^2_{I_j}=1$	0.05	2	0.897	-	0.663
$\sigma_{V_rI_r}/\sigma_{V_jI_j}=1$	0.05	2	0.183	-	0.0703
$\sigma_{V_rI_j}/\sigma_{V_jI_r}=-1$	0.05	2	0.506	-	0.570
$\sigma_{V_rV_j}=0$	0.025	1	0.170	0.180	0.115
$\sigma_{I_rI_j}=0$	0.025	1	0.0773	-	0.365

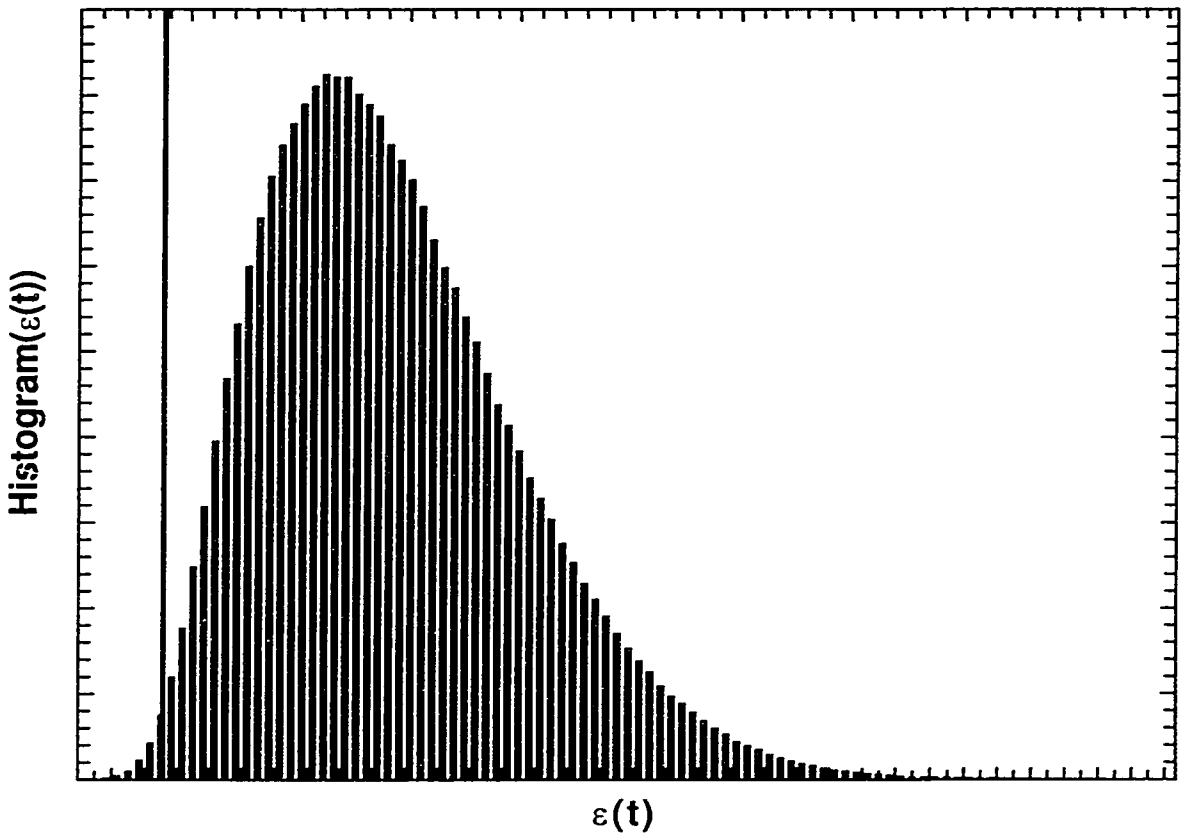

Figure 7.1: Distribution of values for typical waveform of colored noise. Solid black line on left of chart is zero.

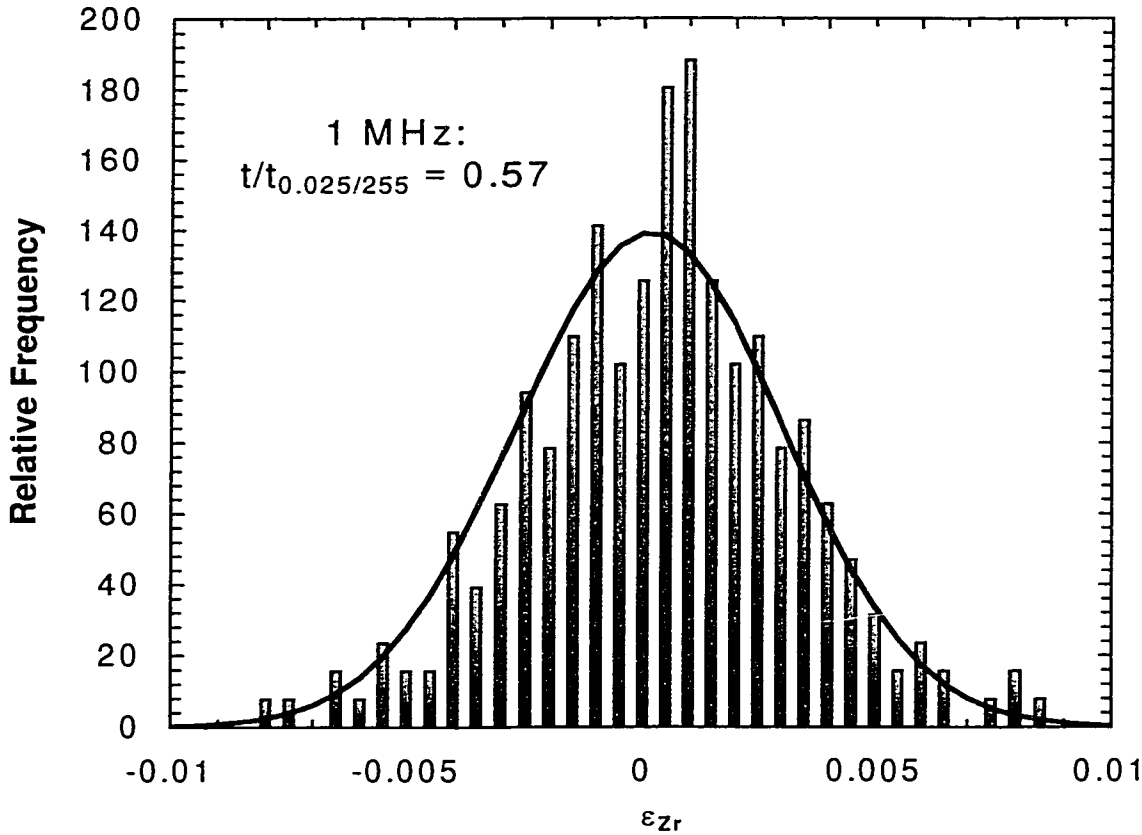

Figure 7.2: Distribution of frequency-domain errors of the real impedance calculated 500 times at 1 MHz with colored noise (see Figure 7.1) added to the input signal, output signal in the frequency-domain, and output signal in the time-domain.

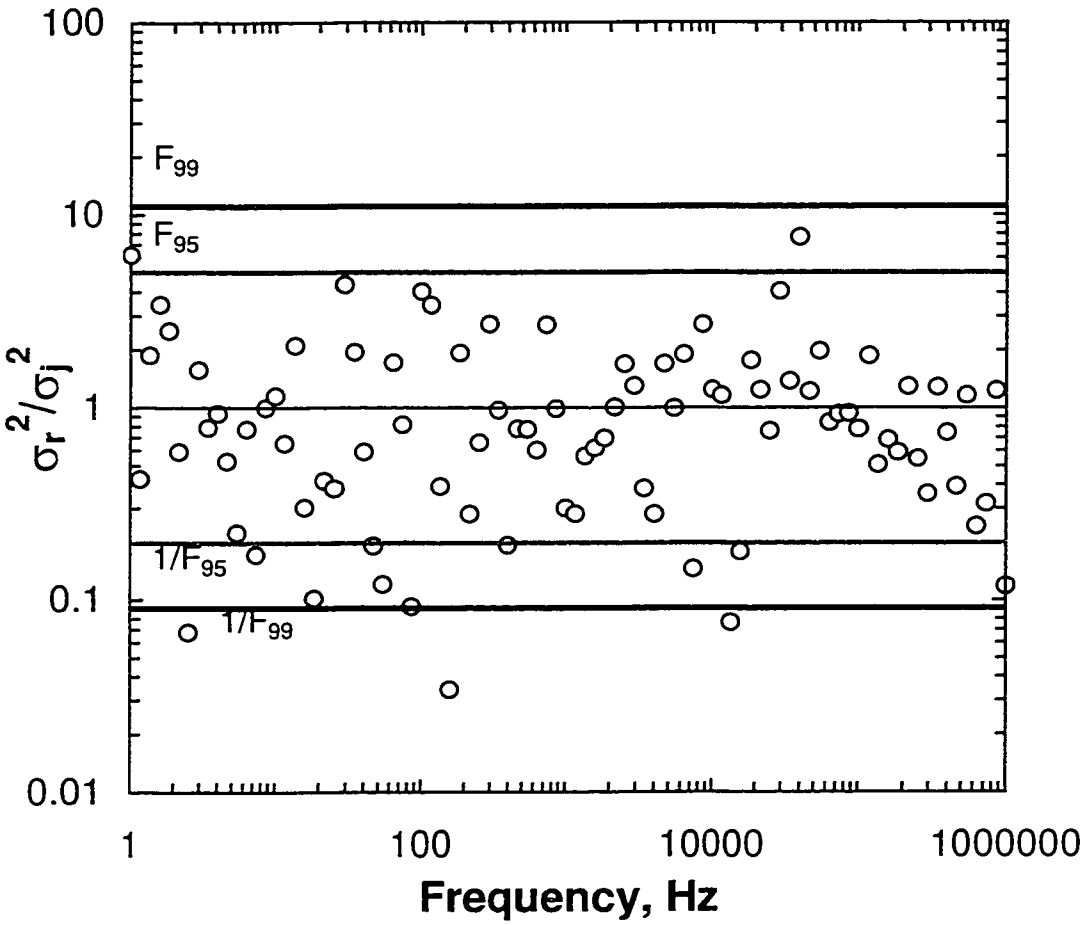

Figure 7.3: F-test for ratio of variance in real impedance to variance in imaginary impedance as a function of frequency. Impedance calculated using the FRA technique (Bode quadrature) with colored noise added to both the input and output signals (CASE 3). The ratio is generally scattered around unity, and most points fall within the 1% level of significance. Thus, there is 99% confidence that the hypothesis that the variances are unequal is false.

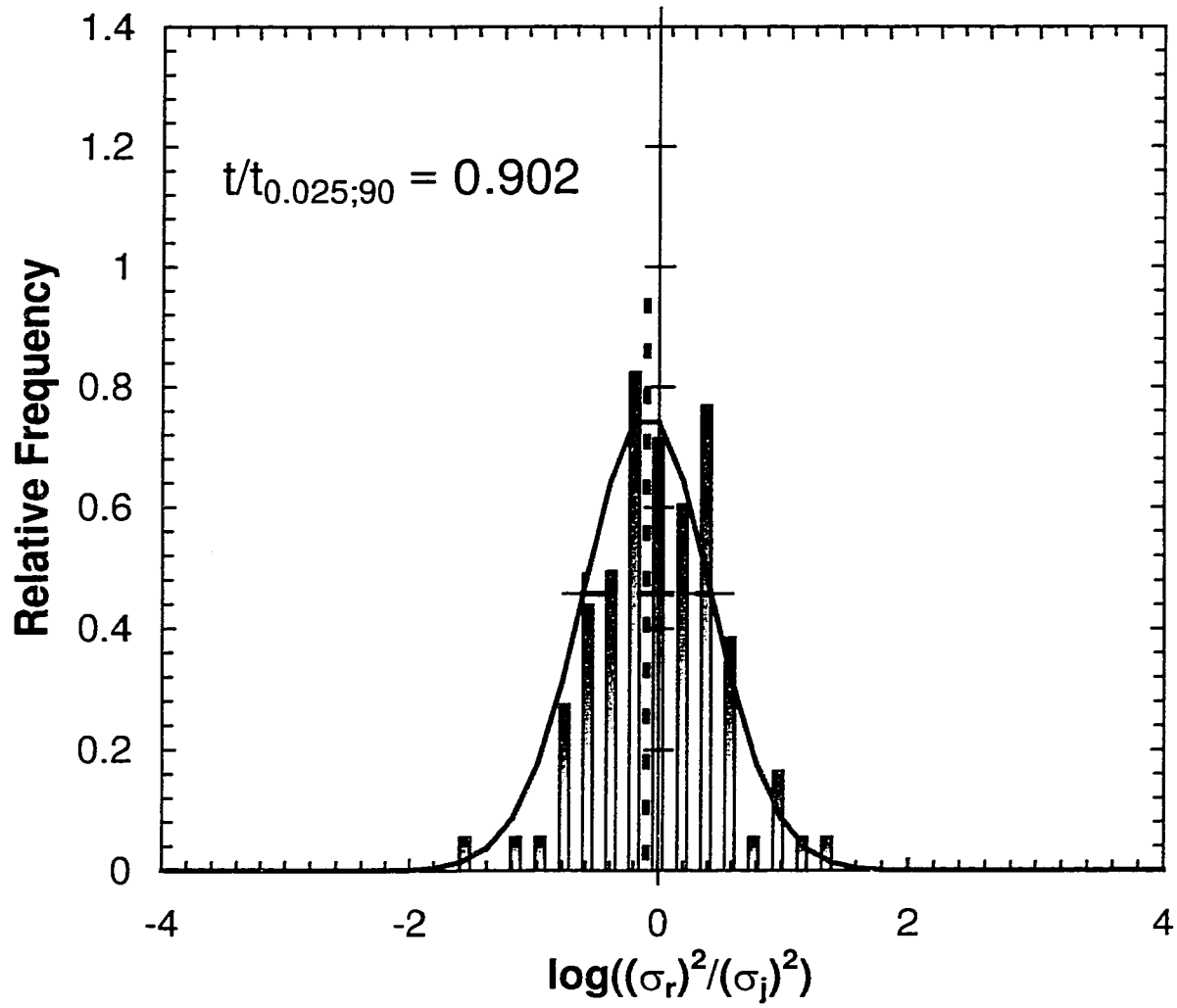

Figure 7.4: Distribution of the logarithm of the ratio of the variance in the real impedance to the variance in the imaginary impedance calculated for CASE 3. This ratio is normally distributed about zero. Thus, the expectations of the variances over the spectrum are equivalent for the FRA measurement technique.

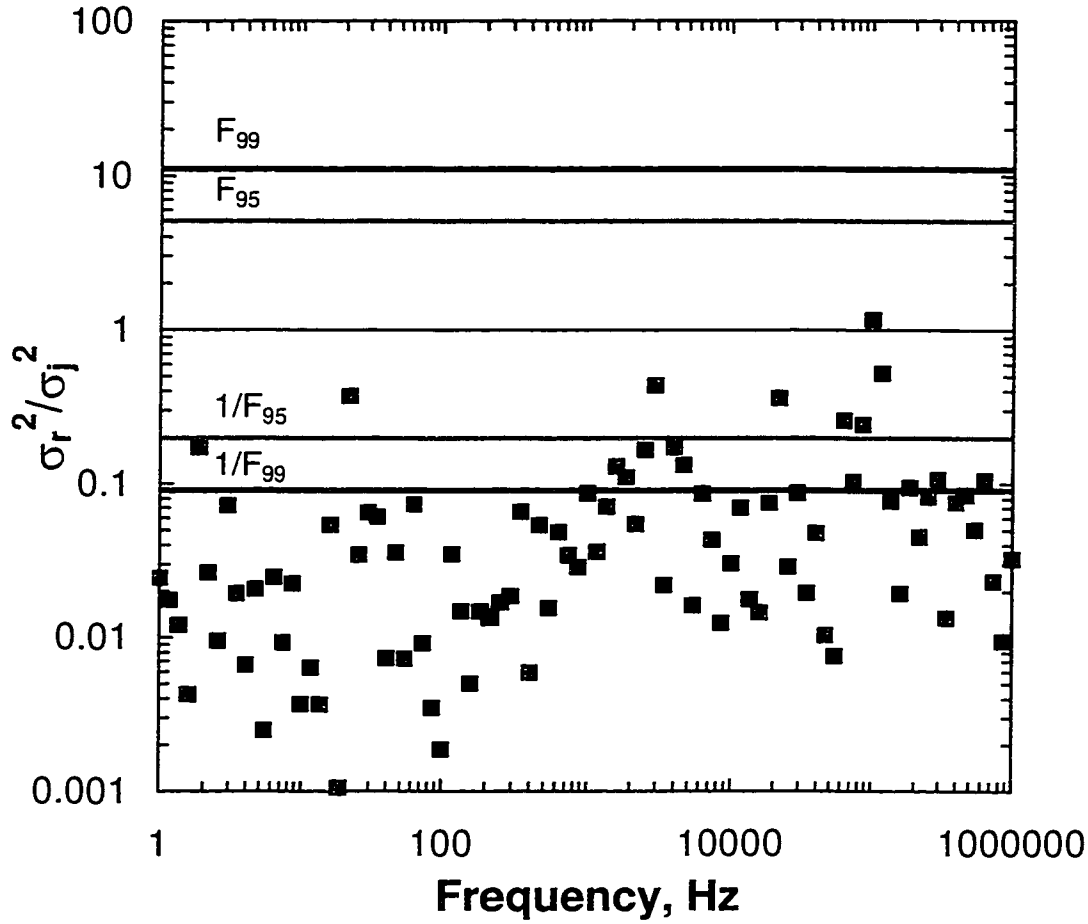

Figure 7.5: F-test for ratio of variance in real impedance to variance in imaginary impedance as a function of frequency. Impedance calculated using the PSD technique with colored noise added to both the input and output signals (CASE 3). The ratio is not scattered around unity, and most points fall outside the 1% level of significance. Thus, there is 99% confidence that the hypothesis that the variances are unequal is true.

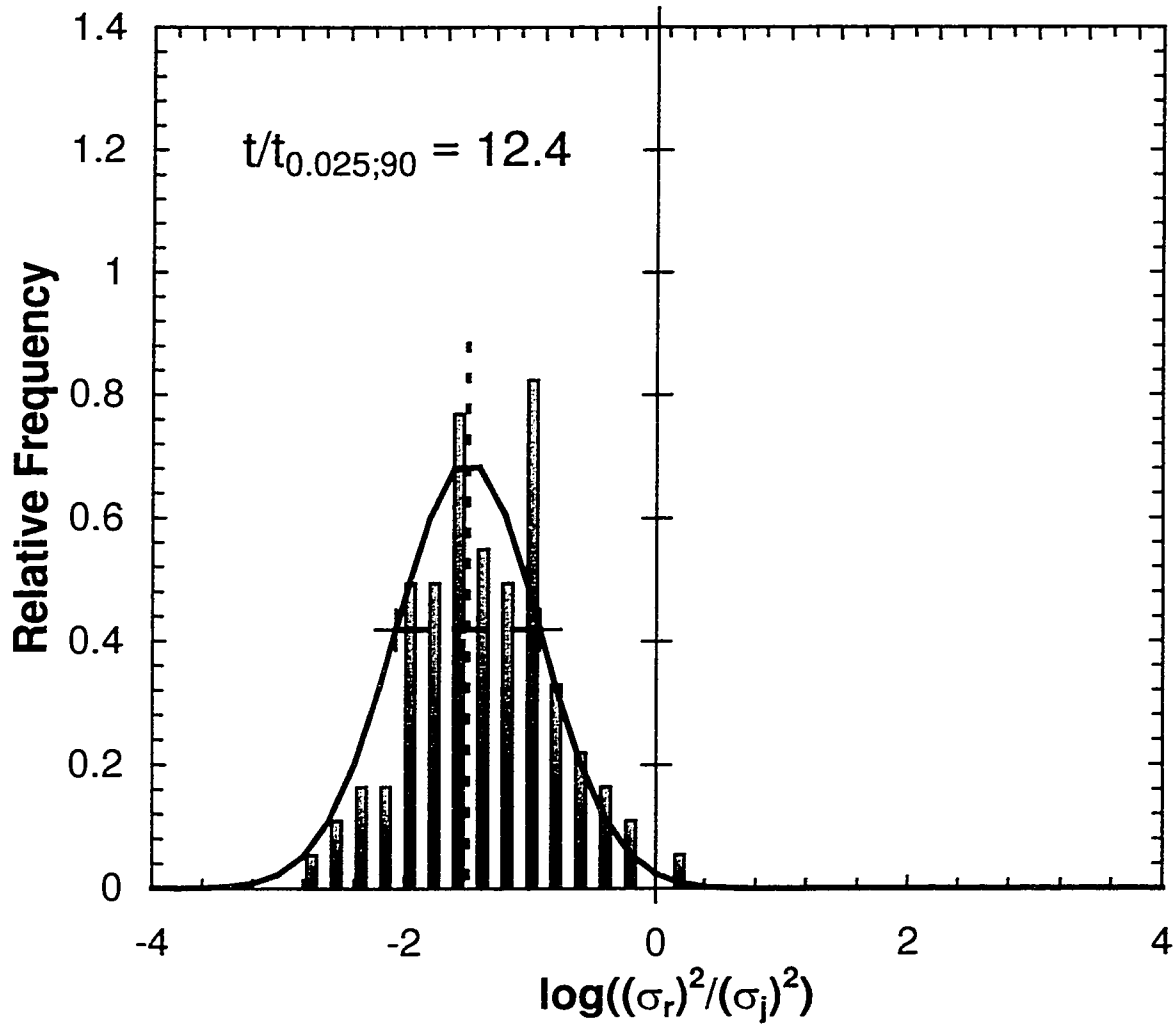

Figure 7.6: Distribution of the logarithm of the ratio of the variance in the real impedance to the variance in the imaginary impedance calculated for CASE 3. This ratio is normally distributed, but not about zero. Thus, the expectations of the variances over the spectrum are not equivalent for the PSD measurement technique.

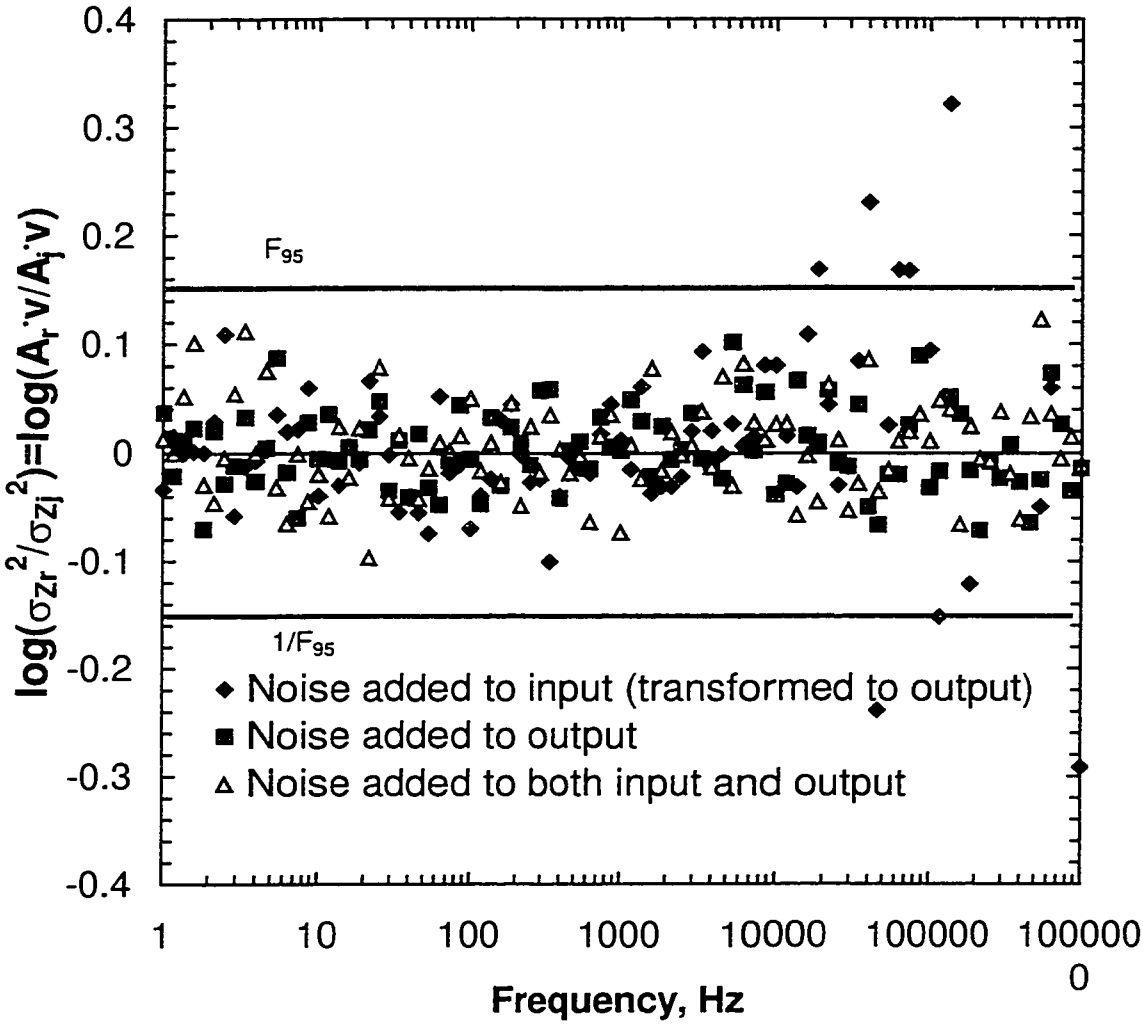

Figure 7.7: Ratio of Taylor series for variance in the real impedance to variance in the imaginary impedance when frequency response analysis is used to calculate the impedance and when the introduced noise in the time-domain had a colored, or skewed distribution. Note that in general the ratio does satisfy the F-test for 5%. Therefore for all three cases, there is less than a 5% probability that the Taylor series for the variances are not equal.

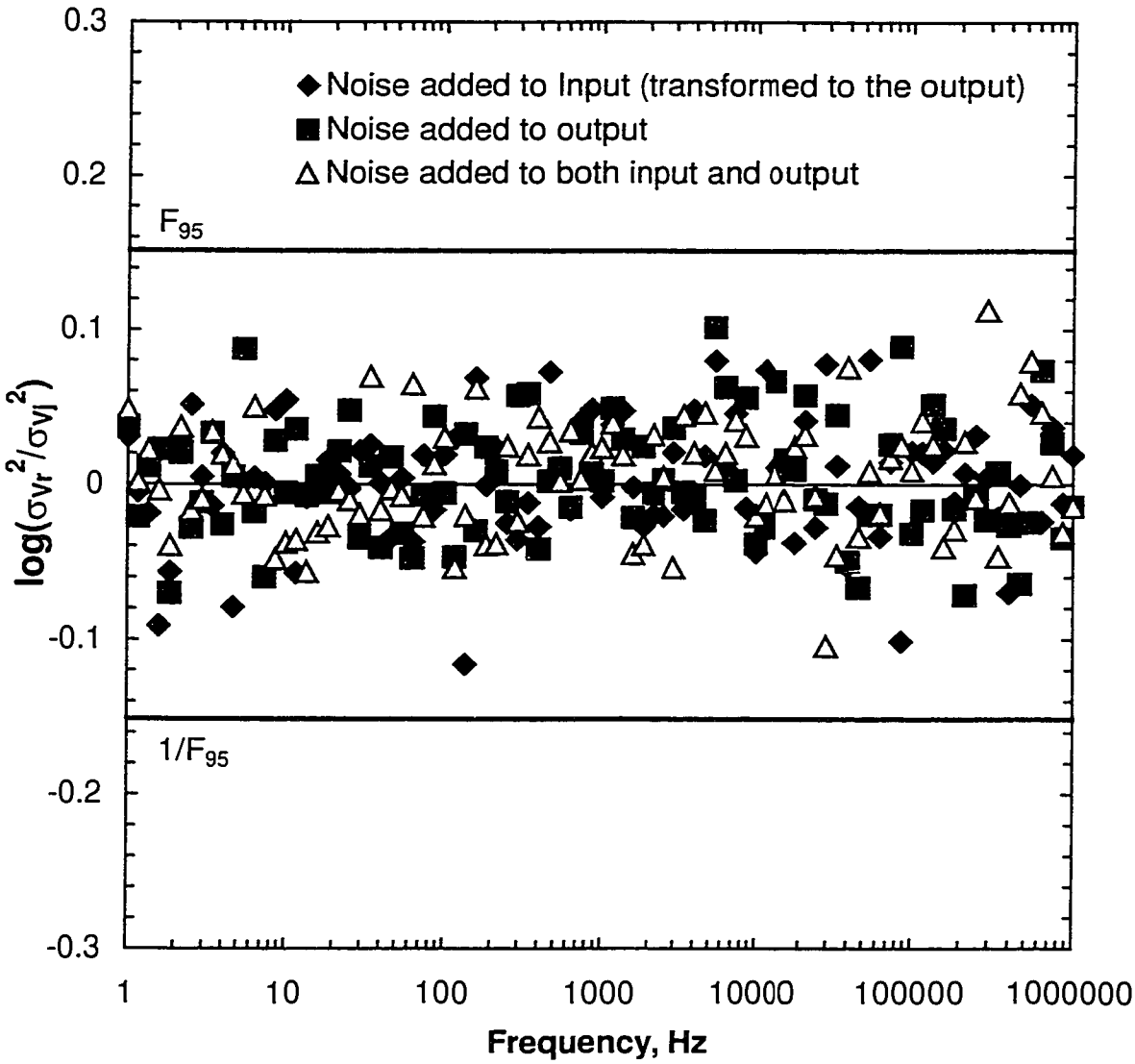

Figure 7.8: Ratio of variance in the real voltage measurement to the variance in the imaginary voltage measurement when colored noise was added to the time-domain signals. Calculation was made using the FRA technique. Note that the ratios for all three cases all fall inside the F-test 5% probability limits. Therefore, there is less than 5% probability that the variances are not equal.

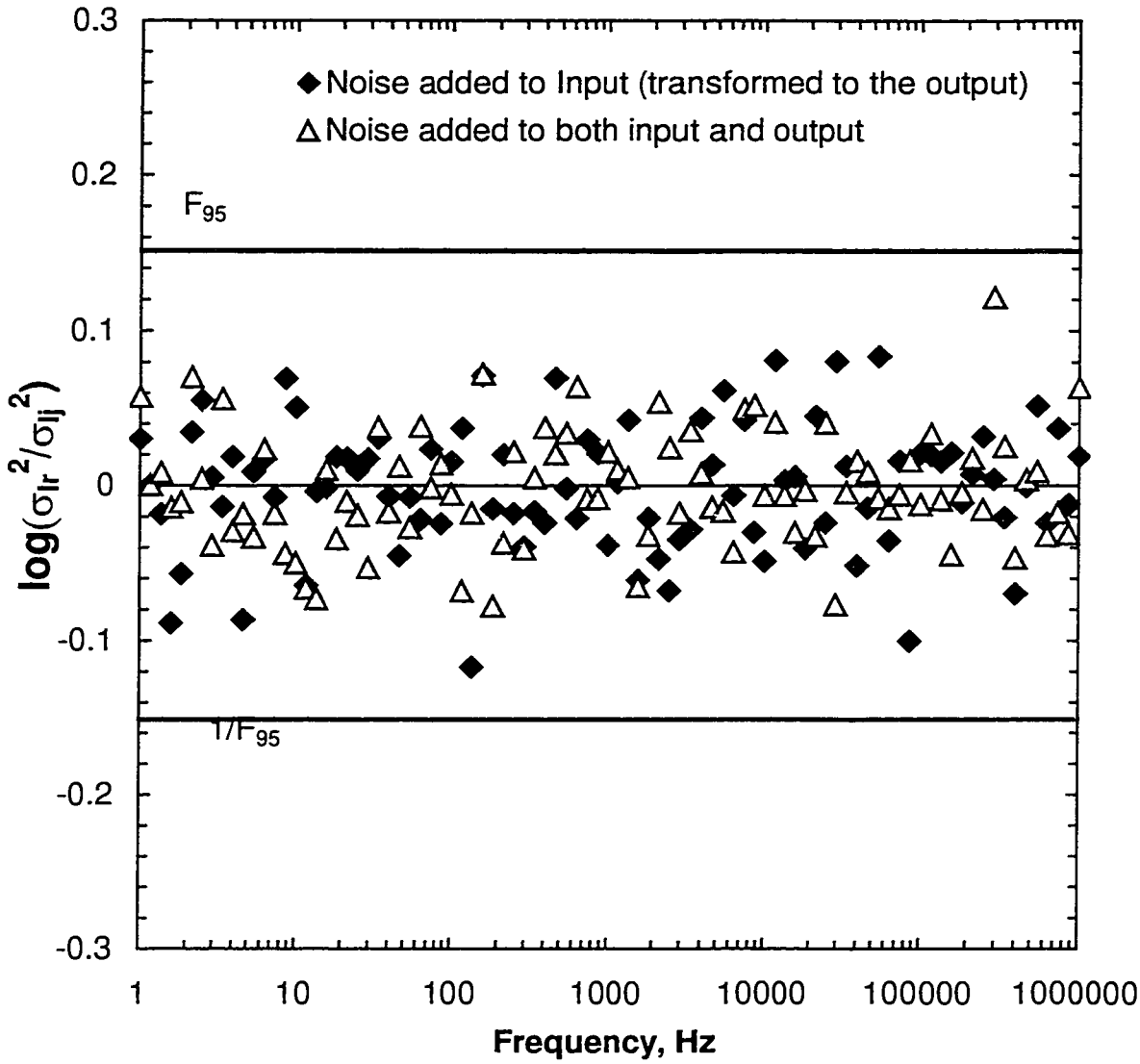

Figure 7.9: Ratio of variance in the real current measurement to the variance in the imaginary current measurement when colored noise was added to the time-domain signals. Calculation was made using the FRA technique. Note that the ratios for all three cases all fall inside the F-test 5% probability limits. Therefore, there is less than 5% probability that the variances are not equal.

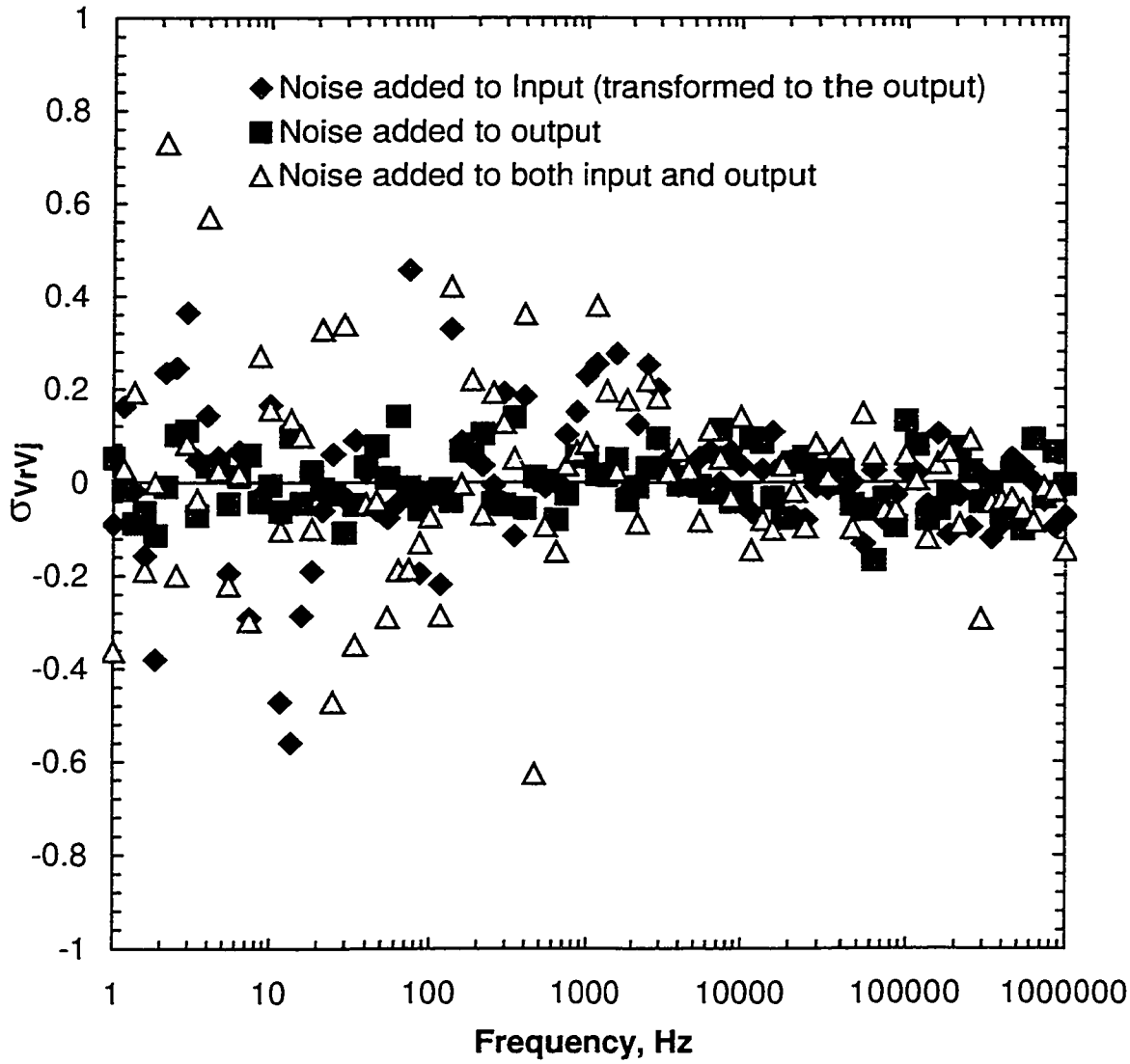

Figure 7.10: Covariance between real and imaginary voltage components when colored noise was added to the time-domain signals. Impedance was calculated using frequency response analysis. The trivial solution to the equality of variances in the complex impedance requires that this covariance be zero.

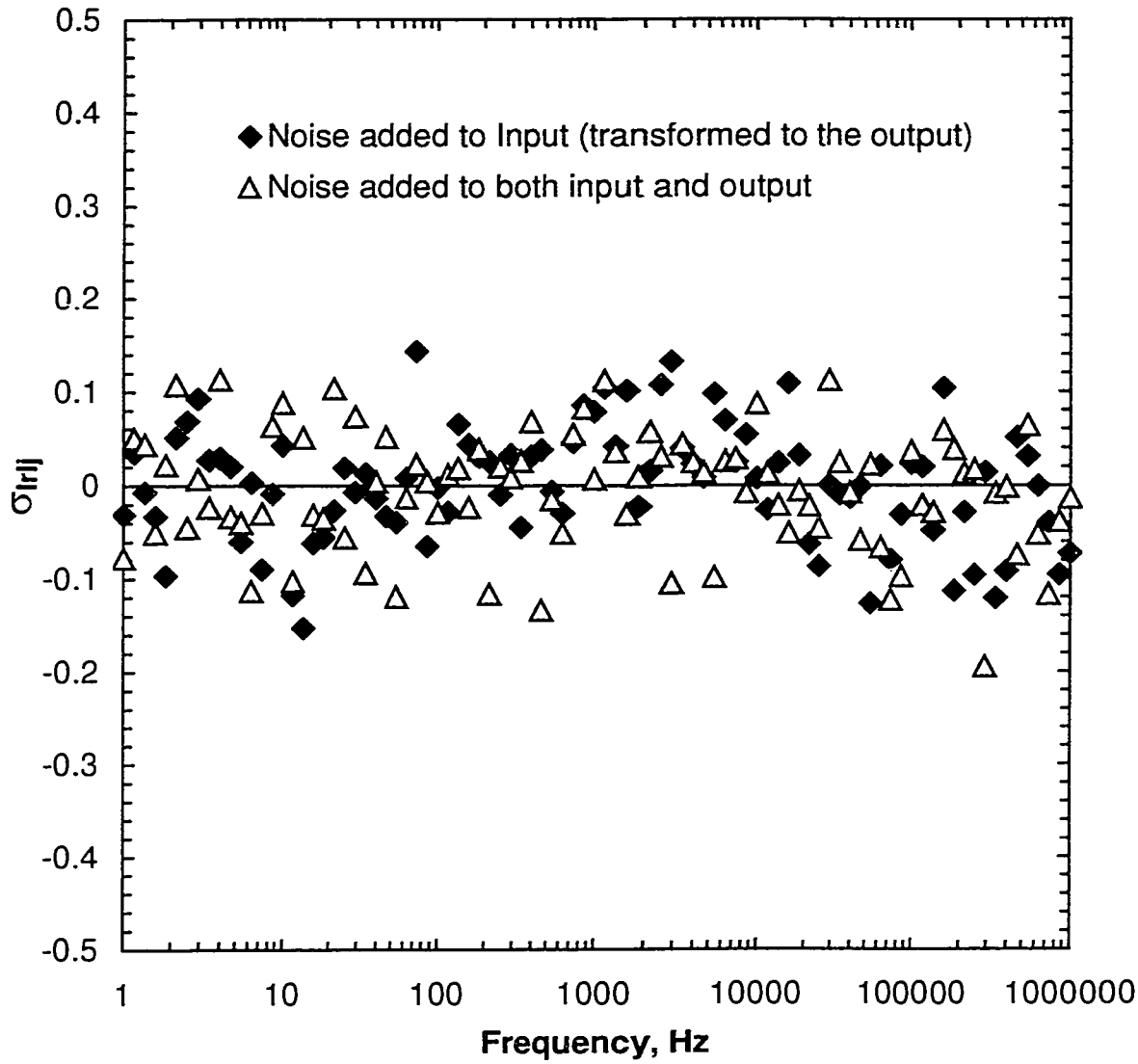

Figure 7.11: Covariance between real and imaginary current components when colored noise was added to the time-domain signals. Impedance was calculated using frequency response analysis. The trivial solution to the equality of variances in the complex impedance requires that this covariance be zero.

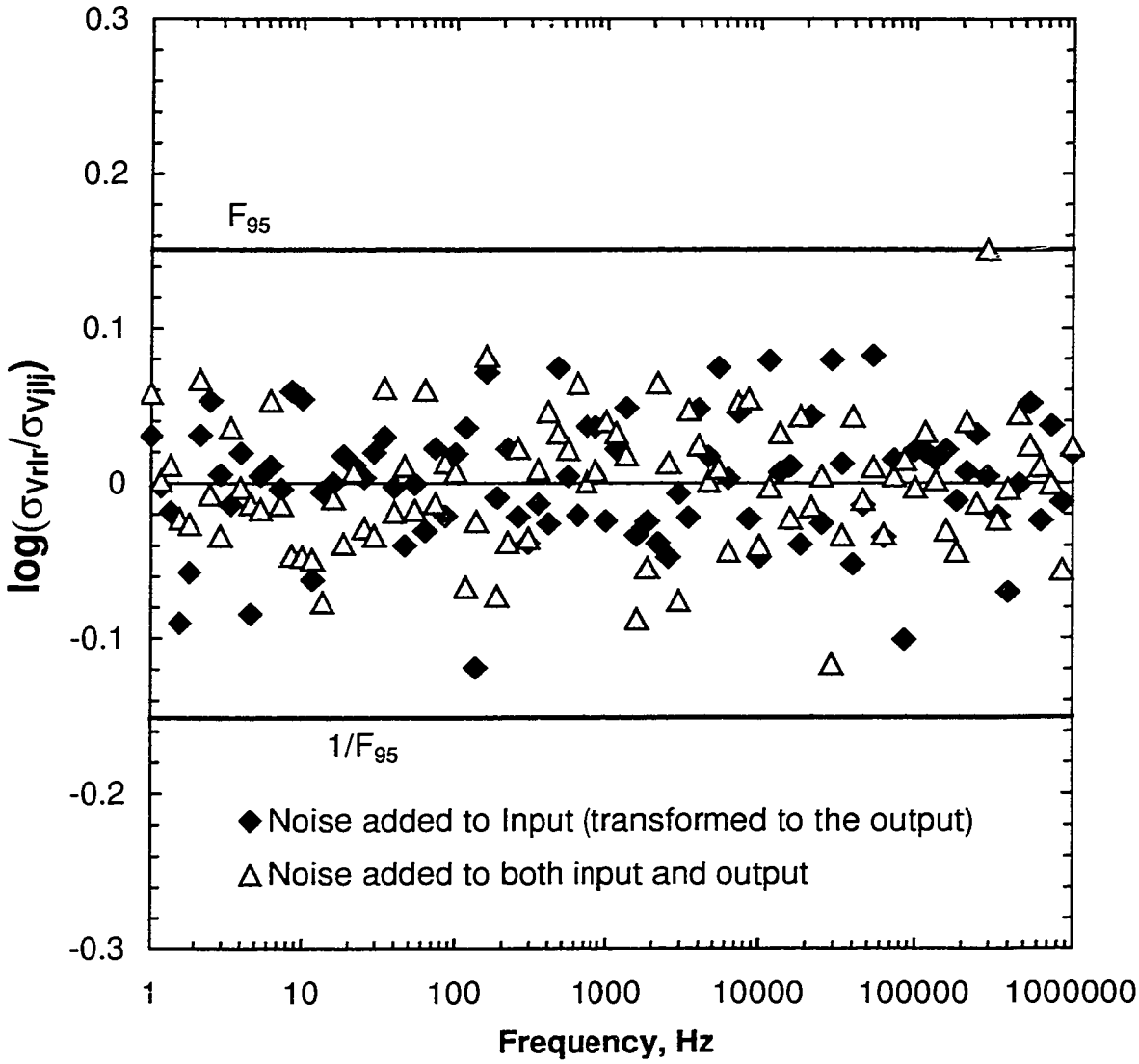

Figure 7.12: Ratio of cross-covariances between real current and voltage to imaginary current and voltage components calculated using frequency response analysis. Noise introduced in the time-domain had a colored, or skewed, distribution. The condition for the equality of variances in the complex impedance requires that this ratio be unity. For all three cases, the ratios generally fall inside the F-test 5% probability limits. There is 5% probability that these cross-covariances are not equal at those frequencies.

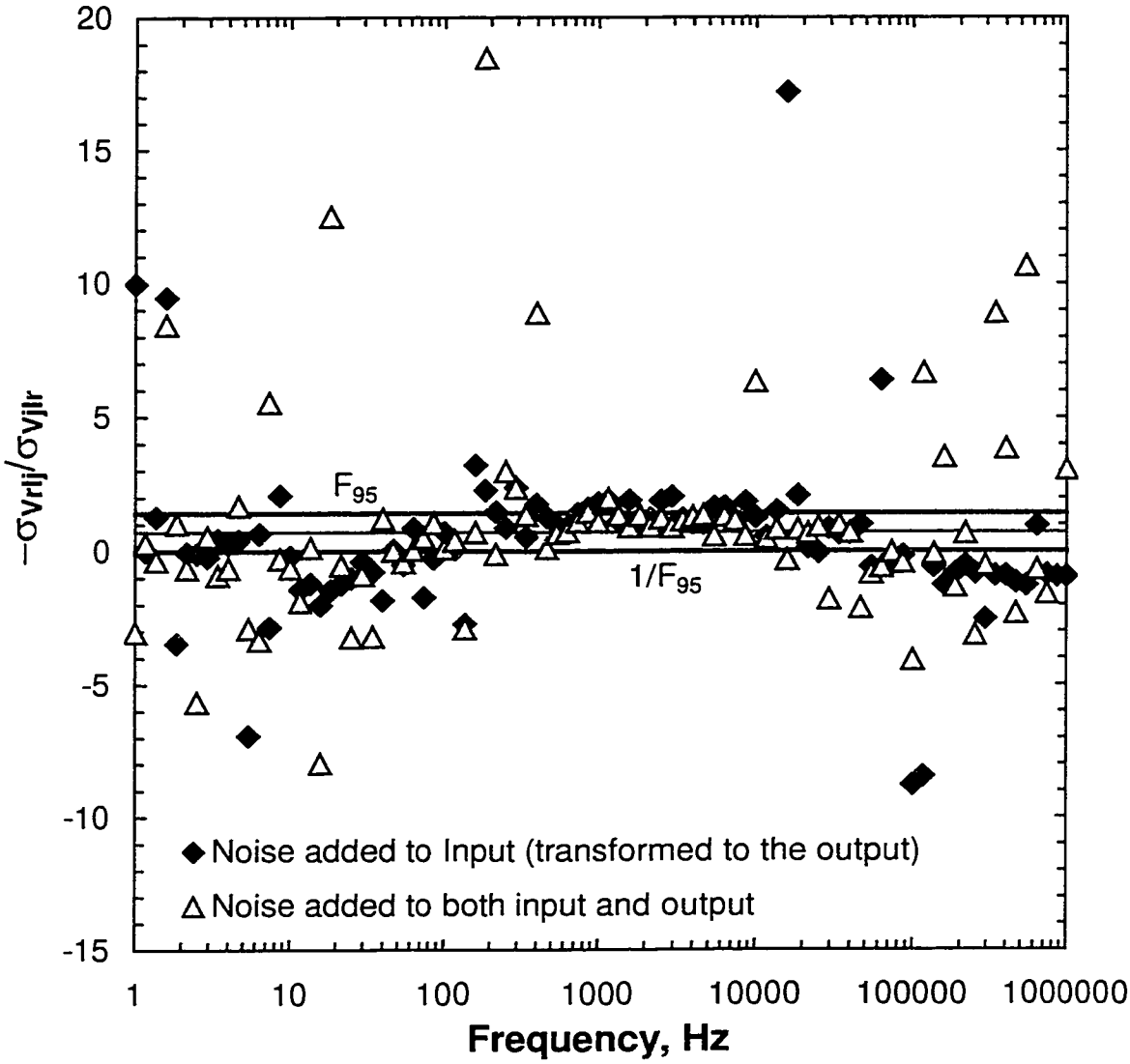

Figure 7.13: Ratio of cross-covariances between imaginary current and real voltage to real current and imaginary voltage components calculated using frequency response analysis. Noise introduced in the time-domain had a colored, or skewed, distribution. The condition for the equality of variances in the complex impedance requires that this ratio be unity. The ratio is generally scattered around one.

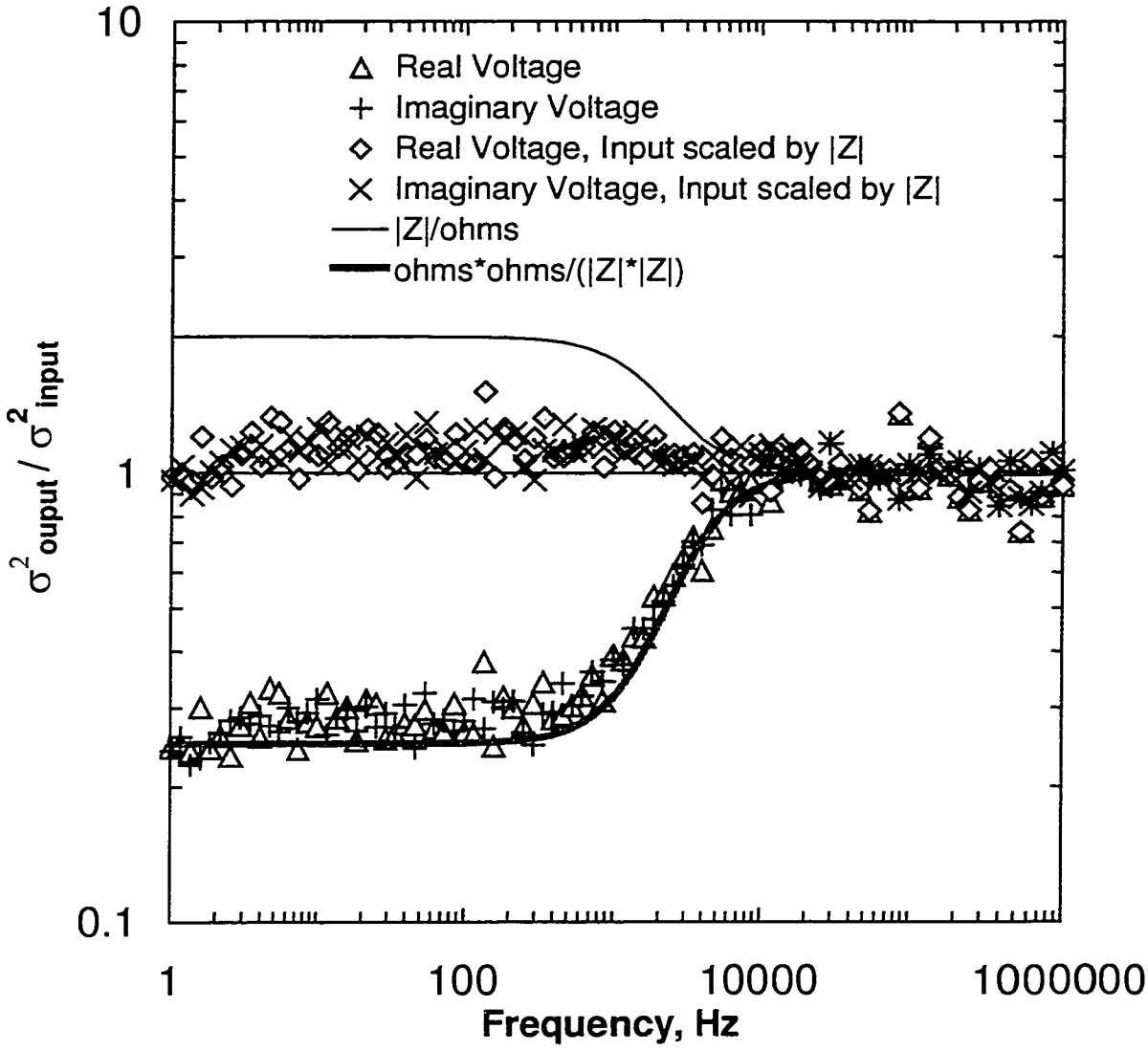

Figure 7.14: Ratios of variances in voltage components for CASE 2 to variances in voltage components for CASE 1, in which colored, or skewed, noise was introduced into the signals. These are the ratios of additive noise to noise transformed by the system. The ratios are clearly frequency dependent, and correlated to the reciprocal of the square of the impedance magnitude. The ratios scaled by the reciprocal of the square of the impedance magnitude are generally scattered about unity.

CHAPTER 8
TRANSFORMATION OF ADDITIVE TIME-DOMAIN NOISE INTO FREQUENCY-DOMAIN ERRORS

Two commonly used techniques for measurement of impedance spectra - Frequency Response Analysis (FRA) and Phase-Sensitive Detection (PSD) - have been discussed in the previous chapters. Both techniques employ time-averaging (integrating) circuitry to calculate the products of the perturbation and response signals with a reference "locked" signal.[5] In frequency response analysis, two reference signals, sine and cosine waves, are employed, while in phase-sensitive detection, a square wave with controlled phase angle is used.[5]

Stochastic errors in the resultant frequency-domain measurement are the result of the calculation on time-domain current and voltage signals via the integration circuitry. The reference signals are not the source of stochastic error. The reference signal can be described as the sum of a pure sinusoid and a noise signal, and the noise signal in the reference signal can be superimposed on the measured signal via the transitive property of addition. Two sources of frequency-domain stochastic error are left: quadrature errors associated with the time-averaging circuitry and noise in the perturbation and response signals. Quadrature error has a deterministic quality, so the primary source of frequency-domain error must propagate from the time-domain noise via the integration process.

In this chapter, the mechanisms through which time-domain stochastic noise is propagated into the frequency-domain complex impedance are described. The

transformation of errors in the current and voltage signals into errors in the complex impedance is derived for the two measurement technologies. The variances of the (stochastic errors in the) real and imaginary impedances will be derived as functions of noise in the current and voltage signals. The influence of the method of measurement - frequency response analysis (sine and cosine waves) or phase-sensitive detection (square wave) - on the impedance error structure will also be assessed. Analytical descriptions of the variance in the frequency-domain quantities (complex impedance, voltage, and current) will be developed. The variance in the complex components of the impedance will be related to the time-domain noise in the constituent current and voltage (perturbation and response) signals.

The analytic description of variance in impedance in terms of the noise in the constituent signals will be derived using two description of variance. The first is the common sample variance, and the second is termed functional variance. The sample variance of a series of measurements of quantity X can be written as[123]

$$\sigma_X^2 = \frac{1}{N-1}\sum_{k=1}^{N}[X_k - E(X)]^2 \tag{8.1}$$

where the expectation is defined by[123]

$$E(X) = \frac{1}{N}\sum_{k=1}^{N} X_k \,. \tag{8.2}$$

The functional variance is a bit more difficult to visualize. It is applied to a function, whereas the sample variance is applied to discrete measurements of some quantity. Thus, if X is defined to be the integral of a function of time, x, over the interval from a to b, then the functional variance can be defined by[116]

$$\sigma_X^2 = \frac{1}{(b-a)}\int_a^b [x(t) - E(x)]^2 dt \tag{8.3}$$

where the expectation here is defined by[116]

$$E(x) = \frac{1}{(b-a)}\int_a^b x(t)dt\,. \tag{8.4}$$

The functional variance is a calculation applied to one signal, while the sample variance is applied to replicate measurements of integrated signals. In the specific case of impedance spectroscopy measurements (or complex spectroscopy measurements), the variances of the real and imaginary impedances are of interest. Thus, in equation (8.3), the time-domain function would be replaced by an appropriate Fourier transformation integral. This will be discussed in detail in the next section.

8.1 Variance as a Result of Frequency Response Analysis

Experimental measurement of the voltage and current signals in an impedance spectroscopy experiment will include stochastic noise in the signals. In frequency response analysis, the complex impedance is calculated as the ratio of the complex voltage to the complex current (with respect to the reference sine wave). The complex components of the voltage and current signals (including noise) are calculated using the technique as

$$V_r(\omega) = \frac{\omega}{2\pi n}\int_0^{2\pi n/\omega} \hat{V}\sin(\omega t + \phi_V)\sin(\omega t)dt + \frac{\omega}{2\pi n}\int_0^{2\pi n/\omega} n_V(t)\sin(\omega t)dt \tag{8.5}$$

$$V_j(\omega) = \frac{\omega}{2\pi n}\int_0^{2\pi n/\omega} \hat{V}\sin(\omega t + \phi_V)\cos(\omega t)dt + \frac{\omega}{2\pi n}\int_0^{2\pi n/\omega} n_V(t)\cos(\omega t)dt \tag{8.6}$$

$$I_r(\omega) = \frac{\omega}{2\pi n}\int_0^{2\pi n/\omega} \hat{I}\sin(\omega t + \phi_I)\sin(\omega t)dt + \frac{\omega}{2\pi n}\int_0^{2\pi n/\omega} n_I(t)\sin(\omega t)dt \tag{8.7}$$

$$I_j(\omega) = \frac{\omega}{2\pi n} \int_0^{2\pi n/\omega} \hat{I} \sin(\omega t + \phi_I) \cos(\omega t) dt + \frac{\omega}{2\pi n} \int_0^{2\pi n/\omega} n_I(t) \cos(\omega t) dt \tag{8.8}$$

The upper limit of integration is an integer number of cycles. As a result of this choice of integration limits, the expectation of the error in the frequency-domain complex voltage and current will be equal to zero if the expectation of the noise signal is equal to zero. Each component is then the sum of the expected value of the component and the appropriate in-phase or out-of-phase integral of the additive noise signal.[116]

$$V_r(\omega) = \hat{V}_r(\omega) + \frac{\omega}{2\pi n} \int_0^{2\pi n/\omega} n_V(t) \sin(\omega t) dt \tag{8.9}$$

$$V_j(\omega) = \hat{V}_j(\omega) + \frac{\omega}{2\pi n} \int_0^{2\pi n/\omega} n_V(t) \cos(\omega t) dt \tag{8.10}$$

$$I_r(\omega) = \hat{I}_r(\omega) + \frac{\omega}{2\pi n} \int_0^{2\pi n/\omega} n_I(t) \sin(\omega t) dt \tag{8.11}$$

$$I_j(\omega) = \hat{I}_j(\omega) + \frac{\omega}{2\pi n} \int_0^{2\pi n/\omega} n_I(t) \cos(\omega t) dt \tag{8.12}$$

Based on this description of the complex components of the constituent current and voltage signals, the variance in the real and imaginary impedance can be determined as the Taylor series expansions in the variances of the constituent signals.

8.1.1 Functional Variance Defined by Expectation Integration over Time

The Taylor series expansions for the variance in real and imaginary impedance developed in Chapter 6 were written as a dot product of a coefficient vector and variance vector. The components of the variance vector were derived in functional variance form. For details of the derivation, refer to Appendix B. The ten components are functions of

the correlation function between the noise signals associated with the variance vector component

$$\sigma_{V_r}^2(\omega)=\left(\frac{\omega}{2\pi n}\right)\int_0^{2\pi n/\omega} d\tau\, \psi_{n_V n_V}(\tau)\left[\left(1-\frac{\tau\omega}{2\pi n}\right)\cos(\omega\tau)+\left(\frac{1}{2\pi n}\right)\sin(\omega\tau)\right] \tag{8.13}$$

$$\sigma_{V_j}^2(\omega)=\left(\frac{\omega}{2\pi n}\right)\int_0^{2\pi n/\omega} d\tau\, \psi_{n_V n_V}(\tau)\left[\left(1-\frac{\tau\omega}{2\pi n}\right)\cos(\omega\tau)-\left(\frac{1}{2\pi n}\right)\sin(\omega\tau)\right] \tag{8.14}$$

$$\sigma_{I_r}^2(\omega)=\left(\frac{\omega}{2\pi n}\right)\int_0^{2\pi n/\omega} d\tau\, \psi_{n_I n_I}(\tau)\left[\left(1-\frac{\tau\omega}{2\pi n}\right)\cos(\omega\tau)+\left(\frac{1}{2\pi n}\right)\sin(\omega\tau)\right] \tag{8.15}$$

$$\sigma_{I_j}^2(\omega)=\left(\frac{\omega}{2\pi n}\right)\int_0^{2\pi n/\omega} d\tau\, \psi_{n_I n_I}(\tau)\left[\left(1-\frac{\tau\omega}{2\pi n}\right)\cos(\omega\tau)-\left(\frac{1}{2\pi n}\right)\sin(\omega\tau)\right] \tag{8.16}$$

$$\sigma_{V_r V_j}(\omega)=0. \tag{8.17}$$

$$\sigma_{I_r I_j}(\omega)=0. \tag{8.18}$$

$$\sigma_{V_r I_r}(\omega)=\left(\frac{\omega}{2\pi n}\right)\int_0^{2\pi n/\omega} d\tau\, \left[\psi_{n_V n_I}(\tau)+\psi_{n_I n_V}(\tau)\right]\left[\begin{array}{l}\left(1-\frac{\tau\omega}{2\pi n}\right)\cos(\omega\tau)\\ +\left(\frac{1}{2\pi n}\right)\sin(\omega\tau)\end{array}\right] \tag{8.19}$$

$$\sigma_{V_r I_j}(\omega)=0 \tag{8.20}$$

$$\sigma_{V_j I_r}(\omega)=0 \tag{8.21}$$

$$\sigma_{V_j I_j}(\omega)=\left(\frac{\omega}{2\pi n}\right)\int_0^{2\pi n/\omega} d\tau\, \left[\psi_{n_V n_I}(\tau)+\psi_{n_I n_V}(\tau)\right]\left[\begin{array}{l}\left(1-\frac{\tau\omega}{2\pi n}\right)\cos(\omega\tau)\\ -\left(\frac{1}{2\pi n}\right)\sin(\omega\tau)\end{array}\right] \tag{8.22}$$

where the variable of integration is defined as the difference between the time-variables of integration associated with the double integral corresponding to the square of the quantity. The integral of the sine of the sum of two angles (see Appendix B) is equal to

zero, therefore, the covariances in equations (8.17) and (8.18) and the cross-covariances in equations (8.20) and (8.21) are zero.

It is clear from these results that the error structure of impedance measurements is a strong function of the correlation between the various errors in the signals. In the next section, simulations will be discussed in which these integral equations are used to calculate the vector of variances, covariances, and cross-covariances of the complex current and voltage signals used in the Taylor series description of the variance in the impedance.

8.1.2 Simulation Studies of the Variance Defined by Expectation Integration over Time

A LabView code was constructed through which the correlation functions associated with the time-domain noise could be calculated and the integral components of the variance vector could be determined. Bode integration was used to calculate the integrals over the time-shift variable. The correlation functions were calculated directly from the noise signals. The ten components of the rectangular coordinate variance vector were calculated for both definitions of the variance. One hundred replicate measurements of the impedance were made at each frequency. Each measurement of the complex impedance was made over three cycles of the current and voltage signal. The long-integration convergence criterion was met at three cycles. The functional variance determined for the reported impedance was averaged over the 100 replicate measurements.

Three simulation conditions were studied. In the CASE 1, noise was added to both the input and the output, but the input noise was not transformed through the system. This simulation followed the analysis conducted by Milocco and Biagiola[117] for noise

introduced only via measurement. The next simulation (CASE 2) was for noise added to the input signal and transformed through the system into the output signal. The final simulation (CASE 3) consisted of adding noise to the input, allowing it to be transformed by the system into the output signal, and introducing an additional noise signal to the output signal. A simulation was not conducted in which noise was added only to the output signal, because it would duplicate the Milocco- and Biagiola-influenced[117] experiment.

The variance vector was calculated at 91 frequencies as the average of 500 replicate measurements of the variance vector. The ratio of the linear Taylor series for the variance in the real impedance to the linear Taylor series for the variance in the imaginary impedance was determined at each frequency. The coefficient vectors were calculated based on the average values of the complex components of the voltage and current. The variance vector was calculated through the integral equations derived in this chapter, and it was also calculated, for comparison, as a sample variance of the replicate estimations of the complex voltage and current signals. At each frequency the F-test ratio was calculated for the 500 replicates. The student's t-test was also calculated to determine if the mean value of the logarithm of the ratio of impedance variances was equal to zero.

8.1.2.1 CASE 1

The F-test spectra are shown in Figure 8.1 for the ratio of variances of the real and imaginary impedances via the variance vectors calculated through the integral equations and calculated as the sample variance of the replicate estimations of the complex signals. Both ratio spectra generally fall within the F-test probability limits over frequency. The student's t-test results are shown in Table 8.1. The student's t-test parameters calculated over the impedance spectra for the two methods of calculation of the variance ratio are

less than the critical value of the parameter. The probabilities associated with the calculated parameters are also shown in the table. The calculated variances in the real and imaginary impedances are equal, as stated by Milocco and Biagiola[117] for noise introduced through measurement of the signals.

8.1.2.2 CASE 2

When the variance vector calculated via the derived integral equations for the simulation where noise added to the input signal is allowed to be transformed by the system into the output signal is introduced into the Taylor series expansions for variance in the complex impedance, the ratio of the variance in the real to the variance in the imaginary impedance is not necessarily unity. The F-test spectra are shown in Figure 8.2 for the ratios of variances in the real to imaginary impedances calculated through the sample variance (observed values of the complex signals) and the derived integral equations. The F-test is generally not satisfied at high frequency for the ratio calculated using the functional variance vector. The student's t-test parameters are listed in Table 8.2. The t-test is not satisfied for the ratio of impedance variances calculated through the derived integral equations, while it is satisfied for the ratio determined through the sample variance calculation.

8.1.2.3 CASE 3

The results for this case are the same as for CASE 2. The statistical tests for the ratio of the variance in the real impedance to the variance in the imaginary impedance are satisfied when the ratio is calculated through the sample variance vector. When the functional variance vector (consisting of the derived integral equations) is used in the Taylor series expansion for the variances in the real and imaginary impedances, the F-test

is not satisfied at high frequency (Figure 8.3). The student's t-test is not satisfied for the probability of five percent (Table 8.3).

8.1.2.4 Influence of System on Propagation of Errors

Again, note that the Taylor series expansions used to define the variances in the real and imaginary impedances in terms of the variances of and between the complex components of the current and voltage signals are comparable to the variance in the stochastic error of the impedances if the expectation of the stochastic error is equal to zero. Thus, the functional description of variance satisfies the experimental observation that the variance (of the stochastic error) in the real impedance is equal to the variance in the imaginary impedance (of the stochastic error) when noise is introduced into the current and voltage signals only through measurement. The observation is not satisfied when noise is transformed through the system. An explanation is required.

The correlation functions involving the noise in the voltage signal are related to the auto-correlation function for the noise in the current signal through the impedance if the noise in the voltage signal is transformed through the system from the noise in the current. The auto-correlation function for the noise in the voltage signal can be written as[116]

$$\psi_{n_V n_V}(\tau) = E[n_V(t) n_V(t+\tau)]. \tag{8.23}$$

This can be written as the product of two integrals

$$\psi_{n_V n_V}(\tau) = E\left\{\int_0^{2\pi n/\omega} dx Z(x) n_I(t-x)\right\} E\left\{\int_0^{2\pi n/\omega} dy Z(y) n_I(t+\tau-y)\right\}. \tag{8.24}$$

The product of the two integrals can be rewritten as a double integral such that

$$\psi_{n_V n_V}(\tau) = E\left\{ \int_0^{2\pi n/\omega} dx Z(x) \int_0^{2\pi n/\omega} dy Z(y) n_I(t-x) n_I(t+\tau-y) \right\}. \tag{8.25}$$

The expectation can be brought into the integrals. Only the noise functions have an expectation different than the function itself, so

$$\psi_{n_V n_V}(\tau) = \int_0^{2\pi n/\omega} dx Z(x) \int_0^{2\pi n/\omega} dy Z(y) E[n_I(t-x) n_I(t+\tau-y)]. \tag{8.26}$$

The expectation of the product of the noise signals is the definition of the correlation function, therefore, the auto-correlation function of the voltage noise signal is related to the auto-correlation function of the current noise signal as

$$\psi_{n_V n_V}(\tau) = \int_0^{2\pi n/\omega} dx Z(x) \int_0^{2\pi n/\omega} dy Z(y) \psi_{n_I n_I}(\tau - y + x). \tag{8.27}$$

The cross-correlation function can be determined through a similar derivation. In this case, however, the impedance is only included in one integral. Therefore, the cross-correlation functions can be written in terms of the auto-correlation function for the noise in the current signal as

$$\psi_{n_I n_V}(\tau) = \int_0^{2\pi n/\omega} dx \int_0^{2\pi n/\omega} dy Z(y) \psi_{n_I n_I}(\tau - y + x) \tag{8.28}$$

$$\psi_{n_V n_I}(\tau) = \int_0^{2\pi n/\omega} dx Z(x) \int_0^{2\pi n/\omega} dy \psi_{n_I n_I}(\tau - y + x). \tag{8.29}$$

The noise in the voltage signal could arise from two sources, namely, that transformed through the system from the noise in the current signal and additive noise contributed to the voltage signal. In this case, the correlation functions in equations (8.13),(8.14), (8.17), and (8.19)-(8.22) will be the sum of four correlation functions. Equation (8.13) would then be rewritten as

$$\sigma_{V_r}^2(\omega) = E\left[\left(\frac{\omega^2}{4\pi^2 n^2}\right)\int_0^{2\pi n/\omega}\int_0^{2\pi n/\omega}\left[n_V^t(x)+n_V^a(x)\right]\left[n_V^t(y)+n_V^a(y)\right]\sin(\omega x)\sin(\omega y)dxdy\right] \tag{8.30}$$

where the superscripts a and t refer to additive noise and transformed noise, respectively. Thus, the variance in the real component of the voltage signal can be considered to be the sum of four integrals

$$\begin{aligned}\sigma_{V_r}^2(\omega) = &\left(\frac{\omega}{2\pi n}\right)\int_0^{2\pi n/\omega} d\tau\, \psi_{n_V^t n_V^t}(\tau)\left[\left(1-\frac{\tau\omega}{2\pi n}\right)\cos(\omega\tau)+\left(\frac{1}{2\pi n}\right)\sin(\omega\tau)\right] \\ &+\left(\frac{\omega}{2\pi n}\right)\int_0^{2\pi n/\omega} d\tau\, \psi_{n_V^t n_V^a}(\tau)\left[\left(1-\frac{\tau\omega}{2\pi n}\right)\cos(\omega\tau)+\left(\frac{1}{2\pi n}\right)\sin(\omega\tau)\right] \\ &+\left(\frac{\omega}{2\pi n}\right)\int_0^{2\pi n/\omega} d\tau\, \psi_{n_V^a n_V^t}(\tau)\left[\left(1-\frac{\tau\omega}{2\pi n}\right)\cos(\omega\tau)+\left(\frac{1}{2\pi n}\right)\sin(\omega\tau)\right] \\ &+\left(\frac{\omega}{2\pi n}\right)\int_0^{2\pi n/\omega} d\tau\, \psi_{n_V^a n_V^a}(\tau)\left[\left(1-\frac{\tau\omega}{2\pi n}\right)\cos(\omega\tau)+\left(\frac{1}{2\pi n}\right)\sin(\omega\tau)\right]\end{aligned} \tag{8.31}$$

The auto-correlation function, $\psi_{n_V^t n_V^t}$, is defined by equation (8.27). The cross-correlation function, $\psi_{n_V^t n_V^a}$, is defined as

$$\psi_{n_V^t n_V^a}(\tau) = E\left[n_V^t(t)n_V^a(t+\tau)\right]. \tag{8.32}$$

and can therefore be written in terms of the cross-correlation function for the noise added to the current signal as

$$\psi_{n_V^t n_V^a}(\tau) = \int_0^{2\pi n/\omega} dx Z(x)\int_0^{2\pi n/\omega} dy\, \psi_{n_I n_V^a}(\tau - y + x). \tag{8.33}$$

Likewise, the other cross-correlation function can be defined in integral form as

$$\psi_{n_V^a n_V^t}(\tau) = \int_0^{2\pi n/\omega} dx \int_0^{2\pi n/\omega} dy\, Z(y)\psi_{n_I n_V^a}(\tau - y + x). \tag{8.34}$$

Substitution into the third integral of equation (8.31) using the symmetry of correlation functions gives

$$\sigma_{V_r}^2(\omega)=\left(\frac{\omega}{2\pi n}\right)\int_0^{2\pi n/\omega} d\tau\, \psi_{n_V^t n_V^t}(\tau)\left[\left(1-\frac{\tau\omega}{2\pi n}\right)\cos(\omega\tau)+\left(\frac{1}{2\pi n}\right)\sin(\omega\tau)\right]$$
$$+\left(\frac{\omega}{2\pi n}\right)\int_0^{2\pi n/\omega} d\tau\, \psi_{n_V^a n_V^a}(\tau)\left[\left(1-\frac{\tau\omega}{2\pi n}\right)\cos(\omega\tau)+\left(\frac{1}{2\pi n}\right)\sin(\omega\tau)\right].$$
$$+\left(\frac{\omega}{\pi n}\right)\int_0^{2\pi n/\omega} d\tau\, \psi_{n_V^t n_V^a}(\tau)\cos(\omega\tau) \tag{8.35}$$

Similarly, the variance in the imaginary component of the voltage signal can be written as

$$\sigma_{V_j}^2(\omega)=\left(\frac{\omega}{2\pi n}\right)\int_0^{2\pi n/\omega} d\tau\, \psi_{n_V^t n_V^t}(\tau)\left[\left(1-\frac{\tau\omega}{2\pi n}\right)\cos(\omega\tau)-\left(\frac{1}{2\pi n}\right)\sin(\omega\tau)\right]$$
$$+\left(\frac{\omega}{2\pi n}\right)\int_0^{2\pi n/\omega} d\tau\, \psi_{n_V^a n_V^a}(\tau)\left[\left(1-\frac{\tau\omega}{2\pi n}\right)\cos(\omega\tau)-\left(\frac{1}{2\pi n}\right)\sin(\omega\tau)\right].$$
$$+\left(\frac{\omega}{\pi n}\right)\int_0^{2\pi n/\omega} d\tau\, \psi_{n_V^t n_V^a}(\tau)\cos(\omega\tau) \tag{8.36}$$

For the case of transformed noise and additive noise in the voltage signal, the two non-zero cross-covariance equations, (8.19) and (8.22) can also be rewritten as

$$\sigma_{V_r I_r}(\omega)=\left(\frac{\omega}{2\pi n}\right)\int_0^{2\pi n/\omega} d\tau\left(\psi_{n_V^t n_I}(\tau)+\psi_{n_I n_V^t}(\tau)\right)\left[\begin{array}{l}\left(1-\frac{\tau\omega}{2\pi n}\right)\cos(\omega\tau)\\ +\left(\frac{1}{2\pi n}\right)\sin(\omega\tau)\end{array}\right]$$
$$+\left(\frac{\omega}{2\pi n}\right)\int_0^{2\pi n/\omega} d\tau\left(\psi_{n_V^a n_I}(\tau)+\psi_{n_I n_V^a}(\tau)\right)\left[\begin{array}{l}\left(1-\frac{\tau\omega}{2\pi n}\right)\cos(\omega\tau)\\ +\left(\frac{1}{2\pi n}\right)\sin(\omega\tau)\end{array}\right]. \tag{8.37}$$

$$\sigma_{V_j I_j}(\omega)=\left(\frac{\omega}{2\pi n}\right)\int_0^{2\pi n/\omega} d\tau\left(\psi_{n_V^t n_I}(\tau)+\psi_{n_I n_V^t}(\tau)\right)\left[\begin{array}{l}\left(1-\frac{\tau\omega}{2\pi n}\right)\cos(\omega\tau)\\ -\left(\frac{1}{2\pi n}\right)\sin(\omega\tau)\end{array}\right]$$
$$+\left(\frac{\omega}{2\pi n}\right)\int_0^{2\pi n/\omega} d\tau\left(\psi_{n_V^a n_I}(\tau)+\psi_{n_I n_V^a}(\tau)\right)\left[\begin{array}{l}\left(1-\frac{\tau\omega}{2\pi n}\right)\cos(\omega\tau)\\ -\left(\frac{1}{2\pi n}\right)\sin(\omega\tau)\end{array}\right]. \tag{8.38}$$

The presence of the convolution integrals in the correlation functions has tremendous affect on the nature of the components of the Taylor series expansion variance vector. If the noise is stochastic and simply additive (no transformed noise in the output) as assumed by Milocco and Biagliola,[117] then the four correlation functions will be identical. Each function will be finite at a time-shift of zero, and zero everywhere else. Introduction of these correlation functions into the integrals for the ten components of the variance vectors leads to a variance vector that satisfies the conditions for equality of the Taylor series expansions of the complex impedance variances, since the equations would reduce to

$$\sigma_{V_r}^2(\omega) = \left(\frac{\omega}{2\pi n}\right)\psi_{n_V n_V}(0) \tag{8.39}$$

$$\sigma_{V_j}^2(\omega) = \left(\frac{\omega}{2\pi n}\right)\psi_{n_V n_V}(0) \tag{8.40}$$

$$\sigma_{I_r}^2(\omega) = \left(\frac{\omega}{2\pi n}\right)\psi_{n_I n_I}(0) \tag{8.41}$$

$$\sigma_{I_j}^2(\omega) = \left(\frac{\omega}{2\pi n}\right)\psi_{n_I n_I}(0) \tag{8.42}$$

$$\sigma_{V_r V_j}(\omega) = 0. \tag{8.43}$$

$$\sigma_{I_r I_j}(\omega) = 0. \tag{8.44}$$

$$\sigma_{V_r I_r}(\omega) = \left(\frac{\omega}{2\pi n}\right)\left[\psi_{n_V n_I}(0) + \psi_{n_I n_V}(0)\right] \tag{8.45}$$

$$\sigma_{V_r I_j}(\omega) = 0 \tag{8.46}$$

$$\sigma_{V_j I_r}(\omega) = 0 \tag{8.47}$$

$$\sigma_{V_j I_j}(\omega) = \left(\frac{\omega}{2\pi n}\right)\left[\psi_{n_V n_I}(0) + \psi_{n_I n_V}(0)\right]. \tag{8.48}$$

where the condition for the equality of the Taylor series expansions for variances in real and imaginary impedances is

$$\sigma^2_{V_r}(\omega) = \sigma^2_{V_j}(\omega). \tag{8.49}$$

$$\sigma^2_{I_r}(\omega) = \sigma^2_{I_j}(\omega) \tag{8.50}$$

$$\sigma_{V_r V_j}(\omega) = \sigma_{I_r I_j}(\omega) = 0 \tag{8.51}$$

$$\sigma_{V_r I_r}(\omega) = \sigma_{V_j I_j}(\omega) \tag{8.52}$$

$$\sigma_{V_j I_r}(\omega) = -\sigma_{V_r I_j}(\omega). \tag{8.53}$$

Equations (8.39)-(8.48) satisfy the conditions of equations (8.49)-(8.53).

By introducing noise transformed through the system into the correlation functions, the correlation functions related to noise in the voltage signal are no longer as simply described as for the Milocco and Biagiola experiment. [117] Peaks will now exist at time-shifts associated with the impedance function. The auto-correlation functions for noise added to the current and the noise in the voltage resulting from the transformed current noise is plotted in Figure 8.4. The system impedance had a characteristic frequency of 10 kHz. A close-up around zero of the auto-correlation functions is shown in Figure 8.5. The peak in the auto-correlation function of the transformed current noise in the voltage was broader than the peak in the auto-correlation function of the current. This broad peak decayed with a time constant consistent with the characteristic time-constant for the system impedance. Thus, the integrand was non-zero at other time-shifts than zero, and therefore, the conditions of equations (8.49)-(8.53) were not met. The products of the auto-correlation functions and the trigonometric functions of the time-

shift variable are shown in Figure 8.6. It is clear that the integrands for current are essentially zero, while the integrands for voltage are not zero, and are not equal to each other. As a result, the conditions of equations (8.49)-(8.53) will no longer be necessarily satisfied. Note that when the variance vector is determined by calculating the sample expectations of the observed replicate estimations of the complex components of the current and voltage signals, the solution to the equality of the Taylor series expansions for variances in the real and imaginary impedances given by equations (8.49)-(8.53) is satisfied.

Further evidence of this result can be found through examination of Table 8.2 and Table 8.3. The solution of the equality of the Taylor series expansions is tested for CASE 1 and CASE 3 by calculating the student's t-test parameter for each equality (equations (8.49)-(8.53)). Each component of the variance vector was calculated at each frequency of the spectrum, and the t-test was applied to the spectrum of values. The conditions of equations (8.49)-(8.53) for equality of the variances in the real and imaginary impedances are satisfied generally by the functional variances for CASE 1, while they are satisfied only for the functional variances in current for CASE 3. The current condition is satisfied for CASE 3 since noise in that signal is purely additive. The functional variances in voltage are not satisfied since the noise in that signal contains a transformed component. Note that in both cases, the sample variances satisfy equations (8.49)-(8.53). Therefore, the functional definition of variance cannot be arbitrarily applied to impedance spectra with an expectation that the variance in the real impedance will be equal to the variance in the imaginary impedance.

8.1.3 Sample Variance Based on Expectation of Discrete Measurements

The form of variance defined in the previous two sections is a functional variance. This means that the variance in the impedance can be determined through one measurement. The observation that the variances in the stochastic errors in the real and imaginary impedances are equal has been made when the variances are calculated as sample variances from replicate measurement of the stochastic errors.[6-9] The previously derived variances are not sample variances; rather they are the variances around the expectation of the individual signals summed over each instance of time. The sample variance can be derived by redefining expectation as an averaging of samples rather than as an integral average over time.

Details of the following derivation can be found in Appendix B. The components of the Taylor series variance vector determined using the definition of sample variance are

$$\sigma_{V_r}^2(\omega)=\frac{\omega^2/4\pi^2n^2}{(N-1)}\int_0^{2\pi n/\omega}\int_0^{2\pi n/\omega}\left\{\sum_{k=1}^{N}\left[\begin{array}{l}[n_{V,k}(u)-E(n_{V,k})]\\ \times[n_{V,k}(v)-E(n_{V,k})]\end{array}\right]\right\}\sin(\omega u)\sin(\omega v)dudv \tag{8.54}$$

$$\sigma_{V_J}^2(\omega)=\frac{\omega^2/4\pi^2n^2}{(N-1)}\int_0^{2\pi n/\omega}\int_0^{2\pi n/\omega}\left\{\sum_{k=1}^{N}\left[\begin{array}{l}[n_{V,k}(u)-E(n_{V,k})]\\ \times[n_{V,k}(v)-E(n_{V,k})]\end{array}\right]\right\}\cos(\omega u)\cos(\omega v)dudv \tag{8.55}$$

$$\sigma_{I_r}^2(\omega)=\frac{\omega^2/4\pi^2n^2}{(N-1)}\int_0^{2\pi n/\omega}\int_0^{2\pi n/\omega}\left\{\sum_{k=1}^{N}\left[\begin{array}{l}[n_{I,k}(u)-E(n_{I,k})]\\ \times[n_{I,k}(v)-E(n_{I,k})]\end{array}\right]\right\}\sin(\omega u)\sin(\omega v)dudv \tag{8.56}$$

$$\sigma_{I_J}^2(\omega)=\frac{\omega^2/4\pi^2n^2}{(N-1)}\int_0^{2\pi n/\omega}\int_0^{2\pi n/\omega}\left\{\sum_{k=1}^{N}\left[\begin{array}{l}[n_{I,k}(u)-E(n_{I,k})]\\ \times[n_{I,k}(v)-E(n_{I,k})]\end{array}\right]\right\}\cos(\omega u)\cos(\omega v)dudv\,. \tag{8.57}$$

$$\sigma_{V_rV_j}(\omega)=\frac{\omega^2/4\pi^2n^2}{(N-1)}\int_0^{2\pi n/\omega}\int_0^{2\pi n/\omega}\left\{\sum_{k=1}^{N}\left[\begin{array}{l}[n_{V,k}(u)-E(n_{V,k})]\\ \times[n_{V,k}(v)-E(n_{V,k})]\end{array}\right]\right\}\sin(\omega u)\cos(\omega v)dudv \tag{8.58}$$

$$\sigma_{I_r I_J}(\omega)=\frac{\omega^2/4\pi^2 n^2}{(N-1)}\int_0^{2\pi n/\omega}\int_0^{2\pi n/\omega}\left\{\sum_{k=1}^{N}\left[\begin{array}{l}\left[n_{I,k}(u)-E(n_{I,k})\right]\\ \times\left[n_{I,k}(v)-E(n_{I,k})\right]\end{array}\right]\right\}\sin(\omega u)\cos(\omega v)dudv \tag{8.59}$$

$$\sigma_{V_r I_r}(\omega)=\frac{\omega^2/4\pi^2 n^2}{(N-1)}\int_0^{2\pi n/\omega}\int_0^{2\pi n/\omega}\left\{\sum_{k=1}^{N}\left[\begin{array}{l}\left[n_{V,k}(u)-E(n_{V,k})\right]\\ \times\left[n_{I,k}(v)-E(n_{I,k})\right]\end{array}\right]\right\}\sin(\omega u)\sin(\omega v)dudv \tag{8.60}$$

$$\sigma_{V_r I_J}(\omega)=\frac{\omega^2/4\pi^2 n^2}{(N-1)}\int_0^{2\pi n/\omega}\int_0^{2\pi n/\omega}\left\{\sum_{k=1}^{N}\left[\begin{array}{l}\left[n_{V,k}(u)-E(n_{V,k})\right]\\ \times\left[n_{I,k}(v)-E(n_{I,k})\right]\end{array}\right]\right\}\sin(\omega u)\cos(\omega v)dudv \tag{8.61}$$

$$\sigma_{V_j I_r}(\omega)=\frac{\omega^2/4\pi^2 n^2}{(N-1)}\int_0^{2\pi n/\omega}\int_0^{2\pi n/\omega}\left\{\sum_{k=1}^{N}\left[\begin{array}{l}\left[n_{V,k}(u)-E(n_{V,k})\right]\\ \times\left[n_{I,k}(v)-E(n_{I,k})\right]\end{array}\right]\right\}\cos(\omega u)\sin(\omega v)dudv \tag{8.62}$$

$$\sigma_{V_j I_J}(\omega)=\frac{\omega^2/4\pi^2 n^2}{(N-1)}\int_0^{2\pi n/\omega}\int_0^{2\pi n/\omega}\left\{\sum_{k=1}^{N}\left[\begin{array}{l}\left[n_{V,k}(u)-E(n_{V,k})\right]\\ \times\left[n_{I,k}(v)-E(n_{I,k})\right]\end{array}\right]\right\}\cos(\omega u)\cos(\omega v)dudv\,. \tag{8.63}$$

Thus, the variance is calculated via integration of the average value of planar waves constructed by the matrix product of two noise signals. In order to calculate these variance components, the noise in each signal must be measured and stored for each replicate measurement of the impedance. This method of calculation requires more data storage than does the functional variance method. It will be shown, however, that this is the appropriate manner to deal with variance in the complex components of the current and voltage signals.

8.1.4 Simulation Studies of Variance Based on Expectation in a Sampling Sense

A LabView® code was constructed through which equations (8.54)-(8.63) were calculated directly. Bode integration[123] was used to calculate the integrals. Three cycles of perturbation and response signal were used to calculate the impedance at each frequency. The calculation was replicated 100 times. The corresponding three cycles of the noise signals were stored for each frequency and each replicate measurement. The components of the sample variance vector were calculated at 16 frequencies. Only one

case was studied due to time restrictions associated with the numerically intensive calculations associated with the sample variance vector. The one case studied consisted of adding noise to the input and output signals, and allowing the noise in the input signal to be transformed by the system into the output signal.

The ratio of variance in the real impedance to variance in the imaginary impedance was calculated from the Taylor series expansions. The ratio was calculated using a sample variance vector defined by equations (8.54)-(8.63) and using the sample variances, covariances, and cross-covariances calculated directly from the replicate estimates of the complex components of the perturbation and response signals. The F-tests for the ratios are shown in Figure 8.7. The test is satisfied for both methods of calculation. The student's t-test parameters are listed in Table 8.4 and the test is satisfied for the probability of five percent in both calculations.

The ratios calculated through the equations or through the replicate observations appear to be equal as shown in Figure 8.7. This was tested by taking the difference between and ratio of the ratios in impedance variances calculated using the two approaches, and applying the student's t-test over the spectrum. The mean difference was equal to zero, and the mean ratio was equal to one (Table 8.5). Thus, equations (8.54)-(8.63) provide means of calculating the variance vector for the Taylor series expansions of the variances in the complex components of the impedance which result in excellent approximation of the observed variances in the same components.

8.2 Variance as a Result of Phase-Sensitive Detection

A similar procedure can be used to calculate the variance of the stochastic errors in the magnitudes of the voltage and current signals. Not all ten components of the polar form of the variance vector for PSD can be determined through the procedure, since the

magnitude and phase angles of the signals are measured independently. The magnitudes of the two signals are calculated as

$$|V(\omega)| = \frac{1}{2\pi n/\omega}\left[\int_0^{2\pi n/\omega} \hat{V}\sin(\omega t+\phi_V)\,\mathrm{square}(\omega t+\phi_{s,V})dt + \int_0^{2\pi n/\omega} n_V(t)\,\mathrm{square}(\omega t+\phi_{s,V})dt\right] \tag{8.64}$$

$$|I(\omega)| = \frac{1}{2\pi n/\omega}\left[\int_0^{2\pi n/\omega} \hat{I}\sin(\omega t+\phi_I)\,\mathrm{square}(\omega t+\phi_{s,I})dt + \int_0^{2\pi n/\omega} n_I(t)\,\mathrm{square}(\omega t+\phi_{s,I})dt\right] \tag{8.65}$$

where the first integral corresponds to the expectation value of the magnitude and the second integral corresponds to any error in the evaluation resulting from the time-averaging of the noise in the signal.

8.2.1 Variance Defined by Expectation Integration over Time

The functional variance of each magnitude can be written as the time-domain expectation of the square of the difference of the magnitude and the expected value of the magnitude. If the expectations of the noise signals are zero, then the functional variances can be written as

$$\sigma_{|V|}^2 = \frac{1}{4\pi^2 n^2/\omega^2} E\left[\int_0^{2\pi n/\omega}\int_0^{2\pi n/\omega} n_V(x)n_V(y)\,\mathrm{square}(\omega x+\phi_{s,V})\,\mathrm{square}(\omega y+\phi_{s,V})dxdy\right] \tag{8.66}$$

$$\sigma_{|I|}^2 = \frac{1}{4\pi^2 n^2/\omega^2} E\left[\int_0^{2\pi n/\omega}\int_0^{2\pi n/\omega} n_I(x)n_I(y)\,\mathrm{square}(\omega x+\phi_{s,I})\,\mathrm{square}(\omega y+\phi_{s,I})dxdy\right]. \tag{8.67}$$

Since the noise signals are considered as purely stochastic functions, then they are uncorrelated with the square waves. Therefore, the phase angles of the two square waves can be neglected, since they should not affect the value of the integrals.

The square waves can be written as Fourier series by

$$\mathrm{square}(\omega t) = \sum_{k=0}^{\infty} \frac{1}{2k+1}\sin[(2k+1)\omega t] \tag{8.68}$$

and introduced into equations (8.66) and (8.67) such that the variances are

$$\sigma_{|V|}^2 = \frac{1}{4\pi^2 n^2/\omega^2} E\left[\int_0^{2\pi n/\omega}\int_0^{2\pi n/\omega}\sum_{k=0}^{\infty}\sum_{l=0}^{\infty}\frac{n_V(x)n_V(y)}{(2k+1)(2l+1)}\begin{Bmatrix}\sin[(2k+1)\omega x]\\ \times\sin[(2l+1)\omega y]\end{Bmatrix}dxdy\right] \tag{8.69}$$

$$\sigma_{|I|}^2 = \frac{1}{4\pi^2 n^2/\omega^2} E\left[\int_0^{2\pi n/\omega}\int_0^{2\pi n/\omega}\sum_{k=0}^{\infty}\sum_{l=0}^{\infty}\frac{n_I(x)n_I(y)}{(2k+1)(2l+1)}\begin{Bmatrix}\sin[(2k+1)\omega x]\\ \times\sin[(2l+1)\omega y]\end{Bmatrix}dxdy\right]. \tag{8.70}$$

where the double summation is the result of the product of the square waves. The expectations can be brought inside the double integrals and double summations. Upon introduction of the definition of the auto-correlation function, the variances can be rewritten as

$$\sigma_{|V|}^2 = \frac{1}{4\pi^2 n^2/\omega^2}\int_0^{2\pi n/\omega}\int_0^{2\pi n/\omega}\psi_{n_V n_V}(\tau)\sum_{k=0}^{\infty}\sum_{l=0}^{\infty}\frac{1}{(2k+1)(2l+1)}\begin{Bmatrix}\sin[(2k+1)\omega x]\\ \times\sin[(2l+1)\omega y]\end{Bmatrix}dxdy \tag{8.71}$$

$$\sigma_{|I|}^2 = \frac{1}{4\pi^2 n^2/\omega^2}\int_0^{2\pi n/\omega}\int_0^{2\pi n/\omega}\psi_{n_I n_I}(\tau)\sum_{k=0}^{\infty}\sum_{l=0}^{\infty}\frac{1}{(2k+1)(2l+1)}\begin{Bmatrix}\sin[(2k+1)\omega x]\\ \times\sin[(2l+1)\omega y]\end{Bmatrix}dxdy\,. \tag{8.72}$$

where

$$\tau = y - x \tag{8.73}$$

Through the definition of the time-shift variable, τ, the variance equations can be expressed as the sum of two sets of double integral over separate domains

$$\begin{aligned}&\left(4\pi^2 n^2/\omega^2\right)\sigma_{|V|}^2 = \\ &\int_0^{2\pi n/\omega} d\tau\,\psi_{n_V n_V}(\tau)\int_0^{(2\pi n/\omega)-\tau}\sum_{k=0}^{\infty}\sum_{l=0}^{\infty}\frac{1}{(2k+1)(2l+1)}\begin{Bmatrix}\sin[(2k+1)\omega x]\\ \times\sin[(2l+1)\omega(x+\tau)]\end{Bmatrix}dx\\ &+\int_0^{2\pi n/\omega} d\tau\,\psi_{n_V n_V}(\tau)\int_0^{(2\pi n/\omega)+\tau}\sum_{k=0}^{\infty}\sum_{l=0}^{\infty}\frac{1}{(2k+1)(2l+1)}\begin{Bmatrix}\sin[(2k+1)\omega(y-\tau)]\\ \times\sin[(2l+1)\omega y]\end{Bmatrix}dy\end{aligned} \tag{8.74}$$

$$\left(4\pi^2 n^2/\omega^2\right)\sigma_{|l|}^2 = \tag{8.75}$$
$$\int_0^{2\pi n/\omega} d\tau\, \psi_{n_l n_l}(\tau) \int_0^{(2\pi n/\omega)-\tau} \sum_{k=0}^{\infty}\sum_{l=0}^{\infty} \frac{1}{(2k+1)(2l+1)} \begin{Bmatrix} \sin[(2k+1)\omega x] \\ \times \sin[(2l+1)\omega(x+\tau)] \end{Bmatrix} dx \;.$$
$$+ \int_0^{2\pi n/\omega} d\tau\, \psi_{n_l n_l}(\tau) \int_0^{(2\pi n/\omega)+\tau} \sum_{k=0}^{\infty}\sum_{l=0}^{\infty} \frac{1}{(2k+1)(2l+1)} \begin{Bmatrix} \sin[(2k+1)\omega(y-\tau)] \\ \times \sin[(2l+1)\omega y] \end{Bmatrix} dy$$

Since the auto-correlation function is symmetric around zero, the variances can be simplified. Note that the choice of summation variable (k or l) is arbitrary, and therefore the first and second double integrals are equal if a negative time-shift is introduced into the second double integral.

$$\left(2\pi^2 n^2/\omega^2\right)\sigma_{|V|}^2 = \tag{8.76}$$
$$\int_0^{2\pi n/\omega} d\tau\, \psi_{n_V n_V}(\tau) \int_0^{(2\pi n/\omega)-\tau} \sum_{k=0}^{\infty}\sum_{l=0}^{\infty} \frac{1}{(2k+1)(2l+1)} \sin[(2k+1)\omega x]\sin[(2l+1)\omega(x+\tau)]dx$$

$$\left(2\pi^2 n^2/\omega^2\right)\sigma_{|l|}^2 = \tag{8.77}$$
$$\int_0^{2\pi n/\omega} d\tau\, \psi_{n_l n_l}(\tau) \int_0^{(2\pi n/\omega)-\tau} \sum_{k=0}^{\infty}\sum_{l=0}^{\infty} \frac{1}{(2k+1)(2l+1)} \sin[(2k+1)\omega x]\sin[(2l+1)\omega(x+\tau)]dx \;.$$

The product of sines can be written as the difference of cosines, making the inner integration possible.

$$\left(4\pi^2 n^2/\omega^2\right)\sigma_{|V|}^2 = \tag{8.78}$$
$$\int_0^{2\pi n/\omega} \begin{Bmatrix} d\tau\, \psi_{n_V n_V}(\tau) \\ \times \int_0^{(2\pi n/\omega)-\tau} dx \sum_{k=0}^{\infty}\sum_{l=0}^{\infty} \frac{1}{(2k+1)(2l+1)} \begin{Bmatrix} \cos[(2k+1)\omega x - (2l+1)\omega(x+\tau)] \\ -\cos[(2k+1)\omega x + (2l+1)\omega(x+\tau)] \end{Bmatrix} \end{Bmatrix}$$

$$\left(4\pi^2 n^2/\omega^2\right)\sigma_{|l|}^2 = \tag{8.79}$$
$$\int_0^{2\pi n/\omega} \begin{Bmatrix} d\tau\, \psi_{n_l n_l}(\tau) \\ \int_0^{(2\pi n/\omega)-\tau} dx \sum_{k=0}^{\infty}\sum_{l=0}^{\infty} \frac{1}{(2k+1)(2l+1)} \begin{Bmatrix} \cos[(2k+1)\omega x - (2l+1)\omega(x+\tau)] \\ -\cos[(2k+1)\omega x + (2l+1)\omega(x+\tau)] \end{Bmatrix} \end{Bmatrix} .$$

The angular expressions can be simplified and the inner integral can be calculated

$$\sigma_{|V|}^2 = \frac{1}{\left(8\pi^2 n^2/\omega^2\right)} \int_0^{2\pi n/\omega} d\tau\, \psi_{n_V n_V}(\tau) \sum_{k=0,k\neq l}^{\infty} \sum_{l=0}^{\infty} \left[\begin{array}{l} \left\{ \frac{1}{(k+l+1)} - \frac{1}{(k-l)} \right\} \\ \times \left\{ \sin[(2k+1)\omega\tau] + \sin[(2l+1)\omega\tau] \right\} \end{array} \right] \tag{8.80}$$

$$\sigma_{|I|}^2 = \frac{1}{\left(8\pi^2 n^2/\omega^2\right)} \int_0^{2\pi n/\omega} d\tau\, \psi_{n_I n_I}(\tau) \sum_{k=0,k\neq l}^{\infty} \sum_{l=0}^{\infty} \left[\begin{array}{l} \left\{ \frac{1}{(k+l+1)} - \frac{1}{(k-l)} \right\} \\ \times \left\{ \sin[(2k+1)\omega\tau] + \sin[(2l+1)\omega\tau] \right\} \end{array} \right] \tag{8.81}$$

where the summation over k does not include the case where k is equal to l. Analysis of the cross-covariance between the magnitudes in the voltage and current follows a similar derivation except at the point at which the symmetry of the auto-correlation function is employed. Therefore, the signal magnitude cross-covariance can be expressed as

$$\sigma_{|I||V|} = \frac{1}{\left(8\pi^2 n^2/\omega^2\right)} \int_0^{2\pi n/\omega} d\tau \left\{ \begin{array}{l} \left[\psi_{n_I n_V}(\tau) + \psi_{n_V n_I}(\tau) \right] \\ \times \sum_{k=0,k\neq l}^{\infty} \sum_{l=0}^{\infty} \left[\begin{array}{l} \left\{ \frac{1}{(k+l+1)} - \frac{1}{(k-l)} \right\} \\ \times \left\{ \sin[(2k+1)\omega\tau] + \sin[(2l+1)\omega\tau] \right\} \end{array} \right] \end{array} \right\} \tag{8.82}$$

The standard deviation in the phase angle measurement is independent of the calculation of the signal magnitudes because the phase angle is reported as the controlled value of the angle for which the PSD integral is maximum. Therefore, a natural correlation between the magnitude variances and the variances of or covariances with the phase angles does not necessarily exist. As a result, there is no expectation that these integral results for the variances of the magnitudes should satisfy the equality of the polar forms of the Taylor series expansion for variance in the real and imaginary impedances.

8.2.2 Variance Based on Expectation in a Sampling Sense

The sample variance can be derived in similar fashion as described for the FRA measurement. The sample variance is determined by averaging the product of noise

signals over each measurement interval. The three components of the Taylor series variance vector that do not include a phase angle measurement are

$$\sigma_{|V|}^2 = \frac{\int_0^{2\pi n/\omega}\int_0^{2\pi n/\omega} dudv \left[\begin{array}{l} \left\{ \sum_{m=1}^{N} \left[n_{V,m}(u) - E(n_{V,m}) \right] \left[n_{V,m}(v) - E(n_{V,m}) \right] \right\} \\ \times \sum_{k=0}^{\infty} \sum_{l=0}^{\infty} \frac{1}{(2k+1)(2l+1)} \sin[(2k+1)\omega u] \sin[(2l+1)\omega v] \end{array} \right]}{2\pi n(N-1)/\omega} \tag{8.83}$$

$$\sigma_{|I|}^2 = \frac{\int_0^{2\pi n/\omega}\int_0^{2\pi n/\omega} dudv \left[\begin{array}{l} \left\{ \sum_{m=1}^{N} \left[n_{I,m}(u) - E(n_{I,m}) \right] \left[n_{I,m}(v) - E(n_{I,m}) \right] \right\} \\ \times \sum_{k=0}^{\infty} \sum_{l=0}^{\infty} \frac{1}{(2k+1)(2l+1)} \sin[(2k+1)\omega u] \sin[(2l+1)\omega v] \end{array} \right]}{2\pi n(N-1)/\omega} \tag{8.84}$$

$$\sigma_{|I||V|} = \frac{\int_0^{2\pi n/\omega}\int_0^{2\pi n/\omega} dudv \left[\begin{array}{l} \left\{ \sum_{m=1}^{N} \left[n_{I,m}(u) - E(n_{I,m}) \right] \left[n_{V,m}(v) - E(n_{V,m}) \right] \right\} \\ \times \sum_{k=0}^{\infty} \sum_{l=0}^{\infty} \frac{1}{(2k+1)(2l+1)} \sin[(2k+1)\omega u] \sin[(2l+1)\omega v] \end{array} \right]}{2\pi n(N-1)/\omega} \tag{8.85}$$

For details on this derivation, refer to Appendix B. Again, the standard deviation of the voltage and current phase angles will be dependent upon the phase controller used in the PSD measurement. Therefore, these integral results cannot be calculated and introduced into the polar forms of the Taylor series expansions for the variances in the real and imaginary impedances since the seven components of the variance vector that contain the standard deviations in the phase angles are unknown.

8.3 Conclusions

The variance in the real and imaginary impedance are correlated to the complex current and voltage through ten-term Taylor series expansions as shown in Chapter 6. Thus, to determine analytically the variance in the real and imaginary impedance as a

function of the noise in the constituent current and voltage signals, it was necessary to analytically determine the ten components of the variance vector associated with the Taylor series expansions. The components were determined for both the FRA and PSD techniques.

Two definitions of variance were considered. One was a functional variance, and the other was a sample variance. The functional variance was defined to be the variance of the quantity with respect to its time-domain functionality. As the mean of a function is proportional to the integral of that function, the variance of a signal was considered to be the integral over time of the frequency-domain description of the square of the signal. Since the frequency-domain description of the square of the signal was calculated as a double integral over time, the functional variance was calculated as the triple integral over time of the square of the signal. For covariances, the square was replaced with the product of two signals. The sample (co)variance was calculated as the average of replicate observations of the frequency-domain description of the square of the signal (or product of two signals).

The ten components of the variance vector were calculated for both FRA definitions of the variance. One hundred replicate measurements of the impedance were made at each frequency. Each measurement of the complex impedance was made over three cycles of the current and voltage signal. The long-integration convergence criterion was met at three cycles. The functional variance determined for the reported impedance was averaged over the 100 replicate measurements. The integral form of the sample variance was calculated for the sample population of 100 at each frequency. A sample variance was also calculated from the 100 observation of complex current and voltage.

The variances in the real and imaginary impedances were calculated by taking the vector product of an estimated variance vector and the appropriate Taylor series coefficient vector. The variances in the real and imaginary impedances were equal when the variance vector components were estimated as either form of the sample variances. The ratio of the variance in the real impedance to the variance in the imaginary impedance was a function of frequency when the functional variance was used to calculate the components of the variance vector. The sample variance calculations were similar to the variance estimation used in the Measurement Model Tools designed by Orazem and co-workers.[6-9] Their observation of the equivalence of the variances in the stochastic errors in the real and imaginary impedances is consistent with the result of the Taylor series expansions for variance using the sample variance estimation of the variance vector. The proposal by Milocco[117] that the variances in the real and imaginary impedance were equal was stated for variances calculated in the functional form. The results of these simulations suggest that the Milocco proposal only holds true if the noise in the signal is not transformed by the system. When there was noise in the current that was propagated into the voltage, the functional variances of the real and imaginary impedances were not equal.

Simulations could not be performed to determine the variance vector for the PSD definitions of the variance since only the three components of the vector which are independent of phase angle can be determined analytically. The other seven components would be set by the noise associated with the phase angle controller. This is another example of the inability of the PSD technique to measure impedance that have equivalent variances in the real and imaginary components. It was shown in the previous chapter

that the equality of the variances in the complex impedance components was a result of the satisfaction of a set of six equality conditions. These conditions can not necessarily be met if the error in the phase angle of each signal is independent of (not from the same source as) the error in the magnitude.

Table 8.1: Student's t-test results for ratio of variance in real impedance to variance in imaginary impedance calculated through Taylor series expansions for variance in complex components of the impedance. Variance vector was calculated as functional variance (F) through the integral equations and as sample variance (S) from observed replicate values of the complex components of the voltage and current signals

CASE	VARIANCE	t_{calc}	$t_{0.025,n-1}$	$t_{calc}/ t_{0.025,n-1}$
1	F	1.289	1.987	0.649
1	S	0.587	1.987	0.296
2	F	12.1	1.987	6.11
2	S	0.787	1.987	0.396
3	F	10.9	1.987	5.48
3	S	0.391	1.987	0.197

Table 8.2: Student's t-tests for trivial solution conditions for equality of variance in the real and imaginary impedances described by the linear Taylor series expansion. Calculations were conducted for the CASE 1 scenario, noise added to the input and output signal, without input noise transformed by the system.

	FUNCTIONAL VARIANCE		SAMPLE VARIANCE	
RATIO	t_{calc}	$t_{calc}/t_{0.025,n-1}$	t_{calc}	$t_{calc}/t_{0.025,n-1}$
$\sigma^2_{V_r}/\sigma^2_{V_j}=1$	1.687	0.849	0.375	0.189
$\sigma^2_{I_r}/\sigma^2_{I_j}=1$	0.479	0.241	0.175	0.088
$\sigma_{V_rI_r}/\sigma_{V_jI_j}=1$	0.664	0.334	0.868	0.437
$\sigma_{V_rI_j}/\sigma_{V_jI_r}=-1$	-	-	4.72	2.38
$\sigma_{V_rV_j}=0$	-	-	1.411	0.710
$\sigma_{I_rI_j}=0$	-	-	0.494	0.248

Table 8.3: Student's t-tests for trivial solution conditions for equality of variance in the real and imaginary impedances described by the linear Taylor series expansion. Calculations were conducted for the CASE 3 scenario, noise added to the input and output signal, with output noise including input noise transformed by the system.

	FUNCTIONAL VARIANCE		SAMPLE VARIANCE	
RATIO	t_{calc}	$t_{calc}/t_{0.025,n-1}$	t_{calc}	$t_{calc}/t_{0.025,n-1}$
$\sigma^2_{V_r}/\sigma^2_{V_j}=1$	10.7	5.40	1.087	0.547
$\sigma^2_{I_r}/\sigma^2_{I_j}=1$	0.0833	0.0419	0.961	0.484
$\sigma_{V_rI_r}/\sigma_{V_jI_j}=1$	10.9	5.46	1.189	0.598
$\sigma_{V_rI_j}/\sigma_{V_jI_r}=-1$	-	-	1.474	0.742
$\sigma_{V_rV_j}=0$	-	-	1.760	0.886
$\sigma_{I_rI_j}=0$	-	-	1.473	0.742

Table 8.4: Student's t-test results for ratio of variance in real impedance to variance in imaginary impedance calculated through Taylor series expansions for variance in complex components of the impedance. Variance vector was calculated as the analytical sample variance (A) through the integral equations and as sample variance (S) from observed replicate values of the complex components of the voltage and current signals

VARIANCE	t_{calc}	$t_{0.025,n-1}$	$t_{calc}/ t_{0.025,n-1}$
A	0.907	2.131	0.426
S	1.016	2.131	0.477

Table 8.5: Student's t-test results for the difference between and ratio of the ratio of variance in real impedance to variance in imaginary impedance calculated through Taylor series expansions for variance in complex components of the impedance. The variance vector was calculated as the analytical sample variance through the integral equations and as sample variance from observed replicate values of the complex components of the voltage and current signals

Operation	t_{calc}	$t_{0.025,n-1}$	$t_{calc}/ t_{0.025,n-1}$
Difference	0.806	2.131	0.378
Ratio	1.132	2.131	0.531
log(Ratio)	1.160	2.131	0.544

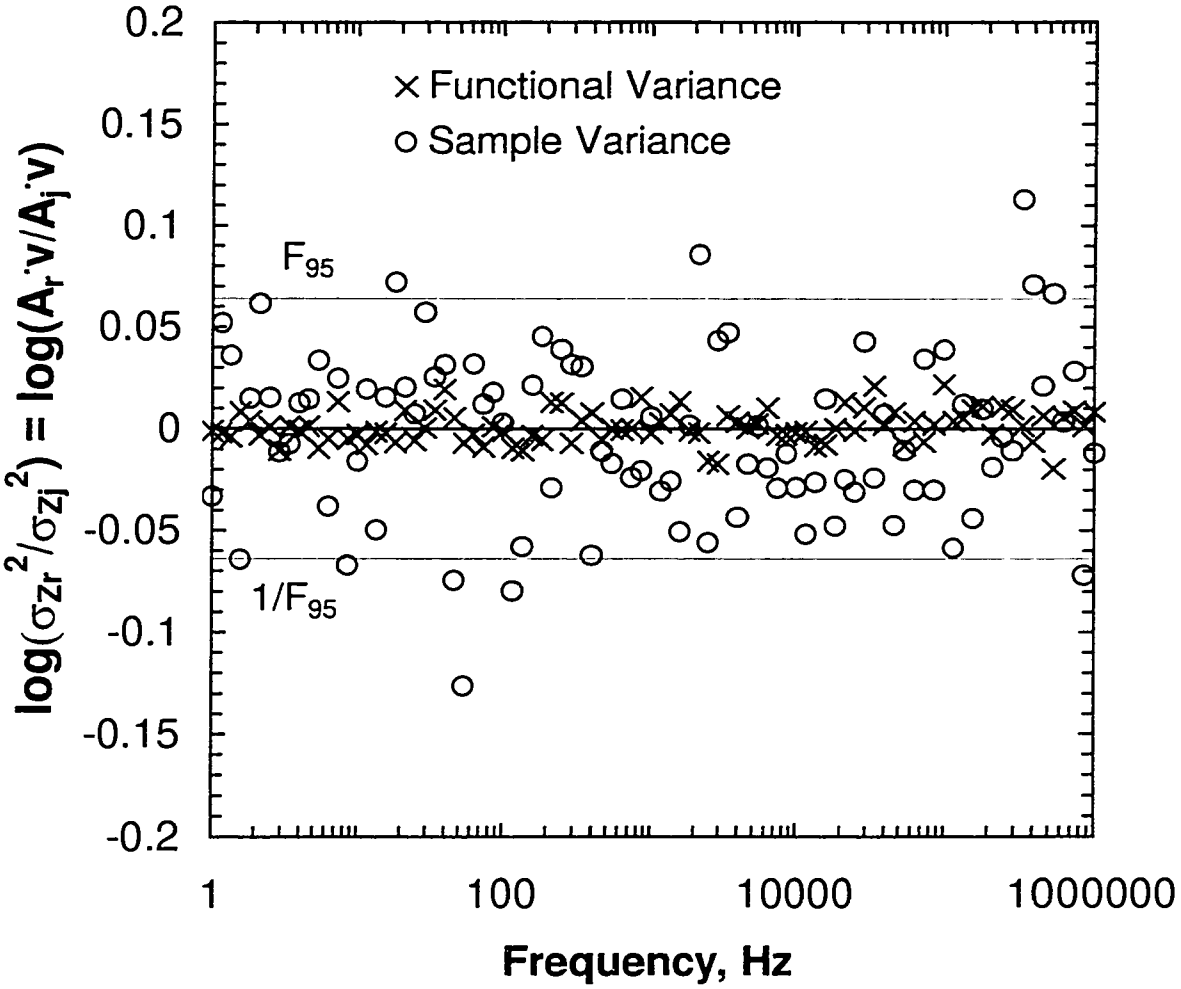

Figure 8.1: F-test for CASE 1, in which noise was added to input and output signals and not transformed through system. Functional variance is calculated through the derived integral equations, while the sample variance was calculated by sample expectation of the observed replicate calculations of the complex components of the voltage and current signals.

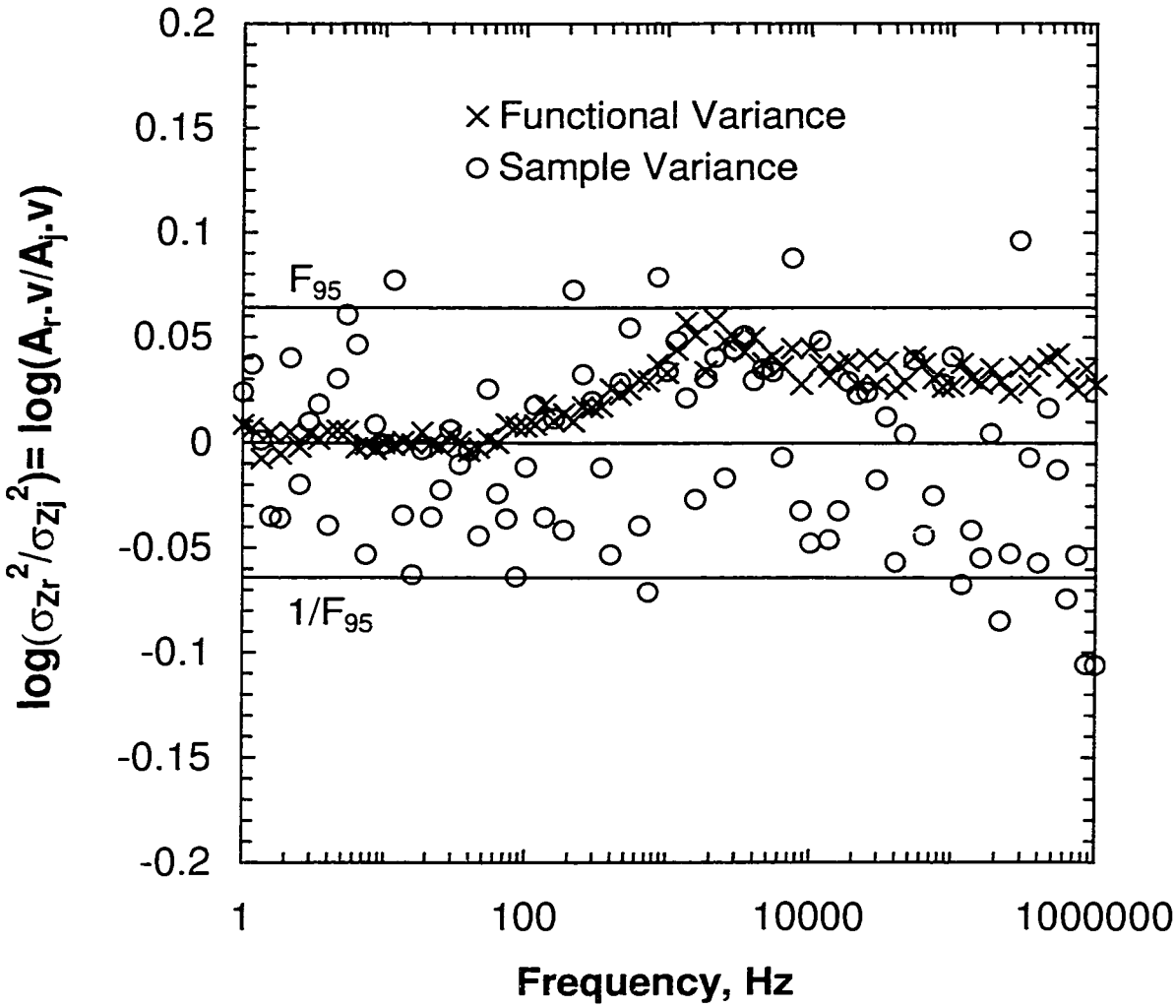

Figure 8.2: F-test for CASE 2, in which noise was added to input signal and transformed through system. Functional variance is calculated through the derived integral equations, while the sample variance was calculated by sample expectation of the observed replicate calculations of the complex components of the voltage and current signals.

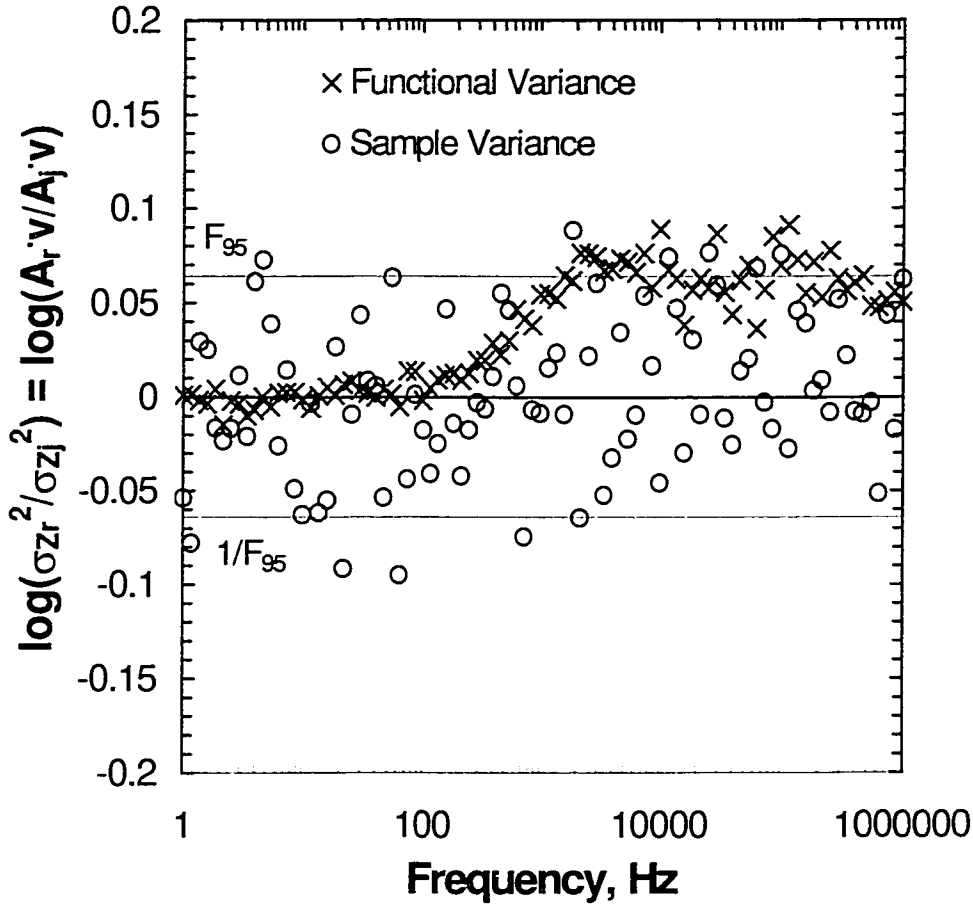

Figure 8.3: F-test for CASE 3, in which noise was added to input and output signals and transformed through system. Functional variance was calculated through the derived integral equations, while the sample variance was calculated by sample expectation of the observed replicate calculations of the complex components of the voltage and current signals.

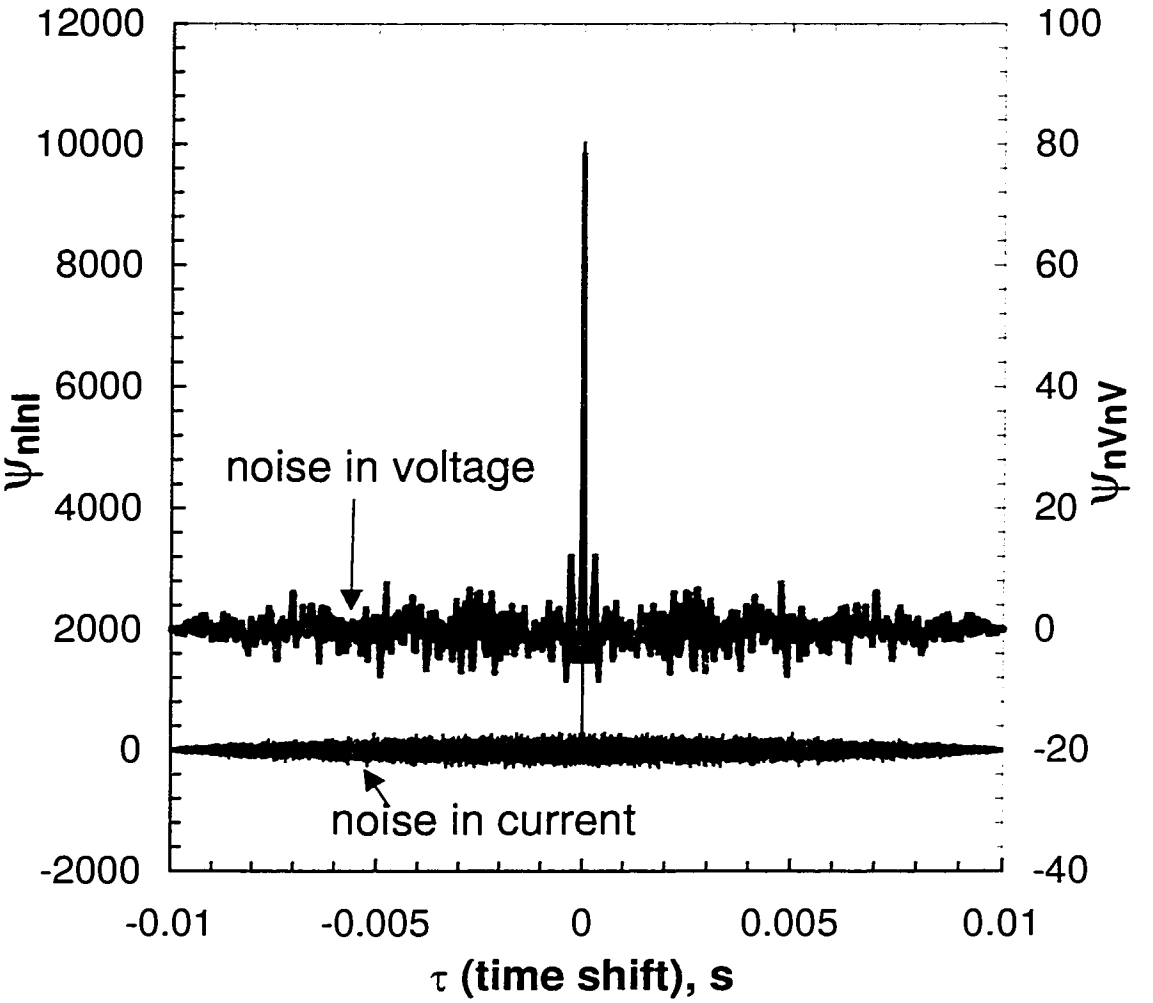

Figure 8.4: Auto-correlation function for noise in current signal and transformed noise in voltage signal from the noise in current for a Voigt element transfer function with a characteristic frequency of 10 kHz.

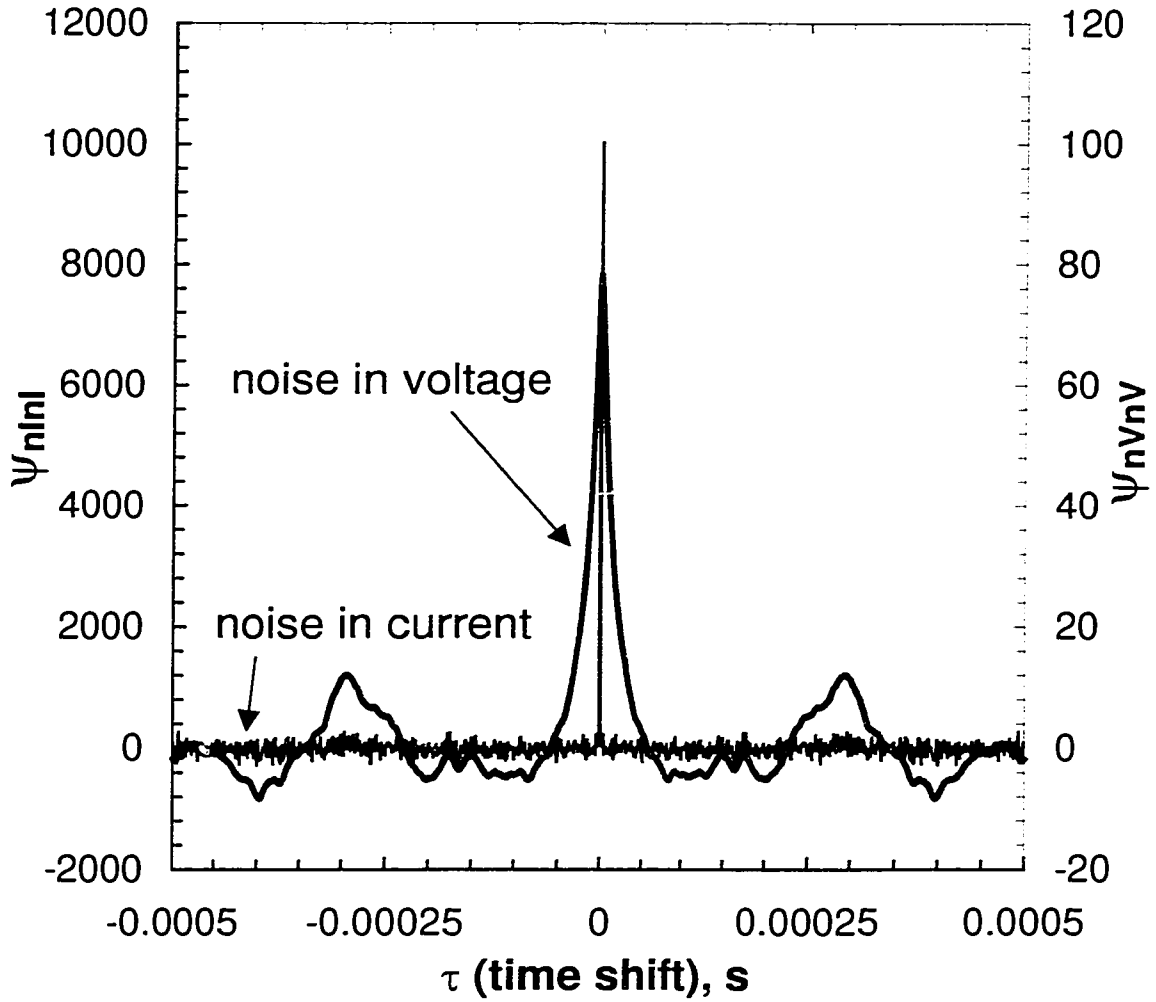

Figure 8.5: Close-up around zero of the auto-correlation functions for noise in current signal and transformed noise in voltage signal from the noise in current for a Voigt element transfer function with a characteristic frequency of 10 kHz.

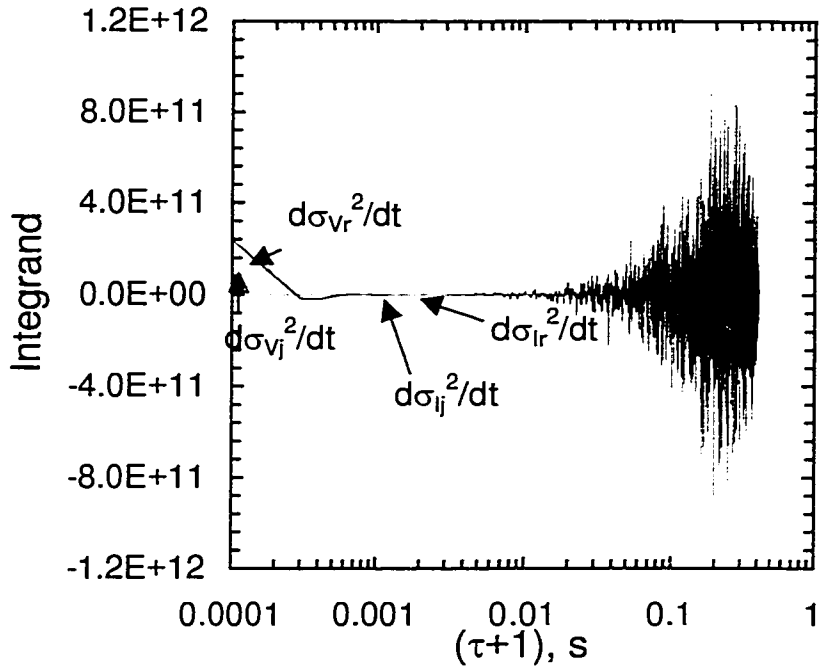

(a)

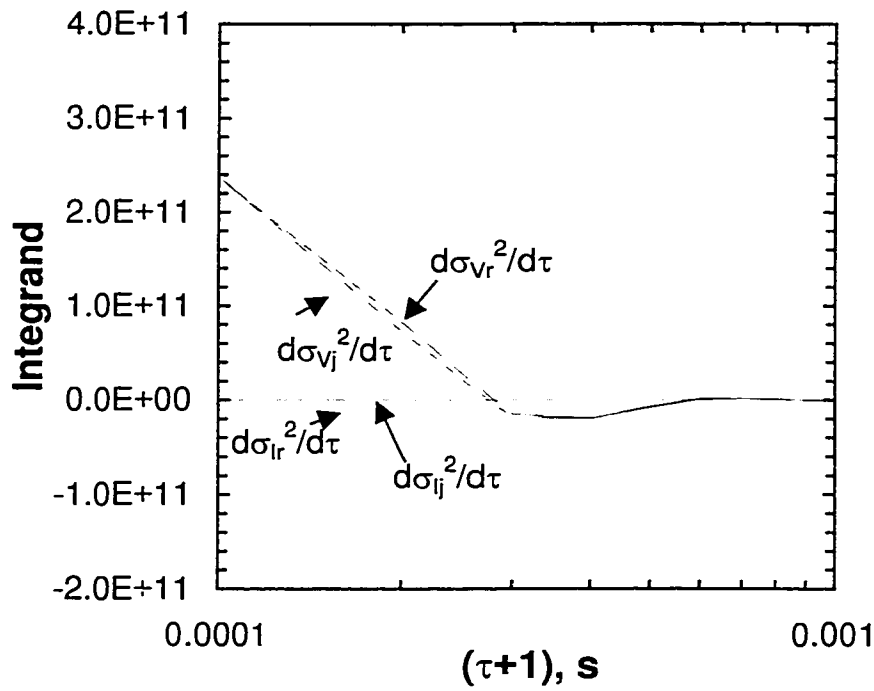

(b)

Figure 8.6: Integrands functions for the variance in real and imaginary voltage and real and imaginary current. (a) Integrand in voltage is significantly different than integrand in current. (b) Integrand for real voltage is different that integrand for imaginary voltage.

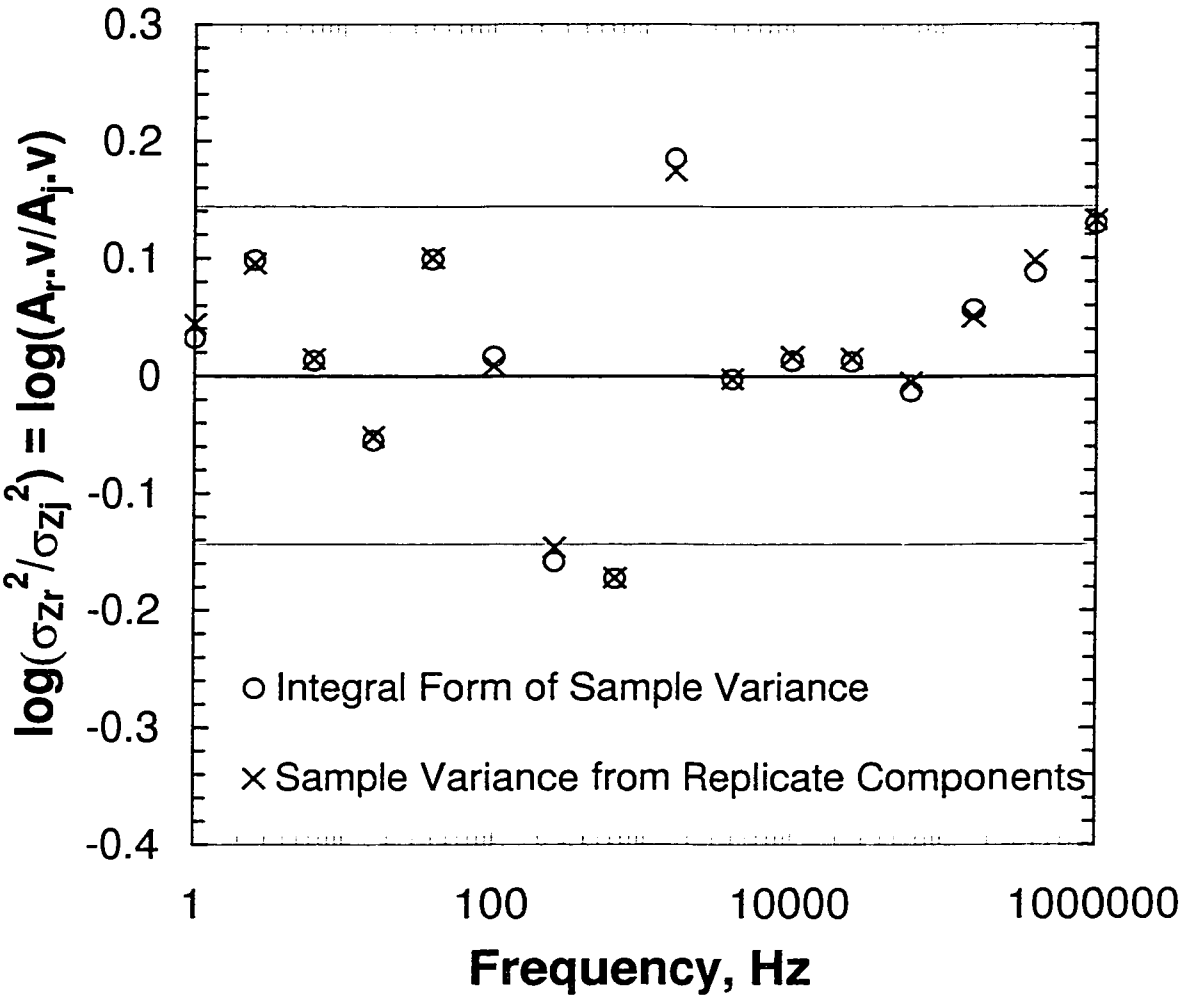

Figure 8.7: F-test for sample variance simulation, in which noise was added to input and output signals and transformed through system. The integral form of the sample variance was calculated through the derived integral equations, while the sample variance was calculated by sample expectation of the observed replicate calculations of the complex components of the voltage and current signals.

CHAPTER 9
CONVERGENCE OF THE STANDARD DEVIATION OF IMPEDANCE AT A SINGLE FREQUENCY

Some researchers have suggested that integrating over a large number of cycles can reduce errors in complex spectroscopy measurements.[116] As the number of cycles of integration increases the noise level in the measurement should decrease.[116,117] This result was found when the variance in the stochastic errors was determined using the functional definition of variance reported in Chapter 8. It has not been reported for sample variance. One implication of this result is that the choice of auto-integration criterion is arbitrary and that the noise level can be made insignificant by reducing the criterion. A simulation was conducted to determine if the standard deviation approaches zero asymptotically or some non-zero value as the number of cycles over which the complex impedance is measured becomes large. Several criterion were considered to determine the asymptotic behavior of the errors in the impedance and the standard deviations in the voltage, current, and impedance as a function of the number of cycles over which the signals were integrated.

An iterative criterion, C_{it}, was calculated as difference between the average magnitude calculated over the current number of cycles and the average magnitude calculated over the previous number of cycles.

$$C_{it} = \langle Z \rangle_n - \langle Z \rangle_{n-1}. \tag{9.1}$$

Here the average is represented by the angle brackets, and the subscript letter of the bracket represents the number of cycles over which the average is calculated (n being the current number of cycles). Two impedance convergence ratios were calculated. The first, C_{Z_p}, was the ratio of the standard deviation of the magnitude of the impedance to the average magnitude of the impedance calculated over the current number of cycles.

$$C_{Z_p,n} = \frac{\sigma_{|Z|,n}}{\langle |Z| \rangle_n}. \tag{9.2}$$

The second, C_{Z_c}, was the ratio of the standard deviation of the impedance magnitude to the magnitude of the average values of the real and imaginary impedance calculated over the current number of cycles.

$$C_{Z_c,n} = \frac{\sigma_{|Z|,n}}{\sqrt{\langle Z_r \rangle_n^2 + \langle Z_j \rangle_n^2}}. \tag{9.3}$$

The same two convergence ratios were calculated for the current and voltage (perturbation and response) signals by

$$C_{I_p,n} = \frac{\sigma_{|I|,n}}{\langle |I| \rangle_n}. \tag{9.4}$$

$$C_{I_c,n} = \frac{\sigma_{|I|,n}}{\sqrt{\langle I_r \rangle_n^2 + \langle I_j \rangle_n^2}}. \tag{9.5}$$

$$C_{V_p,n} = \frac{\sigma_{|V|,n}}{\langle |V| \rangle_n}. \tag{9.6}$$

$$C_{V_c,n} = \frac{\sigma_{|V|,n}}{\sqrt{\langle V_r \rangle_n^2 + \langle V_j \rangle_n^2}}. \tag{9.7}$$

The FRA and PSD techniques listed in Chapter 5 were applied to the same pair of current-voltage signals, and the impedance was calculated over 200 cycles. Each of the convergence criteria described in equations (9.1)-(9.7) was calculated for each cycle at each frequency for each technique and saved to file. The ratio criteria did not approach zero as the number of cycles became large.

The mean and median values of the iterative criterion defined by equation (9.1) is shown as a function of cycle number in Figure 9.1 for the FRA calculation and in Figure 9.2 for the PSD calculation. The mean and median were calculated at each cycle number over all frequencies calculated in the spectrum. The maximum and minimum values over all the frequencies at each cycle number is also plotted. The mean of the ratio defined by equation (9.2) as a function of number of cycles is plotted in Figure 9.3 for the FRA calculation using Bode quadrature and in Figure 9.4 for the PSD calculation. The mean was calculated at each cycle over all frequencies. Only the ratios calculated for the FRA technique (with Bode quadrature) and PSD technique are shown since these are the two simulated techniques most likely to be used in marketed impedance spectroscopy instrumentation. It is clear that the ratio reaches an asymptote bounded by the maximum

and minimum values of the ratio determined over all frequencies. The mean of the ratio defined by equation (9.3) also reaches a non-zero asymptote as illustrated in Figure 9.5 for the FRA calculation and in Figure 9.6 for the PSD calculation. The minimum value of the ratios from all the frequencies as the cycle number becomes large also does not reach zero.

The means of the ratios defined by equations (9.6) and (9.7) are shown as functions of cycle number in Figure 9.7 and Figure 9.8 for the FRA determination method and in Figure 9.9 and Figure 9.10 for the PSD technique, respectively. The means were again calculated over all frequencies at the cycle number. Note that the ratios all converge to a non-zero value. The convergence criteria in current behave similarly to the voltage criterion and are not shown here.

As a result of these calculations, it can be concluded that the "long-integration" convergence criterion of one percent is a reasonable one, since at most, one could expect maybe an order of magnitude better in integral convergence. Second, the variance in the measurement of any signal does not converge to zero as the number of cycles is increased, which is contrary to the described results of the Milocco group.[117] Therefore, it is appropriate to deal with a definition of error structure variance that provides for a finite value as the number of cycles over which the impedance is measured goes to infinity.

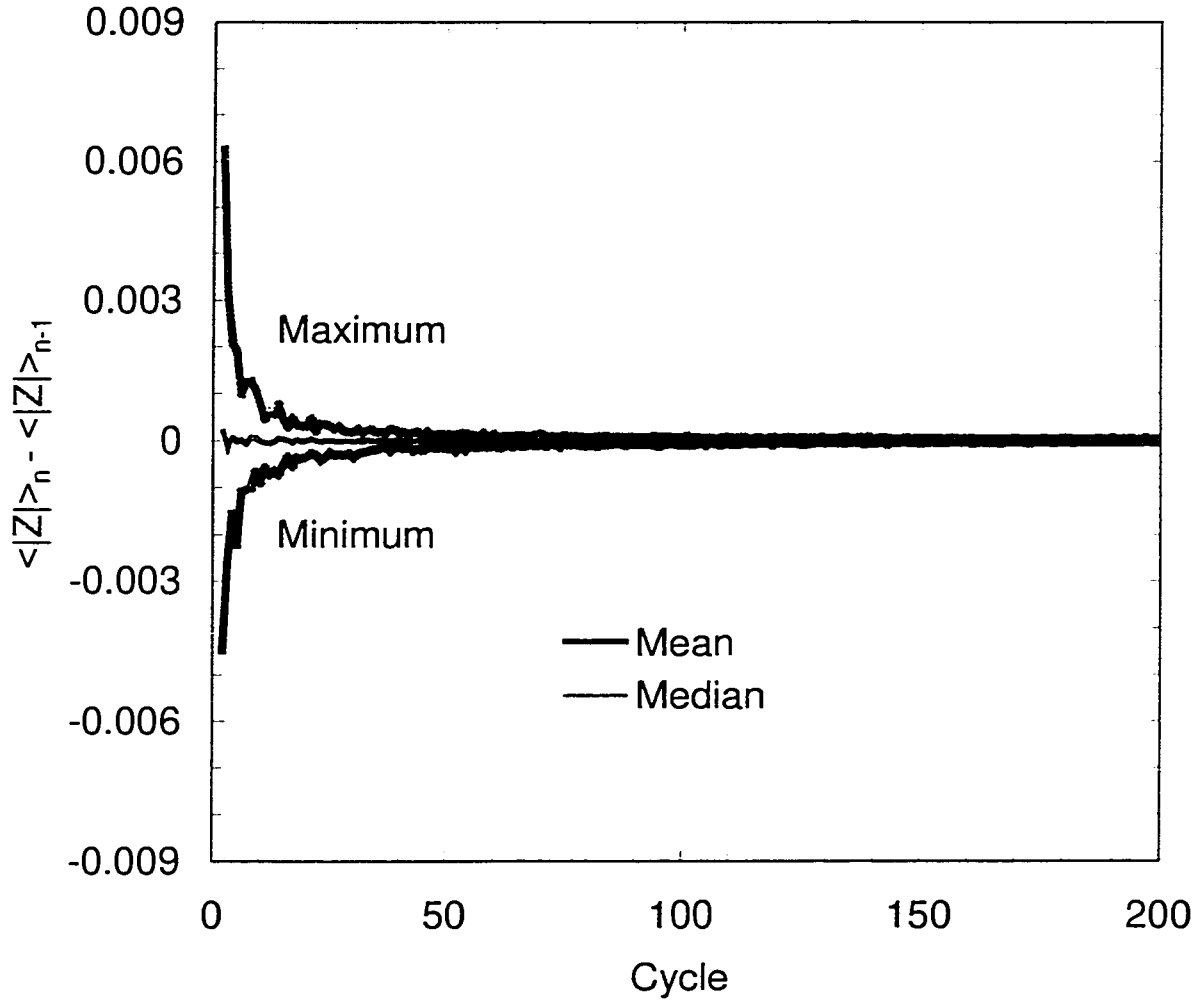

Figure 9.1: Convergence of impedance calculated using the FRA algorithm as a function of cycle number as defined by equation (9.1). At a given frequency, the average value of the impedance was calculated over all cycles up to the value of n. The plotted mean, median, maximum, and minimum was then calculated at each cycle number n over all frequencies in the spectrum.

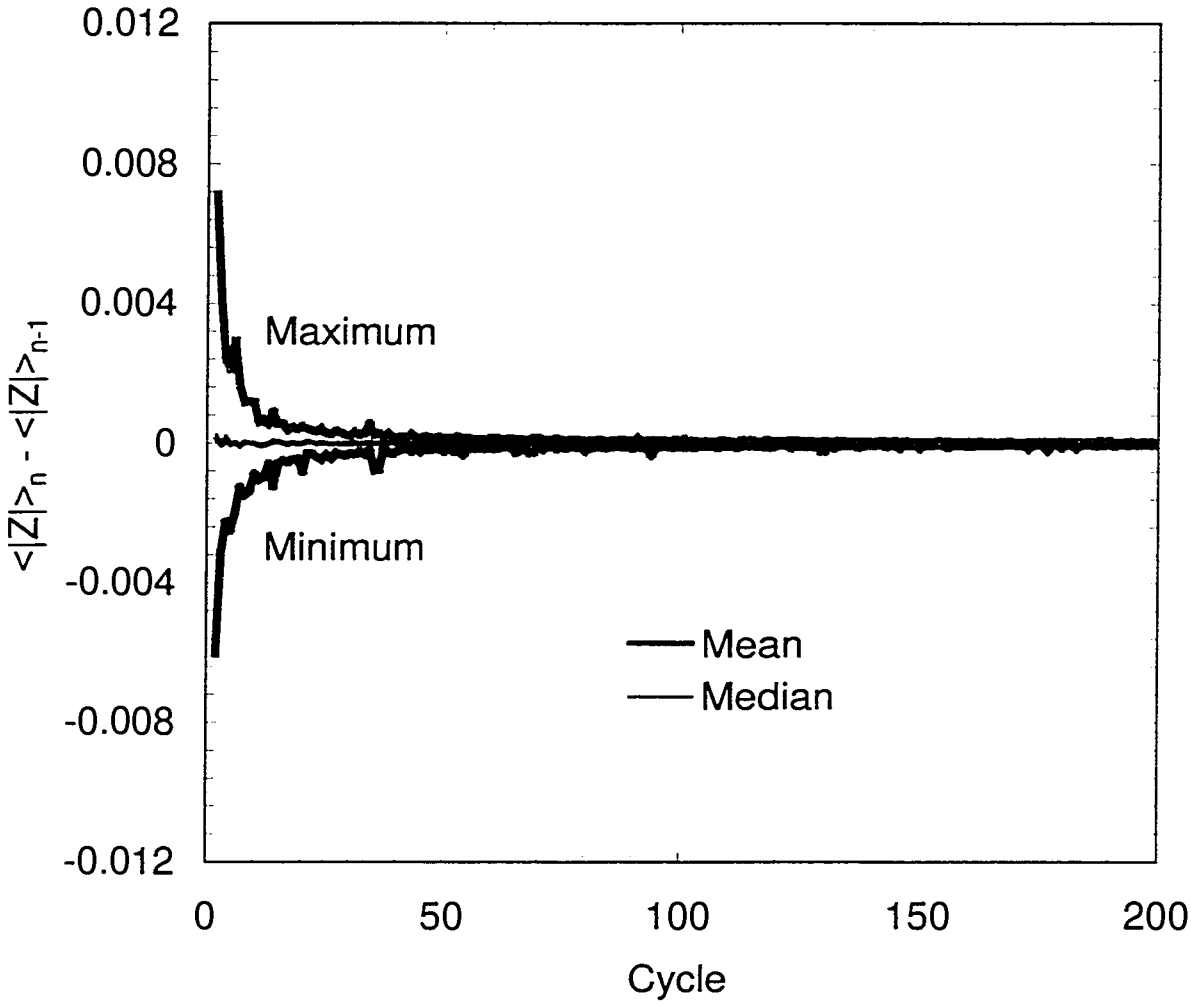

Figure 9.2: Convergence of impedance calculated using the PSD algorithm as a function of cycle number as defined by equation (9.1). At a given frequency, the average value of the impedance was calculated over all cycles up to the value of n. The plotted mean, median, maximum, and minimum was then calculated at each cycle number n over all frequencies in the spectrum.

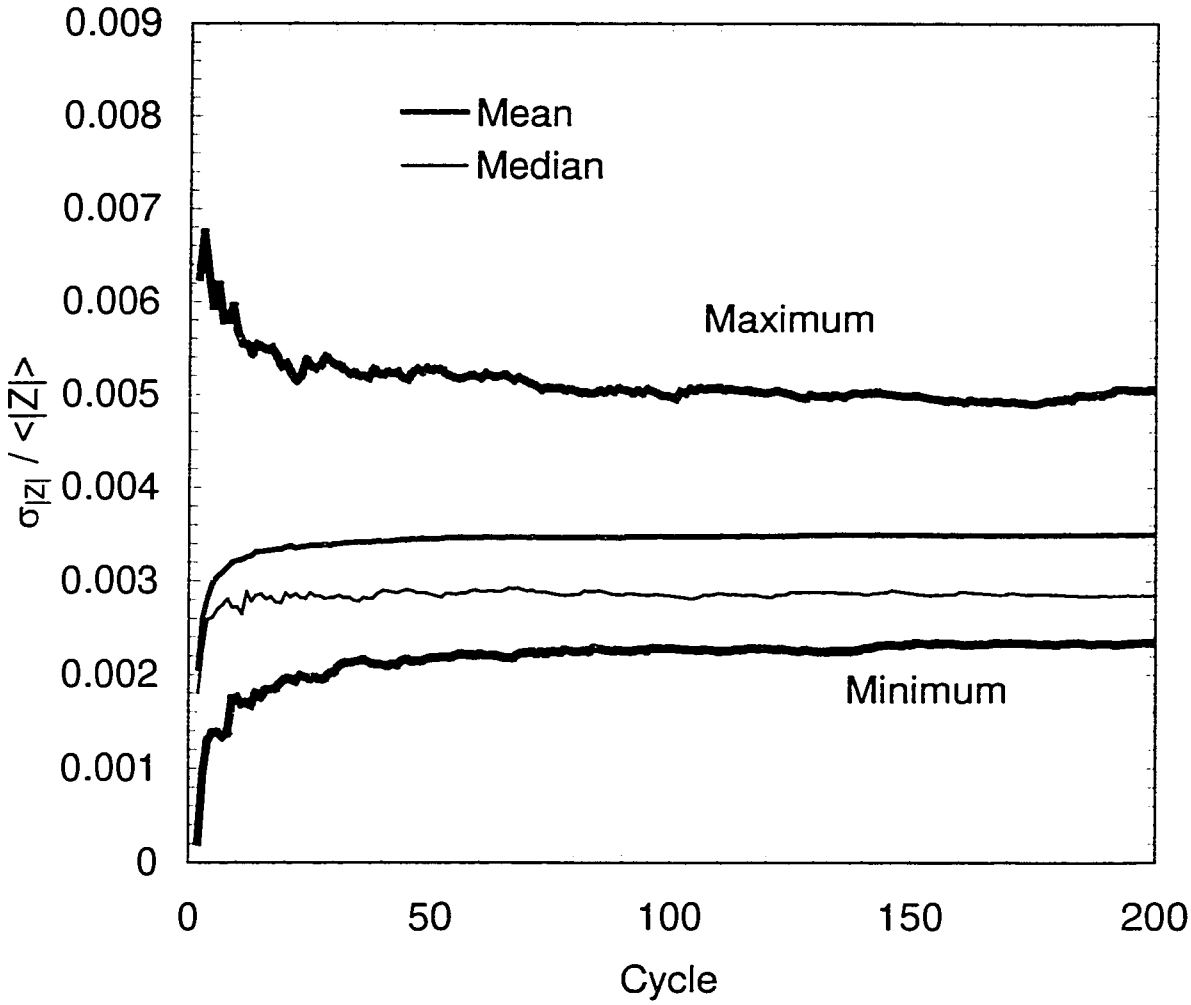

Figure 9.3: Convergence of impedance calculated using the FRA algorithm as a function of cycle number as defined by equation (9.2). At a given frequency, the average value of the impedance was calculated over all cycles up to the value of n. The plotted mean, median, maximum, and minimum was then calculated at each cycle number n over all frequencies in the spectrum.

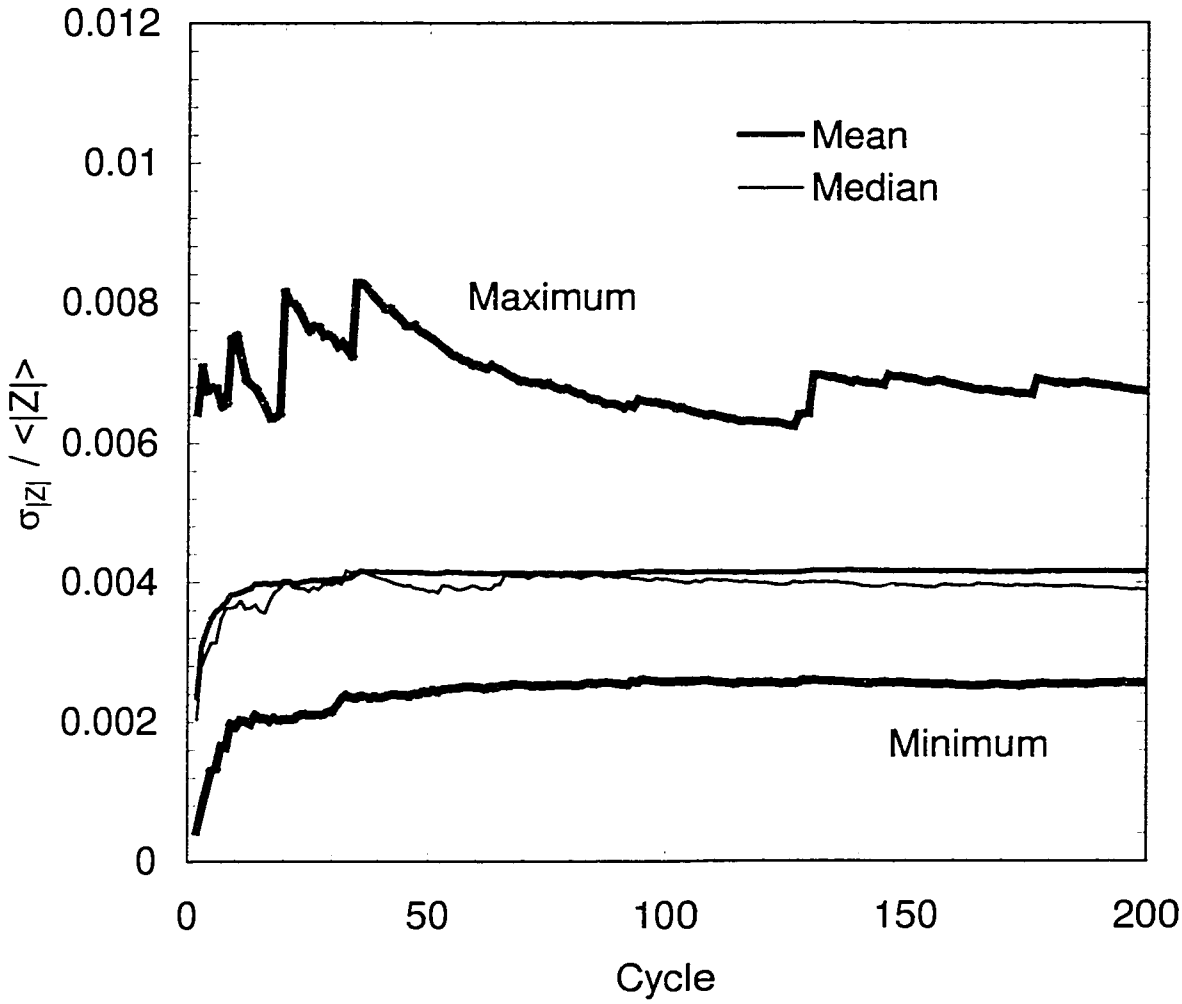

Figure 9.4: Convergence of impedance calculated using the PSD algorithm as a function of cycle number as defined by equation (9.2). At a given frequency, the average value of the impedance was calculated over all cycles up to the value of n. The plotted mean, median, maximum, and minimum was then calculated at each cycle number n over all frequencies in the spectrum.

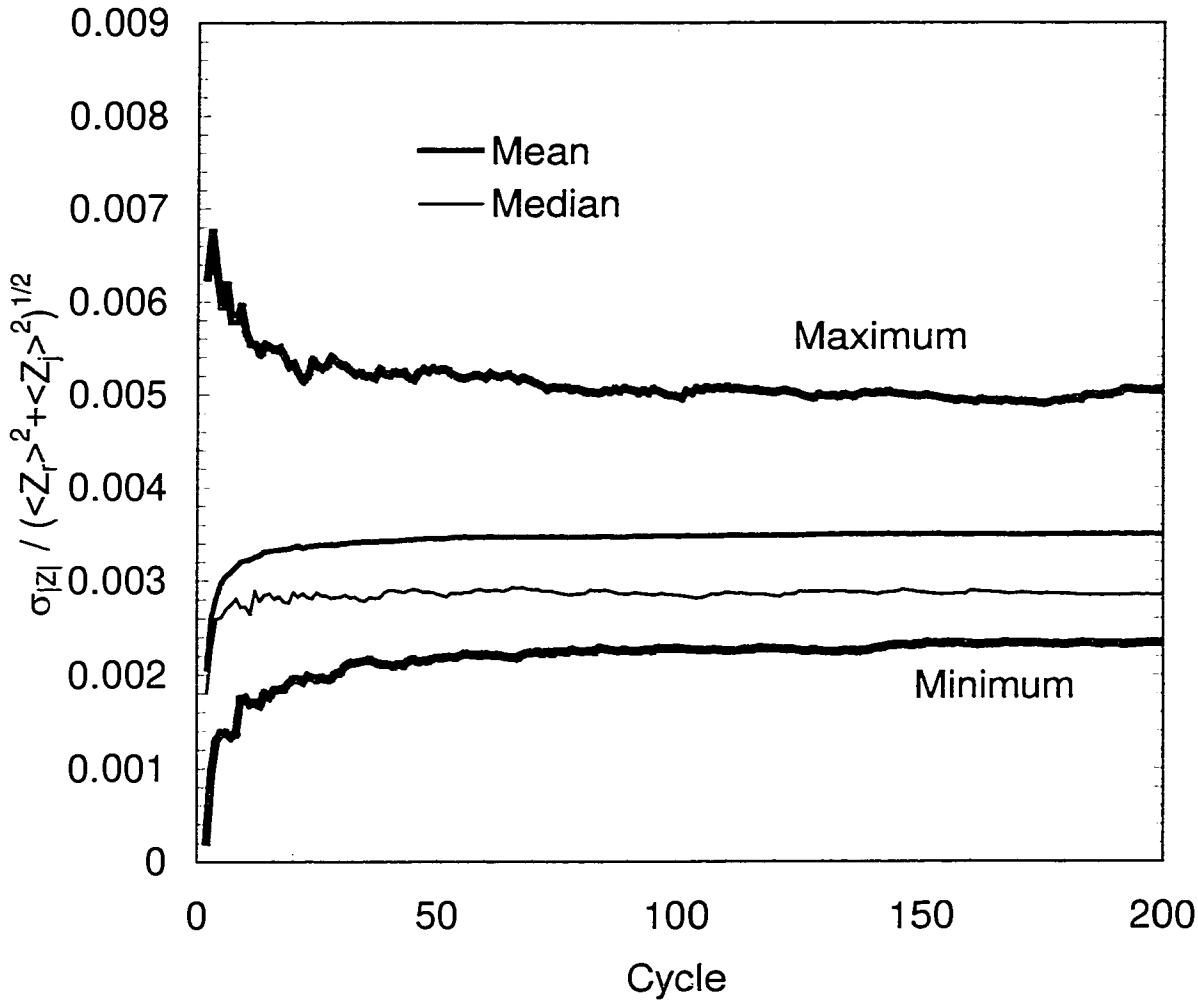

Figure 9.5: Convergence of impedance calculated using the FRA equation (9.3). At a given frequency, the average value of the impedance was calculated over all cycles up to the value of n. The plotted mean, median, maximum, and minimum was then calculated at each cycle number n over all frequencies in the spectrum.

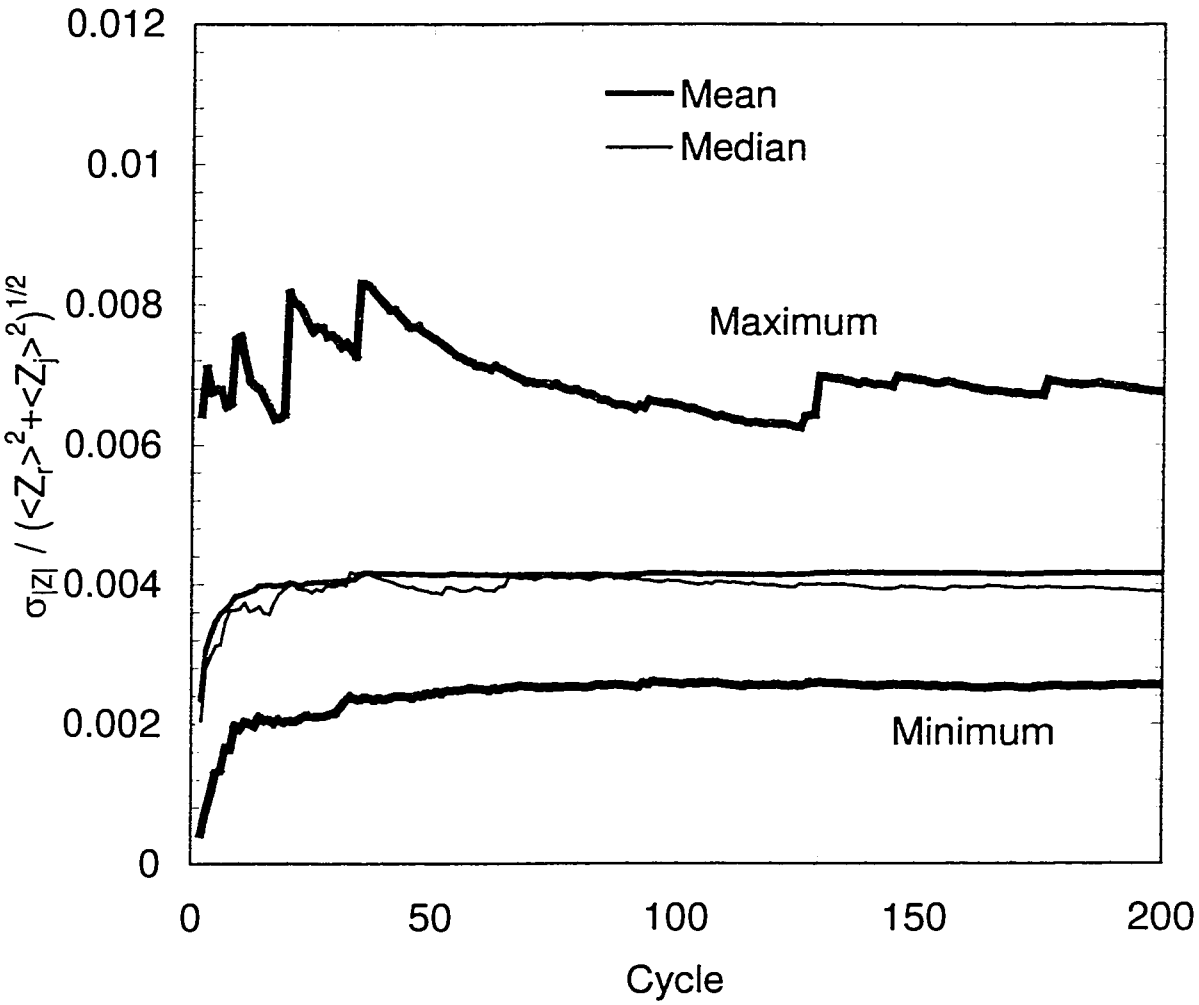

Figure 9.6: Convergence of impedance calculated using the PSD equation (9.3). At a given frequency, the average value of the impedance was calculated over all cycles up to the value of n. The plotted mean, median, maximum, and minimum was then calculated at each cycle number n over all frequencies in the spectrum.

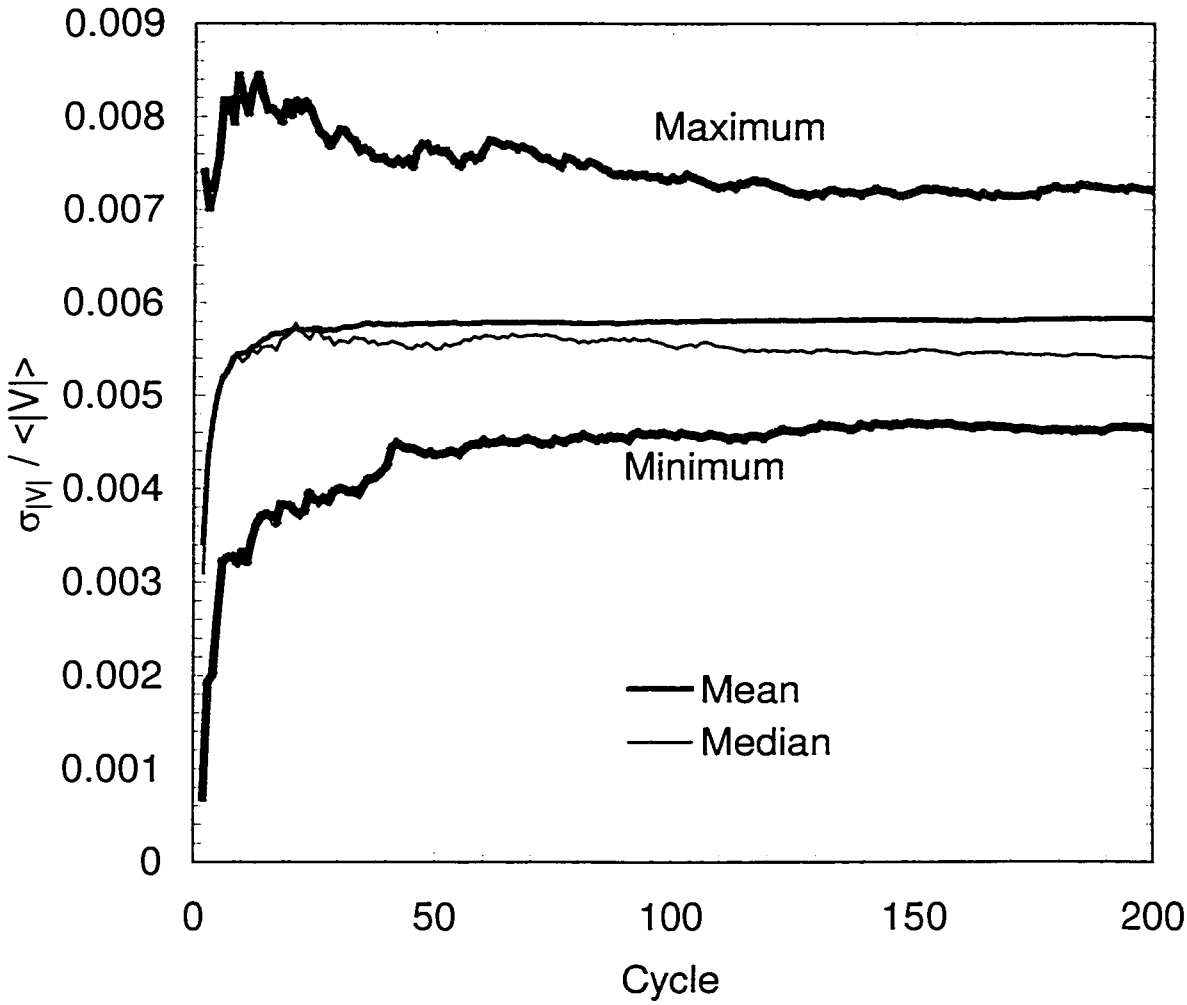

Figure 9.7: Convergence of impedance calculated using the FRA equation (9.6). At a given frequency, the average value of the impedance was calculated over all cycles up to the value of n. The plotted mean, median, maximum, and minimum was then calculated at each cycle number n over all frequencies in the spectrum.

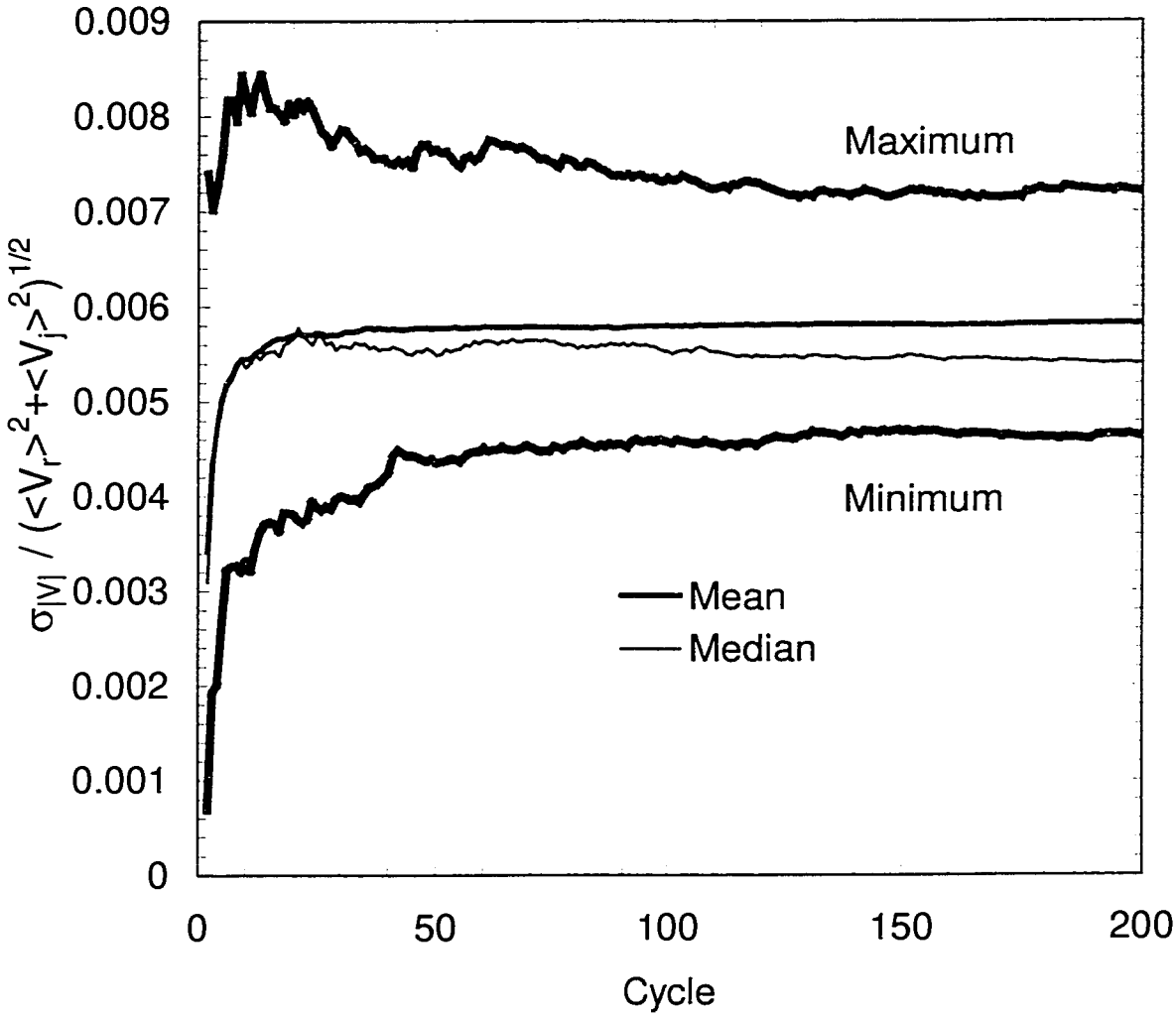

Figure 9.8: Convergence of impedance calculated using the FRA equation (9.7). At a given frequency, the average value of the impedance was calculated over all cycles up to the value of n. The plotted mean, median, maximum, and minimum was then calculated at each cycle number n over all frequencies in the spectrum.

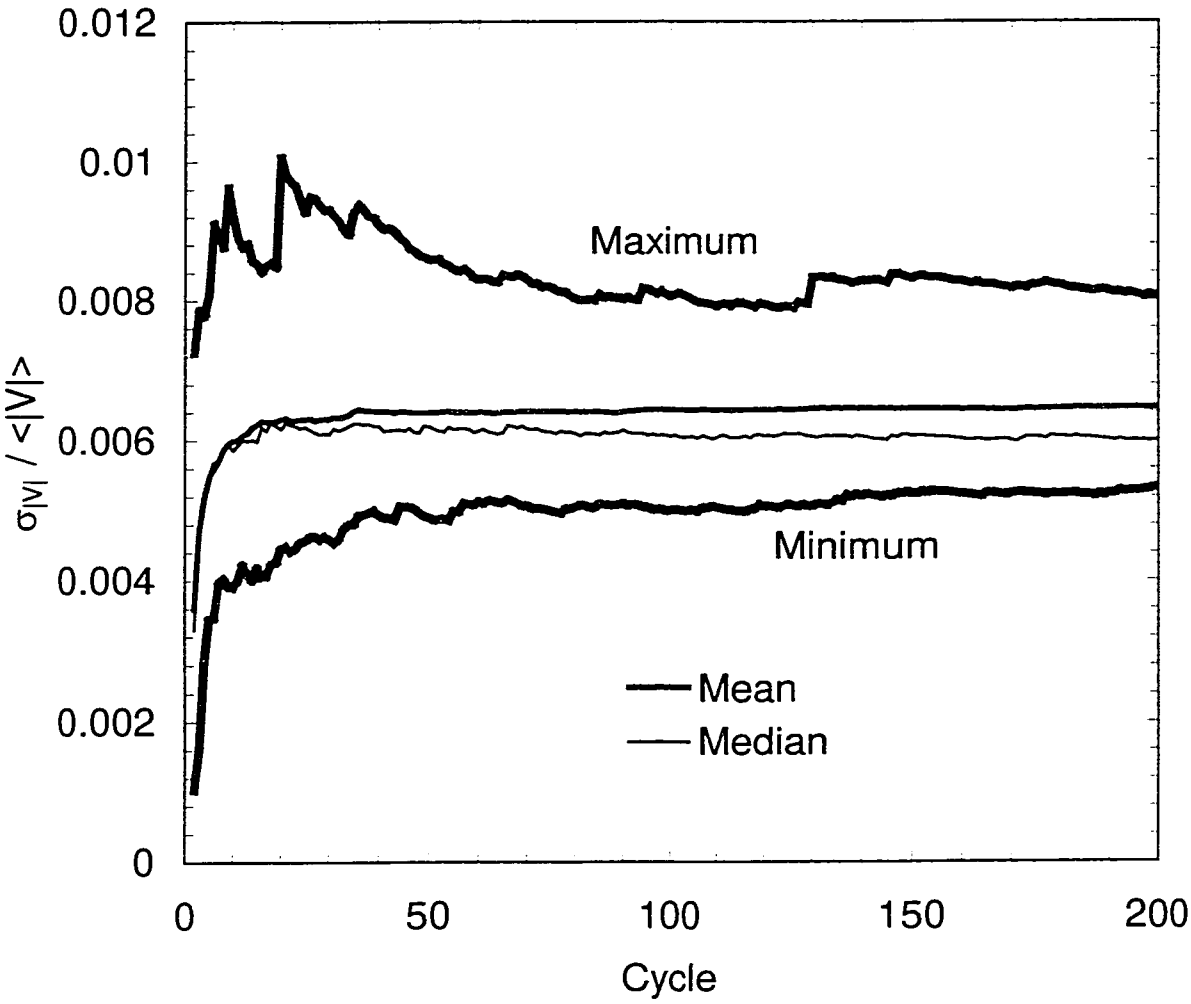

Figure 9.9: Convergence of impedance calculated using the PSD equation (9.6). At a given frequency, the average value of the impedance was calculated over all cycles up to the value of n. The plotted mean, median, maximum, and minimum was then calculated at each cycle number n over all frequencies in the spectrum.

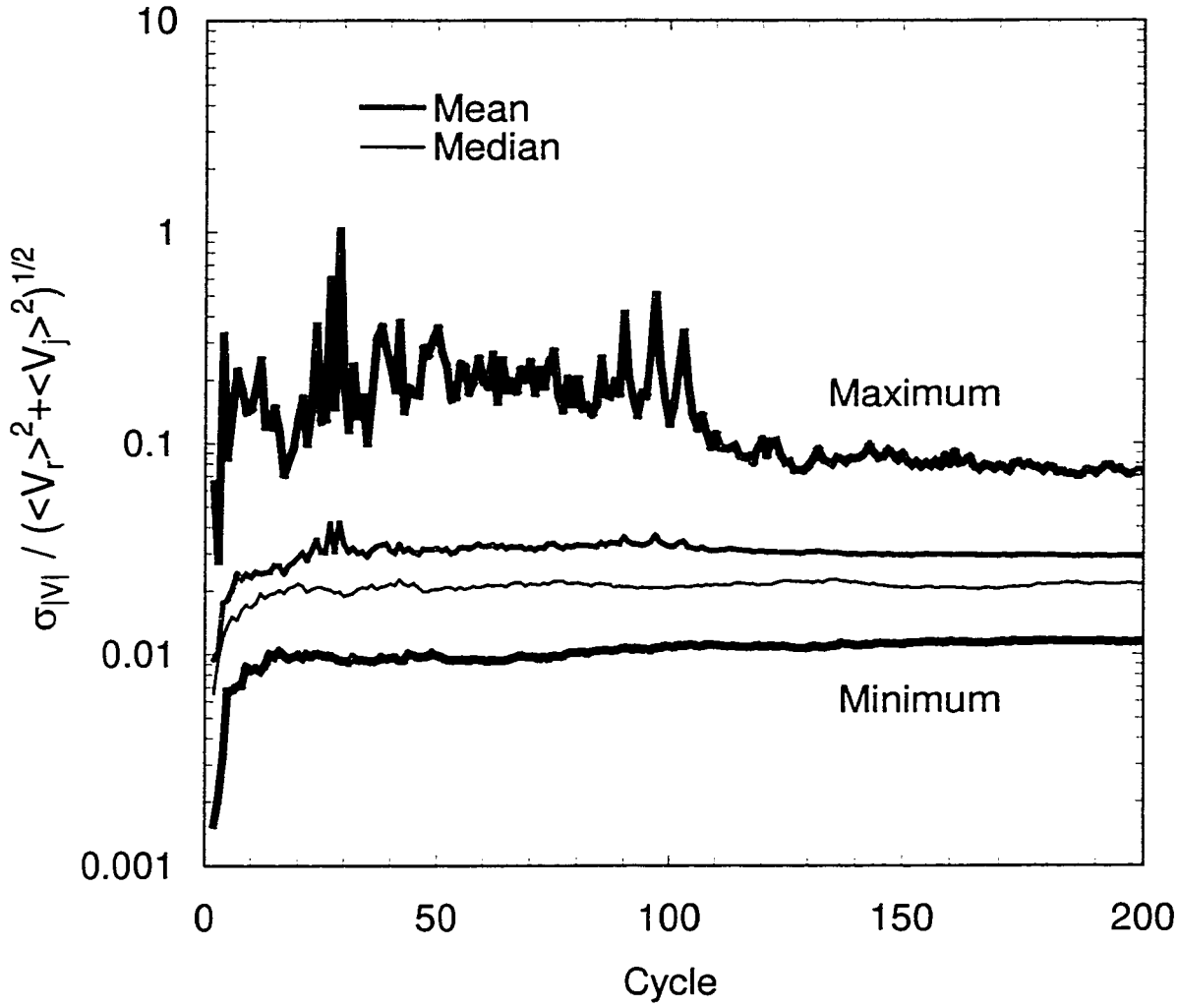

Figure 9.10: Convergence of impedance calculated using the PSD equation (9.7). At a given frequency, the average value of the impedance was calculated over all cycles up to the value of n. The plotted mean, median, maximum, and minimum was then calculated at each cycle number n over all frequencies in the spectrum.

CHAPTER 10
CONCLUSIONS

A new complex spectroscopy technique, Rotational Electrophoretic Spectroscopy, for the characterization of particles in suspension was developed which integrates electrochemical impedance spectroscopy and UV/Vis light scattering. In support of the development of RES, a program of numerical simulations and statistical analysis was conducted for the assessment and characterization of errors in spectroscopy measurements. Implications can be drawn from the results of this program that apply to general applications of complex spectroscopy measurement techniques, such as complex viscometry, acoustophoresis, and electrohydrodynamic impedance spectroscopy.[118]

10.1 Rotational Electrophoretic Spectroscopy

Complex spectroscopy techniques are employed in a diverse range of disciplines for a broad array of applications. In comparison to time-domain measurements with a single measurement at a single time, the complex measurement contains two pieces of information at each frequency. Proof of concept was established for a new complex spectroscopy technique for characterization of a joint property distribution of particles in suspension. This joint property distribution included particle size distribution, zeta potential distribution, particle shape, and surface charge heterogeneity. The technique, termed "Rotational Electrophoretic Spectroscopy," measured the transfer function defined by the ratio of frequency-domain electric field (perturbation) and photodiode (response) signals. The photodiode signal was proportional to the light forward scattered by an

ensemble of non-spherical particles responding to the applied electric field by rotational electrophoresis and induction of a dipole moment.

The rotation of rod-like particles was confirmed by observation through video microscopy of frequency-dependent rotation of suspended particles under an alternating applied field. The assumption that the rotation of particles was a reversible process was verified by using an oscilloscope to monitor the photodiode response. Relaxation processes in response to a square wave potential input were observed to be repeatable. The rotation of particles was observed in the presence of a superimposed flow field, which confirms the suitability of this approach for on-line sensing.

Measurement of the Rotational Electrophoretic Spectroscopy transfer function was accomplished using Fast Fourier Transforms on digitally stored pairs of applied voltage and photodiode response signals. The magnitude of the transfer function was determined at the frequency of the applied voltage signal. Power spectral analysis of the perturbation and response signals provided evidence of a linear response of the light scattering signal to a perturbation in the rotational electrophoretic driving force. The out-of-phase component was not independently assessed because of the low signal-to-noise level in that component.

The RES measurement is extremely difficult to conduct. Oscillations in the light-scattering signal have the same signal level as the noise in that signal. Thus, visual verification of sinusoidal oscillations in the photodiode signal on an oscilloscope could not be made; FFT analysis was required for that verification. The measurement technique was unable to conduct reliable and repeatable measurements of the borosilicate suspension using the RES system. However, the particulate response was observed

several times using video microscopy, and the transient response in the photodiode signal was observed on several occasions although it could not be reliably reproduced.

The technique shows promise as a tool for characterization of particles in suspension. The biggest hurdle to overcome is improving the signal-to-noise ratio of the measurement. Some ideas for increasing the signal level or minimizing the noise level are presented in Chapter 3.

10.2 Characterization of Frequency-Domain Errors

Complex Nonlinear Least Squares (CNLS) regression techniques[5-17] have been employed to estimate the parameters of complex impedance models. CNLS can not fully capture the features of impedance spectra unless appropriate weighting strategies are implemented. Several different strategies have been suggested in the literature. The primary differences between them deal with the correlation between the noise level in the real impedance and the noise level in the imaginary impedance.

An important point that has been missed in this controversy, however, is the evolution of the noise in impedance spectra. The errors in measured spectra are the result of errors in the measurement technique and errors that have been transformed from the measured time-domain signals to the calculated frequency-domain quantities. Thus, studies were conducted to determine the distribution of frequency-domain errors, the relationship between the variances in the complex impedance components, and the relationship between the frequency-domain errors and the noise associated with the time-domain signals under study and with the employed measurement technique.

Several conclusions can be drawn from the results of these studies. The first is that errors in impedance spectra are normally distributed as long as the measurement technology satisfies the Central Limit Theorem. This requirement is satisfied if the

instrument employs signal integration or averaging. For example, the Solartron Instruments 1250 FRA and 1260 Gain Phase Analyzer use algorithms that satisfy the Central Limit Theorem requirements for normal distribution of errors in spectra. Also, in practice, the variance in the real impedance is equal to the variance in the imaginary impedance. The variances were not equal for the PSD technique, but this was the result of the bias introduced from the independent measures of magnitude and phase angle. Thus, the assumptions associated with the derivation of Durbha *et al.*[9] which demonstrated that the variances in the real and imaginary parts of the impedance were equal as a result of the satisfaction of the conditions of the Kramers-Kronig relations are valid for frequency response analysis but not for phase-sensitive detection. The results of the simulations described in this document also support that another implicit assumption associated with that derivation was that there was no error in the frequency at which the impedance was measured.

The variance in the complex impedance cannot be described simply in terms of the variances in the current and voltage signals. It is necessary to account for all of the correlation between the four complex components from the two signals. Correlations between the complex components of the constituent signals were estimated. The errors in the real and imaginary impedance were not correlated when the FRA technique was used for impedance calculation. The same errors were correlated when the PSD technique was employed for determination of the impedance. This result was consistent with the experimental finding that the errors in the real and imaginary impedance were not correlated when there was no bias error contribution to the impedance error structure.[7] A set of conditions on the ten variances of the Taylor series was observed for the equality of

the Taylor series expansions for the variances of the real and imaginary impedances. Therefore, not only are the variances of the stochastic errors in the real and imaginary impedances equal, but the relationship between the ten components of the variance vector is known. Namely, the variances in the stochastic errors in the real and imaginary voltage are equal. The variances in the stochastic errors in the real and imaginary current are also equal. The covariances between the real and imaginary current and real and imaginary voltage are equal to zero. The cross-covariances between the real current and voltage and between the imaginary current and voltage are equal. And, the final two cross-covariances are of equal magnitude but opposite sign.

Replicate measurement of impedance spectra is required to determine accurately the impedance that generates errors in the real and imaginary impedances for which the variances are equal. Determination of the variance from a single measurement of a signal will not necessarily satisfy the equality. Therefore, the error structure described by functional variances of the real and imaginary impedances does not apply to all systems or spectra. Thus, the results of these simulations suggest that the approach taken by the laboratory of Prof. Mark E. Orazem,[6-9,74,118] which incorporates an experimental determination of the variances from replicated measurements, is the most robust of the published methods for measurement and interpretation of impedance spectra. Frequency response analysis, Lissajous parameterization, and to a lesser degree fast Fourier transforms of white noise signals are preferable techniques for measurement of complex impedance spectra because they do not introduce the bias error associated with the PSD technique. Error structure weighting of CNLS regressions should be used, and the error structure should be a function of the variances in the stochastic errors in the real and

imaginary impedances. In order to determine the error structure of the measurement, replicate spectra must be taken. Sample variance must be used for the error structure, or the weighting strategy may fail for non-simulated systems.

CHAPTER 11
SUGGESTIONS FOR FUTURE WORK

This document has focused on two primary points of research: the development of Rotational Electrophoretic Spectroscopy and the propagation of errors into complex spectra. As a result, suggestions for future work must be divided between these two thrusts.

11.1 Rotational Electrophoretic Spectroscopy

This technique is still under development. The current status of the technique is that the physics behind the technique are verified and observed, but the RES measurement is neither reproducible nor reliable. Further work is required to fully realize the technique. First of all, a more robust UV/Vis spectroscopy system is required. Ideally, a multi-wavelength spectroscopy system would be used for the optical sensing. A fast A/D card on a PC would allow a large number of wavelengths to be sampled over time. FFT analysis could be applied to the time signal for each wavelength, and the best signal to noise ratio could be quickly ascertained. Presently, an A/D card would have to be programmed by the researcher to perform in this manner. Available UV/Vis instrumentation is not designed for this purpose.

A better cell design may be required. One possible cause of the poor signal-to-noise ratio in the current RES design may be the translational motion of the suspended particles due to the application of an electric field. A cross flow cell may be required to minimize the translation mobility of particles. In principle, a pressure gradient could be applied

across the cell so that the fluid in the sampling chamber has a velocity equal and opposite to the translationally mobile particles.

11.2 Propagation of Errors into Complex Spectra

Simulations were conducted to answer the questions posed in this portion of the dissertation. They were employed to determine the influence of instrumentation on errors in complex spectra, the relationship between the errors in complex spectra and errors in the constituent complex perturbation and response signals, the propagation of colored noise in the time-domain into the frequency-domain, and the integral transformation of time-domain errors into the frequency-domain. At this point, little experimental evidence is available to support these results.

Thus, the focus of future research on this topic should be on gathering experimental data to test the results of the simulations reported here. Certainly, the influence of instrumentation on the error structure of impedance measurements can be determined by measuring the impedance on the same pair of current and voltage signals using both an FRA and a lock-in amplifier (for PSD). The pair of signals can be treated simultaneously with both instruments by splitting the signals and then passing each split signal through a high impedance voltage follower to minimize the effect of ground loops between the instruments. The error structure of the complex frequency-domain transforms of the current and voltage signals can also be determined by either measuring the complex signals individually or simultaneously using a multi-channel FRA (such as the SI 1254). The propagation of colored noise is more difficult to determine experimentally, since the noise in impedance experiments is not normally a controlled quantity. However, various distributions of stochastic noise can be added to the current and voltage signals using a digital-to-analog card on a computer and two operational amplifier summer circuits. The

integral transformation of time-domain errors is also difficult to determine experimentally. One approach would be to capture the voltage and current signals from impedance measurements onto a PC hard drive. Each signal could be regressed to a generalized sinusoidal wave. The regressed wave could be subtracted from the respective signal; the difference would be the noise in the signal. The noise could then be integrated via the equations in Chapter 8. These experiments could be extended to a variety of spectroscopies including dielectric spectroscopy, complex viscometry, acoustophoresis, and electrohydrodynamic impedance spectroscopy.

APPENDIX A
TAYLOR SERIES EXPANSION OF VARIANCE

This appendix provides the reader with the details of the derivations presented in Chapter 6. Many steps in the derivations are presented here so that the reader does not get lost in the algebra of the manipulations.

A.1 Variance of Real and Imaginary Impedance from Complex Taylor Series Expansion of Complex Impedance

The variance in the complex impedance can be written in terms of variances and co-variances in the complex current and voltage as

$$\sigma_{\tilde{Z}}^2 = \left[E\left(\frac{\partial \tilde{Z}}{\partial \tilde{V}}\right)\right]^2 \sigma_{\tilde{V}}^2 + \left[E\left(\frac{\partial \tilde{Z}}{\partial \tilde{I}}\right)\right]^2 \sigma_{\tilde{I}}^2 + \left[E\left(\frac{\partial \tilde{Z}}{\partial \tilde{V}}\right)\right]\left[E\left(\frac{\partial \tilde{Z}}{\partial \tilde{I}}\right)\right]\sigma_{\tilde{I}\tilde{V}}. \tag{A.1}$$

The complex variance can be expanded into its rectangular coordinate representation as

$$\begin{aligned}\sigma_{Z_r}^2 - \sigma_{Z_j}^2 + 2j\sigma_{Z_rZ_j} = &\left(\frac{1}{\tilde{I}_0^2}\right)\left(\sigma_{V_r}^2 - \sigma_{V_j}^2 + 2j\sigma_{V_rV_j}\right) + \left(\frac{\tilde{Z}_0^2}{\tilde{I}_0^2}\right)\left(\sigma_{I_r}^2 - \sigma_{I_j}^2 + 2j\sigma_{I_rI_j}\right) \\ &- 2\left(\frac{\tilde{Z}_0}{\tilde{I}_0^2}\right)\left(\sigma_{V_rI_r} - \sigma_{V_jI_j} + j\left(\sigma_{V_rI_j} + \sigma_{V_jI_r}\right)\right)\end{aligned} \tag{A.2}$$

The complex quantities that result from the partial derivatives in the Taylor series can be written as

$$\begin{aligned}\frac{1}{\tilde{I}_0^2} &= \frac{1}{(I_r + jI_j)^2} = \frac{1}{I_r^2 - I_j^2 + 2jI_rI_j} = \frac{I_r^2 - I_j^2 - 2jI_rI_j}{\left(I_r^2 - I_j^2\right)^2 + 4I_r^2I_j^2} \\ &= \frac{I_r^2 - I_j^2 - 2jI_rI_j}{\left(I_r^2 + I_j^2\right)^2}\end{aligned} \tag{A.3}$$

$$\frac{\tilde{Z}_0^{\,2}}{\tilde{I}_0^{\,2}} = \frac{\left(I_r^{\,2} - I_j^{\,2} - 2jI_rI_j\right)\left(Z_r^{\,2} - Z_j^{\,2} + 2jZ_rZ_j\right)}{\left(I_r^{\,2} + I_j^{\,2}\right)^2} \tag{A.4}$$

$$= \frac{\left[\left(I_r^{\,2} - I_j^{\,2}\right)\left(Z_r^{\,2} - Z_j^{\,2}\right) + 4\left(I_rI_j\right)\left(Z_rZ_j\right)\right]}{\left(I_r^{\,2} + I_j^{\,2}\right)^2}$$

$$+ \frac{2j\left[\left(I_r^{\,2} - I_j^{\,2}\right)\left(Z_rZ_j\right) - \left(I_rI_j\right)\left(Z_r^{\,2} - Z_j^{\,2}\right)\right]}{\left(I_r^{\,2} + I_j^{\,2}\right)^2}$$

$$\frac{\tilde{Z}_0}{\tilde{I}_0^{\,2}} = \frac{\left(I_r^{\,2} - I_j^{\,2} - 2jI_rI_j\right)\left(Z_r + jZ_j\right)}{\left(I_r^{\,2} + I_j^{\,2}\right)^2} \tag{A.5}$$

$$= \frac{\left[\left(I_r^{\,2} - I_j^{\,2}\right)\left(Z_r\right) + 2\left(I_rI_j\right)\left(Z_j\right)\right] + j\left[\left(I_r^{\,2} - I_j^{\,2}\right)\left(Z_j\right) - 2\left(I_rI_j\right)\left(Z_r\right)\right]}{\left(I_r^{\,2} + I_j^{\,2}\right)^2}$$

The results of equations (A.3)-(A.5) have been used to determine equations (6.17) and (6.18) of Chapter 6.

A.2 Variance of the Real and Imaginary Impedance from the Real Taylor Series Expansions of the Impedance Components

The variances in the real and imaginary impedance can be written as a function of the variances of and covariances between the complex components of the current and voltage signals by

$$\sigma_{Z_r}^2 = \left(\frac{\partial \hat{Z}_r}{\partial V_r}\right)^2 \sigma_{V_r}^2 + \left(\frac{\partial \hat{Z}_r}{\partial Vj}\right)^2 \sigma_{V_j}^2 + \left(\frac{\partial \hat{Z}_r}{\partial I_r}\right)^2 \sigma_{I_r}^2 + \left(\frac{\partial \hat{Z}_r}{\partial I_j}\right)^2 \sigma_{I_j}^2 \tag{A.6}$$

$$+ 2\left(\frac{\partial \hat{Z}_r}{\partial V_r}\right)\left(\frac{\partial \hat{Z}_r}{\partial Vj}\right)\sigma_{V_rV_j} + 2\left(\frac{\partial \hat{Z}_r}{\partial V_r}\right)\left(\frac{\partial \hat{Z}_r}{\partial I_r}\right)\sigma_{V_rI_r} + 2\left(\frac{\partial \hat{Z}_r}{\partial V_r}\right)\left(\frac{\partial \hat{Z}_r}{\partial I_j}\right)\sigma_{V_rI_j}$$

$$+ 2\left(\frac{\partial \hat{Z}_r}{\partial V_j}\right)\left(\frac{\partial \hat{Z}_r}{\partial I_r}\right)\sigma_{V_jI_r} + 2\left(\frac{\partial \hat{Z}_r}{\partial V_j}\right)\left(\frac{\partial \hat{Z}_r}{\partial I_j}\right)\sigma_{V_jI_j} + 2\left(\frac{\partial \hat{Z}_r}{\partial I_r}\right)\left(\frac{\partial \hat{Z}_r}{\partial I_j}\right)\sigma_{I_rI_j}$$

$$\sigma_{Z_j}^2 = \left(\frac{\partial \hat{Z}_j}{\partial V_r}\right)^2 \sigma_{V_r}^2 + \left(\frac{\partial \hat{Z}_j}{\partial Vj}\right)^2 \sigma_{V_j}^2 + \left(\frac{\partial \hat{Z}_j}{\partial I_r}\right)^2 \sigma_{I_r}^2 + \left(\frac{\partial \hat{Z}_j}{\partial I_j}\right)^2 \sigma_{I_j}^2$$
$$+2\left(\frac{\partial \hat{Z}_j}{\partial V_r}\right)\left(\frac{\partial \hat{Z}_j}{\partial V_j}\right)\sigma_{V_rV_j} + 2\left(\frac{\partial \hat{Z}_j}{\partial V_r}\right)\left(\frac{\partial \hat{Z}_j}{\partial I_r}\right)\sigma_{V_rI_r} + 2\left(\frac{\partial \hat{Z}_j}{\partial V_r}\right)\left(\frac{\partial \hat{Z}_j}{\partial I_j}\right)\sigma_{V_rI_j}$$
$$+2\left(\frac{\partial \hat{Z}_j}{\partial V_j}\right)\left(\frac{\partial \hat{Z}_j}{\partial I_r}\right)\sigma_{V_jI_r} + 2\left(\frac{\partial \hat{Z}_j}{\partial V_j}\right)\left(\frac{\partial \hat{Z}_j}{\partial I_j}\right)\sigma_{V_jI_j} + 2\left(\frac{\partial \hat{Z}_j}{\partial I_r}\right)\left(\frac{\partial \hat{Z}_j}{\partial I_j}\right)\sigma_{I_rI_j} \tag{A.7}$$

where $\hat{Z}_n$ represents the expectation value of the impedance.

From this point, all variables besides the variance and covariance terms will be considered as the expectation values. The carets and subscripts will be dropped. Then, the individual derivatives can be written as

$$\left(\frac{\partial \hat{Z}_r}{\partial V_r}\right) = \frac{I_r}{I_r^{\,2} + I_j^{\,2}} \tag{A.8}$$

$$\left(\frac{\partial \hat{Z}_r}{\partial Vj}\right) = \frac{I_j}{I_r^{\,2} + I_j^{\,2}} \tag{A.9}$$

$$\left(\frac{\partial \hat{Z}_r}{\partial I_r}\right) = \frac{V_r}{I_r^{\,2} + I_j^{\,2}} - \frac{2(I_r)[V_rI_r + V_jI_j]}{\left(I_r^{\,2} + I_j^{\,2}\right)^2} \tag{A.10}$$

$$\left(\frac{\partial \hat{Z}_r}{\partial I_j}\right) = \frac{V_j}{I_r^{\,2} + I_j^{\,2}} - \frac{2(I_j)[V_rI_r + V_jI_j]}{\left(I_r^{\,2} + I_j^{\,2}\right)^2} \tag{A.11}$$

$$\left(\frac{\partial \hat{Z}_j}{\partial V_r}\right) = \frac{-I_j}{I_r^{\,2} + I_j^{\,2}} \tag{A.12}$$

$$\left(\frac{\partial \hat{Z}_j}{\partial Vj}\right) = \frac{I_r}{I_r^{\,2} + I_j^{\,2}} \tag{A.13}$$

$$\left(\frac{\partial \hat{Z}_j}{\partial I_r}\right) = \frac{V_j}{I_r^{\,2} + I_j^{\,2}} - \frac{2(I_r)[V_j I_r - V_r I_j]}{\left(I_r^{\,2} + I_j^{\,2}\right)^2} \tag{A.14}$$

$$\left(\frac{\partial \hat{Z}_j}{\partial I_j}\right) = \frac{-V_r}{I_r^{\,2} + I_j^{\,2}} - \frac{2(I_j)[V_j I_r - V_r I_j]}{\left(I_r^{\,2} + I_j^{\,2}\right)^2} \tag{A.15}$$

Then, the squares of all these derivatives are

$$\left(\frac{\partial \hat{Z}_r}{\partial V_r}\right)^2 = \frac{I_r^2}{\left(I_r^{\,2} + I_j^{\,2}\right)^2} \tag{A.16}$$

$$\left(\frac{\partial \hat{Z}_r}{\partial Vj}\right)^2 = \frac{I_j^2}{\left(I_r^{\,2} + I_j^{\,2}\right)^2} \tag{A.17}$$

$$\left(\frac{\partial \hat{Z}_r}{\partial I_r}\right)^2 = \frac{V_r^2}{\left(I_r^{\,2} + I_j^{\,2}\right)^2} - \frac{4(I_r)(V_r)[V_r I_r + V_j I_j]}{\left(I_r^{\,2} + I_j^{\,2}\right)^3} + \frac{4\left(I_r^2\right)[V_r I_r + V_j I_j]^2}{\left(I_r^{\,2} + I_j^{\,2}\right)^4} \tag{A.18}$$

$$\left(\frac{\partial \hat{Z}_r}{\partial I_j}\right)^2 = \frac{V_j^2}{\left(I_r^{\,2} + I_j^{\,2}\right)^2} - \frac{4(I_j)(V_j)[V_r I_r + V_j I_j]}{\left(I_r^{\,2} + I_j^{\,2}\right)^3} + \frac{4\left(I_j^{\,2}\right)[V_r I_r + V_j I_j]^2}{\left(I_r^{\,2} + I_j^{\,2}\right)^4} \tag{A.19}$$

$$\left(\frac{\partial \hat{Z}_j}{\partial V_r}\right)^2 = \frac{I_j^{\,2}}{\left(I_r^{\,2} + I_j^{\,2}\right)^2} \tag{A.20}$$

$$\left(\frac{\partial \hat{Z}_j}{\partial Vj}\right)^2 = \frac{I_r^{\,2}}{\left(I_r^{\,2} + I_j^{\,2}\right)^2} \tag{A.21}$$

$$\left(\frac{\partial \hat{Z}_j}{\partial I_r}\right)^2 = \frac{V_j^2}{\left(I_r^{\,2} + I_j^{\,2}\right)^2} - \frac{4(I_r)(V_j)[V_j I_r - V_r I_j]}{\left(I_r^{\,2} + I_j^{\,2}\right)^3} + \frac{4\left(I_r^{\,2}\right)[V_j I_r - V_r I_j]^2}{\left(I_r^{\,2} + I_j^{\,2}\right)^4} \tag{A.22}$$

$$\left(\frac{\partial \hat{Z}_j}{\partial I_j}\right)^2 = \frac{V_r^2}{\left(I_r^{\,2} + I_j^{\,2}\right)^2} + \frac{4(I_j)(V_r)[V_j I_r - V_r I_j]}{\left(I_r^{\,2} + I_j^{\,2}\right)^3} + \frac{4\left(I_j^{\,2}\right)[V_j I_r - V_r I_j]^2}{\left(I_r^{\,2} + I_j^{\,2}\right)^4} \tag{A.23}$$

The twelve cross products are

$$\left(\frac{\partial \hat{Z}_r}{\partial V_r}\right)\left(\frac{\partial \hat{Z}_r}{\partial Vj}\right)=\frac{I_r I_j}{\left(I_r^{\,2}+I_j^{\,2}\right)^2} \tag{A.24}$$

$$\left(\frac{\partial \hat{Z}_r}{\partial V_r}\right)\left(\frac{\partial \hat{Z}_r}{\partial I_r}\right)=\frac{V_r I_r}{\left(I_r^{\,2}+I_j^{\,2}\right)^2}-\frac{2\left(I_r^{\,2}\right)\left[V_r I_r+V_j I_j\right]}{\left(I_r^{\,2}+I_j^{\,2}\right)^3} \tag{A.25}$$

$$\left(\frac{\partial \hat{Z}_r}{\partial V_r}\right)\left(\frac{\partial \hat{Z}_r}{\partial I_j}\right)=\frac{V_j I_r}{\left(I_r^{\,2}+I_j^{\,2}\right)^2}-\frac{2\left(I_j\right)\left(I_r\right)\left[V_r I_r+V_j I_j\right]}{\left(I_r^{\,2}+I_j^{\,2}\right)^3} \tag{A.26}$$

$$\left(\frac{\partial \hat{Z}_r}{\partial V_j}\right)\left(\frac{\partial \hat{Z}_r}{\partial I_r}\right)=\frac{V_r I_j}{\left(I_r^{\,2}+I_j^{\,2}\right)^2}-\frac{2\left(I_r\right)\left(I_j\right)\left[V_r I_r+V_j I_j\right]}{\left(I_r^{\,2}+I_j^{\,2}\right)^3} \tag{A.27}$$

$$\left(\frac{\partial \hat{Z}_r}{\partial V_j}\right)\left(\frac{\partial \hat{Z}_r}{\partial I_j}\right)=\frac{V_j I_j}{\left(I_r^{\,2}+I_j^{\,2}\right)^2}-\frac{2\left(I_j^{\,2}\right)\left[V_r I_r+V_j I_j\right]}{\left(I_r^{\,2}+I_j^{\,2}\right)^3} \tag{A.28}$$

$$\begin{aligned}\left(\frac{\partial \hat{Z}_r}{\partial I_r}\right)\left(\frac{\partial \hat{Z}_r}{\partial I_j}\right)=&\frac{V_r V_j}{\left(I_r^{\,2}+I_j^{\,2}\right)^2}-\frac{2\left(I_r\right)\left(V_j\right)\left[V_r I_r+V_j I_j\right]}{\left(I_r^{\,2}+I_j^{\,2}\right)^3}\\&-\frac{2\left(I_j\right)\left(V_r\right)\left[V_r I_r+V_j I_j\right]}{\left(I_r^{\,2}+I_j^{\,2}\right)^3}+\frac{4\left(I_r\right)\left(I_j\right)\left[V_r I_r+V_j I_j\right]^2}{\left(I_r^{\,2}+I_j^{\,2}\right)^4}\end{aligned} \tag{A.29}$$

$$\left(\frac{\partial \hat{Z}_j}{\partial V_r}\right)\left(\frac{\partial \hat{Z}_j}{\partial Vj}\right)=\frac{-I_r I_j}{\left(I_r^{\,2}+I_j^{\,2}\right)^2} \tag{A.30}$$

$$\left(\frac{\partial \hat{Z}_j}{\partial V_r}\right)\left(\frac{\partial \hat{Z}_j}{\partial I_r}\right)=\frac{-V_j I_j}{\left(I_r^{\,2}+I_j^{\,2}\right)^2}+\frac{2\left(I_r\right)\left(I_j\right)\left[V_j I_r-V_r I_j\right]}{\left(I_r^{\,2}+I_j^{\,2}\right)^3} \tag{A.31}$$

$$\left(\frac{\partial \hat{Z}_j}{\partial V_r}\right)\left(\frac{\partial \hat{Z}_j}{\partial I_j}\right)=\frac{V_r I_j}{I_r^{\,2}+I_j^{\,2}}+\frac{2\left(I_j^{\,2}\right)\left[V_j I_r-V_r I_j\right]}{\left(I_r^{\,2}+I_j^{\,2}\right)^3} \tag{A.32}$$

$$\left(\frac{\partial \hat{Z}_j}{\partial V_j}\right)\left(\frac{\partial \hat{Z}_j}{\partial I_r}\right)=\frac{V_j I_r}{I_r^{\,2}+I_j^{\,2}}-\frac{2\left(I_r^{\,2}\right)\left[V_j I_r-V_r I_j\right]}{\left(I_r^{\,2}+I_j^{\,2}\right)^3} \tag{A.33}$$

$$\left(\frac{\partial \hat{Z}_j}{\partial V_j}\right)\left(\frac{\partial \hat{Z}_j}{\partial I_j}\right)=\frac{-V_r I_r}{I_r^{\,2}+I_j^{\,2}}-\frac{2(I_r)(I_j)[V_j I_r - V_r I_j]}{\left(I_r^{\,2}+I_j^{\,2}\right)^3} \tag{A.34}$$

$$\left(\frac{\partial \hat{Z}_j}{\partial I_r}\right)\left(\frac{\partial \hat{Z}_j}{\partial I_j}\right)=\frac{-V_r V_j}{\left(I_r^{\,2}+I_j^{\,2}\right)^2}+\frac{2(V_r)(I_r)[V_j I_r - V_r I_j]}{\left(I_r^{\,2}+I_j^{\,2}\right)^3} \tag{A.35}$$

$$-\frac{2(V_j)(I_j)[V_j I_r - V_r I_j]}{\left(I_r^{\,2}+I_j^{\,2}\right)^3}+\frac{4(I_r)(I_j)[V_j I_r - V_r I_j]^2}{\left(I_r^{\,2}+I_j^{\,2}\right)^4}$$

These results have been introduced into equations (A.6) and (A.7) to produce equations (28) and (29) of Chapter 6.

A.3 Vector Representation of Variance in Impedance

In Chapter 6, the question was raised as to the equivalence of the two methods of Taylor series expansion. The following equality was tested to answer that question.

$$\mathbf{D} = \mathbf{A}_r - \mathbf{A}_j . \tag{A.36}$$

The difference of the two vectors on the right hand side of the equation can be written as

$$\mathbf{A}_r - \mathbf{A}_j = \begin{bmatrix} \dfrac{I_r^2 - I_j^2}{\left(I_r^2 + I_j^2\right)^2} \\ \dfrac{I_j^2 - I_r^2}{\left(I_r^2 + I_j^2\right)^2} \\ \left[\dfrac{V_r^2 - V_j^2}{\left(I_r^2 + I_j^2\right)^2} - \dfrac{4(I_r)(V_r)[V_r I_r + V_j I_j] - 4(I_r)(V_j)[V_j I_r - V_r I_j]}{\left(I_r^2 + I_j^2\right)^3} + \dfrac{4\left(I_r^2\right)[V_r I_r + V_j I_j]^2 - 4\left(I_r^2\right)[V_j I_r - V_r I_j]^2}{\left(I_r^2 + I_j^2\right)^4}\right] \\ \left[\dfrac{V_j^2 - V_r^2}{\left(I_r^2 + I_j^2\right)^2} - \dfrac{4(I_j)(V_j)[V_r I_r + V_j I_j] + 4(I_j)(V_r)[V_j I_r - V_r I_j]}{\left(I_r^2 + I_j^2\right)^3} + \dfrac{4\left(I_j^2\right)[V_r I_r + V_j I_j]^2 - 4\left(I_j^2\right)[V_j I_r - V_r I_j]^2}{\left(I_r^2 + I_j^2\right)^4}\right] \\ \dfrac{4 I_r I_j}{\left(I_r^2 + I_j^2\right)^2} \\ \left[\dfrac{4 V_r V_j}{\left(I_r^2 + I_j^2\right)^2} - \dfrac{4[V_j I_r + V_r I_j][V_r I_r + V_j I_j] + 4[V_r I_r - V_j I_j][V_j I_r - V_r I_j]}{\left(I_r^2 + I_j^2\right)^3} + \dfrac{8(I_r)(I_j)[V_r I_r + V_j I_j]^2 - 8(I_r)(I_j)[V_j I_r - V_r I_j]}{\left(I_r^2 + I_j^2\right)^4}\right] \\ \dfrac{2V_r I_r + 2V_j I_j}{\left(I_r^2 + I_j^2\right)^2} - \dfrac{4\left(I_r^2\right)[V_r I_r + V_j I_j] + 4(I_r)(I_j)[V_j I_r - V_r I_j]}{\left(I_r^2 + I_j^2\right)^3} \\ \dfrac{2V_j I_r - 2V_r I_j}{\left(I_r^2 + I_j^2\right)^2} - \dfrac{4(I_j)(I_r)[V_r I_r + V_j I_j] + 4\left(I_j^2\right)[V_j I_r - V_r I_j]}{\left(I_r^2 + I_j^2\right)^3} \\ \dfrac{2V_r I_j - 2V_j I_r}{\left(I_r^2 + I_j^2\right)^2} - \dfrac{4(I_r)(I_j)[V_r I_r + V_j I_j] - 4\left(I_r^2\right)[V_j I_r - V_r I_j]}{\left(I_r^2 + I_j^2\right)^3} \\ \dfrac{2V_j I_j + 2V_r I_r}{\left(I_r^2 + I_j^2\right)^2} - \dfrac{4\left(I_j^2\right)[V_r I_r + V_j I_j] - 4(I_r)(I_j)[V_j I_r - V_r I_j]}{\left(I_r^2 + I_j^2\right)^3} \end{bmatrix} \tag{A.37}$$

The first element of the difference of the two vectors can be written as

$$\mathbf{A}_r(1) - \mathbf{A}_j(1) = \frac{I_r^2 - I_j^2}{\left(I_r^2 + I_j^2\right)^2} \tag{A.38}$$

$$\mathbf{A}_r(2)-\mathbf{A}_j(2)=\frac{I_j^2-I_r{}^2}{\left(I_r{}^2+I_j{}^2\right)^2}=\frac{-\left(I_r{}^2-I_j^2\right)}{\left(I_r{}^2+I_j{}^2\right)^2} \tag{A.39}$$

$$\begin{aligned}\mathbf{A}_r(3)-\mathbf{A}_j(3)&=\frac{V_r^2-V_j^2}{\left(I_r{}^2+I_j{}^2\right)^2}-\frac{4(I_r)(V_r)\left[V_rI_r+V_jI_j\right]-4(I_r)(V_j)\left[V_jI_r-V_rI_j\right]}{\left(I_r{}^2+I_j{}^2\right)^3}\\&\quad+\frac{4\left(I_r^2\right)\left[V_rI_r+V_jI_j\right]^2-4\left(I_r{}^2\right)\left[V_jI_r-V_rI_j\right]^2}{\left(I_r{}^2+I_j{}^2\right)^4}\\&=\frac{1}{\left(I_r{}^2+I_j{}^2\right)^4}\left\{\begin{array}{l}\left(V_r^2-V_j^2\right)\left(I_r{}^2+I_j{}^2\right)^2-4(I_r)(V_r)\left[V_rI_r+V_jI_j\right]\left(I_r{}^2+I_j{}^2\right)\\+4(I_r)(V_j)\left[V_jI_r-V_rI_j\right]\left(I_r{}^2+I_j{}^2\right)+4\left(I_r^2\right)\left[V_rI_r+V_jI_j\right]^2\\-4\left(I_r{}^2\right)\left[V_jI_r-V_rI_j\right]^2\end{array}\right\}\\&=\frac{1}{\left(I_r{}^2+I_j{}^2\right)^4}\left\{\begin{array}{l}V_r^2I_r{}^4+2V_r^2I_r{}^2I_j{}^2+V_r^2I_j{}^4-V_j^2I_r{}^4-2V_j^2I_r{}^2I_j{}^2-V_j^2I_j{}^4\\-4V_r{}^2I_r{}^4-4V_r{}^2I_r{}^2I_j{}^2-4V_rV_jI_r{}^3I_j-4V_rV_jI_rI_j{}^3\\+4V_j{}^2I_r{}^4+4V_j{}^2I_r{}^2I_j{}^2-4V_rV_jI_r{}^3I_j-4V_rV_jI_rI_j{}^3\\+4V_r{}^2I_r{}^4+8V_rV_jI_r{}^3I_j+4V_j{}^2I_r^2I_j{}^2\\-4V_j{}^2I_r{}^4+8V_rV_jI_r{}^3I_j-4V_r{}^2I_r{}^2I_j{}^2\end{array}\right\}\\&=\frac{1}{\left(I_r{}^2+I_j{}^2\right)^4}\left\{\begin{array}{l}V_r^2I_r{}^4+V_r^2I_j{}^4-V_j{}^2I_r{}^4-2V_j^2I_r{}^2I_j{}^2-V_j^2I_j{}^4\\+8V_rV_jI_r{}^3I_j-8V_rV_jI_rI_j{}^3-6V_r{}^2I_r{}^2I_j{}^2+6V_j{}^2I_r^2I_j{}^2\end{array}\right\}\\&=\frac{1}{\left(I_r{}^2+I_j{}^2\right)^4}\left\{\begin{array}{l}\left[\begin{array}{l}\left(V_r^2I_r{}^4+2V_rV_jI_r{}^3I_j+V_j^2I_r{}^2I_j{}^2\right)\\-\left(V_r{}^2I_r{}^2I_j{}^2+2V_rV_jI_rI_j{}^3+V_j^2I_j{}^4\right)\end{array}\right]\\-\left[\begin{array}{l}\left(V_j{}^2I_r{}^4+V_r{}^2I_r{}^2I_j{}^2-2V_rV_jI_r{}^3I_j\right)\\-\left(V_j^2I_r{}^2I_j{}^2+V_r^2I_j{}^4-2V_rV_jI_rI_j{}^3\right)\end{array}\right]\\+4\left(I_rI_j\right)\left(\begin{array}{l}V_j^2I_rI_j\\-V_r{}^2I_rI_j+V_rV_jI_r{}^2-V_rV_jI_j{}^2\end{array}\right)\end{array}\right\}\\&=\frac{1}{\left(I_r{}^2+I_j{}^2\right)^2}\left[\left(I_r{}^2-I_j{}^2\right)\left(Z_r^2-Z_j^2\right)+4\left(I_rI_j\right)\left(Z_rZ_j\right)\right]\end{aligned} \tag{A.40}$$

$$
\begin{aligned}
\mathbf{A}_r(4)-\mathbf{A}_j(4) &= \frac{V_j^2-V_r^2}{\left(I_r^{\,2}+I_j^{\,2}\right)^2} \\
&\quad - \frac{4\left(I_j\right)\left(V_j\right)\left[V_rI_r+V_jI_j\right]+4\left(I_j\right)\left(V_r\right)\left[V_jI_r-V_rI_j\right]}{\left(I_r^{\,2}+I_j^{\,2}\right)^3} \\
&\quad + \frac{4\left(I_j^{\,2}\right)\left[V_rI_r+V_jI_j\right]^2-4\left(I_j^{\,2}\right)\left[V_jI_r-V_rI_j\right]^2}{\left(I_r^{\,2}+I_j^{\,2}\right)^4} \\
&= \frac{\left\{\begin{array}{l} V_j^2\left(I_r^{\,2}+I_j^{\,2}\right)^2-V_r^2\left(I_r^{\,2}+I_j^{\,2}\right)^2 \\ -4\left(I_j\right)\left(V_j\right)\left[V_rI_r\left(I_r^{\,2}+I_j^{\,2}\right)+V_jI_j\left(I_r^{\,2}+I_j^{\,2}\right)\right] \\ -4\left(I_j\right)\left(V_r\right)\left[V_jI_r\left(I_r^{\,2}+I_j^{\,2}\right)-V_rI_j\left(I_r^{\,2}+I_j^{\,2}\right)\right] \\ +4\left(I_j^{\,2}\right)\left[V_rI_r+V_jI_j\right]^2-4\left(I_j^{\,2}\right)\left[V_jI_r-V_rI_j\right]^2 \end{array}\right\}}{\left(I_r^{\,2}+I_j^{\,2}\right)^4} \\
&= \frac{\left\{\begin{array}{l} V_j^2I_r^{\,4}+2V_j^2I_r^{\,2}I_j^{\,2}+V_j^2I_j^{\,4}-V_r^2I_r^{\,4}-2V_r^2I_r^{\,2}I_j^{\,2} \\ -V_r^2I_j^{\,4}-4V_rV_jI_r^{\,3}I_j-4V_rV_jI_rI_j^{\,3}-4V_j^{\,2}I_r^{\,2}I_j^{\,2} \\ -4V_j^{\,2}I_j^{\,4}-4V_rV_jI_r^{\,3}I_j-4V_rV_jI_rI_j^{\,3}+4V_r^{\,2}I_r^{\,2}I_j^{\,2} \\ +4V_r^{\,2}I_j^{\,4}+4V_r^{\,2}I_r^{\,2}I_j^{\,2}+8V_rV_jI_rI_j^{\,3}+4V_j^{\,2}I_j^{\,4} \\ -4V_j^{\,2}I_r^{\,2}I_j^{\,2}+8V_rV_jI_rI_j^{\,3}-4V_r^{\,2}I_j^{\,4} \end{array}\right\}}{\left(I_r^{\,2}+I_j^{\,2}\right)^4} \\
&= \left\{\begin{array}{l} V_j^2I_r^{\,4}-6V_j^2I_r^{\,2}I_j^{\,2}+V_j^2I_j^{\,4}-V_r^2I_r^{\,4}+6V_r^2I_r^{\,2}I_j^{\,2} \\ -V_r^2I_j^{\,4}-8V_rV_jI_r^{\,3}I_j+8V_rV_jI_rI_j^{\,3}+4V_r^{\,2}I_r^{\,2}I_j^{\,2} \end{array}\right\} \\
&= \frac{1}{\left(I_r^{\,2}+I_j^{\,2}\right)^4}\left\{\begin{array}{l} \left[\begin{array}{l} \left(V_j^2I_r^{\,4}+V_r^2I_r^{\,2}I_j^{\,2}-2V_rV_jI_r^{\,3}I_j\right) \\ -\left(V_r^2I_r^{\,4}+2V_rV_jI_r^{\,3}I_j+V_j^2I_r^{\,2}I_j^{\,2}\right) \end{array}\right] \\ -\left[\begin{array}{l} \left(V_j^2I_r^{\,2}I_j^{\,2}+V_r^2I_j^{\,4}-2V_rV_jI_rI_j^{\,3}\right) \\ -\left(V_r^2I_r^{\,2}I_j^{\,2}+2V_rV_jI_rI_j^{\,3}+V_j^2I_j^{\,4}\right) \end{array}\right] \\ -4\left(I_rI_j\right)\left[\begin{array}{l} V_j^2I_rI_j-V_r^2I_rI_j \\ +V_rV_jI_r^{\,2}-V_rV_jI_j^{\,2} \end{array}\right] \end{array}\right\} \\
&= \frac{-\left[\left(I_r^{\,2}-I_j^{\,2}\right)\left(Z_r^2-Z_j^2\right)+4\left(I_rI_j\right)\left(Z_rZ_j\right)\right]}{\left(I_r^{\,2}+I_j^{\,2}\right)^2}
\end{aligned}
\tag{A.41}
$$

$$\mathbf{A}_r(5)-\mathbf{A}_j(5)=\frac{4I_rI_j}{\left(I_r^{\,2}+I_j^{\,2}\right)^2} \tag{A.42}$$

$$\begin{aligned}
\mathbf{A}_r(6)-\mathbf{A}_j(6)&=\frac{4V_rV_j}{\left(I_r^{\,2}+I_j^{\,2}\right)^2}-\frac{4\left[V_jI_r+V_rI_j\right]\left[V_rI_r+V_jI_j\right]+4\left[V_rI_r-V_jI_j\right]\left[V_jI_r-V_rI_j\right]}{\left(I_r^{\,2}+I_j^{\,2}\right)^3}\\
&\quad+\frac{8(I_r)(I_j)\left[V_rI_r+V_jI_j\right]^2-8(I_r)(I_j)\left[V_jI_r-V_rI_j\right]^2}{\left(I_r^{\,2}+I_j^{\,2}\right)^4}\\
&=\frac{1}{\left(I_r^{\,2}+I_j^{\,2}\right)^4}\left\{\begin{array}{l}
4V_rV_jI_r^{\,4}+8V_rV_jI_r^{\,2}I_j^{\,2}+4V_rV_jI_j^{\,4}\\
-4V_rV_jI_r^{\,4}-4V_j^{\,2}I_r^{\,3}I_j-4V_r^{\,2}I_r^{\,3}I_j-4V_rV_jI_r^{\,2}I_j^{\,2}\\
-4V_rV_jI_r^{\,2}I_j^{\,2}-4V_j^{\,2}I_rI_j^{\,3}-4V_r^{\,2}I_rI_j^{\,3}-4V_rV_jI_j^{\,4}\\
-4V_rV_jI_r^{\,4}+4V_r^{\,2}I_r^{\,3}I_j+4V_j^{\,2}I_r^{\,3}I_j-4V_rV_jI_r^{\,2}I_j^{\,2}\\
-4V_rV_jI_r^{\,2}I_j^{\,2}+4V_r^{\,2}I_rI_j^{\,3}+4V_j^{\,2}I_rI_j^{\,3}-4V_rV_jI_j^{\,4}\\
+8V_r^{\,2}I_r^{\,3}I_j+16V_rV_jI_r^{\,2}I_j^{\,2}+8V_j^{\,2}I_rI_j^{\,3}\\
-8V_j^{\,2}I_r^{\,3}I_j+16V_rV_jI_r^{\,2}I_j^{\,2}-8V_r^{\,2}I_rI_j^{\,3}
\end{array}\right\}\\
&=\frac{-4}{\left(I_r^{\,2}+I_j^{\,2}\right)^4}\left\{\begin{array}{l}
V_rV_jI_r^{\,4}+V_rV_jI_j^{\,4}-2V_r^{\,2}I_r^{\,3}I_j-6V_rV_jI_r^{\,2}I_j^{\,2}\\
-2V_j^{\,2}I_rI_j^{\,3}+2V_j^{\,2}I_r^{\,3}I_j+2V_r^{\,2}I_rI_j^{\,3}
\end{array}\right\}\\
&=\frac{-4}{\left(I_r^{\,2}+I_j^{\,2}\right)^4}\left\{\begin{array}{l}
\left[\begin{array}{l}\left(V_rV_jI_r^{\,4}+V_j^{\,2}I_r^{\,3}I_j-V_r^{\,2}I_r^{\,3}I_j-V_rV_jI_r^{\,2}I_j^{\,2}\right)\\
-\left(V_rV_jI_r^{\,2}I_j^{\,2}+V_j^{\,2}I_rI_j^{\,3}-V_r^{\,2}I_rI_j^{\,3}-V_rV_jI_j^{\,4}\right)\end{array}\right]\\
-\left[\begin{array}{l}\left(V_r^{\,2}I_r^{\,3}I_j+V_rV_jI_r^{\,2}I_j^{\,2}+V_j^{\,2}I_rI_j^{\,3}\right)\\
-\left(V_j^{\,2}I_r^{\,3}I_j+V_r^{\,2}I_rI_j^{\,3}-2V_rV_jI_r^{\,2}I_j^{\,2}\right)\end{array}\right]
\end{array}\right\}\\
&=\frac{-4\left[\left(I_r^{\,2}-I_j^{\,2}\right)\left(Z_rZ_j\right)-\left(I_rI_j\right)\left(Z_r^{\,2}-Z_j^{\,2}\right)\right]}{\left(I_r^{\,2}+I_j^{\,2}\right)^2}
\end{aligned} \tag{A.43}$$

$$\mathbf{A}_r(7)-\mathbf{A}_j(7)=\frac{2V_rI_r+2V_jI_j}{\left(I_r^{\,2}+I_j^{\,2}\right)^2}-\frac{4\left(I_r^{\,2}\right)\left[V_rI_r+V_jI_j\right]+4\left(I_r\right)\left(I_j\right)\left[V_jI_r-V_rI_j\right]}{\left(I_r^{\,2}+I_j^{\,2}\right)^3} \tag{A.44}$$

$$=\frac{1}{\left(I_r^{\,2}+I_j^{\,2}\right)^3}\left\{\begin{array}{l}\left(2V_rI_r+2V_jI_j\right)\left(I_r^{\,2}+I_j^{\,2}\right)\\-4\left[V_rI_r^{\,3}+V_jI_r^{\,2}I_j\right]\\-4\left[V_jI_r^{\,2}I_j-V_rI_rI_j^{\,2}\right]\end{array}\right\}$$

$$=\frac{-2}{\left(I_r^{\,2}+I_j^{\,2}\right)^3}\left\{V_rI_r^{\,3}-V_jI_j^{\,3}+3V_jI_r^{\,2}I_j-3V_rI_rI_j^{\,2}\right\}$$

$$=\frac{-2}{\left(I_r^{\,2}+I_j^{\,2}\right)^3}\left\{\begin{array}{l}\left[\left(V_rI_r^{\,3}+V_jI_r^{\,2}I_j\right)-\left(V_rI_rI_j^{\,2}+V_jI_j^{\,3}\right)\right]\\+\left[2\left(I_rI_j\right)\left(V_jI_r-V_rI_j\right)\right]\end{array}\right\}$$

$$=\frac{-2\left[\left(I_r^{\,2}-I_j^{\,2}\right)\left(Z_r\right)+2\left(I_rI_j\right)\left(Z_j\right)\right]}{\left(I_r^{\,2}+I_j^{\,2}\right)^2}$$

$$\mathbf{A}_r(8)-\mathbf{A}_j(8)=\frac{2V_jI_r-2V_rI_j}{\left(I_r^{\,2}+I_j^{\,2}\right)^2}-\frac{4\left(I_j\right)\left(I_r\right)\left[V_rI_r+V_jI_j\right]+4\left(I_j^{\,2}\right)\left[V_jI_r-V_rI_j\right]}{\left(I_r^{\,2}+I_j^{\,2}\right)^3} \tag{A.45}$$

$$=\frac{2}{\left(I_r^{\,2}+I_j^{\,2}\right)^3}\left\{V_jI_r^{\,3}-3V_rI_r^{\,2}I_j-3V_jI_rI_j^{\,2}+V_rI_j^{\,3}\right\}$$

$$=\frac{2}{\left(I_r^{\,2}+I_j^{\,2}\right)^3}\left\{\begin{array}{l}\left[\left(V_jI_r^{\,3}-V_rI_r^{\,2}I_j\right)-\left(V_jI_rI_j^{\,2}-V_rI_j^{\,3}\right)\right]\\-\left[2\left(I_rI_j\right)\left(V_rI_r+V_jI_j\right)\right]\end{array}\right\}$$

$$=\frac{2\left[\left(I_r^{\,2}-I_j^{\,2}\right)\left(Z_j\right)-2\left(I_rI_j\right)\left(Z_r\right)\right]}{\left(I_r^{\,2}+I_j^{\,2}\right)^3}$$

$$\mathbf{A}_r(9)-\mathbf{A}_j(9)=\frac{2V_rI_j-2V_jI_r}{\left(I_r^{\,2}+I_j^{\,2}\right)^2}-\frac{4(I_r)(I_j)[V_rI_r+V_jI_j]-4\left(I_r^{\,2}\right)[V_jI_r-V_rI_j]}{\left(I_r^{\,2}+I_j^{\,2}\right)^3} \tag{A.46}$$

$$=\frac{2}{\left(I_r^{\,2}+I_j^{\,2}\right)^3}\begin{Bmatrix}V_rI_r^{\,2}I_j-V_jI_r^{\,3}+V_rI_j^{\,3}-V_jI_rI_j^{\,2}\\-2V_rI_r^{\,2}I_j-2V_jI_rI_j^{\,2}+2V_jI_r^{\,3}-2V_rI_r^{\,2}I_j\end{Bmatrix}$$

$$=\frac{2}{\left(I_r^{\,2}+I_j^{\,2}\right)^3}\left\{V_rI_j^{\,3}-3V_jI_rI_j^{\,2}-3V_rI_r^{\,2}I_j+V_jI_r^{\,3}\right\}$$

$$=\frac{2}{\left(I_r^{\,2}+I_j^{\,2}\right)^3}\begin{Bmatrix}\left[\left(V_jI_r^{\,3}-V_rI_r^{\,2}I_j\right)-\left(V_jI_rI_j^{\,2}-V_rI_j^{\,3}\right)\right]\\-\left[2(I_rI_j)(V_jI_j+V_rI_r)\right]\end{Bmatrix}$$

$$=\frac{2\left[\left(I_r^{\,2}-I_j^{\,2}\right)(Z_j)-2(I_rI_j)(Z_r)\right]}{\left(I_r^{\,2}+I_j^{\,2}\right)^3}$$

$$\mathbf{A}_r(10)-\mathbf{A}_j(10)=\frac{2V_jI_j+2V_rI_r}{\left(I_r^{\,2}+I_j^{\,2}\right)^2}-\frac{4\left(I_j^{\,2}\right)[V_rI_r+V_jI_j]-4(I_r)(I_j)[V_jI_r-V_rI_j]}{\left(I_r^{\,2}+I_j^{\,2}\right)^3} \tag{A.47}$$

$$=\frac{2}{\left(I_r^{\,2}+I_j^{\,2}\right)^3}\begin{Bmatrix}V_jI_r^{\,2}I_j+V_rI_r^{\,3}+V_jI_j^{\,3}+V_rI_rI_j^{\,2}\\-2V_rI_rI_j^{\,2}-2V_jI_j^{\,3}+2V_jI_r^{\,2}I_j-2V_rI_rI_j^{\,2}\end{Bmatrix}$$

$$=\frac{2}{\left(I_r^{\,2}+I_j^{\,2}\right)^3}\left\{V_rI_r^{\,3}-V_jI_j^{\,3}+3V_jI_r^{\,2}I_j-3V_rI_rI_j^{\,2}\right\}$$

$$=\frac{2}{\left(I_r^{\,2}+I_j^{\,2}\right)^3}\begin{Bmatrix}\left[\left(V_rI_r^{\,3}+V_jI_r^{\,2}I_j\right)-\left(V_rI_rI_j^{\,2}+V_jI_j^{\,3}\right)\right]\\+\left[2(I_rI_j)(V_jI_r-V_rI_j)\right]\end{Bmatrix}$$

$$=\frac{2\left[\left(I_r^{\,2}-I_j^{\,2}\right)(Z_r)+2(I_rI_j)(Z_j)\right]}{\left(I_r^{\,2}+I_j^{\,2}\right)^3}$$

Thus, equation (A.37) can be rewritten as

$$\mathbf{A}_r - \mathbf{A}_j = \frac{1}{\left(I_r^{\,2} + I_j^{\,2}\right)^2}\begin{bmatrix} \left(I_r^{\,2} - I_j^{\,2}\right) \\ -\left(I_r^{\,2} - I_j^{\,2}\right) \\ \left[\left(I_r^{\,2} - I_j^{\,2}\right)\left(Z_r^{\,2} - Z_j^{\,2}\right) + 4\left(I_r I_j\right)\left(Z_r Z_j\right)\right] \\ -\left[\left(I_r^{\,2} - I_j^{\,2}\right)\left(Z_r^{\,2} - Z_j^{\,2}\right) + 4\left(I_r I_j\right)\left(Z_r Z_j\right)\right] \\ 4\left(I_r I_j\right) \\ -4\left[\left(I_r^{\,2} - I_j^{\,2}\right)\left(Z_r Z_j\right) - \left(I_r I_j\right)\left(Z_r^{\,2} - Z_j^{\,2}\right)\right] \\ -2\left[\left(I_r^{\,2} - I_j^{\,2}\right)\left(Z_r\right) + 2\left(I_r I_j\right)\left(Z_j\right)\right] \\ 2\left[\left(I_r^{\,2} - I_j^{\,2}\right)\left(Z_j\right) - 2\left(I_r I_j\right)\left(Z_r\right)\right] \\ 2\left[\left(I_r^{\,2} - I_j^{\,2}\right)\left(Z_j\right) - 2\left(I_r I_j\right)\left(Z_r\right)\right] \\ 2\left[\left(I_r^{\,2} - I_j^{\,2}\right)\left(Z_r\right) + 2\left(I_r I_j\right)\left(Z_j\right)\right] \end{bmatrix}. \tag{A.48}$$

that is the result reported in Chapter 6. This vector can be used to test the equality of the difference between the variances in the stochastic errors in the real and imaginary impedances with zero. The ratio of the two variances can be compared to unity via the individual expressions for the real and imaginary coefficient vectors.

APPENDIX B
DERIVATION OF VARIANCE IN FREQUENCY-DOMAIN ERRORS FROM ADDITIVE ERRORS IN TIME-DOMAIN

This appendix provides the details of the derivations presented in Chapter 8. More steps are presented here than are probably required to follow the derivation, but the additional steps save the reader from getting lost in the algebra of the derivation.

B.1 Variance for Frequency Response Analysis

The complex components of the current and voltage signals measured using Frequency Response Analysis can be written

$$V_r(\omega) = \frac{\omega}{2\pi n}\int_0^{2\pi n/\omega} \hat{V}\sin(\omega t + \phi_V)\sin(\omega t)dt + \frac{\omega}{2\pi n}\int_0^{2\pi n/\omega} n_V(t)\sin(\omega t)dt \tag{B.1}$$

$$V_j(\omega) = \frac{\omega}{2\pi n}\int_0^{2\pi n/\omega} \hat{V}\sin(\omega t + \phi_V)\cos(\omega t)dt + \frac{\omega}{2\pi n}\int_0^{2\pi n/\omega} n_V(t)\cos(\omega t)dt \tag{B.2}$$

$$I_r(\omega) = \frac{\omega}{2\pi n}\int_0^{2\pi n/\omega} \hat{I}\sin(\omega t + \phi_I)\sin(\omega t)dt + \frac{\omega}{2\pi n}\int_0^{2\pi n/\omega} n_I(t)\sin(\omega t)dt \tag{B.3}$$

$$I_j(\omega) = \frac{\omega}{2\pi n}\int_0^{2\pi n/\omega} \hat{I}\sin(\omega t + \phi_I)\cos(\omega t)dt + \frac{\omega}{2\pi n}\int_0^{2\pi n/\omega} n_I(t)\cos(\omega t)dt \tag{B.4}$$

where the limits of integration are zero to the time associated with an integral number of cycles. The expectation of the error resulting from the difference between the observed value of a signal and its expected value will be simply the expected value of the integral of the product of the noise signal and the reference signal since the expectation can move into the integrals of equations (B.1)-(B.4)

$$E\left[\varepsilon_{V_r}(\omega)\right] = E\left[V_r(\omega) - \hat{V}_r(\omega)\right] = E\left[\int_0^{2\pi/\omega} n_V(t)\sin(\omega t)dt\right] \tag{B.5}$$

$$E\left[\varepsilon_{V_j}(\omega)\right] = E\left[V_j(\omega) - \hat{V}_j(\omega)\right] = E\left[\int_0^{2\pi/\omega} n_V(t)\cos(\omega t)dt\right] \tag{B.6}$$

$$E\left[\varepsilon_{I_r}(\omega)\right] = E\left[I_r(\omega) - \hat{I}_r(\omega)\right] = E\left[\int_0^{2\pi/\omega} n_I(t)\sin(\omega t)dt\right] \tag{B.7}$$

$$E\left[\varepsilon_{I_j}(\omega)\right] = E\left[I_j(\omega) - \hat{I}_j(\omega)\right] = E\left[\int_0^{2\pi/\omega} n_I(t)\cos(\omega t)dt\right] \tag{B.8}$$

B.1.1 Variance Defined by Expectation Integration over Time

At this point, two definitions of the variance can be studied. One is the sample variance based upon repeated measurements of the integrals. The other definition is a functional variance, that is, the variance of the function with respect to its time-domain expectation defined by[116]

$$E[f(t)] = \frac{1}{b-a}\int_a^b t f(t)dt \tag{B.9}$$

The variance of the stochastic errors of each component of the two signals can be written

$$E\left[\sigma_{V_r}^2(\omega)\right] = E\left\{\left[\left(\int_0^{2\pi/\omega} n_V(t)\sin(\omega t)dt\right) - E\left[\int_0^{2\pi/\omega} n_V(t)\sin(\omega t)dt\right]\right]^2\right\} \tag{B.10}$$

$$E\left[\sigma_{V_j}^2(\omega)\right] = E\left\{\left[\left(\int_0^{2\pi/\omega} n_V(t)\cos(\omega t)dt\right) - E\left[\int_0^{2\pi/\omega} n_V(t)\cos(\omega t)dt\right]\right]^2\right\} \tag{B.11}$$

$$E\left[\sigma_{I_r}^2(\omega)\right] = E\left\{\left[\left(\int_0^{2\pi/\omega} n_I(t)\sin(\omega t)dt\right) - E\left[\int_0^{2\pi/\omega} n_I(t)\sin(\omega t)dt\right]\right]^2\right\} \tag{B.12}$$

$$E\left[\sigma_{I_j}^2(\omega)\right] = E\left\{\left[\left(\int_0^{2\pi/\omega} n_I(t)\cos(\omega t)dt\right) - E\left[\int_0^{2\pi/\omega} n_I(t)\cos(\omega t)dt\right]\right]^2\right\} \tag{B.13}$$

If the expectation in the noise signals is zero, then the variance of each signal component and the cross-covariances between the different components of the signals can be written[116]

$$E\left[\sigma_{V_r}^2(\omega)\right] = E\left\{\left[\int_0^{2\pi/\omega} n_V(t)\sin(\omega t)dt\right]^2\right\} \tag{B.14}$$

$$E\left[\sigma_{V_j}^2(\omega)\right] = E\left\{\left[\int_0^{2\pi/\omega} n_V(t)\cos(\omega t)dt\right]^2\right\} \tag{B.15}$$

$$E\left[\sigma_{I_r}^2(\omega)\right] = E\left\{\left[\int_0^{2\pi/\omega} n_I(t)\sin(\omega t)dt\right]^2\right\} \tag{B.16}$$

$$E\left[\sigma_{I_j}^2(\omega)\right] = E\left\{\left[\int_0^{2\pi/\omega} n_I(t)\cos(\omega t)dt\right]^2\right\} \tag{B.17}$$

$$E\left[\sigma_{V_rV_j}(\omega)\right] = E\left\{\left[\int_0^{2\pi/\omega} n_V(t)\sin(\omega t)dt\right]\left[\int_0^{2\pi/\omega} n_V(t)\cos(\omega t)dt\right]\right\} \tag{B.18}$$

$$E\left[\sigma_{I_rI_j}(\omega)\right] = E\left\{\left[\int_0^{2\pi/\omega} n_I(t)\sin(\omega t)dt\right]\left[\int_0^{2\pi/\omega} n_I(t)\cos(\omega t)dt\right]\right\} \tag{B.19}$$

$$E\left[\sigma_{V_rI_r}(\omega)\right] = E\left\{\left[\int_0^{2\pi/\omega} n_V(t)\sin(\omega t)dt\right]\left[\int_0^{2\pi/\omega} n_I(t)\sin(\omega t)dt\right]\right\} \tag{B.20}$$

$$E\left[\sigma_{V_rI_j}(\omega)\right] = E\left\{\left[\int_0^{2\pi/\omega} n_V(t)\sin(\omega t)dt\right]\left[\int_0^{2\pi/\omega} n_I(t)\cos(\omega t)dt\right]\right\} \tag{B.21}$$

$$E\left[\sigma_{V_j I_r}(\omega)\right] = E\left\{\left[\int_0^{2\pi/\omega} n_V(t)\cos(\omega t)dt\right]\left[\int_0^{2\pi/\omega} n_I(t)\sin(\omega t)dt\right]\right\} \tag{B.22}$$

$$E\left[\sigma_{V_j I_j}(\omega)\right] = E\left\{\left[\int_0^{2\pi/\omega} n_V(t)\cos(\omega t)dt\right]\left[\int_0^{2\pi/\omega} n_I(t)\cos(\omega t)dt\right]\right\} \tag{B.23}$$

These ten products of integral can be rewritten as double integrals, i.e., [116]

$$\sigma_{V_r}^2(\omega) = E\left[\left(\frac{\omega^2}{4\pi^2 n^2}\right)\int_0^{2\pi n/\omega}\int_0^{2\pi n/\omega} n_V(x)n_V(y)\sin(\omega x)\sin(\omega y)dxdy\right] \tag{B.24}$$

$$\sigma_{V_j}^2(\omega) = E\left[\left(\frac{\omega^2}{4\pi^2 n^2}\right)\int_0^{2\pi n/\omega}\int_0^{2\pi n/\omega} n_V(x)n_V(y)\cos(\omega x)\cos(\omega y)dxdy\right] \tag{B.25}$$

$$\sigma_{I_r}^2(\omega) = E\left[\left(\frac{\omega^2}{4\pi^2 n^2}\right)\int_0^{2\pi n/\omega}\int_0^{2\pi n/\omega} n_I(x)n_I(y)\sin(\omega x)\sin(\omega y)dxdy\right] \tag{B.26}$$

$$\sigma_{I_j}^2(\omega) = E\left[\left(\frac{\omega^2}{4\pi^2 n^2}\right)\int_0^{2\pi n/\omega}\int_0^{2\pi n/\omega} n_I(x)n_I(y)\cos(\omega x)\cos(\omega y)dxdy\right] \tag{B.27}$$

$$\sigma_{V_r V_j}(\omega) = E\left[\left(\frac{\omega^2}{4\pi^2 n^2}\right)\int_0^{2\pi n/\omega}\int_0^{2\pi n/\omega} n_V(x)n_V(y)\sin(\omega x)\cos(\omega y)dxdy\right] \tag{B.28}$$

$$\sigma_{I_r I_j}(\omega) = E\left[\left(\frac{\omega^2}{4\pi^2 n^2}\right)\int_0^{2\pi n/\omega}\int_0^{2\pi n/\omega} n_I(x)n_I(y)\sin(\omega x)\cos(\omega y)dxdy\right] \tag{B.29}$$

$$\sigma_{V_r I_r}(\omega) = E\left[\left(\frac{\omega^2}{4\pi^2 n^2}\right)\int_0^{2\pi n/\omega}\int_0^{2\pi n/\omega} n_V(x)n_I(y)\sin(\omega x)\sin(\omega y)dxdy\right] \tag{B.30}$$

$$\sigma_{V_r I_j}(\omega) = E\left[\left(\frac{\omega^2}{4\pi^2 n^2}\right)\int_0^{2\pi n/\omega}\int_0^{2\pi n/\omega} n_V(x)n_I(y)\sin(\omega x)\cos(\omega y)dxdy\right] \tag{B.31}$$

$$\sigma_{V_j I_r}(\omega) = E\left[\left(\frac{\omega^2}{4\pi^2 n^2}\right)\int_0^{2\pi n/\omega}\int_0^{2\pi n/\omega} n_V(x)n_I(y)\cos(\omega x)\sin(\omega y)dxdy\right] \tag{B.32}$$

$$\sigma_{V_j I_j}(\omega) = E\left[\left(\frac{\omega^2}{4\pi^2 n^2}\right)\int_0^{2\pi n/\omega}\int_0^{2\pi n/\omega} n_V(x) n_I(y)\cos(\omega x)\cos(\omega y)dxdy\right] \tag{B.33}$$

Each double integral can then be evaluated to reduce each equation to a single integral.[116] If a difference variable is defined to be

$$\tau = y - x \tag{B.34}$$

and the correlation function is given by

$$\psi_{n_A n_A}(\tau) = E[n_A(x) n_A(y)], \tag{B.35}$$

then equation (B.24) can be rewritten as

$$\begin{aligned}\sigma_{V_r}^2(\omega) = &\left(\frac{\omega^2}{4\pi^2 n^2}\right)\int_0^{2\pi n/\omega} d\tau\, \psi_{n_V n_V}(\tau)\int_0^{(2\pi n/\omega)-\tau}\sin(\omega x)\sin(\omega(x+\tau))dx \\ &+\left(\frac{\omega^2}{4\pi^2 n^2}\right)\int_0^{2\pi n/\omega} d\tau\, \psi_{n_V n_V}(\tau)\int_0^{(2\pi n/\omega)+\tau}\sin(\omega y)\sin(\omega(y-\tau))dx\end{aligned} \tag{B.36}$$

Since the correlation function in equation (B.36) is actually the auto-correlation function, and since

$$\psi_{n_A n_A}(\tau) = \psi_{n_A n_A}(-\tau), \tag{B.37}$$

the integral can be rewritten as

$$\sigma_{V_r}^2(\omega) = \left(\frac{\omega^2}{2\pi^2 n^2}\right)\int_0^{2\pi n/\omega} d\tau\, \psi_{n_V n_V}(\tau)\int_0^{(2\pi n/\omega)-\tau}\sin(\omega x)\sin(\omega(x+\tau))dx. \tag{B.38}$$

Upon substitution of the trigonometric identity for the product of two sine waves into the second integral of equation (B.38), the variance in the real component of the voltage signal can be rewritten as

$$\sigma_{I_r}^2(\omega) = \left(\frac{\omega^2}{2\pi^2 n^2}\right)\int_0^{2\pi n/\omega} d\tau\, \psi_{n_V n_V}(\tau)\int_0^{(2\pi n/\omega)-\tau}\left[\frac{1}{2}\cos(\omega\tau) - \frac{1}{2}\cos(\omega(2x+\tau))\right]dx. \tag{B.39}$$

The second integral can be calculated, and the variance in the real component of the voltage signal is therefore[116]

$$\sigma_{V_r}^2(\omega)=\left(\frac{\omega}{2\pi n}\right)\int_0^{2\pi n/\omega} d\tau\, \psi_{n_V n_V}(\tau)\left[\left(1-\frac{\tau\omega}{2\pi n}\right)\cos(\omega\tau)+\left(\frac{1}{2\pi n}\right)\sin(\omega\tau)\right]. \tag{B.40}$$

Equation (B.25) is simplified following a similar procedure. The derivation proceeds through the substitution of the auto-correlation function and transformation of variables. The variance integral can be rewritten as

$$\sigma_{V_j}^2(\omega)=\left(\frac{\omega^2}{2\pi^2 n^2}\right)\int_0^{2\pi n/\omega} d\tau\, \psi_{n_V n_V}(\tau)\int_0^{(2\pi n/\omega)-\tau}\cos(\omega x)\cos(\omega(x+\tau))dx. \tag{B.41}$$

The trigonometric identity used for substitution in the second integral is now for the product of two cosine signals. Equation (B.41) can then be simplified by estimating the second integral. The result is[116]

$$\sigma_{V_j}^2(\omega)=\left(\frac{\omega}{2\pi n}\right)\int_0^{2\pi n/\omega} d\tau\, \psi_{n_V n_V}(\tau)\left[\left(1-\frac{\tau\omega}{2\pi n}\right)\cos(\omega\tau)-\left(\frac{1}{2\pi n}\right)\sin(\omega\tau)\right]. \tag{B.42}$$

Finally, the covariance between the real and imaginary components of the voltage signal can be written in terms of the transformed variables and auto-correlation function as

$$\sigma_{V_r V_j}(\omega)=\left(\frac{\omega^2}{2\pi^2 n^2}\right)\int_0^{2\pi n/\omega} d\tau\, \psi_{n_V n_V}(\tau)\int_0^{(2\pi n/\omega)-\tau}\begin{bmatrix}\sin(\omega x)\cos(\omega(x+\tau))\\ +\cos(\omega x)\sin(\omega(x+\tau))\end{bmatrix}dx. \tag{B.43}$$

This can be rewritten by substituting the trigonometric identity for the sine of the sum of two angles

$$\sigma_{V_r V_j}(\omega)=\left(\frac{\omega^2}{2\pi^2 n^2}\right)\int_0^{2\pi n/\omega} d\tau\, \psi_{n_V n_V}(\tau)\int_0^{(2\pi n/\omega)-\tau}\sin(\omega(2x+\tau))dx. \tag{B.44}$$

The second integral is identically zero; therefore the covariance between the real and imaginary components of the voltage signal is equal to zero, i.e.,[116]

$$\sigma_{V_r V_j}(\omega) = 0. \tag{B.45}$$

Similar results can be estimated for the variances of and covariance between the real and imaginary components of the current signal. The results are[116]

$$\sigma_{I_r}^2(\omega) = \left(\frac{\omega}{2\pi n}\right)\int_0^{2\pi n/\omega} d\tau\, \psi_{n_I n_I}(\tau)\left[\left(1-\frac{\tau\omega}{2\pi n}\right)\cos(\omega\tau)+\left(\frac{1}{2\pi n}\right)\sin(\omega\tau)\right] \tag{B.46}$$

$$\sigma_{I_j}^2(\omega) = \left(\frac{\omega}{2\pi n}\right)\int_0^{2\pi n/\omega} d\tau\, \psi_{n_I n_I}(\tau)\left[\left(1-\frac{\tau\omega}{2\pi n}\right)\cos(\omega\tau)-\left(\frac{1}{2\pi n}\right)\sin(\omega\tau)\right] \tag{B.47}$$

$$\sigma_{I_r I_j}(\omega) = 0. \tag{B.48}$$

The four cross-covariances can also be estimated in similar fashion. Equation (B.30) can be rewritten after the transformation of variables and introduction of the cross-correlation function as

$$\begin{aligned}\sigma_{V_r I_r}(\omega) = &\left(\frac{\omega^2}{4\pi^2 n^2}\right)\int_0^{2\pi n/\omega} d\tau\, \psi_{n_V n_I}(\tau)\int_0^{(2\pi n/\omega)-\tau}\sin(\omega x)\sin(\omega(x+\tau))dx \\ &+\left(\frac{\omega^2}{4\pi^2 n^2}\right)\int_0^{2\pi n/\omega} d\tau\, \psi_{n_V n_I}(\tau)\int_0^{(2\pi n/\omega)+\tau}\sin(\omega y)\sin(\omega(y-\tau))dx\end{aligned} \tag{B.49}$$

For the cross-correlation function,

$$\psi_{n_A n_B}(\tau) = \psi_{n_B n_A}(-\tau), \tag{B.50}$$

therefore, the cross-covariance can be reduced to

$$\sigma_{V_r I_r}(\omega) = \left(\frac{\omega^2}{4\pi^2 n^2}\right)\int_0^{2\pi n/\omega} d\tau\, \left[\psi_{n_V n_I}(\tau)+\psi_{n_I n_V}(\tau)\right]\int_0^{(2\pi n/\omega)-\tau}\sin(\omega x)\sin(\omega(x+\tau))dx\,. \tag{B.51}$$

The second integral is calculated through the substitution of the appropriate trigonometric identity simplifying equation (B.51) to

$$\sigma_{V_r I_r}(\omega)=\left(\frac{\omega}{2\pi n}\right)\int_0^{2\pi n/\omega} d\tau \left\{\begin{array}{l}\left[\psi_{n_V n_I}(\tau)+\psi_{n_I n_V}(\tau)\right]\times \\ \left[\left(1-\frac{\tau\omega}{2\pi n}\right)\cos(\omega\tau)+\left(\frac{1}{2\pi n}\right)\sin(\omega\tau)\right]\end{array}\right\}. \tag{B.52}$$

The other three cross-covariances are determined via the same procedure, and therefore, equations (B.31)-(B.33) can be rewritten as

$$\sigma_{V_r I_j}(\omega)=0 \tag{B.53}$$

$$\sigma_{V_j I_r}(\omega)=0 \tag{B.54}$$

$$\sigma_{V_j I_j}(\omega)=\left(\frac{\omega}{2\pi n}\right)\int_0^{2\pi n/\omega} d\tau \left\{\begin{array}{l}\left[\psi_{n_V n_I}(\tau)+\psi_{n_I n_V}(\tau)\right]\times \\ \left[\left(1-\frac{\tau\omega}{2\pi n}\right)\cos(\omega\tau)-\left(\frac{1}{2\pi n}\right)\sin(\omega\tau)\right]\end{array}\right\}. \tag{B.55}$$

The cross-covariances in equations (B.53) and (B.54) are zero because of the integral of the sine of the sum of two angles as seen in equation (B.43).

B.1.2 Variance Based on Expectation in a Sampling Sense

The sample variance can be derived by redefining expectation as an averaging of samples rather than as an integral average over time. This can be related to the sample variance description of impedance errors of Orazem, et al.[6-9] by defining

$$E[V_r(\omega)]=E\left[\int_0^{2\pi n/\omega}\hat{V}\sin(\omega t+\phi_V)\sin(\omega t)dt+\int_0^{2\pi n/\omega}n_V(t)\sin(\omega t)dt\right] \tag{B.56}$$

$$E[V_j(\omega)]=E\left[\int_0^{2\pi n/\omega}\hat{V}\sin(\omega t+\phi_V)\cos(\omega t)dt+\int_0^{2\pi n/\omega}n_V(t)\cos(\omega t)dt\right] \tag{B.57}$$

$$E[I_r(\omega)]=E\left[\int_0^{2\pi n/\omega}\hat{I}\sin(\omega t+\phi_I)\sin(\omega t)dt+\int_0^{2\pi n/\omega}n_I(t)\sin(\omega t)dt\right] \tag{B.58}$$

$$E[I_j(\omega)]=E\left[\int_0^{2\pi n/\omega}\hat{I}\sin(\omega t+\phi_I)\cos(\omega t)dt+\int_0^{2\pi n/\omega}n_I(t)\cos(\omega t)dt\right] \tag{B.59}$$

The expectation value of the first integral will just be the value of the first integral since each term in the integrand is fully described in a deterministic sense. The trigonometric term in the second integral is deterministic, therefore, the expectation is applied only to the noise signal, i.e.,

$$E[V_r(\omega)] = \int_0^{2\pi n/\omega} \hat{V}\sin(\omega t + \phi_V)\sin(\omega t)dt + \int_0^{2\pi n/\omega} E[n_V(t)]\sin(\omega t)dt \tag{B.60}$$

$$E[V_j(\omega)] = \int_0^{2\pi n/\omega} \hat{V}\sin(\omega t + \phi_V)\cos(\omega t)dt + \int_0^{2\pi n/\omega} E[n_V(t)]\cos(\omega t)dt \tag{B.61}$$

$$E[I_r(\omega)] = \int_0^{2\pi n/\omega} \hat{I}\sin(\omega t + \phi_I)\sin(\omega t)dt + \int_0^{2\pi n/\omega} E[n_I(t)]\sin(\omega t)dt \tag{B.62}$$

$$E[I_j(\omega)] = \int_0^{2\pi n/\omega} \hat{I}\sin(\omega t + \phi_I)\cos(\omega t)dt + \int_0^{2\pi n/\omega} E[n_I(t)]\cos(\omega t)dt \tag{B.63}$$

The sample variance of each signal can then be written

$$\sigma_{V_r}^2(\omega) = E\{[V_r(\omega) - E[V_r(\omega)]]^2\} \tag{B.64}$$

$$\sigma_{V_j}^2(\omega) = E\{[V_j(\omega) - E[V_j(\omega)]]^2\} \tag{B.65}$$

$$\sigma_{I_r}^2(\omega) = E\{[I_r(\omega) - E[I_r(\omega)]]^2\} \tag{B.66}$$

$$\sigma_{I_j}^2(\omega) = E\{[I_j(\omega) - E[I_j(\omega)]]^2\} \tag{B.67}$$

Upon substitution of equations (B.1)-(B.4) and (B.60)-(B.63) into (B.64)-(B.67), the variances can be written

$$\sigma_{V_r}^2(\omega) = E\left\{\left[\int_0^{2\pi n/\omega} \{n_V(t) - E[n_V(t)]\}\sin(\omega t)dt\right]^2\right\} \tag{B.68}$$

$$\sigma_{V_j}^2(\omega) = E\left\{\left[\int_0^{2\pi n/\omega} \{n_V(t) - E[n_V(t)]\}\cos(\omega t)dt\right]^2\right\} \tag{B.69}$$

$$\sigma_{I_r}^2(\omega) = E\left\{\left[\int_0^{2\pi n/\omega} \{n_I(t) - E[n_I(t)]\}\sin(\omega t)dt\right]^2\right\} \tag{B.70}$$

$$\sigma_{I_j}^2(\omega) = E\left\{\left[\int_0^{2\pi n/\omega} \{n_I(t) - E[n_I(t)]\}\cos(\omega t)dt\right]^2\right\} \tag{B.71}$$

The square of each integral can be rewritten as a double integral, i.e.,

$$\sigma_{V_r}^2(\omega) = E\left\{\int_0^{2\pi n/\omega}\int_0^{2\pi n/\omega} \{n_V(u) - E[n_V(u)]\}\{n_V(v) - E[n_V(v)]\}\sin(\omega u)\sin(\omega v)dudv\right\} \tag{B.72}$$

$$\sigma_{V_j}^2(\omega) = E\left\{\int_0^{2\pi n/\omega}\int_0^{2\pi n/\omega} \{n_V(u) - E[n_V(u)]\}\{n_V(v) - E[n_V(v)]\}\cos(\omega u)\cos(\omega v)dudv\right\} \tag{B.73}$$

$$\sigma_{I_r}^2(\omega) = E\left\{\int_0^{2\pi n/\omega}\int_0^{2\pi n/\omega} \{n_I(u) - E[n_I(u)]\}\{n_I(v) - E[n_I(v)]\}\sin(\omega u)\sin(\omega v)dudv\right\} \tag{B.74}$$

$$\sigma_{I_r}^2(\omega) = E\left\{\int_0^{2\pi n/\omega}\int_0^{2\pi n/\omega} \{n_I(u) - E[n_I(u)]\}\{n_I(v) - E[n_I(v)]\}\cos(\omega u)\cos(\omega v)dudv\right\} \tag{B.75}$$

It is important to note, at this point, that the expectation that is applied within the integrand implies a summation over time, whereas the expectation applied to the double integrals refers to a summation over replicated frequency-domain measurements. Therefore, the expectation in the integrand will be referred to as E_t and the expectation applied to the double integrals will be referred to as E_f. Equations (B.72)-(B.75) can be rewritten

$$\sigma_{V_r}^2(\omega) = \int_0^{2\pi n/\omega}\int_0^{2\pi n/\omega} E_f\{n_V(u)n_V(v)\}\sin(\omega u)\sin(\omega v)dudv$$
$$- \int_0^{2\pi n/\omega}\int_0^{2\pi n/\omega} E_f\{n_V(v)E_t[n_V(u)]\}\sin(\omega u)\sin(\omega v)dudv$$
$$- \int_0^{2\pi n/\omega}\int_0^{2\pi n/\omega} E_f\{n_V(u)E_t[n_V(v)]\}\sin(\omega u)\sin(\omega v)dudv$$
$$+ \int_0^{2\pi n/\omega}\int_0^{2\pi n/\omega} E_f\{E_t[n_V(u)]E_t[n_V(v)]\}\sin(\omega u)\sin(\omega v)dudv \tag{B.76}$$

$$\sigma_{V_J}^2(\omega) = \int_0^{2\pi n/\omega}\int_0^{2\pi n/\omega} E_f\{n_V(u)n_V(v)\}\cos(\omega u)\cos(\omega v)dudv$$
$$- \int_0^{2\pi n/\omega}\int_0^{2\pi n/\omega} E_f\{n_V(v)E_t[n_V(u)]\}\cos(\omega u)\cos(\omega v)dudv$$
$$- \int_0^{2\pi n/\omega}\int_0^{2\pi n/\omega} E_f\{n_V(u)E_t[n_V(v)]\}\cos(\omega u)\cos(\omega v)dudv$$
$$+ \int_0^{2\pi n/\omega}\int_0^{2\pi n/\omega} E_f\{E_t[n_V(u)]E_t[n_V(v)]\}\cos(\omega u)\cos(\omega v)dudv \tag{B.77}$$

$$\sigma_{I_r}^2(\omega) = \int_0^{2\pi n/\omega}\int_0^{2\pi n/\omega} E_f\{n_I(u)n_I(v)\}\sin(\omega u)\sin(\omega v)dudv$$
$$- \int_0^{2\pi n/\omega}\int_0^{2\pi n/\omega} E_f\{n_I(v)E_t[n_I(u)]\}\sin(\omega u)\sin(\omega v)dudv$$
$$- \int_0^{2\pi n/\omega}\int_0^{2\pi n/\omega} E_f\{n_I(u)E_t[n_I(v)]\}\sin(\omega u)\sin(\omega v)dudv$$
$$+ \int_0^{2\pi n/\omega}\int_0^{2\pi n/\omega} E_f\{E_t[n_I(u)]E_t[n_I(v)]\}\sin(\omega u)\sin(\omega v)dudv \tag{B.78}$$

$$\sigma_{I_J}^2(\omega) = \int_0^{2\pi n/\omega}\int_0^{2\pi n/\omega} E_f\{n_I(u)n_I(v)\}\cos(\omega u)\cos(\omega v)dudv$$
$$- \int_0^{2\pi n/\omega}\int_0^{2\pi n/\omega} E_f\{n_I(v)E_t[n_I(u)]\}\cos(\omega u)\cos(\omega v)dudv$$
$$- \int_0^{2\pi n/\omega}\int_0^{2\pi n/\omega} E_f\{n_I(u)E_t[n_I(v)]\}\cos(\omega u)\cos(\omega v)dudv$$
$$+ \int_0^{2\pi n/\omega}\int_0^{2\pi n/\omega} E_f\{E_t[n_I(u)]E_t[n_I(v)]\}\cos(\omega u)\cos(\omega v)dudv \tag{B.79}$$

If the time-domain expectations of the noise signals are equal to zero,

$$E_t[n_I(t)] = E_t[n_V(t)] = 0, \tag{B.80}$$

and the frequency-domain expectation is written for N sampled noise signals as

$$E_f[n_X(t)] = \frac{1}{N}\sum_{k=1}^{N} n_{X,k}(t), \tag{B.81}$$

then equations can be rewritten as

$$\sigma_{V_r}^2(\omega) = \frac{1}{N}\int_0^{2\pi n/\omega}\int_0^{2\pi n/\omega}\left\{\sum_{k=1}^{N}[n_{V,k}(u)n_{V,k}(v)]\right\}\sin(\omega u)\sin(\omega v)dudv \tag{B.82}$$

$$\sigma_{V_J}^2(\omega) = \frac{1}{N}\int_0^{2\pi n/\omega}\int_0^{2\pi n/\omega}\left\{\sum_{k=1}^{N}[n_{V,k}(u)n_{V,k}(v)]\right\}\cos(\omega u)\cos(\omega v)dudv \tag{B.83}$$

$$\sigma_{I_r}^2(\omega) = \frac{1}{N}\int_0^{2\pi n/\omega}\int_0^{2\pi n/\omega}\left\{\sum_{k=1}^{N}[n_{I,k}(u)n_{I,k}(v)]\right\}\sin(\omega u)\sin(\omega v)dudv \tag{B.84}$$

$$\sigma_{I_J}^2(\omega) = \frac{1}{N}\int_0^{2\pi n/\omega}\int_0^{2\pi n/\omega}\left\{\sum_{k=1}^{N}[n_{I,k}(u)n_{I,k}(v)]\right\}\cos(\omega u)\cos(\omega v)dudv. \tag{B.85}$$

Through a similar derivation, the other six covariances and cross-covariances of the Taylor series variance vector can be determined by

$$\sigma_{V_rV_j}(\omega) = \frac{1}{N}\int_0^{2\pi n/\omega}\int_0^{2\pi n/\omega}\left\{\sum_{k=1}^{N}[n_{V,k}(u)n_{V,k}(v)]\right\}\sin(\omega u)\cos(\omega v)dudv \tag{B.86}$$

$$\sigma_{I_rI_J}(\omega)=\frac{1}{N}\int_0^{2\pi n/\omega}\int_0^{2\pi n/\omega}\left\{\sum_{k=1}^{N}\left[n_{I,k}(u)n_{I,k}(v)\right]\right\}\sin(\omega u)\cos(\omega v)dudv \tag{B.87}$$

$$\sigma_{V_rI_r}(\omega)=\frac{1}{N}\int_0^{2\pi n/\omega}\int_0^{2\pi n/\omega}\left\{\sum_{k=1}^{N}\left[n_{V,k}(u)n_{I,k}(v)\right]\right\}\sin(\omega u)\sin(\omega v)dudv \tag{B.88}$$

$$\sigma_{V_rI_J}(\omega)=\frac{1}{N}\int_0^{2\pi n/\omega}\int_0^{2\pi n/\omega}\left\{\sum_{k=1}^{N}\left[n_{V,k}(u)n_{I,k}(v)\right]\right\}\sin(\omega u)\cos(\omega v)dudv. \tag{B.89}$$

$$\sigma_{V_jI_r}(\omega)=\frac{1}{N}\int_0^{2\pi n/\omega}\int_0^{2\pi n/\omega}\left\{\sum_{k=1}^{N}\left[n_{V,k}(u)n_{I,k}(v)\right]\right\}\cos(\omega u)\sin(\omega v)dudv \tag{B.90}$$

$$\sigma_{V_jI_J}(\omega)=\frac{1}{N}\int_0^{2\pi n/\omega}\int_0^{2\pi n/\omega}\left\{\sum_{k=1}^{N}\left[n_{V,k}(u)n_{I,k}(v)\right]\right\}\cos(\omega u)\cos(\omega v)dudv. \tag{B.91}$$

In complete form, the components of the variance vector would be

$$\begin{aligned}\sigma_{V_r}^2(\omega)=&\frac{1}{N}\int_0^{2\pi n/\omega}\int_0^{2\pi n/\omega}\sum_{k=1}^{N}\left[n_{V,k}(u)n_{V,k}(v)\right]\sin(\omega u)\sin(\omega v)dudv\\&-\frac{2}{N}\int_0^{2\pi n/\omega}\int_0^{2\pi n/\omega}\sum_{k=1}^{N}\left[\mu_{n_V,k}n_{V,k}(u)\right]\sin(\omega u)\sin(\omega v)dudv\\&+\frac{1}{N}\int_0^{2\pi n/\omega}\int_0^{2\pi n/\omega}\sum_{k=1}^{N}\mu_{n_V,k}^2\sin(\omega u)\sin(\omega v)dudv\end{aligned} \tag{B.92}$$

$$\begin{aligned}\sigma_{V_j}^2(\omega)=&\frac{1}{N}\int_0^{2\pi n/\omega}\int_0^{2\pi n/\omega}\sum_{k=1}^{N}\left[n_{V,k}(u)n_{V,k}(v)\right]\cos(\omega u)\cos(\omega v)dudv\\&-\frac{2}{N}\int_0^{2\pi n/\omega}\int_0^{2\pi n/\omega}\sum_{k=1}^{N}\left[\mu_{n_V,k}n_{V,k}(u)\right]\cos(\omega u)\cos(\omega v)dudv\\&+\frac{1}{N}\int_0^{2\pi n/\omega}\int_0^{2\pi n/\omega}\sum_{k=1}^{N}\mu_{n_V,k}^2\cos(\omega u)\cos(\omega v)dudv\end{aligned} \tag{B.93}$$

$$\sigma_{I_r}^2(\omega)=\frac{1}{N}\int_0^{2\pi n/\omega}\int_0^{2\pi n/\omega}\sum_{k=1}^{N}\left[n_{I,k}(u)n_{I,k}(v)\right]\sin(\omega u)\sin(\omega v)dudv$$
$$-\frac{2}{N}\int_0^{2\pi n/\omega}\int_0^{2\pi n/\omega}\sum_{k=1}^{N}\left[\mu_{n_I,k}n_{I,k}(u)\right]\sin(\omega u)\sin(\omega v)dudv$$
$$+\frac{1}{N}\int_0^{2\pi n/\omega}\int_0^{2\pi n/\omega}\sum_{k=1}^{N}\mu_{n_I,k}^2\sin(\omega u)\sin(\omega v)dudv \tag{B.94}$$

$$\sigma_{I_J}^2(\omega)=\frac{1}{N}\int_0^{2\pi n/\omega}\int_0^{2\pi n/\omega}\sum_{k=1}^{N}\left[n_{I,k}(u)n_{I,k}(v)\right]\cos(\omega u)\cos(\omega v)dudv$$
$$-\frac{2}{N}\int_0^{2\pi n/\omega}\int_0^{2\pi n/\omega}\sum_{k=1}^{N}\left[\mu_{n_I,k}n_{I,k}(u)\right]\cos(\omega u)\cos(\omega v)dudv$$
$$+\frac{1}{N}\int_0^{2\pi n/\omega}\int_0^{2\pi n/\omega}\sum_{k=1}^{N}\mu_{n_I,k}^2\cos(\omega u)\cos(\omega v)dudv \tag{B.95}$$

$$\sigma_{V_rV_j}(\omega)=\frac{1}{N}\int_0^{2\pi n/\omega}\int_0^{2\pi n/\omega}\sum_{k=1}^{N}\left[n_{V,k}(u)n_{V,k}(v)\right]\sin(\omega u)\cos(\omega v)dudv$$
$$-\frac{1}{N}\int_0^{2\pi n/\omega}\int_0^{2\pi n/\omega}\sum_{k=1}^{N}\left[\mu_{n_V,k}n_{V,k}(u)\right]\sin(\omega u)\cos(\omega v)dudv$$
$$-\frac{1}{N}\int_0^{2\pi n/\omega}\int_0^{2\pi n/\omega}\sum_{k=1}^{N}\left[\mu_{n_V,k}n_{V,k}(v)\right]\sin(\omega u)\cos(\omega v)dudv$$
$$+\frac{1}{N}\int_0^{2\pi n/\omega}\int_0^{2\pi n/\omega}\sum_{k=1}^{N}\mu_{n_V,k}^2\sin(\omega u)\cos(\omega v)dudv \tag{B.96}$$

$$\sigma_{I_rI_j}(\omega)=\frac{1}{N}\int_0^{2\pi n/\omega}\int_0^{2\pi n/\omega}\sum_{k=1}^{N}\left[n_{I,k}(u)n_{I,k}(v)\right]\sin(\omega u)\cos(\omega v)dudv$$
$$-\frac{1}{N}\int_0^{2\pi n/\omega}\int_0^{2\pi n/\omega}\sum_{k=1}^{N}\left[\mu_{n_I,k}n_{I,k}(u)\right]\sin(\omega u)\cos(\omega v)dudv$$
$$-\frac{1}{N}\int_0^{2\pi n/\omega}\int_0^{2\pi n/\omega}\sum_{k=1}^{N}\left[\mu_{n_I,k}n_{I,k}(v)\right]\sin(\omega u)\cos(\omega v)dudv$$
$$+\frac{1}{N}\int_0^{2\pi n/\omega}\int_0^{2\pi n/\omega}\sum_{k=1}^{N}\mu_{n_I,k}^2\sin(\omega u)\cos(\omega v)dudv \tag{B.97}$$

$$\sigma_{V_r I_r}(\omega) = \frac{1}{N}\int_0^{2\pi n/\omega}\int_0^{2\pi n/\omega}\sum_{k=1}^{N}\left[n_{V,k}(u)n_{I,k}(v)\right]\sin(\omega u)\sin(\omega v)dudv$$
$$-\frac{1}{N}\int_0^{2\pi n/\omega}\int_0^{2\pi n/\omega}\sum_{k=1}^{N}\left[\mu_{n_V,k}n_{I,k}(u)\right]\sin(\omega u)\sin(\omega v)dudv$$
$$-\frac{1}{N}\int_0^{2\pi n/\omega}\int_0^{2\pi n/\omega}\sum_{k=1}^{N}\left[\mu_{n_I,k}n_{V,k}(u)\right]\sin(\omega u)\sin(\omega v)dudv$$
$$+\frac{1}{N}\int_0^{2\pi n/\omega}\int_0^{2\pi n/\omega}\sum_{k=1}^{N}\left[\mu_{n_V,k}\mu_{n_I,k}\right]\sin(\omega u)\sin(\omega v)dudv \tag{B.98}$$

$$\sigma_{V_r I_j}(\omega) = \frac{1}{N}\int_0^{2\pi n/\omega}\int_0^{2\pi n/\omega}\sum_{k=1}^{N}\left[n_{V,k}(u)n_{I,k}(v)\right]\sin(\omega u)\cos(\omega v)dudv$$
$$-\frac{1}{N}\int_0^{2\pi n/\omega}\int_0^{2\pi n/\omega}\sum_{k=1}^{N}\left[\mu_{n_I,k}n_{V,k}(u)\right]\sin(\omega u)\cos(\omega v)dudv$$
$$-\frac{1}{N}\int_0^{2\pi n/\omega}\int_0^{2\pi n/\omega}\sum_{k=1}^{N}\left[\mu_{n_V,k}n_{I,k}(v)\right]\sin(\omega u)\cos(\omega v)dudv$$
$$+\frac{1}{N}\int_0^{2\pi n/\omega}\int_0^{2\pi n/\omega}\sum_{k=1}^{N}\left[\mu_{n_V,k}\mu_{n_I,k}\right]\sin(\omega u)\cos(\omega v)dudv \tag{B.99}$$

$$\sigma_{V_j I_r}(\omega) = \frac{1}{N}\int_0^{2\pi n/\omega}\int_0^{2\pi n/\omega}\sum_{k=1}^{N}\left[n_{V,k}(u)n_{I,k}(v)\right]\cos(\omega u)\sin(\omega v)dudv$$
$$-\frac{1}{N}\int_0^{2\pi n/\omega}\int_0^{2\pi n/\omega}\sum_{k=1}^{N}\left[\mu_{n_I,k}n_{V,k}(u)\right]\cos(\omega u)\sin(\omega v)dudv$$
$$-\frac{1}{N}\int_0^{2\pi n/\omega}\int_0^{2\pi n/\omega}\sum_{k=1}^{N}\left[\mu_{n_V,k}n_{I,k}(v)\right]\cos(\omega u)\sin(\omega v)dudv$$
$$+\frac{1}{N}\int_0^{2\pi n/\omega}\int_0^{2\pi n/\omega}\sum_{k=1}^{N}\left[\mu_{n_V,k}\mu_{n_I,k}\right]\cos(\omega u)\sin(\omega v)dudv \tag{B.100}$$

$$\sigma_{V_j I_j}(\omega) = \frac{1}{N}\int_0^{2\pi n/\omega}\int_0^{2\pi n/\omega}\sum_{k=1}^{N}\left[n_{V,k}(u)n_{I,k}(v)\right]\cos(\omega u)\cos(\omega v)dudv$$
$$-\frac{1}{N}\int_0^{2\pi n/\omega}\int_0^{2\pi n/\omega}\sum_{k=1}^{N}\left[\mu_{n_I,k}n_{V,k}(u)\right]\cos(\omega u)\cos(\omega v)dudv$$
$$-\frac{1}{N}\int_0^{2\pi n/\omega}\int_0^{2\pi n/\omega}\sum_{k=1}^{N}\left[\mu_{n_V,k}n_{I,k}(u)\right]\cos(\omega u)\cos(\omega v)dudv$$
$$+\frac{1}{N}\int_0^{2\pi n/\omega}\int_0^{2\pi n/\omega}\sum_{k=1}^{N}\left[\mu_{n_V,k}\mu_{n_I,k}\right]\cos(\omega u)\cos(\omega v)dudv \tag{B.101}$$

These ten components are presented as the sample variance vector in Chapter 8. If the signals are discrete (digital), then the calculation of each component would require the construction of three-dimensional arrays: one dimension in time, another dimension in time (for the squaring of the integral) and a final dimension for the replicate measurements of the signals. The double integration would be conducted over the first two listed dimensions, and then averaged over the third dimension of the array.

B.2 Sample Variance as a Result of Phase Sensitive Detection

A similar procedure can be used to calculate the variance of the stochastic errors in the magnitudes of the voltage and current signals. Not all ten components of the polar form of the variance vector for PSD can be determined through the procedure, because the magnitude and phase angles of the signals are measured independently. The magnitudes of the two signals are calculated as

$$|V(\omega)| = \frac{1}{2\pi n/\omega}\left[\begin{array}{l}\int_0^{2\pi n/\omega}\hat{V}\sin(\omega t+\phi_V)\text{square}(\omega t+\phi_{s,V})dt \\ +\int_0^{2\pi n/\omega} n_V(t)\text{square}(\omega t+\phi_{s,V})dt\end{array}\right] \tag{B.102}$$

$$|I(\omega)| = \frac{1}{2\pi n/\omega}\left[\begin{array}{l}\int_0^{2\pi n/\omega} \hat{I}\sin(\omega t + \phi_I)\text{square}(\omega t + \phi_{s,I})dt \\ + \int_0^{2\pi n/\omega} n_I(t)\text{square}(\omega t + \phi_{s,I})dt\end{array}\right] \tag{B.103}$$

where the first integral corresponds to the expectation value of the magnitude and the second integral corresponds to any error in the evaluation resulting from the time-averaging of the noise in the signal.

The sample variance can be derived in similar fashion as described for the FRA measurement. To begin, the expectation of the magnitude measurements must be defined. This expectation is through the time-domain integration, and the result is

$$E[|V(\omega)|] = \hat{V} + \frac{1}{2\pi n/\omega}\left[\int_0^{2\pi n/\omega} E[n_V(t)]\text{square}(\omega t + \phi_{s,V})dt\right] \tag{B.104}$$

$$E[|I(\omega)|] = \hat{I} + \frac{1}{2\pi n/\omega}\left[\int_0^{2\pi n/\omega} E[n_I(t)]\text{square}(\omega t + \phi_{s,I})dt\right] \tag{B.105}$$

Again, the phase angle of the square wave in the noise signal integral can be neglected because the square wave should be uncorrelated with the stochastic noise signal. The sample variance of each signal can then be written as

$$\sigma^2_{|V|}(\omega) = E_f\{|V(\omega)| - E_t[|V(\omega)|]^2\} \tag{B.106}$$

$$\sigma^2_{|I|}(\omega) = E_f\{|I(\omega)| - E_t[|I(\omega)|]^2\} \tag{B.107}$$

$$\sigma_{|V||I|}(\omega) = E_f\{|V(\omega)| - E_t[|V(\omega)|]\}\{|I(\omega)| - E_t[|I(\omega)|]\} \tag{B.108}$$

Upon substitution of equations (B.102)-(B.105) into (B.106)-(B.108), the variances can be written as

$$\sigma_{|V|}^2 = \frac{1}{2\pi n/\omega} E_f \left[\int_0^{2\pi n/\omega} \{n_V(t) - E[n_V(t)]\} \text{square}(\omega t) dt \right]^2 \tag{B.109}$$

$$\sigma_{|I|}^2 = \frac{1}{2\pi n/\omega} E_f \left[\int_0^{2\pi n/\omega} \{n_I(t) - E[n_I(t)]\} \text{square}(\omega t) dt \right]^2 \tag{B.110}$$

$$\sigma_{|V||I|} = \frac{1}{2\pi n/\omega} E_f \left\{ \begin{array}{l} \left[\int_0^{2\pi n/\omega} \{n_V(t) - E[n_V(t)]\} \text{square}(\omega t) dt \right] \\ \times \left[\int_0^{2\pi n/\omega} \{n_I(t) - E[n_I(t)]\} \text{square}(\omega t) dt \right] \end{array} \right\} \tag{B.111}$$

The squares and products of these integral can be rewritten as double integrals.

$$\sigma_{|V|}^2 = \frac{1}{2\pi n/\omega} E_f \left[\int_0^{2\pi n/\omega} \int_0^{2\pi n/\omega} \left[\begin{array}{l} \{n_V(x) - E[n_V(x)]\}\{n_V(y) - E[n_V(y)]\} \\ \times \text{square}(\omega x)\text{square}(\omega y) dx dy \end{array} \right] \right] \tag{B.112}$$

$$\sigma_{|I|}^2 = \frac{1}{2\pi n/\omega} E_f \left[\int_0^{2\pi n/\omega} \int_0^{2\pi n/\omega} \left[\begin{array}{l} \{n_I(x) - E[n_I(x)]\}\{n_I(y) - E[n_I(y)]\} \\ \times \text{square}(\omega x)\text{square}(\omega y) dx dy \end{array} \right] \right] \tag{B.113}$$

$$\sigma_{|V||I|} = \frac{1}{2\pi n/\omega} E_f \left[\int_0^{2\pi n/\omega} \int_0^{2\pi n/\omega} \left[\begin{array}{l} \{n_V(x) - E[n_V(x)]\}\{n_I(y) - E[n_I(y)]\} \\ \times \text{square}(\omega x)\text{square}(\omega y) dx dy \end{array} \right] \right] \tag{B.114}$$

The product of differences in the integrands can be expanded to provide the sum of integrals as

$$\sigma_{|V|}^2 = \frac{1}{2\pi n/\omega} E_f \left[\begin{array}{l} \int_0^{2\pi n/\omega} \int_0^{2\pi n/\omega} \{n_V(x) n_V(y)\} \text{square}(\omega x)\text{square}(\omega y) dx dy \\ - \int_0^{2\pi n/\omega} \int_0^{2\pi n/\omega} \{n_V(x) E[n_V(y)]\} \text{square}(\omega x)\text{square}(\omega y) dx dy \\ - \int_0^{2\pi n/\omega} \int_0^{2\pi n/\omega} \{n_V(y) E[n_V(x)]\} \text{square}(\omega x)\text{square}(\omega y) dx dy \\ + \int_0^{2\pi n/\omega} \int_0^{2\pi n/\omega} \{E[n_V(x)] E[n_V(y)]\} \text{square}(\omega x)\text{square}(\omega y) dx dy \end{array} \right] \tag{B.115}$$

$$\sigma_{|I|}^2 = \frac{1}{2\pi n/\omega} E_f \left[\begin{array}{l} \int_0^{2\pi n/\omega} \int_0^{2\pi n/\omega} \{n_I(x) n_I(y)\} \text{square}(\omega x) \text{square}(\omega y) dx dy \\ - \int_0^{2\pi n/\omega} \int_0^{2\pi n/\omega} \{n_I(x) E[n_I(y)]\} \text{square}(\omega x) \text{square}(\omega y) dx dy \\ - \int_0^{2\pi n/\omega} \int_0^{2\pi n/\omega} \{n_I(y) E[n_I(x)]\} \text{square}(\omega x) \text{square}(\omega y) dx dy \\ + \int_0^{2\pi n/\omega} \int_0^{2\pi n/\omega} \{E[n_I(x)] E[n_I(y)]\} \text{square}(\omega x) \text{square}(\omega y) dx dy \end{array} \right] \tag{B.116}$$

$$\sigma_{|V||I|} = \frac{1}{2\pi n/\omega} E_f \left[\begin{array}{l} \int_0^{2\pi n/\omega} \int_0^{2\pi n/\omega} \{n_V(x) n_I(y)\} \text{square}(\omega x) \text{square}(\omega y) dx dy \\ - \int_0^{2\pi n/\omega} \int_0^{2\pi n/\omega} \{n_V(x) E[n_I(y)]\} \text{square}(\omega x) \text{square}(\omega y) dx dy \\ - \int_0^{2\pi n/\omega} \int_0^{2\pi n/\omega} \{n_I(y) E[n_V(x)]\} \text{square}(\omega x) \text{square}(\omega y) dx dy \\ + \int_0^{2\pi n/\omega} \int_0^{2\pi n/\omega} \{E[n_V(x)] E[n_I(y)]\} \text{square}(\omega x) \text{square}(\omega y) dx dy \end{array} \right] \tag{B.117}$$

The remaining expectation can be written as an average of samplings, and the square waves can be rewritten in their Fourier series expansions.

$$\sigma_{|V|}^2 = \frac{\omega}{2\pi n M}\sum_{m=1}^{M}\left\{\begin{array}{l}\displaystyle\int_0^{2\pi n/\omega}\int_0^{2\pi n/\omega} dxdy\left[\begin{array}{l} n_{V,m}(x)n_{V,m}(y) \\ \times\displaystyle\sum_{k=0}^{\infty}\sum_{l=0}^{\infty}\frac{1}{(2k+1)(2l+1)}\left\{\begin{array}{l}\sin[(2k+1)\omega x] \\ \times\sin[(2l+1)\omega y]\end{array}\right\}\end{array}\right] \\ \displaystyle-\int_0^{2\pi n/\omega}\int_0^{2\pi n/\omega} dxdy\left[\begin{array}{l} \mu_{n_V,m}n_{V,m}(x) \\ \times\displaystyle\sum_{k=0}^{\infty}\sum_{l=0}^{\infty}\frac{1}{(2k+1)(2l+1)}\left\{\begin{array}{l}\sin[(2k+1)\omega x] \\ \times\sin[(2l+1)\omega y]\end{array}\right\}\end{array}\right] \\ \displaystyle-\int_0^{2\pi n/\omega}\int_0^{2\pi n/\omega} dxdy\left[\begin{array}{l} \mu_{n_V,m}n_{V,m}(y) \\ \times\displaystyle\sum_{k=0}^{\infty}\sum_{l=0}^{\infty}\frac{1}{(2k+1)(2l+1)}\left\{\begin{array}{l}\sin[(2k+1)\omega x] \\ \times\sin[(2l+1)\omega y]\end{array}\right\}\end{array}\right] \\ \displaystyle+\int_0^{2\pi n/\omega}\int_0^{2\pi n/\omega} dxdy\left[\begin{array}{l} \mu_{n_V,m}^2 \\ \times\displaystyle\sum_{k=0}^{\infty}\sum_{l=0}^{\infty}\frac{1}{(2k+1)(2l+1)}\left\{\begin{array}{l}\sin[(2k+1)\omega x] \\ \times\sin[(2l+1)\omega y]\end{array}\right\}\end{array}\right]\end{array}\right\} \tag{B.118}$$

$$\sigma_{|I|}^2 = \frac{\omega}{2\pi n M}\sum_{m=1}^{M}\left\{\begin{array}{l}\displaystyle\int_0^{2\pi n/\omega}\int_0^{2\pi n/\omega} dxdy\left[\begin{array}{l} n_{I,m}(x)n_{I,m}(y) \\ \times\displaystyle\sum_{k=0}^{\infty}\sum_{l=0}^{\infty}\frac{1}{(2k+1)(2l+1)}\left\{\begin{array}{l}\sin[(2k+1)\omega x] \\ \times\sin[(2l+1)\omega y]\end{array}\right\}\end{array}\right] \\ \displaystyle-\int_0^{2\pi n/\omega}\int_0^{2\pi n/\omega} dxdy\left[\begin{array}{l} \mu_{n_I,m}n_{I,m}(x) \\ \times\displaystyle\sum_{k=0}^{\infty}\sum_{l=0}^{\infty}\frac{1}{(2k+1)(2l+1)}\left\{\begin{array}{l}\sin[(2k+1)\omega x] \\ \times\sin[(2l+1)\omega y]\end{array}\right\}\end{array}\right] \\ \displaystyle-\int_0^{2\pi n/\omega}\int_0^{2\pi n/\omega} dxdy\left[\begin{array}{l} \mu_{n_I,m}n_{I,m}(y) \\ \times\displaystyle\sum_{k=0}^{\infty}\sum_{l=0}^{\infty}\frac{1}{(2k+1)(2l+1)}\left\{\begin{array}{l}\sin[(2k+1)\omega x] \\ \times\sin[(2l+1)\omega y]\end{array}\right\}\end{array}\right] \\ \displaystyle+\int_0^{2\pi n/\omega}\int_0^{2\pi n/\omega} dxdy\left[\begin{array}{l} \mu_{n_I,m}^2 \\ \times\displaystyle\sum_{k=0}^{\infty}\sum_{l=0}^{\infty}\frac{1}{(2k+1)(2l+1)}\left\{\begin{array}{l}\sin[(2k+1)\omega x] \\ \times\sin[(2l+1)\omega y]\end{array}\right\}\end{array}\right]\end{array}\right\} \tag{B.119}$$

$$\sigma_{|V||I|} = \frac{\omega}{2\pi n M} \sum_{m=1}^{M} \left\{ \begin{array}{l} \int_0^{2\pi n/\omega} \int_0^{2\pi n/\omega} dxdy \left[\begin{array}{l} n_{V,m}(x) n_{I,m}(y) \\ \times \sum_{k=0}^{\infty} \sum_{l=0}^{\infty} \frac{1}{(2k+1)(2l+1)} \left\{ \begin{array}{l} \sin[(2k+1)\omega x] \\ \times \sin[(2l+1)\omega y] \end{array} \right\} \end{array} \right] \\ - \int_0^{2\pi n/\omega} \int_0^{2\pi n/\omega} dxdy \left[\begin{array}{l} \mu_{n_I,m} n_{V,m}(x) \\ \times \sum_{k=0}^{\infty} \sum_{l=0}^{\infty} \frac{1}{(2k+1)(2l+1)} \left\{ \begin{array}{l} \sin[(2k+1)\omega x] \\ \times \sin[(2l+1)\omega y] \end{array} \right\} \end{array} \right] \\ - \int_0^{2\pi n/\omega} \int_0^{2\pi n/\omega} dxdy \left[\begin{array}{l} \mu_{n_V,m} n_{I,m}(y) \\ \times \sum_{k=0}^{\infty} \sum_{l=0}^{\infty} \frac{1}{(2k+1)(2l+1)} \left\{ \begin{array}{l} \sin[(2k+1)\omega x] \\ \times \sin[(2l+1)\omega y] \end{array} \right\} \end{array} \right] \\ + \int_0^{2\pi n/\omega} \int_0^{2\pi n/\omega} dxdy \left[\begin{array}{l} \mu_{n_V,m} \mu_{n_I,m} \\ \times \sum_{k=0}^{\infty} \sum_{l=0}^{\infty} \frac{1}{(2k+1)(2l+1)} \left\{ \begin{array}{l} \sin[(2k+1)\omega x] \\ \times \sin[(2l+1)\omega y] \end{array} \right\} \end{array} \right] \end{array} \right\} \tag{B.120}$$

As noted in Chapter 8, the entire variance vector cannot be determined for the PSD technique because the phase angle is determined independently of the magnitude of a signal. Thus the seven variance vector components that correlate the phase angle can not be explicitly determined.

BIBLIOGRAPHY

1. Zukowski, C. F. IV and Saville, D. A., *Journal of Colloid and Interface Science*, **107**, 322-333 (1985).

2. O'Brien, R. W., *Handbook on Characterization Techniques for Solid-Solution Interface*, The American Ceramic Society, Westerville, OH (1993).

3. Hiemenz, P. C. and Rajagopalan, R., *Principles of Colloid and Surface Chemistry*, Marcel Dekker, New York (1997).

4. Vold, M. J. and Vold, R. D., *Colloid Chemistry*, Reinhold Publishing Corp., New York (1964).

5. Macdonald, J. R., *Impedance Spectroscopy : Emphasizing Solid Materials and Systems*, Wiley, New York (1987).

6. Agarwal, P., Orazem, M. E., and García-Rubio, L. H., *Journal of the Electrochemical Society*, **139**, 1917-1927 (1992).

7. Agarwal, P., Crisalle, O. D., Orazem, M. E., and García-Rubio, L. H., *Journal of the Electrochemical Society*, **142**, 4149-4158 (1995).

8. Agarwal, P., Orazem, M. E., and García-Rubio, L. H., *Journal of the Electrochemical Society*, **142**, 4159-4168 (1995).

9. Durbha, M., Orazem, M. E., and García-Rubio, L. H., *Journal of the Electrochemical Society*, **144**, 48-55 (1997).

10. Macdonald, J. R. and Franceschetti, D. R., *Journal of Electroanalytical Chemistry*, **307**, 1-11 (1991).

11. Macdonald, J. R. and Potter, L. D., Jr., *Solid State Ionics*, **23**, 61-79 (1987).

12. Macdonald, J. R. and Thompson, W. J., *Communications in Statistics Simulation and Computation*, **20**, 843-886 (1991).

13. Macdonald, J. R. and Thompson, W. J., *American Journal of Physics*, **60**, 66-73 (1992).

14. Wojcik, P. T., Agarwal, P., and Orazem, M. E., *Electrochimica Acta*, **41**, 977-983 (1996).

15. Wojcik, P. T., and Orazem, M. E., Paper #97-435, National Association of Corrosion Engineers, Houston, Texas (1997).

16. Wojcik, P. T., and Orazem, M. E., Paper #97-282, National Association of Corrosion Engineers, Houston, Texas (1997).

17. Macdonald, J. R. and Piterbarg, V. I., *Journal of Electroanalytical Chemistry*, **428**, 1-9 (1997).

18. Henry, D. C., *Proceedings of the Royal Society of London, Series A*, **133**, 106-129 (1931).

19. Fairhurst, D. and Ribitsch, V., *Particle Size Distribution II*, American Chemical Society, Washington, D. C. (1991).

20. Newman, J. S., *Electrochemical Systems*, Prentice Hall, Englewood Cliffs, NJ (1991).

21. Stumm, W. and Morgan, J. J., *Aquatic Chemistry -- An Introduction Emphasizing Chemical Equalibria in Natural Waters*, John Wiley & Sons, New York, NY (1981).

22. Horn, R. G. and Grabbe, A., *Handbook on Characterization Techniques for Solid-Solution Interface*, The American Ceramic Society, Westerville, OH (1993).

23. Giordano-Palmino, F., Denoyel, R., and Rouquerol, J., *Journal of Colloid and Interface Science*, **165**, 82-90 (1994).

24. Booth, F., *Proceedings of the Royal Society of London, Series A*, **203**, 533-551 (1950).

25. De La Rue, R. E. and Tobias, C. W., *Journal of the Electrochemical Society*, **108**, 827-832 (1959).

26. Meredith, R. E. and Tobias, C. W., *Journal of Applied Physics*, **31**, 1270-1273 (1960).

27. Miller, B. V. and Lines, R. W., *Analytical Chemistry*, **20**, 2, 75-116 (1988).

28. Studt, T., *Research & Development Magazine*, **38**, 5, 28-31 (1996).

29. Ennis, B. J., Green, J., and Davies, R., *Chemical Engineering Progress*, **90**, 32-43 (1994).

30. Knowlton, T. M., Carson, J. W., Klinzing, G. E., and Yang, W.-C., *Chemical Engineering Progress*, **90**, 44-54 (1994).

31. Lord Rayleigh, *Phys. Mag.*, **34**, 481-502 (1892).

32. Sumner, C. G. and Henry, D. C., *Proceedings of the Royal Society of London, Series A*, **133**, 106-129 (1931).

33. Ohshima, H., *Journal of Colloid and Interface Science*, **168,** 269-271 (1994).

34. Henry, D. C., *Transactions of the Faraday Society*, **44**, 1021-1026 (1948).

35. Booth, F., *Proceedings of the Royal Society of London, Series A*, **203**, 514-533 (1950).

36. Wiersema, P. H., Loeb, A. L., and Overbeek, J. Th. G., *Journal of Colloid and Interface Science*, **22**, 78-99 (1966).

37. Saville, D. A., *Journal of Colloid and Interface Science*, **71**, 477-490 (1979).

38. Zukowski, C. F. IV and Saville, D. A., *Journal of Colloid and Interface Science*, 115, 422-436 (1987).

39. Saville, D. A., *Journal of Colloid and Interface Science*, 91, 34-50 (1982).

40. O'Brien, R. W., *Journal of Colloid and Interface Science*, **81**, 234-248 (1981).

41. O'Brien, R. W. and Perrins, T. M., *Journal of Colloid and Interface Science*, **99**, 20-31 (1984).

42. Ohshima, H. and Healy, T. W., *Journal of the Chemical Society, Faraday Transactions 2*, **80**, 1643-1667 (1984).

43. Ohshima, H., Healy, T. W., and White, L. R., *Journal of the Chemical Society, Faraday Transactions 2*, **79**, 1613-1628 (1983).

44. Dukhin, S. S., *Advances in Colloid and Interface Science*, **44**, 1-134 (1993).

45. Dukhin, S. S. and Shilov, V. N., *Advances in Colloid and Interface Science*, **13**, 153-195 (1980).

46. Dull, C. E., Metcalfe, H. C., and Williams, J. E., *Modern Physics*, Holt, Rinehart, and Winston, Inc., New York, NY (1960).

47. O'Brien, R. W. and White, L. R., *Journal of the Chemical Society, Faraday Transactions 2*, **74**, 1607-1626 (1978).

48. O'Brien, R. W. and Hunter, R. J., *Canadian Journal of Chemistry*, **59**, 1878-1887 (1981).

49. O'Brien, R. W., *Journal of Colloid and Interface Science*, **92**, 204-216 (1983).

50. O'Brien, R. W. and Ward, D. N., *Journal of Colloid and Interface Science*, **121**, 402-413 (1988).

51. Anderson, J. L., *Journal of Colloid and Interface Science*, **105**, 45-54 (1985).

52. Fair, M. C. and Anderson, J. L., *Journal of Colloid and Interface Science*, **127**, 388-400 (1989).

53. Fair, M. C. and Anderson, J. L., *International Journal of Multiphase Flow*, **16**, 663-679 (1990).

54. Solomentsev, Y. E. and Anderson, J. L., *Journal of Fluid Mechanics*, **279**, 197-215 (1994).

55. Solomentsev, Y. E., Pawar, Y., and Anderson, J. L., *Journal of Colloid and Interface Science*, **158**, 1-9 (1993).

56. Yoon, B. J., *Journal of Colloid and Interface Science*, **142**, 575-581 (1991).

57. Ohshima, H., Healy, T. W., and White, L. R., *Journal of the Chemical Society, Faraday Transactions 2*, **79**, 1613-1628 (1983).

58. Ohshima, H., Healy, T. W., and White, L. R., *Journal of the Chemical Society, Faraday Transactions 2*, **80**, 1299-1317 (1984).

59. Zukowski, C. F. IV and Saville, D. A., *Journal of Colloid and Interface Science*, **114**, 32-44 (1986).

60. Zukowski, C. F. IV and Saville, D. A., *Journal of Colloid and Interface Science*, **114**, 45-53 (1986).

61. Dukhin, A. S. and Van De Ven, T. G. M., *Journal of Colloid and Interface Science*, **165**, 9-18 (1994).

62. Ohshima, H. and Kondo, T., *Colloid & Polymer Science*, **264**, 1080-1084 (1986).

63. Oshima, H., *Journal of Colloid and Interface Science*, **163**, 474-483 (1994).

64. Ohshima, H. and Kondo, T., *Journal of Colloid and Interface Science*, **130**, 281-282 (1987).

65. Ohshima, H. and Kondo, T., *Journal of Colloid and Interface Science*, **116**, 305-311 (1989).

66. Ohshima, H., Nakamura, N. and Kondo, T., *Colloid & Polymer Science*, **270**, 873-877 (1992).

67. Ohshima, H. and Kondo, T., *Journal of Colloid and Interface Science*, **135**, 443-448 (1990).

68. Fair, M. C. and Anderson, J. L., *Langmuir*, **8**, 2850-2854 (1992).

69. James, M., Hunter, R. J., and O'Brien, R. W., *Langmuir*, **8**, 420-423 (1992).

70. Loewenberg, M., *Journal of Fluid Mechanics*, **278**, 149-174 (1994).

71. Fricke, H. and Curtis, H. J., *Journal of Physical Chemistry*, **41**, 729-745 (1937).

72. O'Brien, R. W., *Advances in Colloid and Interface Science*, **16**, 281-320 (1982).

73. DeLacey, E. H. B. and White, L. R., *Journal of the Chemical Society, Faraday Transactions 2*, **77**, 2007-2039 (1981).

74. Orazem, M. E., Agarwal, P., Deslouis, C., and Tribollet, B., *Journal of the Electrochemical Society*, **143**, 948-960 (1996).

75. Hinch, E. J., Sherwood, J. D., Chew, W. C., and Sen, P. N., *Journal of the Chemical Society, Faraday Transactions 2*, **80**, 535-551 (1984).

76. Carmona-Ribeiro, A. M. and Midmore, B. R., *Langmuir*, **8**, 801-806 (1992).

77. Biscan, J. and Kosec, M., *Handbook on Characterization Techniques for Solid-Solution Interface*, The American Ceramic Society, Westerville, OH (1993).

78. Strohmeier, F., *Hewlett-Packard Journal*, **46**, 10-19 (1995).

79. Holloway, R. R., *Hewlett-Packard Journal*, **46**, 6-9 (1995).

80. Kaltenbach, P., *Hewlett-Packard Journal*, **46**, 20-24 (1995).

81. Swedberg, S. A. and Dittmann, M., *Hewlett-Packard Journal*, **46**, 57-61 (1995).

82. Zimmermann, H.-P., *Hewlett-Packard Journal*, **46**, 25-27 (1995).

83. Rowell, R. L., Shiau, S.-J., and Marlow, B. J., *Particle Size Distribution II*, American Chemical Society, Washington, D. C. (1991).

84. Grasselli, Y. and Bossis, G., *Journal of Colloid and Interface Science*, **170**, 269-274 (1995).

85. Xu, R., *Langmuir*, **9**, 2955-2962 (1993).

86. Shubin, V. E., Hunter, R. J., and O'Brien, R. W., *Journal of Colloid and Interface Science*, **159**, 174-183 (1993).

87. Hackley, V. A., Premachdran, R. S., Malghan, S. G., *Handbook on Characterization Techniques for Solid-Solution Interface*, The American Ceramic Society, Westerville, OH (1993).

88. Pollinger, J. P., Newson, D. D., and Nick, J. J., *Handbook on Characterization Techniques for Solid-Solution Interface*, The American Ceramic Society, Westerville, OH (1993).

89. Siano, S., *Research & Development Magazine*, **38**, 2, 45-46 (1996).

90. Myers, D. F. and Saville, D. A., *Journal of Colloid and Interface Science*, **131**, 448-460 (1989).

91. DeLacey, E. H. B. and White, L. R., *Journal of the Chemical Society, Faraday Transactions 2*, **78**, 457-479 (1982).

92. Myers, D. F. and Saville, D. A., *Journal of Colloid and Interface Science*, **131**, 461-470 (1989b).

93. Rosen, L. A. and Saville, D. A., *Langmuir*, **7**, 36-42 (1991).

94. Dunstan, D. E., *Journal of Colloid and Interface Science*, **163**, 235-258 (1994).

95. Zeltner, W. A., Wang, J.-F., Omatete, O. O., Janney, M. A., Tejedor-Tejedor, M. I., Anderson, M. A., Riman, R. E., Shanefield, D. J., and Adair, J. H., *Handbook on Characterization Techniques for Solid-Solution Interface*, The American Ceramic Society, Westerville, OH (1993).

96. Midmore, B. R. and Hunter, R. J., *Journal of Colloid and Interface Science*, **122**, 521-529 (1988).

97. Midmore, B. R., Diggins, D., and Hunter, R. J., *Journal of Colloid and Interface Science*, **129**, 153-161 (1989).

98. Dunstan, D. E., *Journal of Colloid and Interface Science*, **152**, 297-307 (1992).

99. Dunstan, D. E., *Langmuir*, **8**, 1507-1508 (1992).

100. Anderson, J. L., *Annual Review of Fluid Mechanics*, **21**, 61-99 (1989).

101. Koopal, L. K. and Dukhin, S. S., *Colloids and Surfaces A: Physiochemical and Engineering Aspects*, **73**, 201-209 (1993).

102. Dukhin, S. S. and Shilov, V. N., *Dielectric Phenomena and the Double Layer in Disperse Systems and Polyelectrolytes*, Halsted Press, John Wiley & Sons, New York (1974).

103. Van Riemsdijk, W. H., Bolt, G. H., Koopal, L. K., and Blaakmeer, J., *Journal of Colloid and Interface Science*, **109**, 219-228 (1986).

104. Kops-Werkhoven, M. M. and Fijnaut, *Light Scattering in Liquids and Macromolecular Solutions*, Plenum Press, New York (1980).

105. Macdonald, J.R. and Garber, J.A., *Journal of the Electrochemical Society*, **124**, 1022-1030 (1977).

106. Boukamp, B.A., *Solid State Ionics*, **18&19**, 136-140 (1986).

107. Sheppard, R.J., Jordan, B.P., and Grant, E.H., *Journal of Physics D: Applied Physics*, **3**, 1759-1764 (1970).

108. Sheppard, R.J., *Journal of Physics D: Applied Physics*, **6**, 790-794 (1973).

109. Macdonald, J.R., Schoonman, J., and Lehnen, A.P., *Journal of Electroanalytical Chemistry*, **131**, 77-85 (1982).

110. Zoltowski, P., *Journal of Electroanalytical Chemistry*, **178**, 11-19 (1984).

111. Zoltowski, P., *Journal of Electroanalytical Chemistry*, **424**, 173-178 (1997).

112. Boukamp, B.A., *Solid State Ionics*, **20**, 31-44 (1986).

113. Zoltowski, P., *Journal of Electroanalytical Chemistry*, **375**, 45-57 (1994).

114. Dygas, J. R., Bogusz, W., and Krok, F., "Impedance Spectroscopy with Simultaneous Sampling of Error Variance," presented at the Fourth International Symposium on Electrochemical Impedance Spectroscopy, Rio de Janeiro, Brazil (August 2-7, 1998).

115. Atkinson, K. E., *An Introduction to Numerical Analysis*, John Wiley & Sons, New York (1989).

116. Eykhoff, P., *System Identification -- Parameter and State Estimation*, John Wiley & Sons, New York (1974).

117. Milocco, R. H. and Biagiola, S. I., *Current Topics in Electrochemistry*, **3**, 553-567 (1994).

118. Durbha, M., Carson, S., Kalajian, A., Lazzara, M., Orazem, M., "Common Features of Electrochemical and Mechanical Spectroscopy Measurements," paper 98h, Annual Meeting of the American Institute of Chemical Engineerins (November 16-21, 1997).

119. Pichaud, M. P., "Design and Analysis of Dielectric Spectroscopy Instrumentation," High Honors Report, Department of Chemical Engineering, University of Florida (1998).

120. Macdonald, J. R., *Electrochimica Acta*, **38**, 1883-1890 (1993).

121. Gabrielli, C., *Identification of Electrochemical Processes by Frequency Response Analysis*, Technical Report Number 004/83, Solartron Instruments, Issue 2 (August 1984).

122. Beyer, W. H., *CRC Standard Mathematical Tables and Formulae*, 29th Ed., CRC Press, Boca Raton (1991).

123. W. H. Press, B. P. Flannery, S. A. Teukolsky, W. T. Vetterling, *Numerical Recipes: The Art of Scientific Computing (FORTRAN Version)*, Cambridge University Press, New York (1989).

124. Harnett, D. L., Introduction to Statistical Methods, Addison-Wesley Publishing Co., Reading, MA (1971).

BIOGRAPHICAL SKETCH

The author claims St. Louis, Missouri, as his home. In 1988, he left the Midwest to attend the California Institute of Technology in Pasadena, California. After four years of too much fun and too much work, he received the degree of Bachelor of Science in Chemical Engineering from Caltech in 1992. The job market was depressed that year, so the author decided to seek a graduate degree. In 1995, he received the Master of Science degree in chemical engineering from the University of Florida. The author continued his studies at the University of Florida to seek a Ph.D. and working with Dr. Mark E. Orazem.

I certify that I have read this study and that in my opinion it conforms to acceptable standards of scholarly presentation and is fully adequate, in scope and quality, as a dissertation for the degree of Doctor of Philosophy.

Mark E. Orazem, Chairman
Professor of Chemical Engineering

I certify that I have read this study and that in my opinion it conforms to acceptable standards of scholarly presentation and is fully adequate, in scope and quality, as a dissertation for the degree of Doctor of Philosophy.

Oscar D. Crisalle
Associate Professor of Chemical Engineering

I certify that I have read this study and that in my opinion it conforms to acceptable standards of scholarly presentation and is fully adequate, in scope and quality, as a dissertation for the degree of Doctor of Philosophy.

Luis H. García-Rubio
Professor of Chemical Engineering
University of South Florida

I certify that I have read this study and that in my opinion it conforms to acceptable standards of scholarly presentation and is fully adequate, in scope and quality, as a dissertation for the degree of Doctor of Philosophy.

Chang Won Park
Associate Professor of Chemical Engineering

I certify that I have read this study and that in my opinion it conforms to acceptable standards of scholarly presentation and is fully adequate, in scope and quality, as a dissertation for the degree of Doctor of Philosophy.

James D. Winefordner
Graduate Research Professor of
Chemistry

This dissertation was submitted to the Graduate Faculty of the College of Engineering and to the Graduate School and was accepted as partial fulfillment of the requirements for the degree of Doctor of Philosophy.

May, 1999

Winfred M. Phillips
Dean, College of Engineering

M. J. Ohanian
Dean, Graduate School

IMAGE EVALUATION TEST TARGET (QA-3)

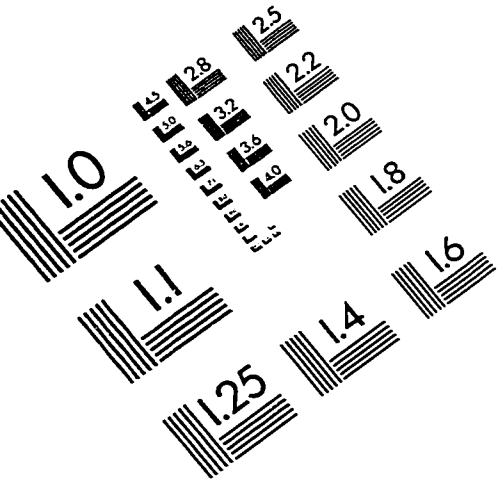

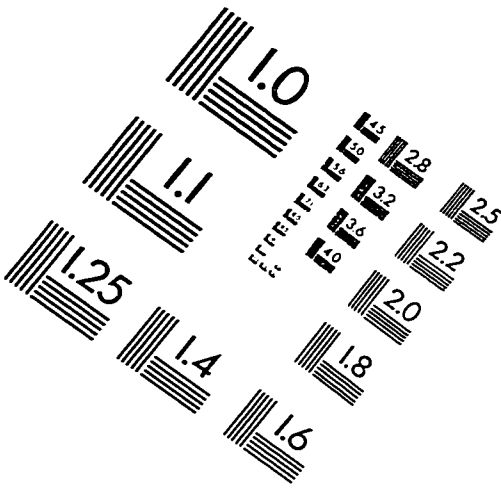

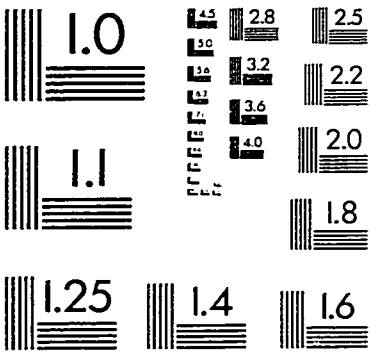

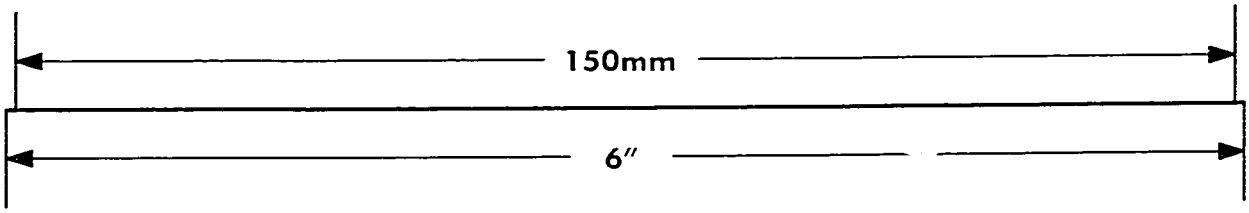

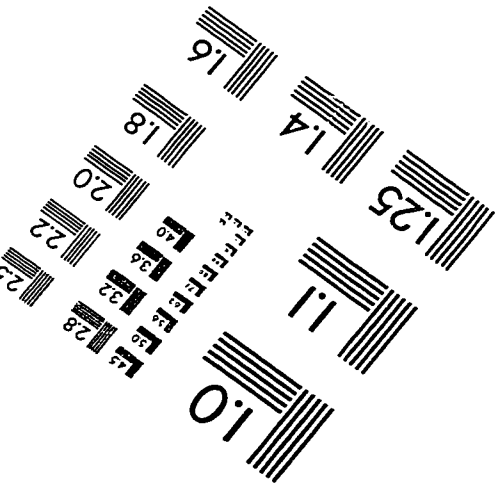

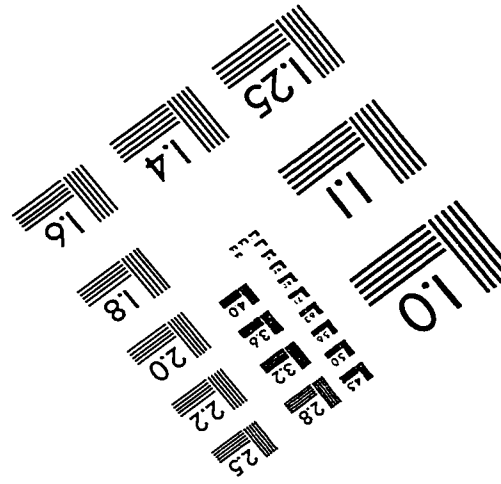

APPLIED IMAGE, Inc
1653 East Main Street
Rochester, NY 14609 USA
Phone: 716/482-0300
Fax: 716/288-5989

© 1993, Applied Image, Inc., All Rights Reserved